



Università degli Studi di Ferrara
Institut National Polytechnique de Grenoble

# Modelling and Characterization of Guiding Micro-structured Devices for Integrated Optics

Ph. D. Thesis

by Andrea Armaroli

Advisers:
Pr. Pierre Benech (INPG)
Pr. Stefano Trillo (UNIFE)
Dr. Alain Morand (UJF)
Dr. Gaetano Bellanca (UNIFE)

defended on
14 March 2008

# Acknowledgements

*I would like to acknowledge my parents, who have never stopped encouraging me during my doctoral course, and particularly when I was abroad. Their suggestions, their support have been among the most valuable contributions to the pursuit of my goals.*

*I wish to acknowledge the other students and colleagues with whom working days has been rich in happy moments; thanks for the jokes, the suggestions, the lunch times spent together. We are still in touch and I hope we will keep time to keep in touch in the future. I am thankful to all the colleagues I met at my beloved University of Ferrara: Chiara, Riccardo, Carlo, Raffaele, who now represent the everyday working environment and are, each in his own way, a funny company.*

*I have appreciated the help of my friends, especially to overcome the many doubts and apprehensions that I had before setting off to France, as well as during my stay abroad. I mention Paolo, a really hard worker, who despite all his occupations, has been always willing to help and comfort me.*

*I wish to thank Prof. Stefano Trillo, who shared with me several of its inspiring ideas and Physics insights, and proposed several interesting research topics. To Dr. Gaetano Bellanca, who devoted much time and effort to assist my activities, to overcome the red tape obstacles, to draw up the agreement that allowed my stay in Grenoble. In order to help me, he also focused his work on new topics and provided many important results.*

*I wish to acknowledge Prof. Pierre Benech and Dr. Alain Morand, who welcomed me in their team at the IMEP laboratory, who proposed a challenging and exciting research activity, to which I devoted much effort, and helped me clarifying many aspects of optical sciences.*

*I would like to mention all the colleagues at IMEP that invited me to several social activities and taught me some basic elements of the French life-style.*

*I recall Prof. Setti and Prof. Clerc who are in charge of the EDITH (European doctorate on information technology) project in Bologna and Grenoble, respectively. They supported me in many situations and dealt with several problems I would have never found a solution to by myself. Thanks to that project, I spent an year in one of the most thriving and lively towns of France, Grenoble. This is an example of what should Europe become to be a real community: the role of Culture, of Science, of advanced technology, the presence of many different nationalities working together (and of course a long-lasting Italian presence) are the strong points of Grenoble and its region.*

# Contents

# Abstract

This thesis is mainly devoted to the description of modelling techniques for integrated optical devices. In recent years we assisted to a renewed interest in this field (also known as *photonics*), since also electronic industry have started to work on these topics in order to, e.g., improve chip to chip communications by means of optical interconnects. This solution needs to develop integrated sources, waveguides, and processing devices. Moreover, since silicon is primarily used in CMOS technology, it would be convenient to implement photonic systems on silicon: this is generally easily used for passive devices (waveguides, taper...), but several fundamental breakthroughs have been obtained in recent years, that prove active features can be brought to this material.

Several design principles and applications are available in integrated optics: in the last years periodic structures and resonators have been thoroughly investigated. Moreover in integrated devices many interesting physical effects can be studied.

Our work is focused on two topics:

- nonlinear optics, specifically spatial soliton propagation;
- microresonators.

Spatial solitons arise from perfect compensation of diffraction and nonlinear focusing. We described how it is possible to achieve trapping in arrays of evanescently-coupled waveguides. As in any periodic systems we have angles corresponding to Bragg reflection, i.e. a band-diagram is used to describe diffraction characteristics, where evanescent wavenumbers correspond to total reflection. By dynamically inducing arrays in photorefractive media, it is possible to implement dynamic routing functionalities. It is possible to have solutions that compensate diffraction at a specific angle, but also nonlinearity could enable to find propagating waves at forbidden longitudinal wavenumbers, i.e. lying inside the band-gap.

We prove that the usual CMT modelling of Kerr solitons, that looks for two envelopes propagating in the proximity of Bragg angle, can be compared with a numerical solution of paraxial wave-equation. We obtain that for index contrasts used in experiments these two approaches give comparable results, except a slight discrepancy at the lower edge of gap. An own implementation of nonlinear BPM is used to further verify this properties.

Also solutions arising in quadratic media are studied and the effect on phase-mismatch at different positions inside gap are shown. In fact at phase-matching, FF and SH can be excited at the same angles, that correspond to first order and second order Bragg reflection, respectively.

The second topic is represented by microcavities: this devices are among the most promising structures in integrated optics. They permit to achieve extreme selectivity, and are applied to passive devices, but also basic physics experiments can be performed, e.g. cavity-quantum-electrodynamics.

We focused on implementing a 3D method based on the rigorous coupled-wave analysis, also known as Fourier modal method (FMM). When applied to waveguide modelling it is named aperiodic-FMM (A-FMM) and approximates modes by Bloch modes of a periodic structure. By applying PMLs we can improve the accuracy, and decoupling successive artificial repetitions. An admittance-impedance formalism is used to account for multiple reflections along the radial direction.

We implement it in cylindrical coordinates, and are thus able to study structures of rotational symmetry, such as microrings and microdisks. We verify that this approach is more accurate than 2D methods, while being faster than *ab-initio* methods, such as FDTD.

We report also an example of a device that relies upon antiguiding confinement along the axis. It is indeed possible to confine light, via interaction of two TM evanescent tails, in a low-index region. Mode volume can be remarkably reduced.

Finally we characterised several integrated structures, specifically microdisk-based filters and add&drops. We detect resonances of a set of devices based on a large-diameter ($8\mu m$) disk. Their high-$Q$ could permit to detect splitting of degeneracies and nonlinear effects. Nevertheless the sensitivity to technological defects hampered the opportunity of providing an extensive and reliable description.

Future work will be devoted to improving our numerical methods, to understand how to properly design microdisk-based devices. Another interesting theme is to detect narrow and short rejection peaks, sometimes masked by Fabry-Pérot oscillations due to reflections inside the straight waveguide.

# Résumé Étendu

Ces dernières années, nous avons assisté à de nouvelles exploitations de l'optique intégrée dont les applications ne sont pas dans le domaine classique des communications longues distances. En effet, de nombreuses découvertes ont été faites dans le traitement de la lumière inter et intra-puce. L'émission continue basée sur l'effet Raman permet au Silicium d'être un candidat possible pour réaliser des composants actifs tout en assurant une bonne efficacité de guidage. Comme la microélectronique CMOS utilise comme matériau de base le Silicium, la fusion de la photonique et de la microélectronique est devenue un axe important de recherche pour les chercheurs des universités mais aussi ceux des industries telles que Intel, STM ou IBM.

Dans ce cadre, deux types de composants sont largement utilisés : les structures périodiques (cristaux photoniques) ou les microcavités à structures réfractives. Ils permettent d'accéder à de nombreuses fonctions à la fois passives et actives ainsi qu'à exploiter des phénomènes physiques innovants. La première configuration sera utilisée pour mettre en avant des phénomènes non-linéaires tels que l'auto-confinement spatial de la lumière sous forme de solitons. La deuxième configuration sera discutée en proposant l'analyse de microcavités optiques et en particulier des microdisques.

La plus grande partie de cette thèse est consacrée à la modélisation de ces structures. Grâce au banc de mesures de l'IMEP, quelques résultats de caractérisation seront présentés en fin thèse.

## Chapitre 1

La modélisation des dispositifs d'optique intégrée est une activité importante pour fournir une base solide au processus de conception. Elle permet aussi de mettre en avant de nouveaux phénomènes et de concevoir de nouveaux composants.

Les équations de Maxwell sont toujours utilisés pour étudier les problèmes d'électromagnétisme et d'optique. Nous les écrivons pour une région sans charges comme

$$\nabla \times \vec{\mathcal{E}}(x,y,z,t) = -\frac{\partial \vec{\mathcal{B}}(x,y,z,t)}{\partial t} \tag{1}$$

$$\nabla \times \vec{\mathcal{H}}(x,y,z,t) = \frac{\partial \vec{\mathcal{D}}(x,y,z,t)}{\partial t} \tag{2}$$

$$\nabla \cdot \vec{\mathcal{D}}(x,y,z,t) = 0 \tag{3}$$

$$\nabla \cdot \vec{\mathcal{B}}(x,y,z,t) = 0 \tag{4}$$

avec la notation symbolique suivante,

- $\vec{\mathcal{E}}$ champ électrique ;
- $\vec{\mathcal{H}}$ champ magnétique ;
- $\vec{\mathcal{D}}$ champ induction électrique ;
- $\vec{\mathcal{B}}$ champ induction magnétique ;

Les relations constitutives, par exemple le champ induction électrique en fonction du champ électrique, permettent de résoudre ce problème. Il est important de classer les méthodes de modélisation selon leur degré d'approximation. En effet, si on calcule une équation d'onde vectorielle, nous avons (pour des matériaux non magnétiques),

$$\nabla^2\vec{\mathcal{E}}(x,y,z,t) - \nabla\left(\nabla \cdot \vec{\mathcal{E}}(x,y,z,t)\right) + \mu_0\frac{\partial^2\vec{\mathcal{D}}(x,y,z,t)}{\partial t^2} = 0 \tag{5}$$

Nous pouvons observer plusieurs dégrées d'approximation :

- approximation semi-vectorielle : on néglige le couplage entre les différentes composantes ce qui est vérifié si le contraste d'indice de réfraction est faible.
  - Cet hypothèse avec la séparation des variables conduit à la méthode de l'indice effectif ;
- approximation scalaire : elle est rigoureusement vraie dans les milieux homogènes infinis ou si la structure à analyser est discontinûment homogène.

La nécessité d'utiliser des méthodes simplifiées dépend des structures à simuler. L'association d'une mise en œuvre facile avec une bonne précision nous a poussé à utiliser la méthode des faisceaux propagés (BPM : Beam Propagation Method). Pour la décrire il faut rappeler l'approximation paraxiale utilisée dans un grand nombre de techniques analytiques ou numériques, comme la théorie des modes couplés (CMT), dans l'optique linéaire et non-linéaire, les faisceaux gaussiens, et finalement la BPM. Elle suppose une propagation quasi directionnelle. Dans ce mémoire ce sera la direction $z$. Les composantes spectrales associées à ce faisceau sont réparties autour de la constante de propagation associée à cette direction,

$$\vec{E}(x,y,z) = \vec{u}(x,y,z)e^{-jk_0n_0z} \tag{6}$$

où les composantes du champ en chaque point peut s'écrire aussi sous la forme suivante :

$$E_i(x,y,z) = u_i(x,y,z)e^{-jk_0n_0z} \tag{7}$$

où $\vec{u}(x,y,z)$ est une enveloppe lentement variable du signal approximé.

L'analyse des phénomènes non-linéaires a été un des thèmes principal de notre travail. Une liste non exhaustive des phénomènes non-linéaires les plus connus est présentée ici pour préciser les domaines liés à ce travail de thèse :

- effets paramétriques
  - Génération du second harmonique ;
  - Effet Kerr ;
  - Génération de fréquence somme ;

  - Effet Pockels ;
- phénomènes de diffusion
  - Diffusion Rayleigh (élastique) ;
  - Diffusion Brillouin (inélastique) ;
  - Diffusion Raman (inélastique) ;

Nous nous sommes concentrés sur les phénomènes paramétriques, qui ont les propriétés fondamentales suivantes :

- le milieu joue un rôle de "catalyseur" pour transférer l'énergie d'une fréquence (d'une polarisation, ou d'un vecteur d'onde) à une autre ;
- la population des niveaux d'énergie au niveau atomique et moléculaire n'est pas affectée ; les distributions à l'état initial et à l'état final sont identiques ;
- en Physique classique, la polarisabilité électronique, représentant l'interaction d'un champ électrique d'une onde optique avec la matière, est constituée d'une série de termes caractérisant la distorsion du mouvement oscillant des électrons qui devient non négligeable avec de fortes intensités optiques ;
  - la réponse est quasi-instantanée ($10^{-15}$ s) ;
  - les susceptibilités non-linéaires $\chi^{(NL)}(\omega)$ sont réelles et faiblement dispersives (excitation hors-résonance).

Nous introduisons alors la relation constitutive non-linéaire suivante

$$\vec{\mathcal{D}}(x,y,z,t) = \varepsilon_0 \vec{\mathcal{E}}(x,y,z,t) + \vec{\mathcal{P}}\left(x,y,z,t,\vec{\mathcal{E}}\right) \tag{8}$$

où $\vec{\mathcal{P}}$ est une fonction non-linéaire de $\vec{\mathcal{E}}$.

La série de Taylor associée à cette fonction nous permet d'identifier plusieurs termes d'ordre différent,

$$\begin{aligned}\vec{\mathcal{P}}\left(x,y,z,t,\vec{\mathcal{E}}\right) = & \\ &= \varepsilon_0 \left(\chi^{(1)}\vec{\mathcal{E}}\right) + \vec{\mathcal{P}}^{(2)}\left(x,y,z,t,\left|\vec{\mathcal{E}}\right|^2\right) + \vec{\mathcal{P}}^{(3)}\left(x,y,z,t,\left|\vec{\mathcal{E}}\right|^3\right) + \dots \\ &= \vec{\mathcal{P}}^{LIN}\left(x,y,z,t,\vec{\mathcal{E}}\right) + \vec{\mathcal{P}}^{NL}\left(x,y,z,t,\vec{\mathcal{E}}\right)\end{aligned} \tag{9}$$

où les termes $\vec{\mathcal{P}}^{(n)}$ représentent le $n$-ième élément du polynôme caractérisant la série de Taylor. Avec l'hypothèse d'une dispersion négligeable, ils sont exprimés sous la forme d'un tenseur de susceptibilité d'ordre $n$, $\chi^{(n)}$.

Beaucoup de facteurs influencent l'efficacité de ces phénomènes. Des propriétés de symétrie des matériaux permettent déjà de classifier deux groupes.

- *centrosymétrique* (invariant aux transformations $\vec{r} \leftrightarrow -\vec{r}$) ;
- *non-centrosymétrique*.

Dans les cristaux centrosymétriques et les matériaux amorphes $\chi^{(2n)} = 0$, donc, par exemple, dans les fibres optiques standards la non-linéarité du troisième ordre est la première disponible.

Enfin, à une fréquence d'excitation donnée, les effets NL créés dépendent aussi beaucoup de la forme structurelle de la zone où se propage le signal. Le transfert d'énergie est

intrinsèquement périodique dû à la nature dispersive des matériaux. Ceci est explicable en terme de *désaccord de phase* entre les différents harmoniques. Pour transférer l'énergie d'une fréquence à une autre, on utilise les propriétés de dispersion des cristaux anisotropes avec une orientation spécifique ou on crée une dispersion contrôlée en utilisant une structure périodique induisant l'accord de phase (*phase-matching*) entre les différents harmoniques générés : nous pouvons atteindre et améliorer considérablement l'efficacité NL pour une polarisation donnée. Un fort confinement du champ est aussi un effet supplémentaire pour augmenter l'efficacité NL. Il s'agit d'une approche très prometteuse pour atteindre des effets NLs à basse intensité.

Les auteurs rapportent deux exemples typiques, la génération du second harmonique (SHG) et l'effet Kerr optique ou Optical Kerr Effect (OKE). Une formulation non-linéaire de la CMT est habituellement utilisée pour décrire l'échange d'énergie entre chaque harmonique durant la propagation. Ceci est normalement obtenu après une dérivation des relations de la CMT en appliquant des simplifications induites par l'optique paraxiale. La SHG est un effet d'ordre 2 (intervention du carré du champ). Les équations données par la CMT (pour des modes guidés avec un profil modal $f_t$, une enveloppe lentement variable $u_t$, étant l'indice $t = 1, 2$ pour identifier chaque harmonique) peuvent s'écrire :

$$\begin{cases} jf_1 \dfrac{\mathrm{d}u_1}{\mathrm{d}z} = \dfrac{\omega^2}{c_0^2} \dfrac{1}{2k_1} \chi^{(2)} f_2 f_1 u_2 u_1^* e^{-j\Delta k z} \\ jf_2 \dfrac{\mathrm{d}u_2}{\mathrm{d}z} = \dfrac{(2\omega)^2}{2c_0^2} \dfrac{1}{2k_2} \chi^{(2)} f_1^2 u_1^2 e^{j\Delta k z} \end{cases} \tag{10}$$

où on pose

$$\Delta k = k_2 - 2k_1 \tag{11}$$

qui représente l' *accord de phase.*

Il est facile de normaliser l'équation et de démontrer que la susceptibilité SHG efficace s'écrit

$$\chi = \frac{2\pi}{\lambda} \sqrt{\frac{\eta_0}{2n_1^2 n_2}} \frac{\chi^{(2)}}{\sqrt{A_{eff}}} \tag{12}$$

$A_{eff}$ caractérise le confinement dans la section transverse des guides,

$$A_{eff} = \int f_2^2 \, dx \, dy \left( \frac{\int f_1^2 \, dx \, dy}{\int f_1^2 f_2 \, dx \, dy} \right)^2 \tag{13}$$

et est mesurée en $m^2$.

L'effet Kerr optique est un auto-effet du troisième ordre, qui est étroitement lié à la focalisation ou à la défocalisation du faisceau optique. Il est représenté comme une modulation de l'indice de réfraction en fonction de l'intensité.

Un ansatz composé par un seul harmonique peut être utilisé pour obtenir

$$jf^2 \frac{\mathrm{d}u}{\mathrm{d}z} = \frac{\omega^2}{c_0^2} \frac{\chi^{(3)}}{4} \frac{1}{2k} f^4 |u|^2 u = k_0 n_2 f^4 |u|^2 u = \chi f^4 |u|^2 u \tag{14}$$

où $n_2$ réprésent un indice non-linéaire équivalent et $u$ est encore l'enveloppe du champ (lentement variable) Si on n'a pas de pertes, l'indice effectif caractérisant la propagation peut

aussi s'écrire :

$$n_2^I = n_2 \frac{2}{c_0 \varepsilon_0 n(\omega)} \frac{1}{A_{eff}} = n_2 \frac{2}{c_0 \varepsilon_0 n(\omega)} \frac{\int f^4 \, dx \, dy}{\left( \int f^2 \, dx \, dy \right)^2}. \tag{15}$$

Les effets non-linéaires jouent également un rôle fondamental dans la propagation de régimes particuliers, comme les solitons spatiaux ou temporels. Dans ces régimes, la diffraction ou la dispersion peuvent être parfaitement compensées par les effets non-linéaires. On peut alors obtenir avec de fortes intensités des faisceaux avec des propriétés non dispersives et/ou sans diffraction.

Un autre élément fondamental des techniques de modélisation est fourni par la décomposition modale. Dans les structures linéaires, nous pouvons décomposer tous les champs en termes d'oscillations naturelles (modes), qui se caractérisent par un profil de propagation invariant $\left( \vec{E}_i, \vec{H}_i \right)$ et son nombre d'onde associé $\beta_i$,

$$\begin{cases} \vec{E}\left(\vec{r}\right) = \sum_i A_i \vec{E}_i \left(\vec{r}_t\right) \exp\left(-j\beta_i z\right) \\ \vec{H}\left(\vec{r}\right) = \sum_i A_i \vec{H}_i \left(\vec{r}_t\right) \exp\left(-j\beta_i z\right) \end{cases} \tag{16}$$

Si ces modes sont représentés par un continuum, les sommes sont remplacés par des intégrales.

Les structures fermées (guide d'onde métallique) n'ont qu'un ensemble discret de modes. Les structures ouvertes (c'est le cas des guides d'ondes diélectriques) ont une base modale composée par un ensemble discret de modes guidés et d'un continuum de modes radiatifs et évanescents.

Dans quelques cas particuliers, on peut connaître facilement la base complète des modes et vérifier leur orthogonalité, point crucial pour projeter une carte de champ sur cette même base. Les méthodes dites modales utilisent cette propriété. Une portion de guide homogène est généralement décrite par une pondération des modes de la base associée à ce guide. Ensuite, un raccordement des champs est fait à chaque interface permettant de remonter à la forme des champs transmis et réfléchis. Une description matricielle peut alors être utilisée.

Le point crucial du raccordement des champs entre deux guides différents (ou deux bases de modes différentes) est le calcul des matrices de projection (projection d'un mode d'un guide sur la base des modes d'un autre guide). Dans ce travail, nous avons cherché à exploiter une méthode facilitant le calcul de ces matrices de projection (A-FMM) pour la modélisation de résonateurs.

Il est opportun de rappeler quelques idées fondamentales de la modélisation en électromagnétisme. Un pas de discrétisation est nécessaire pour obtenir un ensemble discret de données à élaborer sur l'ordinateur. Le premier choix est la construction d'une grille en temps et éspace par differences finies ou éléments finis. Les approches modales sont plutôt représentées par un echantillonage du continuum des nombres d'onde.

La méthode numérique plus populaire en électromagnétisme (FDTD) est basées sur une discrétisation du milieu par des différences finies. La partie temporelle du régime électromagnétique peut être pris en compte en utilisant aussi des différences finies dans le domaine

temporel à partir des équations suivantes

$$\left[\frac{\partial H_y}{\partial x} - \frac{\partial H_x}{\partial y}\right] = \frac{\partial D_z}{\partial t} \tag{17}$$

ce qui donne avec les différences finies pour le temps et l'espace suivant le schéma de Yee (saute-mouton).

$$\begin{aligned} \epsilon \left[\frac{E_z^{t+\Delta t}(x,y,z) - E_z^{t}(x,y,z)}{\Delta t}\right] = \\ = \left[\frac{H_y^{t+\Delta t/2}(x+\Delta x/2,y,z) - H_y^{t+\Delta t/2}(x-\Delta x/2,y,z)}{\Delta x}\right] - \\ = \left[\frac{H_x^{t+\Delta t/2}(x,y+\Delta y/2,z) - H_x^{t+\Delta t/2}(x,y-\Delta y/2,z)}{\Delta y}\right]. \end{aligned} \tag{18}$$

Les autres equations sont écrites de la même manière.

Ce type de discrétisations *ab-initio* exige habituellement de grands temps de calcul et une forte consommation de la mémoire. De nombreuses autres approches ont été proposées comme la BPM, l'une des plus populaires. Elle s'appuie sur l'approximation paraxiale,

$$\frac{\partial u}{\partial z} = \frac{1}{j2k_0 n_0}\left[\frac{\partial^2 u}{\partial x^2} + \frac{\partial^2 u}{\partial y^2} + k_0^2\left(n^2 - n_0^2\right)u\right] \tag{19}$$

où $u(x,y,z)$ est une enveloppe lentement variable qui donne le champ électrique suivant

$$E(x,y,z) = u(x,y,z)\exp\left(-jk_0 n_0 z\right).$$

En supprimant la dépendance exponentielle, on peut utiliser une étape de discrétisation selon $z$, $\Delta z$ largement plus grand que la longueur d'onde au contraire de la FDTD et simplifie la formulation à celle d'un problème aux valeurs initiales.

Nous remarquons que la BPM est beaucoup plus polyvalente que sa version classique. En fait d'autres versions existent maintenant : à grand-angle (par opposition à optique paraxiale), vectorielle, ainsi que d'une version 2D bidirectionnel peut être obtenue en utilisant une matrice S (Scattering Matrix).

Une question fondamentale dans la résolution des équations aux dérivées partielles elliptiques est d'appliquer des conditions aux limites appropriées pour éviter des imprécisions au cours de la propagation (réflexions de la boite de modélisation). Le développement historique de différentes techniques ont permis d'accéder à une technique très fiable, les couches parfaitement adaptée (PMLs). Elles reposent sur l'inclusion de médias à perte qui correspondent exactement et avec continuité à la constante diélectrique de la partie physique adjacente (pas de réflexion à l'interface).Une PML idéale représente un milieu semi-infini.

Il est intéressant de mentionner aussi une autre méthode mélangeant à la fois les différences finies et la technique de mode-matching : la méthode des lignes (MoL). Elle est basée une discrétisation selon l'axe transversal des profils d'indices de réfraction et du champ puis par diagonalisation elle permet de calculer une impédance reliée à la constante de propagation et une base de fonctions modales. Elle utilise aussi ensuite un formalisme d'impédance (ou

d'admittance) similaire à celui utilisé dans les lignes de transmission. Nous la définissons comme une méthode mixte, puisqu'elle utilise les différences finies pour le calcul des modes. C'est un puissant outil largement utilisé, qui permet d'y inclure également des effets non-linéaires.

En effet de nombreuses méthode modales alternatives sont disponibles : par exemple ils s'appuient sur la superposition des solutions homogènes dans une cavité métallique ou par approximations avec des modes de Bloch. Une fois que la valeur propre du mode électromagnétique a été résolue, les matrices S (forme général des formules de Fresnel pour les ondes planes) ou de l'impédance-admittance (pour les lignes de transmission) sont utilisés. Rappelons que la multiplication directe des propagateurs pour tenir compte du chemin optique à travers une couche homogène, c'est-à-dire la méthode de la matrice de transmission, est instable. On évite donc son utilisation.

## Chapitre 2

Dans ce chapitre la mise en œuvre d'une méthode de propagation des faisceaux non-linéaires est décrite. On va montrer la version TE ($\vec{E} = E_y \hat{y}_0$), celle TM n'étant que légerement plus compliquée. On part de l'équation d'Helmholtz

$$\frac{\partial^2 E}{\partial z^2} + \left( \frac{\partial^2}{\partial x^2} + k_0^2 n^2(x,z) \right) E = 0 \tag{20}$$

où $k_0 = \frac{2\pi}{\lambda}$ est le nombre d'onde de l'espace libre, $\lambda$ la longueur d'onde en espace libre et $n(x,z)$ le profil d'indice de réfraction.

Bien que la version classique de la méthode est basée sur l'approximation paraxiale, la propagation à grand angle (wide-angle) peut être obtenue si le problème de propagation unidiréctionel est formulé dans une forme plus générale pour obtenir une meilleure approximation. Enfin la discrétisation permet de résoudre numériquement le problème.

La BPM wide-angle est donc basée sur deux opérateurs, la racine carrée $L$ et le propagateur $P$.

$$L = \sqrt{\frac{\partial^2}{\partial x^2} + k_0^2 n^2(x)} = k_0 n_0 \sqrt{I + \frac{\frac{\partial^2}{\partial x^2} + k_0^2 \left( n^2(x) - n_0^2 \right)}{k_0^2 n_0^2}} = k_0 n_0 \sqrt{I + X}. \tag{21}$$

$L$ répresente la diffraction et le retard de phase, $I$ la matrice identité, $n_0$ est l'indice de réfraction de référence, en analogie avec l'équation paraxiale. Le deuxième s'écrit comme

$$P = \exp\left(-j \Delta z L\right) \tag{22}$$

On réécrit (20) comme

$$\frac{\partial^2 E}{\partial z^2} + L^2 E = 0 \tag{23}$$

et on peut voir dans l'équation suivante que l'opérateur $P$ réprésente la propagation entre deux pas successifs en $z$,

$$E(x, z + \Delta z) = P E(x, z). \tag{24}$$

La difficulté principale est de trouver la formulation correcte de $L$ et de $P$.

Pour modéliser le problème non-linéaire, il est difficile de choisir une discrétisation directe de la propagation et de l'influence de la non-linéarité. Nous calculons d'abord la propagation linéaire puis nous calculons la contribution non-linéaire avant la nouvelle propagation. De plus, un procédé itératif est utilisé qui consistant à re-calculer les contributions non-linéaires et à les re-propager jusqu'à ne pas avoir de changements rémarquables. Ceci permet d'améliorer la précision finale et par conséquent d'utiliser des pas de propagation plus grands.

La déscription de la génération de seconde harmonique

$$\begin{aligned}\frac{\partial^2 u_\omega(x,z)}{\partial z^2} - 2jk_0 n_{0_\omega}\frac{\partial u_\omega(x,z)}{\partial z} + \frac{\partial^2 u_\omega(x,z)}{\partial x^2} + k_0^2\left[n_\omega^2(x) - n_{0_\omega}^2\right]u_\omega(x,z) = \\ = -k_0^2\chi_j^{(2)}(x)\left[u_\omega(x,z)\right]^* u_{2\omega}(x,z)e^{-j\Delta kz}\end{aligned} \tag{25}$$

$$\begin{aligned}\frac{\partial^2 u_{2\omega}(x,z)}{\partial z^2} - 4jk_0 n_{0_{2\omega}}\frac{\partial u_{2\omega}(x,z)}{\partial z} + \frac{\partial^2 u_{2\omega}(x,z)}{\partial x^2} + 4k_0^2\left[n_{2\omega}^2(x) - n_{0_{2\omega}}^2\right]u_{2\omega}(x,z) = \\ = -2k_0^2\chi_j^{(2)}(x)\left[u_\omega(x,z)\right]^2 e^{j\Delta kz}\end{aligned} \tag{26}$$

où $k_0 = \frac{\omega}{c}$ est le nombre d'onde de la fréquence fondamentale, $u_{k\omega}$, avec $k = 1, 2$, réprésentent les deux enveloppes des harmoniques (FF et SH), $n_{0_{k\omega}}$ représente l'indice de réfraction de référence de la BPM et enfin $\Delta k = 2k_0(n_{0_\omega} - n_{0_{2\omega}})$.

Une mise en œuvre de ce problème est décrite de la manière suivante :

$$\begin{aligned}\frac{2jk_0 n_{0_\omega}}{\Delta z}\left(u_\omega^{m,s+1(t)} - u_\omega^{m,s+1(I)}\right) = \\ = \frac{1}{2}k_0^2\left(\chi^{(2)^{m,s}} u_{2\omega}^{m,s+1(I)}\left[u_\omega^{m,s+1(I)}\right]^* + \chi^{(2)^{m,s+1}} u_{2\omega}^{m,s+1(t-1)}\left[u_\omega^{m,s+1(t-1)}\right]^*\right) \\ \frac{4jk_0 n_{0_{2\omega}}}{\Delta z}\left(u_{2\omega}^{m,s+1(t)} - u_{2\omega}^{m,s+1(I)}\right) = \\ = \frac{1}{2}4k_0^2\left(\chi^{(2)^{m,s}} u_\omega^{m,s+1(I)} u_\omega^{m,s+1(I)} + \chi^{(2)^{m,s+1}} u_\omega^{m,s+1(t-1)} u_\omega^{m,s+1(t-1)}\right)\end{aligned} \tag{27}$$

où $(m, s) \to (m\Delta x, \left(s + \frac{1}{2}\right)\Delta z)$ identifie un point de la grille. Les exposants $I$ et $t$ sont utilisés pour dénoter le pas intermédiaire du split-step (entre propagation linéaire et non-linéaire) et la valeur de l'itération, respectivement.

Le calcul de l'effet Kerr est plus direct : l'estimation de l'intensité locale permet d'ajuster l'indice de réfraction selon

$$n(x,z) = n_{lin}(x,z) + n_2^I(x,z)\mathcal{I}(x,z). \tag{28}$$

Cette procédure itérative est stoppée lorsque les variations du profil d'intensité deviennent négligeables.

Une discrétisation avec des différences finies est la base de notre implémentation. On obtient de grandes matrices et le calcul de $L$ et $P$ est trop lourd avec les approches classiques : l'utilisation des approximations rationnelles ou de Padé est utilisée généralement.

$$P_j \approx e^{-jk_0 n_0 \Delta z S_p(X_j)} \tag{29}$$

où $S_p(X_j)$ est un développement de Padé de $\sqrt{I + X_j}$, non-ordinaire, en général.

Effectivement

$$\sqrt{1+x} \simeq 1 + \sum_{n=1}^{p} \frac{a_n^{(p)} x}{1 + b_n^{(p)} x} = \prod_{n=1}^{p} \frac{1 + c_n^{(p)} x}{1 + b_n^{(p)} x} \tag{30}$$

où

$$b_n^{(p)} = \cos^2\left(\frac{n\pi}{2p+1}\right), \quad c_n^{(p)} = \sin^2\left(\frac{n\pi}{2p+1}\right), \quad a_n^{(p)} = \frac{2c_n^{(p)}}{2n+1}. \tag{31}$$

Les coefficients sont tous réels, ce qui implique une mauvaise description des modes évanescents (qui normalement résultent en nombres d'onde purement imaginaires). Si on applique la méthode nommée *rotated branch-cut*, on obtient :

$$\sqrt{1+x} = e^{-j\alpha/2}\sqrt{1 + [(1+x)e^{j\alpha} - 1]} \simeq e^{-j\alpha/2}\left[1 + \sum_{n=1}^{p} \frac{a_n^{(p)} \tilde{x}}{1 + b_n^{(p)} \tilde{x}}\right], \tag{32}$$

Les nombres d'onde évanescents sont par conséquent décrits par des nombres complexes et le problème est évité. Cette idée consiste à tourner le démi-axe $(-\infty, -1]$ du plan complexe (qui est la cause de nos difficultés), d'un angle $\alpha$.

Les PML dans notre BPM sont basés sur des transformées de coordonnées complexes,

$$\hat{x} = x - j\int_0^x \sigma(\xi) d\xi, \tag{33}$$

où $\sigma$ est une fonction appropriée qui représente le profil d'absorption. Cette application est équivalente aux milieux anisotropes, mais est simplement une modification de l'opérateur de la dérivée. L'opérateur fondamental

$$X = \frac{\frac{\partial^2}{\partial x^2} + k_0^2(n^2 - n_0^2)}{k_0^2 n_0^2} \tag{34}$$

devient

$$X = \frac{\frac{1}{1-j\sigma(x)}\frac{\partial}{\partial x}\left(\frac{1}{1-j\sigma(x)}\frac{\partial}{\partial x}\right) + k_0^2(n^2 - n_0^2)}{k_0^2 n_0^2}. \tag{35}$$

# Chapitre 3

Comme nous l'avons mentionné auparavant, les solitons sont un exemple important du régime de propagation non-linéaire. Durant la propagation, il est possible de maintenir leur profil d'intensité sans être gêné par la diffraction de la lumière.

Nous avons étudié tout particulièrement des solutions dans des systèmes périodiques 1D, i.e. une série de guides parallèles ayant la possibilité de se coupler le long de la propagation par des ondes évanescentes. La structure périodique étudiée est réalisée soit dans l'AlGaAs ou dans des matériaux photoréfractifs (modification de l'indice de réfraction induite optiquement ce qui est aussi le cas des couches minces à base de cristaux liquides).

Ces mêmes phénomènes sont observables dans les domaines des condensats de Bose-Einstein sous l'influence de potentiels périodiques.

Il est bien connu dans ce type de réseau qu'il existe des angles d'incidences ou ordres de Bragg pour lesquels la lumière est fortement réfléchie. Ces angles identifient une bande photonique interdite dans laquelle les nombre d'ondes longitudinaux (ou constantes de propagation)

sont associés à des solutions linéaires constituées de composantes transverses évanescentes. Ces zones sont observées aussi sur les courbes de dispersions des cristaux photoniques (en régime harmonique) ($\omega$ suivante $k$, constante de propagation transverse) qui font apparaître les bandes permises ou interdites pour la propagation. Dans notre cas, la diffraction de la lumière dans le réseau de guides dépend de la courbure de ces bandes.

La propagation dans ce type de structure est très différente de celle qui peut exister dans un matériau homogène obéissant à la loi classique de la diffraction. Dans un régime non-linéaire, avec un matériau présentant un effet Kerr, avec de fortes intensités optiques, une auto-focalisation peut apparaître où la non-linéarité permet la compensation des effets de la diffraction. Ce type de propagation est alors couramment appelé un soliton spatial. Le profil du champ transverse est alors inchangé au cours de la propagation le long des guide parallèles. Les exemples les plus simples sont les solitons discrets (DS) qui peuvent être obtenus si on injecte de la lumière à un bout de la structure dans un ou plusieurs guides de la structure précédente.

Dans ce travail nous nous sommes concentrés sur la propagation de profiles de champ avec des nombres d'ondes dans les bandes photoniques interdites, qui deviennent accessibles avec la non-linéarité (en effet, ces bandes sont inaccessibles dans le régime linéaire), les *solitons spatiaux en bande interdite*.

Des modes analogues en 1D (régime pulsé) sont obtenus pour des fréquences se trouvant dans une bande photonique interdite couramment appelé des *gap solitons* (GS).

L'excitation en bout est utilisée pour démontrer ce type de régime. Deux enveloppes de champs couplés dans la structure, associées à deux angles de Bragg opposés, peuvent interférer pour former ou piéger un *gap soliton* qui se propage dans la structure selon un nombre d'onde longitudinal correspondant aux bandes interdites linéaires, comme observé récemment dans différents matériaux et structures.

On obtient donc une carte de champs rapidement modulée, dû à l'interférence de ces deux sources, qui peut se propager sans diffraction.

Cette idée est aussi basée sur le principe de la théorie des modes couplés : si le champ est écrit en terme de deux faisceaux à deux angle de Bragg opposés, les franges qui varient rapidement se seuperposent et çela nous permet alors de calculer la solution analytique en terme de deux enveloppes se propageant dans la structure. Cet approche est sujet à des approximations et donc il faut apprécier ses limites : on propose à cette fin la résolution de l'équation d'ondes paraxiale de façon numérique par une méthode de relaxation.

Nous avons comparés les deux approches. Malgré ses approximations, la CMT permet d'avoir une description analytique des GS dans un grand nombre de cas où une vérification expérimentale serait possible. Cette analyse avec la CMT peut être considérée comme une première étape avant une caractérisation réelle de GS. De plus, cette étude permet de déterminer les domaines où la CMT n'est plus viable. Ces résultats sont validés avec notre code BPM.

Nous avons pris des couches périodiques constituées de diélectrique transparent (sans pertes) avec des indices de réfraction $n_{1,2} = n_0 \pm \Delta n/2$ [$\Delta n = n_2 - n_1 > 0$] et une épaisseur $\Lambda_{1,2}$, caractérisé par une période $\Lambda = \Lambda_1 + \Lambda_2 \equiv 2\pi/k_g$ suivant l'axe transverse $X$. Dans

l'approximation 1+1D ($\partial_Y = 0$), et dans le domaine de faible inhomogénéité et de la condition paraxiale, l'enveloppe du champ suit l'équation d'onde suivante :

$$i\frac{\partial E}{\partial Z} + \frac{1}{2k}\frac{\partial^2 E}{\partial X^2} + k_0 \Delta n_p(X) E + \chi |E|^2 E = 0 \tag{36}$$

où $\chi = k_0 n_{2I}$ est le coefficient non-linéaire globale.

Dans le cas linéaire ($\chi = 0$) la réflection de Bragg est présente pour des angles de propagation $\phi_{Bm}$, par rapport à l'axe $Z$,

$$\phi_{Bm} = \sin^{-1}\left(\frac{mk_g}{2k}\right) = \sin^{-1}\left(\frac{m\lambda}{2n_0\Lambda}\right). \tag{37}$$

Si on prend en compte que les valeurs positives de $m$, la condition de Bragg correspond à des ondes propagées avec un nombre d'onde $k_x = k\sin\phi$ qui est un multiple de la moitié du nombre d'onde lié à la période du réseau, i.e.

$$k_x = \pm k_{xB} = \pm\frac{mk_g}{2} = \pm m\frac{\pi}{\Lambda} \tag{38}$$

Pour deux faisceaux couplés dans la structure à deux angles opposés autour d'un des ordres de Bragg, la CMT peut être développée pour écrire le champ comme la superposition de deux enveloppes proches de leur résonance, $E_\pm(X, Z)$, comme

$$E = \left[E_+(X,Z)e^{ik_{xB}X} + E_-(X,Z)e^{-ik_{xB}X}\right] e^{-i\frac{k_{xB}^2}{2k}Z}, \tag{39}$$

Ce système d'équations couplées des deux faisceaux a une solution analytique si on néglige les termes liés à la diffraction.

La CMT dans le cas linéaire décrit les caractéristiques de la diffraction dans la structure périodique qui peut être exprimée de la manière suivante

$$k_x = \pm\sqrt{\beta^2 - \Gamma^2}\frac{2k}{mk_g} \tag{40}$$

Il est alors intéressant de les comparer avec une approche rigoureuse basée sur une matrice de transmission ; celle-ci est basée sur le théorème de Bloch (le champ décrit sur une période spatiale et dans la première zone de Brillouin est périodique) combiné avec les lois de propagation des onde planes.

Dans la fig. 3.3 nous comparons des résultats obtenus avec la CMT (ligne en pointillée) et ceux calculés avec la méthode rigoureuse (ligne pleine) avec $m = 1$ et les paramètres suivants ($\lambda_0 = 1.55\mu$m, $\Lambda = 4\mu$m, 50% le rapport cyclique, $\Delta n = 0.008$ conduisant à $\Gamma \cong 10^4\text{m}^{-1}$ ; d'autres expériences dans la littérature utilisent des paramètres similaires)

On peut donc voir que les deux résultats sont remarquablement proches (coïncidence entre les deux courbes) autour de la zone supérieure à la région grise qui est le premier gap ($m = 1$) des nombres d'ondes interdits $\beta$ (ou valeurs évanescentes pour les composantes du nombre d'onde transverse $k_x$). La figure montre aussi un gap étroit $m = 2$ (qui disparaît pour un réseau carré de rapport cyclique 50% avec la CMT) et le troisième gap $m = 3$ (qui est encore bien décrit par la CMT si $m = 3$).

Les deux approches commencent à s'écarter pour une différence d'indices de réfraction largement plus grande que celle utilisée dans la réalité. Ces différences sont plus fortes pour les gaps aux ordres $m$ plus élevés.

Nous nous attendons à quelques différences pour les solutions non-linéaires qui peuvent être calculé sous la forme suivante

$$U_{\pm}(z,x) = A_{\pm}\sqrt{\eta(\zeta)}\ \exp\left[i\beta_{\Gamma}z + i\psi_{\pm}(\zeta)\right] \tag{41}$$

où $\zeta \equiv \gamma(x - vz)$ est la coordonnée transverse du référéntiel du GS, $\gamma = (1 - v^2)^{-1/2}$. $\beta_{\Gamma} \equiv \beta/\Gamma_m$ et $v = dx/dz$ sont deux paramètres normalisés qui caractérisent la solution, constituée de l'interférence de deux enveloppes $\eta$ avec un déphasage non-linéaire $\psi_{\pm}$.

En résumé, on peut prouver que les SGS localisés sont situés sur le cercle unitaire du plan défini par les deux paramètres précédents, i.e. $\beta_{\Gamma}^2 + v^2 \leq 1$, et qu'ils possèdent les caractéristiques suivantes :

1. l'amplitude et l'inverse de la largeur des enveloppes du GS sont fixées par l'angle des deux faisceaux à l'entrée du réseau de guides périodiques. Ceci correspond en fait à leur position dans le diagramme de bandes, en s'approchant soit vers le haut ou le bas du bord du gap supérieur ou inférieur ;
2. la frange d'interférence formée par les deux enveloppes présente un décalage par rapport au réseau de guide à cause du terme de phase $\psi_{\pm}(\zeta)$ ;
3. la vitesse transverse du soliton (qui est indépendante de l'angle d'entrée) peut être contrôlée en jouant sur la pondération de l'amplitude des deux faisceaux d'entrée ($A_{\pm}$) et la direction transverse est déterminée par celui-là qui est plus intense.

Nous sommes focalisés sur le cas où la vitesse transverse du soliton est nulle puis nous avons comparé les solutions de la CMT avec ceux donnés par l'équation suivante :

$$-\beta_s U + \frac{1}{2k}\frac{\partial^2 U}{\partial X^2} + k_0 \Delta n_p(X) U + \chi U^3 = 0. \tag{42}$$

cette relation est résolue avec une approche de relaxation, i.e. nous avons discrétisé en différences finies et pour une valeur fixée de $\beta_s$ (nombre d'onde longitudinal du soliton), nous avons trouvé une solution $U$ du système non-linéaire résultant.

Dans la fig. 3.4 nous montrons la forme de base d'un GS stable, qui a un minimum principal au niveau de la couche de plus haut indice de réfraction parce que les deux enveloppes $E_{\pm}$ sont en opposition de phase. Les autres minima sont progressivement décalés par rapport aux couches du réseau à cause du terme de phase non-linéaire [voir la propriété 2]. On donne aussi la comparaison entre différentes solutions pour une variété de nombres d'onde dans la bande interdite et en augmentant le saut d'indice du réseau, voir figures 3.5 et 3.6.

Un bon accord entre la CMT et la relaxation a été trouvé sauf pour le bord inférieur de la bande (voir le cas (c), qui correspond à $\beta_{\Gamma} = -0.9$), où le soliton est obtenu avec des puissances plus basses. Il est aussi très élargi (la diffraction joue un rôle fondamental dans ce cas).

Les simulations BPM permettent de vérifier que les solutions CMT sont une bonne approximation, dans les conditions expérimentales plus habituelles.

Nous avons ensuite considéré un cas plus général : le confinement de la lumière contrôlé l'influence du deuxième ordre, entre deux harmoniques.

Si on considère l'excitation de deux fréquences $\omega$ et $2\omega$ au même angle, ce correspond au premier gap du premier harmonique et au deuxième gap de l'autre. En effet, comme l'angle de Bragg d'ordre $m$ est

$$\phi_{Bm} = \sin^{-1}\left(\frac{mk_g}{2k}\right) = \sin^{-1}\left(\frac{m\lambda}{2n_m\Lambda}\right). \tag{43}$$

$m = 1$ pour $\omega$ et $m = 2$ pour $2\omega$ correspondent au même angle, à condition que $n_1 = n_2$, i.e. SHG est en accord de phase. Celui permet d'imaginer une propagation confinée de deux fréquence grâce à l'interaction non-linéaire, pour des nombres d'onde longitudinales qui sont interdits en régime linéaire pour les deux harmoniques.

Nous rappelons que la CMT linéaire ne prévoit pas un gap du deuxième ordre (si le rapport cyclique est 50%), alors qu'il est décrit par l'approche plus rigoureuse. Si on prend le cas general d'un désaccord de phase fini, le choix des positions des nombres d'onde de chaque harmonique dans sa bande interdite est fondamental pour obtenir des solutions qui diminuent au loin du centre du faisceau. L'application de grandes intensités induit donc un soudain changement de régime.

Le système d'équations couplées, dans l'approximation paraxiale s'écrit

$$\begin{aligned} i\frac{\partial E_1}{\partial Z} + \frac{1}{2k_1}\frac{\partial^2 E_1}{\partial X^2} + \frac{\omega}{c}\Delta n_p(X)E_1 + \chi E_2 E_1^* e^{i\Delta kZ} = 0, \\ i\frac{\partial E_2}{\partial Z} + \frac{1}{2k_2}\frac{\partial^2 E_2}{\partial X^2} + \frac{2\omega}{c}\Delta n_p(X)E_2 + \chi E_1^2 e^{-i\Delta kZ} = 0. \end{aligned} \tag{44}$$

où $\chi = k_0\left(2/\left(\varepsilon_0 c n_2 n_1^2\right)\right)^{1/2}\chi^{(2)}$ et $\Delta k = k_2 - 2k_1$.

Comme auparavant, nous étudions des solitons qui se propagent à des vélocité transverse nulles, i.e.

$$\begin{aligned} E_1(X,Z) &= e_1(X)\exp(i\beta_s Z) \\ E_2(X,Z) &= e_2(X)\exp[i(2\beta_s - \Delta k)Z] \end{aligned}$$

et le calcul se déroule selon l'approche numérique de relaxation qui discrétise directement ce système :

$$\begin{aligned} -\beta_s e_1 + \frac{1}{2k_1}\frac{\partial^2 e_1}{\partial X^2} + k_0\Delta n_p(X)e_1 + \chi e_2 e_1^* = 0 \\ -(2\beta_s - \Delta k)e_2 + \frac{1}{2k_2}\frac{\partial^2 e_2}{\partial X^2} + 2k_0\Delta n_p(X)e_2 + \chi e_1^2 = 0 \end{aligned} \tag{45}$$

Les nombres d'onde des deux harmoniques ($k_1 + \beta_s$ pour FF et $2(k_1 + \beta_s)$ pour le SH) sont calculés par la méthode de la matrice de transfert pour être sur qu'ils se trouvent dans leurs bandes interdites.

On pourrait encore faire confiance à une approximation du type CMT (cette fois on aura un système de quatre équations) : la principal limitation est qu'il n'est pas résoluble analytiquement. Donc on résout l'Eq. (45) directement, à partir d'un vecteur initial de points donnés par le soliton Kerr (cubique, traité précédemment) qui est une bonne approximation si

$|\Delta k|$ est grand. Puis le désaccord de phase est modifié jusqu'aux valeurs de conversion efficaces entre les deux harmoniques. En détails, les solutions pour chaque valeur du désaccord de phase sont utilisées pour initialiser la relaxation a l'étape suivante, qui correspond à un $\Delta k$ plus proche de zéro : la continuité selon les paramètres est la base de cette argumentation.

Un ensemble de SGS quadratique est obtenu pour des rapports cycliques de 50% et superieurs, et l'intensité et la largeur du soliton (pour le premier et le second harmonique) sont decrits en fonction de $\Delta k$, après avoir fixé sa position dans la bande fixé. Cette dernière valeur est critique : l'effet du désaccord sur les solutions est modifié sensiblement par lui, voir les figures 3.15 et 3.16.

## Chapitre 4

Les micro-résonateurs sont une nouvelle classe de composants prometteurs pour la nouvelle génération de circuits intégrés photoniques. De nouvelles découvertes technologiques ont permises de développer des micro-cavités telles que les microspères, les microdisques, les microanneaux, les microgears, les microtores, les micropiliers et les cavités à cristaux photoniques qui ont montré leur efficacité autant dans des applications passives (filtres, add and drop, lignes à retard) que dans des applications actives (modulateurs, lasers, coupleurs, ligne à retard variable). Elles peuvent aussi jouer un rôle clé dans les applications électrodynamiques quantiques de cavité et non-linéaires telles que les lasers Raman ou les structures à résonateurs couplés.

Les résonateurs à symétrie cylindrique comme les microdisques, les microanneaux ou les microtores permettent d'atteindre des coefficients de qualité importants $Q$ (jusqu'à $Q \approx 10^6$ pour un microtore en silice). Les modes de ces structures sont appelés des modes de galerie (WGM), car ils ont été découverts pour la première fois dans le domaine de l'accoustique. Par exemple, dans la figure 4.1 nous avons tracé la solution en TM pour un ordre azimutal $m = 10$ et un ordre radial $l = 1$ d'un microdisque obtenu avec une méthode 2D (étude d'un cylindre).

Ce chapitre est consacré à la description d'une nouvelle méthode numérique basée sur une décomposition de Fourier (A-FMM) en coordonnées cylindriques. Notre objectif était de développer cette méthode pour décrire le champ en 3D dans un microdisque et un microanneau, structures ayant un axe de symétrie qui sont souvent utilisés en optique intégré notamment ces derniers années sur les technologies SOI (Photonique Silicium). Nous montrons que nous sommes capables de calculer les longueurs d'ondes de résonance et les coefficients de qualité. L'utilisation de cette méthode est alors possible pour toute structure respectant ce type de symétrie.

De nombreuses méthodes numériques sont disponibles pour le calcul 3D telles que les éléments finis (FEM), les méthodes intégrales, les différences finies dans le domaine temporel (FDTD) mais elles sont soit onéreuses en temps de calcul et en consommation de mémoire vive soit plus compliquées à mettre en œuvre. Alors que les méthodes basées sur une décomposition modale ou une décomposition en série de Fourier sont généralement plus rapides et permettent d'avoir une vision plus claire du champ électromagnétique dans la

cavité. Une méthode 3D basé sur une décomposition modale est déjà disponible mais elle utilise une expansion des fonctions de Bessel qui limite son application pour des structures cylindriques à faible contraste d'indice de réfraction et pour de grandes rayons de courbure.

Notre approche est basée quant à elle sur une application rigoureuse nommée RCWA (Rigourous Coupled Wave Analysis) dont une version spécifique est utilisée pour modéliser des structures guidantes et est nommée A-FMM (Apériodic Fourier Modal Method) : les modes sont décomposés sur une série de Fourier, qui réduit le recouvrement des modes entre cellules utilisées dans les méthodes modales classiques par une manipulation matricielle.

Notre travail a été d'appliquer cette approche dans un système à symétrie cylindrique $(r, \theta, z)$ et d'utiliser la RCWA pour obtenir des modes selon l'axe de symétrie de la structure, l'axe $z$ [voir la fig. 4.2(a)].

En utilisant le principe de la séparation de variables, et en imposant une fonction azimutale périodique du type $\exp(jm\theta)$, nous avons cherché à calculer la dépendance radiale des modes c'est-à-dire suivant l'axe $r$. Bien que l'étude se réduise à deux variables, la nature vectorielle du problème qui nous intéresse est toujours présente : les six composantes du champ électromagnétique sont significatives pour la description du problème. Comme dans les fibres optiques, nous pouvons décrire le problème avec seulement les composantes $E_z$ et $H_z$. En effet, seules ces composantes sont nécessaires pour reconstruire ensuite l'ensembles des autres composantes du champ. Finalement, comme les autres méthodes modales, la structure à analyser est décomposée en une série de couches uniformes suivant l'axe radial dans notre cas, voir la fig. 4.2(b). Toutes ces couches ou sections sont caractérisées par leur profil d'indice de réfraction suivant l'axe $z$. Le comportement modal est obtenu en appliquant les conditions de bords à chaque interface perpendiculaire à l'axe $r$.

Suivant l'axe de symétrie nous avons un profil de permittivité périodique

$$\epsilon_r = \sum_n \epsilon_n e^{jnKz}, \tag{46}$$

et nous travaillons dans des milieux non-magnétiques. Le champ est décrit alors de la manière suivante

$$\begin{aligned} \vec{E} &= \sum_{n=-M}^{M} \left(S_r^n \mathbf{r}_0 + S_\theta^n \theta_0 + S_z^n \mathbf{z}_0\right) e^{jnKz} e^{jm\theta}, \\ \vec{H} &= -j\sqrt{\frac{\epsilon_0}{\mu_0}} \sum_{n=-M}^{M} \left(U_r^n \mathbf{r}_0 + U_\theta^n \theta_0 + U_z^n \mathbf{z}_0\right) e^{jnKz} e^{jm\theta}, \end{aligned} \tag{47}$$

où $S_{r,\theta}$ et $U_{r,\theta}$ sont reliés à travers les équations de Maxwell à $U_z$ et $S_z$. Ces derniers paramètres sont respectivement reliés aux composantes vectorielles des champs $\vec{E}$ et $\vec{H}$. À cause du saut d'indice de réfraction, $E_z$ est discontinu selon l'axe $z$. Nous devons alors appliquer une règle particulière pour calculer le produit de $\epsilon$ avec $E$. En effet, $\epsilon$ doit être décrit par l'inverse de la série de Fourier de l'inverse de $\epsilon$ et dans ce cas on obtient alors les deux systèmes d'équation

suivants :

$$\begin{aligned}
&\frac{\mathrm{d}^2 S_z^n}{\mathrm{d}r^2} + \frac{1}{r}\frac{\mathrm{d}S_z^n}{\mathrm{d}r} - \frac{m^2}{r^2} S_z^n - nK \sum_p [\epsilon]^{-1}_{n,p}\, pK \sum_l \left[\frac{1}{\epsilon}\right]^{-1}_{p,l} S_z^l + k_0^2 \sum_p \left[\frac{1}{\epsilon}\right]^{-1}_{n,p} S_z^p = 0 \\
&\frac{\mathrm{d}^2 U_z^n}{\mathrm{d}r^2} + \frac{1}{r}\frac{\mathrm{d}U_z^n}{\mathrm{d}r} - \frac{m^2}{r^2} U_z^n - (nK)^2 U_z^n + k_0^2 \sum_p \epsilon_{n-p} U_z^p = 0
\end{aligned} \tag{48}$$

et, en posant

$$S_z = \left[S_z^{-M} \dots S_z^{M}\right]^T$$

et

$$U_z = \left[U_z^{-M} \dots U_z^{M}\right]^T,$$

on obtient alors

$$\begin{aligned}
&\frac{\mathrm{d}^2 S_z}{\mathrm{d}r^2} + \frac{1}{r}\frac{\mathrm{d}S_z}{\mathrm{d}r} - \frac{m^2}{r^2} S_z + k_0^2 \overbrace{\left(\overline{E}^{-1} - K_z E^{-1} K_z \overline{E}^{-1}\right)}^{A} S_z = 0 \\
&\frac{\mathrm{d}^2 U_z}{\mathrm{d}r^2} + \frac{1}{r}\frac{\mathrm{d}U_z}{\mathrm{d}r} - \frac{m^2}{r^2} U_z + k_0^2 \underbrace{\left(E - K_z^2\right)}_{B} U_z = 0
\end{aligned} \tag{49}$$

La solution générale s'exprime de la manière suivante

$$S_z^n = \sum_i w_{ni} \left[a_i J_m\left(k_0 \lambda_i^A r\right) + d_i H_m^{(2)}\left(k_0 \lambda_i^A r\right)\right] \tag{50}$$

$$U_z^n = \sum_i v_{ni} \left[\alpha_i J_m\left(k_0 \lambda_i^B r\right) + \delta_i H_m^{(2)}\left(k_0 \lambda_i^B r\right)\right] \tag{51}$$

Pour améliorer la précision de ce type de calcul, des PML sont ajoutées basées sur une transformée de coordonnée non-linéaire dans le plan complexe.

Les résonateurs que nous avons étudiés ici sont composés d'une série de couche uniforme suivant l'axe radial. Chacune de ces couches a son propre profil d'indice de réfraction suivant l'axe $z$. Tout ces effets sont pris en compte par le biais d'une matrice. Comme les fonctions de Hankel divergent à l'origine, nous avons appliqué une approche matricielle du type admittance-impédance (notée brièvement immittance).

Nous définissons cette matrice immittance $\mathbf{U}$ avec la relation suivante,

$$\frac{1}{k_0}\frac{\mathrm{d}\mathbf{p}}{\mathrm{d}r} = \mathbf{U}(r)\mathbf{p} \tag{52}$$

où $\mathbf{p}$ est le vecteur des poids modales en fonction de l'axe radiale, i.e. nous pouvons écrire Eq. (50) et Eq. (51) sous une forme matricielle

$$\begin{bmatrix} S_z \\ U_z \end{bmatrix} = \begin{bmatrix} W & 0 \\ 0 & V \end{bmatrix} \mathbf{p}(r) \tag{53}$$

En effet les matrices des vecteurs propres $V$ et $W$ représentent les profils modaux (sous forme de coefficient de Fourier), donc ce qui reste est simplement l'évolution de chaque mode suivant la direction radiale.

Pour résoudre ce problème, nous avons besoin d'une étape de propagation pour relier la matrice immittance aux deux interfaces définissant une couche homogène et ensuite de définir la nouvelle matrice caractérisant ensuite le passage à travers une interface,

$$\mathbf{U}_s^R = \mathbf{G}_s - \mathbf{H}_s \cdot \left[\mathbf{U}_s^L - \mathbf{F}_s\right]^{-1} \cdot \mathbf{E}_s, \tag{54}$$

et

$$\mathbf{U}_s^L = \mathbf{H}_s \cdot \left[\mathbf{G}_s - \mathbf{U}_s^R\right]^{-1} \cdot \mathbf{E}_s + \mathbf{F}_s, \tag{55}$$

où une fois encore $R$ et $L$ désignent les positions radiales $r_{s+1}^-$ et $r_s^+$ des interfaces successives respectivement. De plus, nous avons posé

$$\begin{aligned}
\mathbf{E}_s &= N_s \left[H\left(r_s\right)\overline{J}\left(r_s\right) - \overline{H}\left(r_s\right)J\left(r_s\right)\right]\cdot\mathbf{X}_s^{-1},\\
\mathbf{F}_s &= N_s \left[\overline{H}\left(r_s\right)J\left(r_{s+1}\right) - H\left(r_{s+1}\right)\overline{J}\left(r_s\right)\right]\cdot\mathbf{X}_s^{-1},\\
\mathbf{G}_s &= N_s \left[H\left(r_s\right)\overline{J}\left(r_{s+1}\right) - \overline{H}\left(r_{s+1}\right)J\left(r_s\right)\right]\cdot\mathbf{X}_s^{-1},\\
\mathbf{H}_s &= N_s \left[H\left(r_{s+1}\right)\overline{J}\left(r_{s+1}\right) - \overline{H}\left(r_{s+1}\right)J\left(r_{s+1}\right)\right]\cdot\mathbf{X}_s^{-1},
\end{aligned} \tag{56}$$

où

$$\mathbf{X}_s = H\left(r_s\right)J\left(r_{s+1}\right) - H\left(r_{s+1}\right)J\left(r_s\right). \tag{57}$$

Le passage à travers une interface est donné par

$$\begin{aligned}
\mathbf{U}_{s+1}^+ = \begin{bmatrix}\mathbf{U}_{ee}^+ & \mathbf{U}_{eh}^+\\ \mathbf{U}_{he}^+ & \mathbf{U}_{hh}^+\end{bmatrix} = \\
= \begin{bmatrix}W_{s+1}^{-1}\overline{E}_{s+1}C_{s+1}C_s^{-1}\overline{E}_s^{-1}W_s & 0\\ 0 & V_{s+1}^{-1}B_{s+1}B_s^{-1}V_s\end{bmatrix}\overbrace{\begin{bmatrix}\mathbf{U}_{ee}^- & \mathbf{U}_{eh}^-\\ \mathbf{U}_{he}^- & \mathbf{U}_{hh}^-\end{bmatrix}}^{\mathbf{U}_{s+1}^-}\begin{bmatrix}W_s^{-1}W_{s+1} & 0\\ 0 & V_s^{-1}V_{s+1}\end{bmatrix}\\
+ \begin{bmatrix}0 & W_{s+1}^{-1}\overline{E}_{s+1}C_{s+1}C_s^{-1}E_sK_r^{s+1}\overline{E}_sV_{s+1}\\ V_{s+1}^{-1}B_{s+1}B_s^{-1}K_r^{s+1}W_{s+1} & 0\end{bmatrix} +\\
- \begin{bmatrix}0 & W_{s+1}^{-1}K_r^{s+1}\overline{E}_{s+1}V_{s+1}\\ V_{s+1}^{-1}K_r^{s+1}W_{s+1} & 0\end{bmatrix},
\end{aligned} \tag{58}$$

où $+ \mapsto r_{s+1}^+$ et $- \mapsto r_{s+1}^-$ désignent respectivement les côtés droit et gauche de l'interface.

En échangeant les indices $s$ et $s+1$ ainsi que les exposants $+$ et $-$, on obtient l'expression du passage inverse.

Pour établir le problème modal homogène, nous fixons les conditions de bord suivantes : pas de fonction de Hankel au centre, pas d'ondes entrantes venant de l'extérieur. La propagation selon les équations (4.30) (ou (4.29)) et (4.44) permet d'imposer la condition de raccordement à une interface fixé, i.e.

$$\left(\mathbf{U}_{s'}^{L-} - \mathbf{U}_{s'}^{L+}\right)\mathbf{p}\left(r_{s+1}^-\right) = 0. \tag{59}$$

Dans ce cas la solution est la longueur d'onde complexe qui permet ensuite de calculer le facteur de qualité $Q$ en utilisant la relation suivante

$$Q = -\frac{\mathrm{Re}\{\lambda_c\}}{2\,\mathrm{Im}\{\lambda_c\}}. \tag{60}$$

Nous avons consacré beaucoup de temps pour choisir la méthode numérique pour résoudre ce système homogène. Nous avons finalement implémenté une méthode cherchant à faire la décomposition en valeurs singulières de la matrice puis à minimiser la valeur singulière la plus basse.

Différents résultats sont présentés sur un microanneau puis un microdisque, dans les tableaux 4.1, 4.2, 4.3, 4.4.

De plus nous avons aussi appliqué cette méthode sur des structures récentes permettant de confiner le champ dans les zones à faible indice de réfraction. Un disque utilisant ce principe sur l'axe de symétrie est proposé. Dans ce cas, seuls les modes TM permettent d'obtenir le résultat escompté. Cet effet est basé sur l'interférence de deux queues évanescents d'un mode TM, qui montre un saut du champ électrique a chaque interface.

Pour cela, nous décrivons brièvement le paramètre de confinement comme le suivant :

$$\Gamma_i^{TM} = \frac{\int_{layer\,i} |E_x|^2 \, \mathrm{d}x}{\int_{-\infty}^{\infty} |E_x|^2 \, \mathrm{d}x} \tag{61}$$

et l'effet Purcell (accroissement de l'émission spontanée)

$$F_p = \frac{\Gamma}{\Gamma_0} = \frac{6Q\left(\frac{\lambda}{2n}\right)^3}{\pi^2} \frac{\epsilon\left(\vec{r}_{max}\right) \max \left|\vec{E}\left(\vec{r}\right)\right|^2}{\int_{-\infty}^{\infty} \epsilon\left(\vec{r}\right) \left|\vec{E}\left(\vec{r}\right)\right| \, \mathrm{d}\vec{r}} = \frac{6Q\left(\frac{\lambda}{2n}\right)^3}{\pi^2 V_{eff}} = \frac{6Q}{\pi^2 \tilde{V}_{eff}}. \tag{62}$$

Cette structure a comme avantage de réduire le volume modal $\tilde{V}_{eff}$. Dans la figure 4.16 nous montrons une forte amélioration de ce facteur.

## Chapitre 5

Le dernier chapitre est consacré à la description de plusieurs configurations optiques utilisant des microdisques et réalisées en SOI. Ils ont comme point commun d'être tout le temps associé à au moins un guide droit.

Il introduit des pertes supplémentaires représentées sous la forme suivante :

$$\Psi \propto \exp\left[\left(j\omega_{res} - \alpha - \alpha_c\right) t\right] \tag{63}$$

où $\omega_{res}$ est la pulsation résonante, $\alpha$ les pertes intrinsèques du résonateur, et $\alpha_c$ les pertes de couplage : comme $Q_{tot} = \omega_{res}/(2\alpha_{tot})$, le coefficient de qualité est dépendant de toutes sources de fuites et il est exprimé par la formule suivante :

$$\frac{1}{Q_{tot}} = \frac{1}{Q_{int}} + \frac{1}{Q_{coupling}} \tag{64}$$

où $Q_{int}$ est le coefficient de qualité intrinsèque (i.e. causée par la géométrie du résonateur et par conséquent donnée par la cavité isolée), $Q_{coupling}$ représente les fuites supplémentaires induites par des perturbations extérieures et $Q_{tot}$ le coefficient général que l'on peut mesurer. Il est évident que la valeur de la limite du facteur de qualité total est liée au coefficient de qualité le plus faible.

Un guide monomode couplé à un résonateur à fort coefficient de qualité $Q$ permet d'obtenir la fonction de filtrage réjecteur de bande. Si deux guides sont utilisés, on peut obtenir un démultiplexeur ou un mutliplexeur (add&drop), voir les figures. 5.2 et 5.4.

Beaucoup de structures intégrées en SOI sont accessibles à l'IMEP : nous avons étudié quelques composants tels que des disques de $8\mu m$ de diamètre associés à un guide. Sa forte sélectivité en longueur d'onde ($Q > 50000$) permet d'observer beaucoup de résonances. Un phénomène de levée de dégénérescence est observée du à une rupture de symétrie créée par l'approche du guide à côté du disque.

Il est possible aussi de détecter des effets non-linéaires causés par des effets thermiques.

Nous avons fait des caractérisations avec une source continue et accordable en longueur d'onde. Malheureusement, très peu de résultats intéressants ont été obtenus. Des problèmes dues à la rugosité, à des imprécisions sur la séparation guide disque ou des problèmes de la qualité de la gravure peuvent être à l'origine de ces résultats.

En effet, une petite variation du gap guide-disque est suffisant pour modifier l'efficacité du couplage. De plus si le couplage est trop faible, le pic de résonance est masqué par les oscillations de la cavité Fabry-Pérot induites par la cavité définie par le guide droit seul. La précision des mécanismes du micropositionneur influence aussi les résultats.

Les composants à base de microgears ont aussi été étudiés. Le microgear est un disque constitué d'un réseau de trous périodique à sa périphérie. Ceci permet d'obtenir des effets de Bragg et d'avoir une sélectivité des modes d'ordre azimutal différent. Le couplage dans ce cas avec le guide est moins efficace due à une levée de dégénérescence importante du mode dans le microgear. Ceci est intrinsèquement lié à l'effet Bragg (onde stationnaire) et représente une différence importante par rapport au simple microdisque, qui est un composant à ondes progressives.

## Conclusion

L'objectif de ce travail a été d'étudier de nouveaux composants d'optique intégrée pour des applications passives ou actives dans le domaine de la photoniques. Des propriétés non-linéaires intéressantes peuvent être analysées dans des structures périodiques : SGS permet de contrôler optiquement le routage de la lumière. Le confinement de la lumière dans des cavités à fort coefficient de qualité $Q$ permettent de filtrer les signaux lumineux. De nouvelles expériences non-linéaires ou d'électrodynamique quantique sont maintenant envisageables. Une grande partie du travail a été consacrée à l'implémentation de deux méthodes numériques dans le but d'avoir une mise en œuvre simple et d'accéder à une grande rapidité de calcul. L'étude d'une BPM et d'une méthode modale efficace tel que l'A-FMM nous ont permis d'apprendre et maîtriser des techniques dominantes très avantageuses. La partie expérimentale a montré la difficulté de fabriquer et caractériser des composants intégrés à grande sélectivité, bien que beaucoup d'applications importantes soient possibles.

# Introduction

In recent years we have assisted to contradictory trends in the evolution of integrated optics. This field, also referred to as *Photonics*, in analogy with electronics to indicate processing of data by means of photons, has had a striking impact on communication industry. The invention of optical fibres (as signal transmitters) and of the laser, that date back to the fifties of the twentieth century, have provided the technical background to the development of the global communication network, Internet.

Nonetheless laser has allowed to set up fundamental physical experiments, e.g. laser trapping, to improve the accuracy of experimental optics owing to laser light coherence, and to reveal previously disregarded light-matter interactions, such as nonlinear effects.

Laser technology is widespread, from industrial applications to communications, and optical fibres are used as reliable link in a large variety of environments.

Moreover optical fibres represent a mature and reliable product, with even small margins of improvement; this is a remarkable peculiarity among other high-technology industries and consequently an economic issue for the field.

As a comparison we can consider Electronics: Moore's law[1] have been a fair representation of its development trend for more than thirty years. Indeed MOSFET scaling was for ages a straightforward process, that allowed to gain efficiency (voltage, power consumption, switching speed), without facing severe physical limits.

In recent years, however, many structural limitations have been tackled and new technological nodes accomplished: each step requires a careful study of materials, fabrication techniques, parasitic side-effects etc... Moreover power consumption in integrated circuits is a serious problem, along with time delay and signal integrity that limit chip to chip bandwidth on boards.

In a rough economic model, electronic industry, as a general purpose technology, with a seemingly everlasting expansion and innovation, owes its pace to frequent introduction of new systems, solutions, and products, whose advanced capabilities induce to replace old products. The resulting revenues have funded innovative research projects, among which also photonics plays an important role, in order to implement next-generation systems.

Integrated optics provides fast (at the speed of light) electric interference-free signalling and processing of wide-band signals; optical storage and several computing functionalities can also be considered.

In optics many different materials are employed, III-V compound semiconductors, like

1. Transistor density and integrated circuit performance nearly doubling every eighteen-months.

GaAs, InP, AlGaAs, more peculiar compounds as $LiNO_3$, a variety of glasses, organic films and so on. Each corresponds to a specific fabrication technique (growth, lithography, etching), as well as guiding properties and optical activity.

Electronics has instead developed Silicon as first choice, because it guarantees high yields at low cost, its oxidation produces one the best available insulators, and it guarantees fast CMOS operations.

Silicon and silica are exceptionally good to build a micro-integrated waveguide, but one of the main issues to bring optoelectronics to Silicon is to develop active devices, considering that both lasing and modulation are hard to obtain, owing respectively to indirect electronic band-gap and the absence of strong nonlinear effects. In fact thermal induced shifts of refractive index is dominant, but extremely slow.

In spite of those difficulties, many breakthroughs have been made, e.g. the first demonstration of a continuous-wave laser based on Raman effect [1], and fast modulation based on electronic-plasma dispersion, [2].

Nonetheless, a lot of active research is being performed in silicon photonics; lasing and amplification capabilities could be reached perhaps by modifying microscopic structure departing from bulk crystal, e.g. nanoclusters and nanocrystals embedded in silica; micro- and nano-technology have allowed to implement e.g. hybrid InP laser on a silicon chip, see [3]. We mention also the astonishing properties of metamaterials, that exhibit negative index of refraction, that depends more on the structure of the material rather than on intrinsic material properties, see [4].

Moreover architecture plays a crucial role: there exist devices in which modulation, programmable filters and multiplexers, and switches could benefit from low-threshold nonlinear optics.

Considering that nano-technology will probably permit to attain new capabilities, inconceivable in bulk materials, and that electronics will take the risk to adopt new materials, we can reckon that photonics will benefit from silicon processing techniques, as well as electronics will avoid to slow down its extraordinary pace, exploiting new features provided by the photonic domain, tolerating or even proposing hybrid structures and processes, employing new materials and concepts.

A more detailed analysis of the state of the art of photonics and its relations to the electronic industry can be found in [5].

Basically, this work is focused on micro-structured integrated optical devices, which can be used to process lightwave signals.

By means of micro-fabrication techniques, deposition, lithography, doping (suitable to modulators or active devices), magnetic periodic poling (to achieve phase-matching in nonlinear optics), propagation can be moulded to better exploit light-matter interactions.

Two device families have attracted a lot of attention in recent-years:

- periodic structures and photonic crystals;
- integrated micro-cavities.

The first group is based on the existence of modes that are not scattered in propagation along with modes that are not allowed to propagate, due to Bragg reflection, the second relies on confining light by internal reflection mechanisms for extremely long times.

Each guiding and confining mechanism enables to achieve specific properties in light-matter interactions.

Photonic crystals provide a complete framework to implement optical integrated systems: waveguides with peculiar properties (e.g. slow light applications) have been obtained as line defects, cavities as point defects, i.e. missing or excess hole/rod that lead to an additional localised state to the periodic structure. A high $Q$-factor cavity is achieved in this case due to symmetry breaking induced by the defect as opposed to the extreme regularity of the surrounding periodic repetition.

Integrated microcavities, such as microdisks, microrings, microtori, and microspheres, obtain even better performance due to their regular shape (microtori have quality factor $Q \approx 10^6$, microspheres up to $Q \approx 10^8$). For this reason they seem particularly suitable to cavity QED (C-QED) applications, from Purcell factor enhancement to strong coupling, since their resonances can be made extremely narrow, see [6–8], but can be also exploited to store or modulate light. Nevertheless those effects are being investigated also in photonic crystal cavities.

Applications of microcavities also encompass active devices, indeed via a nonlinear effect, e.g. thermo-optical, Pockels, or carrier injection, we can shift a resonant peak and allow or forbid the light coupling inside, a sort of switching functionality; layers of active materials permit to achieve quantum interactions and light generation.

Finally it is worth recalling an innovative guiding mechanism provided by arrays of coupled-resonators that are used to tailor pulse propagation, e.g. obtaining dispersionless propagation, we refer to coupled-resonator optical waveguides (CROWs), see [9, 10]. Many authors propose the terms *photonic atom* and *photonic molecule*, see [11, 12] to express the opportunity of studying not only simple building blocks (atoms, such as cavities) but also compounds obtained by their use (molecules, among which CROWs are the simplest example). In this way we have a conceptual framework that includes both of the above-mentioned families and many new ideas, based on them.

In order to clarify our activity, we remark that many other applications of photonic crystals have been investigated in recent years: several interesting phenomena are admitted, see [13]. Soliton propagation, i.e. a dispersion- or diffraction-less regime, can be attained, and the effect of periodicity and improved confinement of selected field patterns results in unique dynamical properties (e.g. bifurcations and stability) as well as a lower threshold to achieve effective nonlinear interactions.

Many features of solitonic regimes in periodic devices are being studied, both analytical and modelling (e.g. identification of stability regions, role of approximations), as well as experimental (e.g. how to excite a stable pulse or profile, possible applications to routing or switching, materials and set-ups). We concentrated on modelling strategies applied to spatial gap solitons in 1D periodic media, with both Kerr and quadratic nonlinearities.

As we have just mentioned, resonators provide an alternative processing building block

and can be widely exploited. Cylindrical microresonators, such as microrings or microdisks are suitable to planar integration, specifically in silicon on insulator (SOI), and theoretical, design and fabrication limits have to be thoroughly investigated in order to obtain reliable devices for industrial production.

Having joined a European project, a year of doctoral work was spent at the IMEP laboratory in Grenoble, where this research topic have been active for several years. As far as small cylindrical cavities are considered, the hybrid character of their linear modal structures requires a full 3D analysis. Then we implemented a novel numerical method based on the simple aperiodic Fourier modal method (A-FMM), that overcomes several limits of previously proposed approaches.

Moreover those structures are quite sensitive, as other optical devices, to fabrication misfits, e.g. roughness, shape defects, impurities, distances between elements. Let us consider their high-$Q$: a disturbance may affect remarkably the final behaviour. Thus a thorough experimental characterization have to be performed, in order to compare different fabrication techniques and to assess design procedures: we focused on disk-based filters and add&drops implemented in SOI. The study of those integrated chips, actually quite simple structures, has been aimed to optimise waveguide coupling, to qualify fabrication limits (e.g. surface scattering and the splitting of counter-propagating modes), sensitivity to environment perturbation, and to investigate nonlinear effects (e.g. thermal effect arises also at low power.)

The structure of this thesis is as follows. After an overview of modelling in Optics, specifically of parametric nonlinear phenomena, such as Kerr effect and second harmonic generation (SHG), and modal methods, chapter 1, in chapter 2 the nonlinear beam-propagation method is recalled; then we specifically analyse the self-trapping regime called *spatial gap-soliton*. In chapter 4 we describe our modal method approach to cylindrical microresonators.

The experimental work on SOI waveguide-coupled microdisk resonators is discussed in chapter 5, where, after a brief outline of design principles, some results of characterization are presented.

Conclusion and perspectives for future work are then presented; a few appendices follow to report more detail about related topics.

# Chapter 1

# A Survey on the Modelling of Integrated Optical Devices

Since a large part of the research work has been focused on numerical techniques in integrated optics, we believe it is worth providing a brief survey on modelling approaches, in the classical framework of Maxwell equations.

We are thus going to report a sort of classification of methods, that could be distinguished by their level of approximation (e.g. 1D, 2D, or 3D), their conceptual framework (i.e. are we starting from wave equation, or from an approximation, does we discretize the space or compute modes?), and by their capability to deal with a variety of phenomena (dispersion, nonlinearities, electronic distribution).

Let us start from Maxwell equations.

## 1.1 Maxwell Equation in a Charge-free Region

In optics we usually study dielectric materials and the effect of a free electromagnetic field on it, thus we can consider source- and charge-free Maxwell equations, that read as

$$\nabla \times \vec{\mathcal{E}}(x,y,z,t) = -\frac{\partial \vec{\mathcal{B}}(x,y,z,t)}{\partial t} \tag{1.1}$$

$$\nabla \times \vec{\mathcal{H}}(x,y,z,t) = \frac{\partial \vec{\mathcal{D}}(x,y,z,t)}{\partial t} \tag{1.2}$$

$$\nabla \cdot \vec{\mathcal{D}}(x,y,z,t) = 0 \tag{1.3}$$

$$\nabla \cdot \vec{\mathcal{B}}(x,y,z,t) = 0 \tag{1.4}$$

where we used the common compact vectorial notation and symbols,

- $\vec{\mathcal{E}}$ electric field;
- $\vec{\mathcal{H}}$ magnetic field;
- $\vec{\mathcal{D}}$ electric induction;

- $\vec{\mathcal{B}}$ magnetic induction.

Constitutive equations of a general class of materials can be expressed as

$$\vec{\mathcal{D}}(x,y,z,t) = \left[\bar{\bar{\epsilon}}(x,y,z,\omega,|\vec{\mathcal{E}}|) \otimes \vec{\mathcal{E}}(x,y,z,t)\right] \tag{1.5}$$

$$\vec{\mathcal{B}}(x,y,z,t) = \left[\bar{\bar{\mu}}(x,y,z,\omega,|\vec{\mathcal{H}}|) \otimes \vec{\mathcal{H}}(x,y,z,t)\right] \tag{1.6}$$

The two relations (1.5) and (1.6) account for the opportunity of including anisotropic, inhomogeneous, nonlinear effects. The $\otimes$ is intended as a functional operation, such as convolution, necessary to describe dispersive contributions.

To provide a solution of an electromagnetic problem, boundary conditions are required; in dielectrics they reduce to continuity of normal components of $\vec{\mathcal{D}}$ and $\vec{\mathcal{B}}$, as well as of tangential components of $\vec{\mathcal{E}}$ and $\vec{\mathcal{H}}$.

Moreover, we do usually deal with non-magnetic materials, i.e. $\mu = \mu_0 = 4\pi \times 10^{-7}\, H/m$, then we realize that continuity conditions imply different behavior of electric and magnetic field across an interface between two different media.

## 1.2 Wave Equation as Inspiration for Modelling

Electromagnetic problems, as those described by eqs. (1.1)–(1.4) are generally quite hard, thus we have basically to introduce several hypotheses to reduce to more practical forms.

We have mainly to deal with:

- the material properties and models;
- the device structure.

It is well known that the choice of an approximation instead of another is based on a trade-off between accuracy and computation time. Moreover in most situations, a conceptually simple algorithm (e.g. finite-difference time-domain method (FDTD)) provides good results and fits a large variety of problems, but is also very time and resource demanding. Passing to a more sophisticated approach (e.g. FEM) requires much more effort in implementation, but could guarantee better performance. As an alternative, models derived by simple approximations or exploiting mathematical properties, that are suitable to specific structures, are generally beneficial in terms of implementation ease and time-consumption.

We firstly consider anisotropic, linear, non-dispersive dielectric materials, in order to obtain a simple form of vectorial wave equation. Further on we will provide some details about nonlinear propagation.

Let us apply the curl to eq. (1.1) and insert in it eq. (1.2), then, using the well-known identity

$$\nabla \times \nabla \times \vec{A} = \nabla\left(\nabla \cdot \vec{A}\right) - \nabla^2 \vec{A}$$

we can derive a full-vectorial equation for the electric field.

$$\nabla^2 \vec{\mathcal{E}}(x,y,z,t) - \nabla\left(\nabla \cdot \vec{\mathcal{E}}(x,y,z,t)\right) + \mu_0 \frac{\partial^2 \vec{\mathcal{D}}(x,y,z,t)}{\partial t^2} = 0 \tag{1.7}$$

We remark that, since the electric induction $\vec{\mathcal{D}}$ is not expressed in a specific form, we can still use the latter equation to study nonlinear phenomena.

We can now impose the linearity hypothesis

$$\vec{\mathcal{D}}(x,y,z,t) = \varepsilon(x,y,z)\vec{\mathcal{E}}(x,y,z,t) \tag{1.8}$$

Since we will study in detail time-harmonic methods, a time-dependence $\exp(j\omega t)$ is assumed; to account for finite bandwidth pulses, we span over a frequency range.

From eq. (1.7), inserting (1.8), we can obtain

$$\nabla^2\vec{E}(x,y,z) + k_0^2 n^2(x,y,z)\vec{E}(x,y,z) = \nabla\left(\nabla\cdot\vec{E}(x,y,z)\right) \tag{1.9}$$

In eq. (1.9) $\vec{E}$ is the complex vector representing the electric field, $k_0 = \frac{2\pi}{\lambda}$ is the free-space wavenumber, with $\lambda$ the free-space wavelegth, and $n(x,y,z) = \sqrt{\frac{\mu\varepsilon(x,y,z)}{\mu_0\varepsilon_0}}$ is the refractive index profile of the medium.

Substituting the suitable constitutive relation, we recast eq. (1.3) as

$$0 = \nabla\cdot\vec{D}(x,y,z,t) = \nabla\cdot\left(\varepsilon(x,y,z)\vec{E}(x,y,z)\right)$$

and

$$\nabla\cdot\vec{E}(x,y,z) = -\frac{\nabla\varepsilon(x,y,z)}{\varepsilon(x,y,z)}\cdot\vec{E}(x,y,z) = -\frac{\nabla n^2(x,y,z)}{n^2(x,y,z)}\cdot\vec{E}(x,y,z)$$

Applying the latter expression to (1.9), we obtain

$$\nabla^2\vec{E}(x,y,z) + k_0^2 n^2(x,y,z)\vec{E}(x,y,z) = -\nabla\left(\nabla\ln n^2(x,y,z)\cdot\vec{E}(x,y,z)\right) \tag{1.10}$$

that component-wise reads as

$$\begin{aligned}&\frac{\partial^2 E_i(x,y,z)}{\partial x^2} + \frac{\partial^2 E_i(x,y,z)}{\partial y^2} + \frac{\partial^2 E_i(x,y,z)}{\partial z^2} + \\ &+ k_0^2 n^2(x,y,z)E_i(x,y,z) = -\frac{\partial}{\partial i}\left[E_x(x,y,z)\frac{\partial\ln n^2(x,y,z)}{\partial x} + \right. \\ &\left. + E_y(x,y,z)\frac{\partial\ln n^2(x,y,z)}{\partial y} + E_z(x,y,z)\frac{\partial\ln n^2(x,y,z)}{\partial z}\right]\end{aligned} \tag{1.11}$$

. Eq. (1.11), for $i = x,y,z$, constitutes the so-called vectorial Helmholtz equations.

Let us present two further simplifications of eq. (1.10) or (1.11), that are usually applied to reduce the formal complexity as well as the computational load of a numerical solver. Their accuracy depends on the structure under analysis, but they are less and less generic:

- refractive index variations are negligible compared to a mean index, used as reference:

$$\frac{\Delta n}{n} \ll 1 \tag{1.12}$$

  right-hand side terms

$$\frac{\partial}{\partial j}\left[\frac{\partial\ln n^2(x,y,z)}{\partial i}\right], \text{ with } j \neq i$$

can be neglected, leading to *reduced vectorial equations* or *semi-vectorial Helmholtz equations*:

$$\frac{\partial^2 E_i}{\partial x^2} + \frac{\partial^2 E_i}{\partial y^2} + \frac{\partial^2 E_i}{\partial z^2} + \omega^2 \mu_0 \varepsilon E_i = -\frac{\partial}{\partial i}\left(E_i \frac{1}{\varepsilon}\frac{\partial \epsilon}{\partial i}\right) \tag{1.13}$$

with $i = x, y, z$.

- moreover, if dielectric permittivity inhomogeneity is nearly zero on a wavelength scale, i.e.

$$\frac{\nabla \varepsilon(x, y, z)}{\varepsilon(x, y, z)} \ll \frac{1}{\lambda} \tag{1.14}$$

we can cancel all the right-hand side and reduce to *scalar Helmholtz equations*:

$$\frac{\partial^2 E}{\partial x^2} + \frac{\partial^2 E}{\partial y^2} + \frac{\partial^2 E}{\partial z^2} + \omega^2 \mu_0 \varepsilon E = 0 \tag{1.15}$$

$E$ designates a generic component of the electric field.

A special care should be taken while using semivectorial approximation, (1.13): they assume the absence of coupling between different field components: this is a good assumption in guided-optics, provided that we deal with a weak-guiding regime. Scalar approximation is suitable to homogeneous areas. Despite the seeming uselessness of this assumption, it plays a key role if a device can be decomposed in nearly homogeneous regions. Imposing interface/boundary conditions between adjacent volumes permits to solve the electromagnetic problem neglecting transitions from one to another.

The latter formulation can be expressed also as:

$$\nabla^2 \vec{E} + \omega^2 \mu_0 \varepsilon \vec{E} = 0 \tag{1.16}$$

From (1.10), by application of the *duality principle* of electrodynamics, i.e.

$$\vec{E} \leftrightarrow \vec{H}$$
$$\vec{H} \leftrightarrow -\vec{E}$$
$$\epsilon \leftrightarrow \mu$$
$$\mu \leftrightarrow \epsilon$$

we obtain a wave equation for the magnetic field, that results merely scalar on the assumption of non-magnetic materials, i.e.

$$\nabla^2 \vec{H} + k_0^2 n^2(x, y, z)\vec{H} = 0 \tag{1.17}$$

### 1.2.1 Paraxial approximation

In this work we are treating chiefly propagative problems, i.e. computing the evolution of an electromagnetic field in a structure starting from a known excitation profile at one of its ends. Instead of solving a boundary-value problem, as results in general from eqs. (1.15) and (1.17), the solution of an initial-value approximated formulation is often made.

Hence it is worthwhile to report a widely used approximation technique, the *paraxial approximation* or slowly-varying envelope approximation (SVEA), that originates in the field of *geometric optics*, but is employed in beam propagation method (BPM) and constitutes a fundamental basis in coupled-mode theory (CMT) calculations; as another example, *gaussian beams* are solutions of such an approximated formulation. It simplifies the problem and reduces computational time, providing a reliable solution of a large number of problems.

Let us assume that a light wave propagates mainly in a specified direction, say $z$, i.e. in the plane-wave spectrum the contributions of wavevector $\vec{k}$ corresponding to other orientations are less important,

$$k_z^2 \approx k_0^2 n_0^2 \gg \left(k_x^2 + k_y^2\right)$$

where $n_0$ is a suitable reference index.

In this spirit, we can express a field as

$$\vec{E}(x,y,z) = \vec{u}(x,y,z)e^{-jk_0n_0z} \tag{1.18}$$

or equivalently component-wise

$$E_i(x,y,z) = u_i(x,y,z)e^{-jk_0n_0z} \tag{1.19}$$

where $\vec{u}(x,y,z)$ is a slowly-varying envelope.

It is easy to understand that this approximation is equivalent to considering only a limited set of propagation angles about the main propagation direction.

We now substitute ansatz (1.19) in (1.11) and specify it for the $x$ component to obtain

$$\begin{aligned}\frac{\partial^2(u_xe^{-jk_0n_0z})}{\partial x^2} + \frac{\partial^2(u_xe^{-jk_0n_0z})}{\partial y^2} + \frac{\partial^2(u_xe^{-jk_0n_0z})}{\partial z^2} + k_0^2n^2u_xe^{-jk_0n_0z} = \\ = -\frac{\partial}{\partial x}\left(u_xe^{-jk_0n_0z}\frac{\partial \ln n^2}{\partial x} + u_ye^{-jk_0n_0z}\frac{\partial \ln n^2}{\partial y} + u_ze^{-jk_0n_0z}\frac{\partial \ln n^2}{\partial z}\right).\end{aligned} \tag{1.20}$$

After expanding derivatives, we can apply the SVEA, i.e.

$$\left|\frac{\partial^2 u_i}{\partial z^2}\right| \ll 2k_0n_0\left|\frac{\partial u_i}{\partial z}\right|, \tag{1.21}$$

and obtain an approximated propagative equation in the form

$$\begin{aligned}j\frac{\partial u_x}{\partial z} = \frac{1}{2k_0n_0}\left[\frac{\partial^2 u_x}{\partial x^2} + \frac{\partial^2 u_x}{\partial y^2} + \left(k_0^2(n^2 - n_0^2)\right)u_x + \right. \\ \left. + \frac{\partial}{\partial x}\left(u_x\frac{\partial \ln n^2}{\partial x} + u_y\frac{\partial \ln n^2}{\partial y} + u_z\frac{\partial \ln n^2}{\partial z}\right)\right]\end{aligned} \tag{1.22}$$

Repeating the same calculations for the other transverse component $u_y$ [1] and rearranging in matrix form we obtain, see [14, 15]:

$$\frac{\partial}{\partial z}\begin{bmatrix}u_x\\u_y\end{bmatrix} = \frac{1}{2jk_0n_0}\begin{bmatrix}M_{11} & M_{12}\\M_{21} & M_{22}\end{bmatrix}\begin{bmatrix}u_x\\u_y\end{bmatrix} + \begin{bmatrix}R_x(u_z)\\R_y(u_z)\end{bmatrix} \tag{1.23}$$

1. As usual in other approaches, the whole fields can be obtained from two components

where matries $M_{11}$, $M_{12}$, $M_{21}$, $M_{22}$, $R_x(u_z)$, $R_y(u_z)$ represent formal operators defined as

$$M_{11} = \frac{\partial^2}{\partial x^2} + \frac{\partial^2}{\partial y^2} + k_0^2(n^2 - n_0^2) + \frac{\partial \ln n^2}{\partial x}\frac{\partial}{\partial x} + \frac{\partial^2 \ln n^2}{\partial x^2}$$

$$M_{12} = \frac{\partial \ln n^2}{\partial y}\frac{\partial}{\partial x} + \frac{\partial^2 \ln n^2}{\partial x \partial y}$$

$$M_{21} = \frac{\partial \ln n^2}{\partial x}\frac{\partial}{\partial y} + \frac{\partial^2 \ln n^2}{\partial x \partial y}$$

$$M_{22} = \frac{\partial^2}{\partial x^2} + \frac{\partial^2}{\partial y^2} + k_0^2(n^2 - n_0^2) + \frac{\partial \ln n^2}{\partial y}\frac{\partial}{\partial y} + \frac{\partial^2 \ln n^2}{\partial y^2}$$

$$R_x = \frac{1}{2jk_0n_0}\frac{\partial}{\partial x}\left(u_z\frac{\partial \ln n^2}{\partial z}\right)$$

$$R_y = \frac{1}{2jk_0n_0}\frac{\partial}{\partial y}\left(u_z\frac{\partial \ln n^2}{\partial z}\right)$$

a formal solution of (1.23), that represents propagation from $z$ to $z + \Delta z$ reads as

$$\begin{aligned}\begin{bmatrix} u_x(z+\Delta z) \\ u_y(z+\Delta z)\end{bmatrix} &= e^{-j\int_z^{z+\Delta z} P\, d\xi}\begin{bmatrix} u_x(z) \\ u_y(z)\end{bmatrix} + \\ &+ e^{-j\int_z^{z+\Delta z} P\, d\xi} \cdot \int_z^{z+\Delta z} e^{-j\int_z^{\xi} P\, d\eta}\begin{bmatrix} R_x \\ R_y\end{bmatrix} d\xi\end{aligned} \tag{1.24}$$

where $P = \frac{1}{2k_0n_0}M$.

The latter operator $P$ can be expanded as $P = P^{prop} + P^{ph} + P^{inhom} + P^{cc} + P^{pol}$, where the following positions have to be made:

$$P^{prop} = \frac{1}{2k_0n_0}\begin{bmatrix} \frac{\partial^2}{\partial x^2} + \frac{\partial^2}{\partial y^2} & 0 \\ 0 & \frac{\partial^2}{\partial x^2} + \frac{\partial^2}{\partial y^2}\end{bmatrix} \tag{1.25}$$

$$P^{ph} = \frac{1}{2k_0n_0}\begin{bmatrix} k_0^2\left(n^2 - n_0^2\right) & 0 \\ 0 & k_0^2\left(n^2 - n_0^2\right)\end{bmatrix} \tag{1.26}$$

$$P^{inhom} = \frac{1}{2k_0n_0}\begin{bmatrix} \frac{\partial^2 \ln n^2}{\partial x^2} + \frac{\partial \ln n^2}{\partial x}\frac{\partial}{\partial x} & 0 \\ 0 & \frac{\partial^2 \ln n^2}{\partial y^2} + \frac{\partial \ln n^2}{\partial y}\frac{\partial}{\partial y}\end{bmatrix} \tag{1.27}$$

$$P^{cc} = \frac{1}{2k_0n_0}\begin{bmatrix} 0 & \frac{\partial \ln n^2}{\partial y}\frac{\partial}{\partial x} \\ \frac{\partial \ln n^2}{\partial x}\frac{\partial}{\partial y} & 0\end{bmatrix} \tag{1.28}$$

$$P^{pol} = \frac{1}{2k_0n_0}\begin{bmatrix} 0 & \frac{\partial^2 \ln n^2}{\partial x \partial y} \\ \frac{\partial^2 \ln n^2}{\partial x \partial y} & 0\end{bmatrix} \tag{1.29}$$

By means of definitions (1.25)–(1.29), we identify the characteristics of 3D propagation: we can now discern which model is most suitable to the structure in question.

$P^{prop}$ is the propagation in a homogeneous medium of refractive index $n_0$.

$P^{ph}$ is a phase correction to account for the proper index.

$P^{inhom}$ considers the effect of cross section inhomogeneity.

$P^{cc}$ represents how transverse index variations, if any, couple field components $u_x$ e $u_y$.

$P^{pol}$ accounts for the polarization rotation induced by the index profile.

By inspection of eqs. (1.25)–(1.29), following [15] and [16], we can state that vectorial model (solution provided in [14, 15]) corresponds to the retention of every term. If $P^{cc}$ and $P^{pol}$ are neglected semi-vectorial equation is obtained; elimination of $P^{inhom}$ leads to scalar algorithms.

Earlier BPM implementations, based on paraxial approximation, show many accuracy issues that, see for example [17], can be partly mitigated by *wide-angle* versions that, by improving the paraxial approximation, seek to consider propagation of narrow field profiles (i.e. larger spatial spectra). Finally, notice that the SVEA implies a unique direction and orientation of propagation: bi-directional propagation is feasible only on account of other techniques, in a limited set of configurations.

## 1.3 Nonlinear Propagation

As it is stated in the introduction, laser technology have allowed to analyse many physical phenomena nearly unimaginable before: nonlinear Optics (NLO) is among them.

Light-matter interaction encompasses a variety of different effects: electronic transitions (as in LEDs or lasers), interplay with other excitons (as with phonon in Raman effect), or as dipole-polarization effects on a microscopic scale (e.g. frequency mixing nonolinear phenomena).

The latter example is generally rather sensitive to illumination intensity, giving rise to frequency conversion, modulation and/or self-modulation effect.

Let us briefly outline the framework of NLO (an extensive treatment can be found, e.g., in [18]):

- parametric effects
  - Second Harmonic Generation;
  - Kerr Effect;
  - Sum Frequency Generation;
  - Pockels Effect;
- scattering phenomena
  - Rayleigh Scattering (elastic);
  - Brillouin Scattering (inelastic);
  - Raman Scattering (inelastic);

We will deal chiefly with parametric processes, that will be studied according to the classical model of high-order electric susceptibility. They play an important role in signal processing at optical frequencies.

It is worth recalling some fundamental properties of these phenomena:

- the medium plays a role as a "catalyst" of the energy transfer from one frequency (or polarization, or wave-vector) to another;
- the population of energy levels at atomic or molecular level is not affected, initial and final populations are the same;
- the classical model provides a representation in terms of distortion of electronic oscillating motions
  - nearly-instantaneous response ($10^{-15}s$);
  - nonlinear (NL) susceptibilities $\chi^{NL}(\omega)$ are real and weakly dispersive (off-resonance stimulus). [2]

Let us rewrite eq. (1.5) as

$$\vec{\mathcal{D}}(x,y,z,t) = \varepsilon_0 \vec{\mathcal{E}}(x,y,z,t) + \vec{\mathcal{P}}\left(x,y,z,t,\vec{\mathcal{E}}\right) \tag{1.30}$$

where $\vec{\mathcal{P}}$ is a nonlinear function of $\vec{\mathcal{E}}$.

Polarization can be developed in Taylor series, i.e.

$$\begin{aligned}\vec{\mathcal{P}}\left(x,y,z,t,\vec{\mathcal{E}}\right) = & \\ &= \varepsilon_0 \left(\chi^{(1)}\vec{\mathcal{E}}\right) + \\ &+ \vec{\mathcal{P}}^{(2)}\left(x,y,z,t,\left|\vec{\mathcal{E}}\right|^2\right) + \vec{\mathcal{P}}^{(3)}\left(x,y,z,t,\left|\vec{\mathcal{E}}\right|^3\right) + \dots \\ &= \vec{\mathcal{P}}^{LIN}\left(x,y,z,t,\vec{\mathcal{E}}\right) + \vec{\mathcal{P}}^{NL}\left(x,y,z,t,\vec{\mathcal{E}}\right)\end{aligned} \tag{1.31}$$

where the terms in the form $\vec{\mathcal{P}}^{(n)}$ represent the $n$-th order element of the polynomial expansion and, under the hypothesis of negligible dispersion, they are expressed in terms of a dielectric susceptibility tensor of order $n$, $\chi^{(n)}$.

The latter equations would not contain convolution-like integrals, usually referred to as Volterra series expansion. Nevertheless, to obtain a general formulation of nonlinear polarization the tensor character of susceptibilities has to be taken into account, as we make to compute linear polarization of anisotropic media, along with the complexity of higher order tensors. In fact the $n$-th order susceptibility is written as

$$\chi^{(n)}\left(\omega_1 + \omega_2 + \dots + \omega_n = \omega_f\right)$$

2. In the quantum mechanical picture, these effects are explained as interactions of external photons with electrons populating energy levels reached via virtual transitions (i.e. involving nonstationary states), justifying in this way the need of a strong radiation intensity, since photons are required to interact with electronic states that have an extremely small life-time.

to account for the interaction of $n$ electric field vectors.

Taylor expansion contains multiplication terms that result in energy transfer towards frequency contributions not included in the input.

It is worth specifying some more assumptions that allow to reduce the complexity of the final equations:

- field are Continuous Wave (CW), i.e. linear combinations of harmonic terms.
- no absorption (transparent media);
- real-valued $\chi^{NL}$, i.e. neither losses nor scattering phenomena are considered.
- perturbative nature of nonlinear effects.

This latter hypothesis permits to consider electric field as solenoidal, despite it is not rigorously so.

$$\nabla \cdot \vec{\mathcal{D}} = 0 \Rightarrow \varepsilon_0 \varepsilon_r \, \nabla \cdot \vec{\mathcal{E}} = -\nabla \cdot \vec{\mathcal{P}}^{NL}$$
$$\nabla \cdot \vec{\mathcal{E}} \simeq 0 \tag{1.32}$$

From 1.32, inserting 1.30 and 1.31 in 1.7, we have:

$$\nabla^2 \vec{\mathcal{E}}(x,y,z,t) - \mu_0 \varepsilon \frac{\partial^2 \vec{\mathcal{E}}(x,y,z,t)}{\partial t^2} = \mu_0 \frac{\partial^2 \vec{\mathcal{P}}^{NL}(x,y,z,t)}{\partial t^2} \tag{1.33}$$

### 1.3.1 Selection rules for a nonlinear optical process

Many different processes can occur at the same time, but each with different efficiency. It is worth investigating which mechanisms affect them, usually referred to as *selection rules*.

First of all, convergence of Taylor series in eq. (1.31) implies that coefficients vanish as long as we add terms.

As far as the material characteristics are concerned, crystal/molecular conformation influences nonlinear response.

Indeed crystal structures can be divided in two classes:

- *centrosymmetric* (invariant to $\vec{r} \leftrightarrow -\vec{r}$ transformation);
- *non-centrosymmetric*.

In centrosymmetric crystals and amorphous materials $\chi^{(2n)} = 0$, thus, e.g., in optical fibres third order nonlinearity is the first available.

Finally, given a specific device (structures and media involved), the choice of the excitation frequency as well as the field distribution affect the impact of NL effects. Since materials are generally dispersive, energy is transferred from one frequency to another in periodic fashion, that depends upon the relative phase at which harmonics combine. This is usually called the *phase-mismatch* effect, and by employing anisotropic crystals at proper orientation we can achieve *phase-matching* and dramatically improve interaction efficiency for a specific polarization. Moreover NL effects can be enhanced by confining fields in a tiny region. It is a quite promising approach to benefit from NL processing at low intensities.

We will provide two examples of NL propagation

- SHG;
- (optical) Kerr (self-)effect (OKE).

### 1.3.2 Second harmonic generation

Let

$$\mathcal{P}^{(NL)}(x,y,z,t) = \mathcal{P}^{(2)}(x,y,z,t) = \varepsilon_0 \chi^{(2)} \mathcal{E}^2 \tag{1.34}$$

and consider a propagative solution composed by two plane-wave or guided-modes, propagating at frequency $\omega$ e $2\omega$. Nonlinear perturbation impresses a modulation along $z$ direction, in the form of two slowly varying envelopes $u_1$ and $u_2$

$$\begin{aligned}\mathcal{E}(x,y,z,t) =& \frac{1}{2} f_1(x,y) u_1(z) e^{-jk_1 z + j\omega t} + \frac{1}{2} f_2(x,y) u_2(z) e^{-jk_2 z + j2\omega t} + \\ &+ \frac{1}{2} f_1(x,y)^* u_1^*(z) e^{jk_1 z - j\omega t} + \frac{1}{2} f_2(x,y)^* u_2^*(z) e^{jk_2 z - j2\omega t}\end{aligned} \tag{1.35}$$

where $k_1 = k_0 n_1$ and $k_2 = 2k_0 n_2$, with $k_0$ the free-space wavenumber, are the propagation constants at $\omega$ and $2\omega$ respectively, $f_1(x,y)$ and $f_2(x,y)$ are the corresponding modal profiles, i.e. solutions of

$$\left( \frac{\partial^2}{\partial x^2} + \frac{\partial^2}{\partial y^2} \right) f_i + k_0^2 \left( n^2(x,y) - n_i^2 \right) f_i = 0 \tag{1.36}$$

We then insert ansatz (1.35) in (1.33), considering that to substitute (1.35) in (1.34), we have to neglect harmonic terms at multiples of $\omega$ higher that those imposed by input field.

$$\mathcal{E}^2 = \frac{1}{4} \left[ f_1^2 u_1^2 e^{-j2k_1 z + j2\omega t} + 2 f_2 f_1 u_2 u_1^* e^{-j(k_2 - k_1) z + j\omega t} + \text{c.c.} + \underbrace{(0, 3\omega, 4\omega)}_{neglected} \right] \tag{1.37}$$

Applying (1.21), considering that time derivatives correspond to multiplication by $j\omega$ or $j2\omega$, and cancelling terms according to (1.36), we separate the envelope evolutions at the two wavelengths and write

$$\begin{cases} j f_1 \dfrac{\mathrm{d}u_1}{\mathrm{d}z} = \dfrac{\omega^2}{c_0^2} \dfrac{1}{2k_1} \chi^{(2)} f_2 f_1 u_2 u_1^* e^{-j\Delta k z} \\ j f_2 \dfrac{\mathrm{d}u_2}{\mathrm{d}z} = \dfrac{(2\omega)^2}{2c_0^2} \dfrac{1}{2k_2} \chi^{(2)} f_1^2 u_1^2 e^{j\Delta k z} \end{cases} \tag{1.38}$$

where we have posed

$$\Delta k = k_2 - 2k_1 \tag{1.39}$$

that represents the *phase-mismatch* mentioned earlier.

To obtain a standard form, many normalization can be made, but we introduce only a simple scaling, i.e.

$$U_i = \left( \sqrt{\frac{1}{2\eta_0} n_i \int f_i^2 \, dx \, dy} \right) u_i \tag{1.40}$$

The squared of fields thus gives local optical intensity.

Substituting eq. (1.40) in (1.38), integrating over the transverse profile, we can write

$$\begin{cases} j\dfrac{\mathrm{d}U_1}{\mathrm{d}z} = \chi U_2 U_1^* e^{-j\Delta kz} \\ j\dfrac{\mathrm{d}U_2}{\mathrm{d}z} = \chi U_1^2 e^{j\Delta kz} \end{cases} \tag{1.41}$$

where

$$\chi = \frac{2\pi}{\lambda}\sqrt{\frac{\eta_0}{2n_1^2 n_2}}\frac{\chi^{(2)}}{\sqrt{A_{eff}}} \tag{1.42}$$

$A_{eff}$ is a measure of the field confinement in the guiding section,

$$A_{eff} = \int f_2^2\, dx\, dy \left(\frac{\int f_1^2\, dx\, dy}{\int f_1^2 f_2\, dx\, dy}\right)^2 \tag{1.43}$$

whose unit is $m^2$. We notice that from eq. (1.42) second order NLO interactions can be enhanced by decreasing the square-root of field confinement.

### 1.3.3 Kerr effect

If we consider a cubic nonlinearity, we could deal with a self-action or a frequency mixing effect analogous to SHG. The self-action is particularly interesting: it is called optical Kerr effect (OKE) and acts as an illumination-induced modulation of refractive index.[3]

Polarization in a third-order nonlinear medium reads as

$$\mathcal{P}^{(3)}(x,y,z,t) = \varepsilon_0 \chi^{(3)} \mathcal{E}^3 \tag{1.44}$$

In this case the ansatz is a single propagating wave at (angular) frequency $\omega$:

$$\mathcal{E}(x,y,z,t) = \frac{1}{2} f(x,y)u(z)e^{-jkz+j\omega t} + \frac{1}{2} f(x,y)u^*(z)e^{jkz-j\omega t} \tag{1.45}$$

Let us use the same criterion in expanding the polarization field:

$$\mathcal{E}^3 = \frac{1}{8}\left[ f^3 u^2 u^* e^{-jkz+j\omega t} + \text{c.c.} + \underbrace{(3\omega)}_{neglected} \right] \tag{1.46}$$

After applying differential operators and simplifying, we obtain

$$jf^2\frac{\mathrm{d}u}{\mathrm{d}z} = \frac{\omega^2}{c_0^2}\frac{\chi^{(3)}}{4}\frac{1}{2k} f^4 |u|^2 u = k_0 n_2 f^4 |u|^2 u = \chi f^4 |u|^2 u \tag{1.47}$$

$n_2$ represents an equivalent nonlinear refractive index.

If square-root of intensity is used instead of electric field, we can write

$$j\frac{\mathrm{d}U}{\mathrm{d}z} = k_0 n_2^I |U|^2 U \tag{1.48}$$

where

$$U = \left(\sqrt{\frac{1}{2\eta_0} n_0 \int f^2\, dx\, dy}\right) u \tag{1.49}$$

3. OKE has not to be confused with the *static* Kerr effect that is controlled by a d.c. bias.

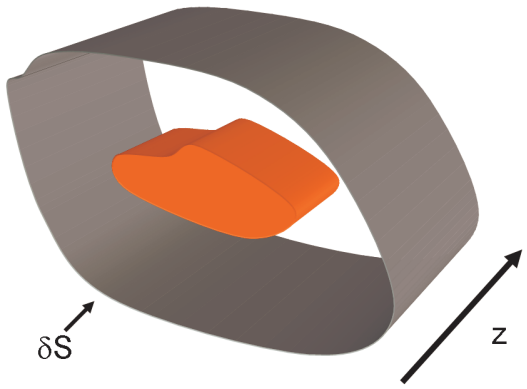


Figure 1.1: An example of z-Invariant Structure

and

$$n_2^I = n_2 \frac{2}{c_0 \varepsilon_0 n(\omega)} \frac{1}{A_{eff}} = n_2 \frac{2}{c_0 \varepsilon_0 n(\omega)} \frac{\int f^4 \, dx \, dy}{\left( \int f^2 \, dx \, dy \right)^2} \tag{1.50}$$

A closed-form solution of (1.48) is available, since if we suppose no losses occur $|U|^2$ is conserved (it is proportional to the energy in the medium and no other components can subtract it energy): it is apparent that Kerr effect can be regarded as a self-induced phase modulation, that can be represented as an intensity-dependent perturbation to the refractive index, i.e.

$$n_{tot} = n(\omega) + n_2 \frac{\int f^4 \, dx \, dy}{\int f^2 \, dx \, dy} |E|^2 = n(\omega) + n_2^I I_\omega \tag{1.51}$$

Again nonlinear efficiency increases as the transverse confinement increases.

Note that in eqs. (1.47) no phase-mismatch term appears: Kerr effect is always active in a cubic medium and cannot be suppressed, even if we are studying other third-order phenomena.

In separating the modal profile from electric field, TE polarization or a weak-guiding effect (approximately valid) is supposed. If plane waves are considered, we cancel the transverse dependence out in all normalization.

## 1.4 Propagation of Guided Waves

Many numerical methods rely upon spatial and/or temporal discretization of fields and can be derived from the equations we have presented above. Nevertheless it is well-known that, in the linear regime, a translational invariance implies the existence of guided waves, provided a proper choice of materials and frequency of operation. It is thus worth recalling the main properties of that kind of solutions, see the textbook [19],

Consider a generic structure as in figure 1.1, where material parameters do not change in $z$-direction and where no sources are present. An external enclosing surface is represented as well, to account for closed structures (and considering that simulation domain is always finite), but in case of open structures it can extend up to infinity.

It can be proven that the fields can be factorised in a transverse profile and a propagation term,

$$\begin{cases} \vec{E}(\vec{r}) = \vec{E}_t(\vec{r}_t)\exp(-j\beta z) \\ \vec{H}(\vec{r}) = \vec{H}_t(\vec{r}_t)\exp(-j\beta z) \end{cases} \tag{1.52}$$

where $\vec{r} = \vec{r}_t + z\hat{z}$, and the transverse profiles $\vec{E}_t$ and $\vec{H}_t$ are the so-called *eigenmodes* of the structure: they are solutions that do not require sources and maintain their shape during propagation. $\beta$ is the propagation constant of the eigenmode. It can be real or complex: in the first case we have rigorously propagating modes, otherwise they undergo a damping or amplification, though its profile is not affected. It is useful to define a related quantity, the effective index of the mode $n_{eff}$ such that

$$\beta = \frac{2\pi}{\lambda} n_{eff}$$

where $\lambda$ is as usual the free-space wavelength of light.

The invariant field configurations are called eigenmodes, since they are solution of a (functional) *eigenvalue problem*, that can be deduced from Maxwell equations, inserting in them the ansatz (1.52),

$$\left(\nabla_t^2 + k_0^2 n^2(\vec{r}_t)\right)\vec{E} = \beta^2 \vec{E} \tag{1.53}$$

and $\beta^2$ is the corresponding *eigenvalue*.

The solution of (1.53) subject to suitable boundary conditions provides a set of eigenmodes $\left(\vec{E}_i, \vec{H}_i\right)$ that, under appropriate hypotheses, constitute an orthogonal complete basis for electromagnetic propagation along the structure: thus a generic field can be expressed as a linear combination of them, i.e.

$$\begin{cases} \vec{E}(\vec{r}) = \sum_i A_i \vec{E}_i(\vec{r}_t)\exp(-j\beta_i z) \\ \vec{H}(\vec{r}) = \sum_i A_i \vec{H}_i(\vec{r}_t)\exp(-j\beta_i z) \end{cases} \tag{1.54}$$

We remark that this is rigorously true if several conditions are satisfied, and as far as open structures are concerned it does not exist a general proof of the completeness of commonly used modal sets.

Regardless the opportunity of computing analytic expressions of modes, they results from the guide cross-section, its composition, and boundary conditions on the surrounding surface or at an infinite distance (for dielectric waveguides, that are usually open structures).

### 1.4.1 Eigenmodes in open structures

Suppose to consider a lossless reciprocal structure with a central region (core) of refractive index $n_{co}$ and a outer region (cladding) of refractive index $n_{cl} < n_{co}$. An example of how effective indices of modes can distribute in the complex plane is provided in fig. 1.2.

Notice the symmetry of eigenvalues around the origin, i.e. if $\beta$ is a solution, also $-\beta$ is. This follows from the formulation of the problem, (1.53), the two solutions are waves propagating in opposite directions, according to the sign of the real part of $\beta$, forward (backward)

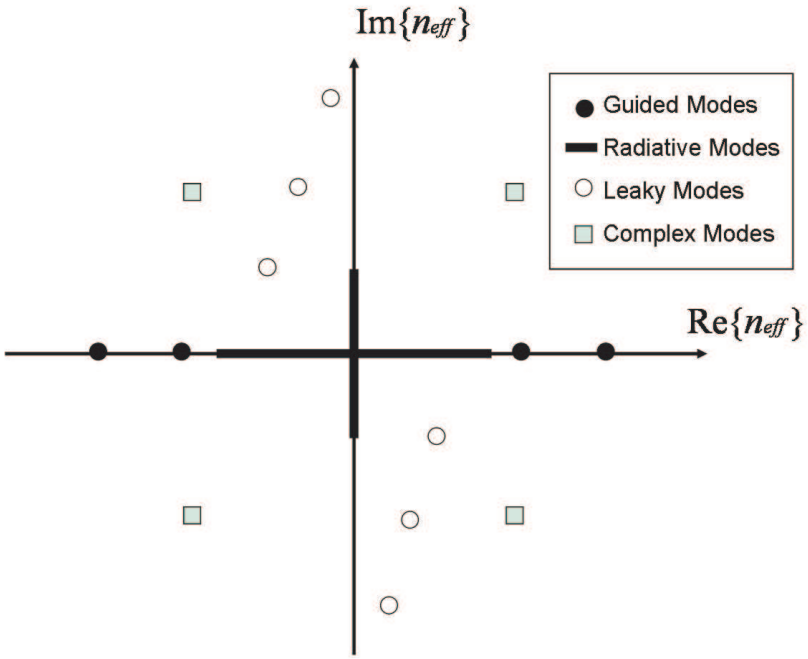


Figure 1.2: Distribution of the effective indexes of the eigenmodes of an open structure.

waves for positive (negative) values. Such a symmetry does not concern non-reciprocal media, such as active or nonlinear materials.

Modes can be classified in four groups:

- *Guided Modes* are located on the real axis. They form a discrete set and have effective indices between $n_{cl}$ and $n_{co}$. The field lies mainly in the core region, on account of its high index, while decreases exponentially in cladding. Real propagation constant implies that energy can be carried along the structure indefinitely, hence their name.

- *Radiative Modes* form a continuum along the real and the imaginary axes. Their field profiles oscillate in the cladding and extend up to infinity: the transverse energy flow justifies the term *radiative*. They can be either *propagative* ($\beta \in \mathbb{R}$) and keep their amplitude along $z$ or *evanescent* ($j\beta \in \mathbb{R}$), that damp exponentially.

- *Leaky Modes* are a discrete set located in the complex plane. They can be seen as a continuation of guided modes, in the sense that increasing frequency they can rejoin the set of confined propagative solutions. Their field profiles undergo a diverging trend in the cladding, hence they are not physical, but can be employed in calculations under certain circumstances.

- *Complex Modes* occur always in quartets $\beta = \pm\beta_{re} \pm j\beta_{im}$ and are very rare. It is impossible to excite a single mode of this set, hence due to their standing nature, they do not carry any energy.

Let us discuss two fundamental aspects of modal decomposition: are the modes *physically meaningful*? is the set of eigensolutions *complete*? The first question concerns the possibility of measuring a mode individually. Guided modes are undoubtedly physical, whereas radiative and leaky modes are not, because they extend toward infinity. Complex mode should appear at least in pair to be physical. Nevertheless we deal with finite analysis domains, thus it often results practical to use leaky and radiative modes to study propagation. Specifically, leaky modes are used in place of radiative modes (of both species) to restrict the choice among their continuum, despite a special care should be taken about it. We will further analyze a modal method that provides a set of radiative and leaky modes directly.

As far as *completeness* is concerned, this requirement corresponds to the opportunity of expanding every field profile in terms of modes and modal weights. Lossless structures that do not support complex modes (e.g. slab waveguides) can be rigorously analysed in such terms: guided and radiation modes constitute a complete set. All other situations (lossy media, or complex-mode-supporting structures) currently lack of rigorous proofs of modal-set completeness.

Lossy media can be studied by using radiative and guided modes, as well, but complex modes have to be included if present.

Beware that the sums of eq. (1.54) have to be replaced by integrals to express the contribution of radiative modes, that constitute a continuum. This means there is no way to avoid approximation in numerical analysis.

### 1.4.2 Eigenmodes in closed and periodic structures

A guiding structure is commonly referred to as *closed* if it is limited by a perfectly conducting lateral surface, that imposes a null tangential electric field on it and thus no propagation outside the system.

In this case only guided or evanescent modes are allowed, except for rare occurrence of complex modes. Indeed a mode is guided if we operate at a frequency above the cut-off, while it vanishes below. It is possible to prove completeness of modal set made of propagating and evanescent modes in lossless media, based upon the spectral properties of hermitian operators.

In figure 1.3 we show an example of eigenvalue distribution of such a structure.

We remark that in closed structures modes do not loose individuality if a too long wavelength does not allow them to be guided, while in open structures we pass from a discrete to a continuous set of modes. In fact, guided waves in dielectric structures are based on total internal reflection or more rigorously on a transverse resonance that limits to a discrete set the propagation wavenumber of guided modes. Increasing wavelength implies a smaller set of wavenumbers satisfy this condition and energy leaks out of the core. Radiation outside the core is allowed to assume a continuity of transverse propagation, since no boundary conditions are imposed (in proximity of the core).

Periodic structures are neither closed nor open structures, if we consider the latter as those described by an infinitely-distant boundary only. In this case, periodic repetition of material properties implies fields evolve in a periodic fashion as well. Equivalently each period

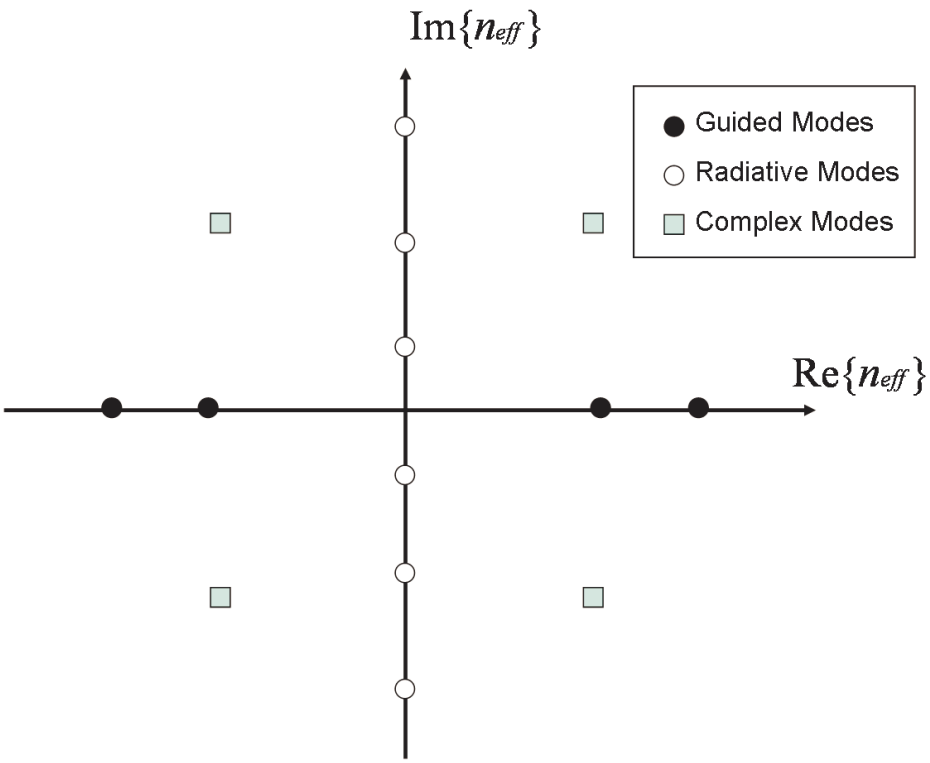


Figure 1.3: Distribution of the effective indexes of the eigenmodes of a closed structure.

or elementary cell is terminated by recurrence conditions. At a fixed frequency we have a discrete set of Bloch wave, propagative or evanescent, that are characterized by a periodic envelope and a plane wave term. Dispersion characteristic is periodic in the wave-vector space and formed by a discrete set of branches separated by gaps, which correspond to frequency intervals that do not correspond to any propagative mode. Analogously a diffraction diagram representing the longitudinal propagation constant as a function of the transverse one permits to identify the above-mentioned propagating and evanescent modes. Recall that there exist a separation condition for wave equation that imposes a relation between the components of wavevector. In chapter 3 we will discuss the properties of diffraction band diagram of 1D periodic arrays, while in 4 a modal method based on periodisation and approximation of modes of open structures by means of Bloch's modes will be reported.

### 1.4.3 Orthogonality conditions and overlap integrals

Orthogonality conditions of modal fields, solutions of the electromagnetic eigenvalue problem, can be derived by Lorentz Reciprocity theorem, that we briefly recall here.

If we consider two different solutions $\vec{E}_1, \vec{H}_1$ and $\vec{E}_2, \vec{H}_2$ imposed by two different sources,

respectively $\vec{J}_1$ and $\vec{J}_2$, the following fundamental theorem of electrodynamics can be obtained

$$\iint_S \left(\vec{E}_1 \times \vec{H}_2 - \vec{E}_2 \times \vec{H}_1\right) dS = \iiint_V \left(\vec{J}_1 \cdot \vec{E}_2 - \vec{J}_2 \cdot \vec{E}_1\right) dV, \tag{1.55}$$

where $V$ is an integration volume, $S$ its boundary surface.

Usually, if we apply to a translationally invariant structure, see fig. 1.2, the lateral surface does not give any contribute: both open (infinity boundary) and closed ones are characterized by a zero field condition. Then, and only for $z$-invariant structures, we can consider a infinitesimal section, and after some manipulation, write

$$\iint_{S_t} \frac{\partial}{\partial z}\left(\vec{E}_1 \times \vec{H}_2 - \vec{E}_2 \times \vec{H}_1\right) \cdot \hat{u}_z \, dS = \iint_{S_t} \left(\vec{J}_1 \cdot \vec{E}_2 - \vec{J}_2 \cdot \vec{E}_1\right) dS \tag{1.56}$$

where $S_t$ indicates the transverse waveguide section.

Now we consider two eigensolutions of the guiding structure, say $\left(\vec{E}_m, \vec{H}_m\right)$ and $\left(\vec{E}_n, \vec{H}_n\right)$, and their eigenvalues $\beta_m$ and $\beta_n$. It is easy to prove that couterpropagating modes have the opposite electric field and opposite wavenumber, while the sign of magnetic field is the same. Hence we apply (1.56) to the mentioned modes, in a couterpropagative configuration, to obtain

$$(\beta_m - \beta_n) \iint_S \left(\vec{E}_m \times \vec{H}_n + \vec{E}_n \times \vec{H}_m\right) \cdot \hat{u}_z \, dS = 0 \tag{1.57}$$

i.e. if modes are not degenerate ($\beta_m \neq \beta_n$) then each vector product have to be zero, i.e.

$$\iint_S \vec{E}_m \times \vec{H}_n \cdot \hat{u}_z \, dS = 0. \tag{1.58}$$

This represents a general form of orthogonality condition.

A useful formalism can be established in terms of reflection and transmission at an interface between two different sections, each having a specific modal expansion.

Let us consider a field impinging on an interface (from medium $I$ to $II$, located at $z = 0$), composed by a single mode

$$\begin{aligned} \vec{E}_p^I + \sum_j R_{j,p} \vec{E}_j^I &= \sum_j T_{j,p} \vec{E}_j^{II} \\ \vec{H}_p^I - \sum_j R_{j,p} \vec{H}_j^I &= \sum_j T_{j,p} \vec{H}_j^{II} \end{aligned} \tag{1.59}$$

This expansion represents the effect of a discontinuity, that excites the full set of modes both before and beyond it.

Defining the scalar product as

$$\left\langle \vec{E}_m, \vec{H}_n \right\rangle = \iint_S \vec{E}_m \times \vec{H}_n \cdot \hat{u}_z \, dS \tag{1.60}$$

we can project the equation (1.60) on a generic mode $\left(\vec{E}_i^I, \vec{H}_i^I\right)$ and write

$$\begin{aligned} \left\langle \vec{E}_p^I, \vec{H}_i^I \right\rangle + \sum_j R_{j,p} \left\langle \vec{E}_j^I, \vec{H}_i^I \right\rangle &= \sum_j T_{j,p} \left\langle \vec{E}_j^{II}, \vec{H}_i^I \right\rangle \\ \left\langle \vec{E}_i^I, \vec{H}_p^I \right\rangle - \sum_j R_{j,p} \left\langle \vec{E}_i^I, \vec{H}_j^I \right\rangle &= \sum_j T_{j,p} \left\langle \vec{E}_i^I, \vec{H}_j^{II} \right\rangle \end{aligned} \tag{1.61}$$

Expressing reflection and transmission coefficients in terms of mixed products and iterating for every mode, we can write

$$\begin{aligned} \mathbf{T}_{I,II} &= 2\left(\mathbf{O}_{I,II} + \mathbf{O}_{II,I}^{T}\right)^{-1} \\ \mathbf{R}_{I,II} &= \frac{1}{2}\left(\mathbf{O}_{II,I}^{T} - \mathbf{O}_{I,II}\right) \cdot \mathbf{T}_{I,II} \end{aligned} \tag{1.62}$$

where, assuming a normalization to one of each mode set, we expressed the overlap matrices $\mathbf{O}_{I,II}$ and $\mathbf{O}_{II,I}$ as

$$\begin{aligned} \mathbf{O}_{I,II} &= \left\langle \vec{E}_i^{I}, \vec{H}_j^{II} \right\rangle \\ \mathbf{O}_{II,I} &= \left\langle \vec{E}_i^{II}, \vec{H}_j^{I} \right\rangle \end{aligned} \tag{1.63}$$

Then from a generic field expressed in terms of a column vector of modal weight, reflected and transmitted fields can be readily obtained.

The next step is represented by the analysis of an integrated device in terms of a sequence of layers, each of a well-defined modal structure. Several approaches have been proposed: a detailed discussion will be provided further, where an application to specific numerical methods will be described, see section 4.3 and appendix A.

## 1.5 An Overview of Numerical Methods

In the study of integrated optical devices a key role is played by numerical techniques, that allow to account for many physical phenomena and hence provide tools for the analysis and design of novel structures. Nowadays digital electronic computers are so widespread and provide such extreme capabilities that even the full 3D electromagnetic problem can be solved and many aspects can be investigated. Time savings in design process permit to concentrate on technological issues and reducing the number of unsuccessful prototypes. Moreover a thorough analysis of as many effects as possible permits to assess pros&cons of new conceptions.

We will now outline the most important numerical approaches, particularly those related to our usual activity. Obviously we will provide further details concerning those we have directly implemented during the doctoral work, see chapters 2, 3, 4, and app. A.

Since we have focused on space or modal discretization, we will describe the principles of finite differences and modal approaches.

### 1.5.1 Finite Difference Discretization and solution of discrete equations

The simplest idea in solving partial differential equations (PDEs) by a numerical algorithm is to approximate derivatives by means of finite differences. The forward difference formula for first order derivative reads as

$$\left.\frac{\mathrm{d}\psi}{\mathrm{d}x}\right|_{x_0} = \frac{\psi(x_0 + \Delta x) - \psi(x_0)}{\Delta x} + O(h) \tag{1.64}$$

while a suitable finite difference analogous of second order derivative is the central difference formula

$$\left.\frac{\mathrm{d}^2\psi}{\mathrm{d}x^2}\right|_{x_0} = \frac{\psi(x_0+\Delta x) - 2\psi(x_0) + \psi(x_0-\Delta x)}{\Delta x^2} + O(h^2). \tag{1.65}$$

Several implementations of a finite difference algorithm are possible, depending upon which points are considered in approximating derivatives:

- Explicit method
- Implicit method
- Crank-Nicolson method

For example, we consider a normalized partial differential equation in the form

$$U_t = U_{xx} \tag{1.66}$$

**Explicit method** Explicit formulation consists in using forward difference at time $t_n$(time step $k$) and second-order central difference for space derivatives at position $x_j$ (discretization step $h$), $u_j^n$ is the generic field value at those time and space grid point

$$\frac{u_j^{n+1} - u_j^n}{k} = \frac{u_{j+1}^n - 2u_j^n + u_{j-1}^n}{h^2} \tag{1.67}$$

we can thus obtain directly the field at time $n+1$ given the values at time $n$.

$$u_j^{n+1} = (1-2r)u_j^n + ru_{j-1}^n + ru_{j+1}^n \tag{1.68}$$

where $r = k/h^2$. Notice that boundary conditions will be imposed by setting the required values at the extremal grid points $u_0^n$ and $u_J^n$ at every time step. Many different formulations of boundary conditions for a finite computational domain are available (and specifically suitable to EM computations) and we will discuss them in detail in a further chapter. The main problem is that stability and convergence of this method is guaranteed if $r \leq 1/2$, i.e. the choice of time step is constrained by discretization in space.

**Implicit method** Implicit formalism is based on backward difference at time $t_{n+1}$ and the second-order central difference for space derivatives at $x_j$, computed at that time instant,

$$\frac{u_j^{n+1} - u_j^n}{k} = \frac{u_{j+1}^{n+1} - 2u_j^{n+1} + u_{j-1}^{n+1}}{h^2} \tag{1.69}$$

It is easy to derive the field $u_j^{n+1}$ as a solution of the following linear system,

$$(1+2r)u_j^{n+1} - ru_{j-1}^{n+1} - ru_{j+1}^{n+1} = u_j^n \;\; j = 1, \ldots, J-1. \tag{1.70}$$

Implicit algorithm is unconditionally stable and convergent.

**Crank-Nicolson method** Crank-Nicolson approach can be considered as a an improvement of the implicit formulation or a compromise between explicit and implicit ones. It is based upon central differences at time $t_{n+1/2}$ and a second-order central difference for the space derivative at position $x_j$, approximated as in trapezium rule.

$$\frac{u_j^{n+1} - u_j^n}{k} = \frac{1}{2}\left(\frac{u_{j+1}^{n+1} - 2u_j^{n+1} + u_{j-1}^{n+1}}{h^2} + \frac{u_{j+1}^n - 2u_j^n + u_{j-1}^n}{h^2}\right) \tag{1.71}$$

Again the solution $u_j^{n+1}$ can be obtained by solving the linear system

$$(2+2r)u_j^{n+1} - ru_{j-1}^{n+1} - ru_{j+1}^{n+1} = (2-2r)u_j^n + ru_{j-1}^n + ru_{j+1}^n \;\; j = 1, \ldots, J-1. \tag{1.72}$$

Comparison of the three algorithms permits to state that implicit and Crank-Nicolson schemes are more numerically intensive, but work better for larger time steps, while explicit scheme is absolutely the simplest to implement, but the least accurate and suffers from instabilities.

### 1.5.2 Finite Difference Time Domain Method

The previous section was devoted to understand the general framework of PDE discretization. We are now sketching the principles of the most important and widely used numerical method in electromagnetic computations, the finite-difference time-domain method (FDTD), see the fundamental textbook [20]. It relies upon direct discretization of Maxwell's equations. Since they mutually relate electric and magnetic fields, Yee proposed in a seminal paper to use a staggered grid both in time and space. For example the cartesian $x$-component of $\nabla \times \vec{H}$ equation

$$\left[\frac{\partial H_y}{\partial x} - \frac{\partial H_x}{\partial y}\right] = \frac{\partial D_z}{\partial t} \tag{1.73}$$

can be discretized via central differences in time and space as

$$\begin{aligned}\epsilon\left[\frac{E_z^{t+\Delta t}(x,y,z) - E_z^t(x,y,z)}{\Delta t}\right] = \\ = \left[\frac{H_y^{t+\Delta t/2}(x+\Delta x/2,y,z) - H_y^{t+\Delta t/2}(x-\Delta x/2,y,z)}{\Delta x}\right] - \\ = \left[\frac{H_x^{t+\Delta t/2}(x,y+\Delta y/2,z) - H_x^{t+\Delta t/2}(x,y-\Delta y/2,z)}{\Delta y}\right]\end{aligned} \tag{1.74}$$

the other equations are written in the same form.

We have reported the usual explicit scheme of cartesian equations, that suffers the stability condition limiting the time step, staircase approximation errors, and the subtle issue of numerical dispersion, an artificial perturbation of material properties.

Nevertheless FDTD has been applied to many problems, involving dispersive, nonlinear materials, and to a large variety of geometries and device where other methods are inadequate.

Since it treats time domain problems, it is suitable to describe pulsed propagation, i.e. detect dispersion related effects and dynamical effects, such as self-pulsing [21].

Finally, it can solve even full 3D problems, despite they require a large storage and a very long computation time. Nevertheless explicit formulation is particularly suitable to be split to different machines thus parallel computing can cope with it.

Obviously extensive research have been devoted to boundary conditions that are needed to gain accuracy in finite domains, to exploit symmetries and to the processing of output data.

Analogous approaches mitigate numerical dispersion issues by implementing higher accuracy difference schemes, e.g. pseudo-spectral space discretization that employs fast Fourier-transform to approximate space-derivatives [22].

### 1.5.3 Beam Propagation Method

The beam propagation method (BPM) is one of most popular numerical methods for the modelling of optical devices. It is conceptually simple and easy to implement, very efficient (the most efficient versions can have optimal complexity, i.e. numerical effort proportional to the number of grid points), and it can be extended to describe many different propagation regime (scalar to full vectorial equations, polarization and nonlinear effects). It is a time-harmonic method and unless explicitly specified, we assume a $\exp(j\omega t)$ time dependence.

The first historical approach is based on the scalar paraxial equation, that can be derived from eq. (1.23), under the above-mentioned assumptions,

$$\frac{\partial u}{\partial z} = \frac{1}{j2k_0 n_0}\left[\frac{\partial^2 u}{\partial x^2} + \frac{\partial^2 u}{\partial y^2} + k_0^2\left(n^2 - n_0^2\right)u\right] \tag{1.75}$$

where $u(x, y, z)$ is a slowly varying envelope and the electric field is reconstructed as

$$E(x, y, z) = u(x, y, z)\exp\left(-jk_0 n_0 z\right).$$

In this way once the initial (spatial) condition $u(x, y, z = 0)$ is known, we can determine the evolution of the field for every $z > 0$.

Factoring out an exponential dependence allows us to use a discretization step along $z$, $\Delta z$ far larger than radiation wavelength (provided a scheme that preserves stability), see e.g. [23], and simplifies the formulation to an initial value problem, as we have already reported in section 1.2.1. Obviously, paraxial approximation can be a serious limitation, both for modelling large spatial spectra and devices where phase variations have to be accurately determined. Moreover, that simple model does not include bidirectional propagation and does not account for vectorial propagation and thus polarization effects.

As it will be discussed in the next chapter the most of this limitations can be relaxed to obtain better approximations: the robustness and reliability of the BPM principle relies upon those opportunities. In fact wide-angle (as opposed to paraxial), full vectorial versions are available, as well as a 2D bidirectional version can be obtained by means of scattering matrix formalism.

### Numerical implementation and boundary conditions

We are now applying the formulations of sec. 1.5.1 to eq. 1.75. We describe here some important features that are also involved in FDTD or in modal solvers, since our work has been focused most on time-harmonic propagative algorithms, that are often inspired by BPM concepts.

Let us consider a 2D $Oxz$ domain and apply the Crank-Nicolson scheme. Eq. (1.75) can be transformed to the following difference equation

$$\frac{u_i^{n+1} - u_i^n}{\Delta z} = \frac{1}{j2k_0 n_0} \left[ \frac{\delta^2}{\Delta x^2} + k_0^2 \left( n(x_i, z_{n+1/2})^2 - n_0^2 \right) \right] \frac{u_i^{n+1} + u_i^n}{2} \tag{1.76}$$

where $u_i^n$ is the field at the grid point $(x_i, z_n)$, $\delta^2$ is a second order central difference operator, $\delta^2 u_i = u_{i+1} - 2u_i + u_{i-1}$ (applied to each $z$ step), and $z_{n+1/2} \equiv z_n + \Delta z/2$, i.e. a central difference in $z$ and accordingly the halfway value of refractive index are considered. Eq. (1.76) can be rearranged in the form of a standard tridiagonal matrix equation for the unknown $u_i^{n+1}$, in terms of known quantities, resulting:

$$a_i u_{i-1}^{n+1} + b_i u_i^{n+1} + c_i u_{i+1}^{n+1} = d_i \tag{1.77}$$

If $N$ is the number of points along $x$ a solution can be obtained in $O(N)$ operations, thanks to the tridiagonal nature of the system obtained from eq. (1.77).

Let us now consider the transverse boundaries of computational region; eq. (1.77) involves, at points $i = 1, \quad i = N$, field values laying outside our domain. It is thus necessary to impose suitable boundary conditions. This is a crucial problem, because a poor choice can lead to artificial reflection of light impinging on the boundary back into the computational domain. Indeed many electromagnetic problems are defined in an unbounded region and then the analysis of a finite region can lead to inaccurate solutions.

In sections 2.5 and 4.2.3 we will describe accurately an example of commonly used boundary condition. Here we summarize the possible choices.

- the simplest case is represented by Dirichlet conditions, i.e. field are zero at each edge: this is equivalent to imposing metallic walls and thus reflections are maximized.
- including absorbing layers in the domain: they were quite popular in the past, but are hard to design and require a trial-error procedure to detect the best absorption.
- *transparent boundary condition* (TBC), [24], which assumes the field to be a plane wave impinging at a given angle and mimics an infinite propagation extension for it.
- *perfectly-matched layer* (PML), [25], [26], [27], the most modern and efficient, widely studied and applied, relies upon the inclusion of lossy media that match exactly and continuously the dielectric constant of the physical part (as opposed to the whole computational domain comprising these layers), defined as that between absorbing layers. perfectly-matched layer (PML) should represent a portion of an infinite domain.

A 3D implementation can be readily obtained. Anyway Crank-Nicolson approach does not lead to a tridiagonal system and thus requires $O(N_x^2 \cdot N_y^2)$ operations; the alternating-direction implicit formulation (ADI) that is an enhanced version of Crank-Nicolson method suited to multidimensional discretization, permits to obtain the optimal complexity $O(N_x \cdot N_y)$.

A 2D wide-angle, nonlinear implementation, that has been employed in our investigations, will be described in detail in the following chapter.

### 1.5.4 Method of Lines

The method of lines (MoL) [28] is a semianalytical tool to solve PDEs, that combines a finite difference discretization with a mode-matching technique (that is based on propagation of modes, the construction of overlap matrices between different modal bases at longitudinal discontinuities, along with a stable approach to account for multiple reflections, see section 1.4). It is inherently suitable to monochromatic propagation and in the field of integrated optics it is used to investigate the properties of many advanced structures, such as propagation effects or modes in dielectric structures (waveguides, Y-branches, resonators...). Many different extension have been proposed, to study 2D and 3D domains, linear, nonlinear, anisotropic materials.

The finite difference discretization is performed along the transverse direction as in BPM, but the propagation is accounted analytically, by means of a diagonalization to obtain a system of decoupled equations (of the same dimension of the discretized domain). The classical transmission-line equations and impedance-admittance formalism are used to analyse the effect of discontinuities along the propagation direction.

To outline the principles of the method we suppose to work in 2D, where TE and TM modes are completely decoupled. Let us assume to obtain from transverse discretization a second order ODE of the form

$$\frac{\mathrm{d}^2\psi}{\mathrm{d}z^2} + \mathbf{Q}\psi = 0 \tag{1.78}$$

where $\mathbf{Q}$ is a square matrix obtained by discretization of a second order transverse differential operator, function of polarization; $\psi$ is thus a column vector of field components at the grid points.

To separate a set of different 'lines' and obtain a sort of modes, we decouple the system equations, i.e. we perform a diagonalization of $\mathbf{Q}$,

$$\mathbf{Q} = \mathbf{T}\boldsymbol{\Gamma}^2\mathbf{T}^{-1} \tag{1.79}$$

and

$$\psi = \mathbf{T}\bar{\psi} \tag{1.80}$$

consequently

$$\frac{\mathrm{d}^2\bar{\psi}}{\mathrm{d}z^2} + \boldsymbol{\Gamma}^2\bar{\psi} = 0 \tag{1.81}$$

The new, decoupled system is in the form of the wave equation obtained in transmission line theory. Thus starting from the final layer in $z$ direction, we perform a impedance-admittance recurrence, in the style of transmission lines, using $\boldsymbol{\Gamma}$ to calculate a diagonal matrix of impedances.

### 1.5.5 Modal methods

A large class of computational approaches for integrated optics is based upon the property of linear translational invariant structures to guide light, that we described in section 1.4. To describe a complex device, we divide it into guide section, each with a rigorously defined modal basis. Then continuity conditions are used to match adjacent sections.

In general we have two problem to solve,

- how to compute a modal basis of a generic section?
- how to match different sections?

the former problem can be solved in a large variety of ways, that identify the considered method. For the latter, few approaches have been proposed, but the choice is limited among those that guarantee numerical stability of the propagation algorithm.

We can cite in the first class, the classical modal method, [29], the coupled-wave, also known as Fourier-modal method [30], the wave-matching method [31], the film-mode matching [32], or even the use of simpler sinusoidal basis in 2D geometries, [33]. The second group includes the elementary transmission-matrix method, that is unstable and then induced much work on its improvement: enhanced transmission matrix, scattering matrix or admittance-impedance, also referred to as R- or immittance matrix formulations are the commonly used techniques, see [34].

The main advantage of this algorithms is that the use of at most few hundreds of modes constitute a reliable representation and that their evolution in propagation is known analytically: no discretization is performed, but only mode matching at interfaces is required.

They are suitable to compute eigenmodes of complex optical devices, but in general not to describe nonlinear devices, despite SHG can be studied under the undepleted pump approximation (the energy flow to the second harmonic does not affect the fundamental frequency), in short devices, see [35], and an iterative procedure to study OKE has been proposed, see [36].

## 1.6 Conclusion: the Need for Modelling

Despite nowadays computational systems permit to perform full detailed analysis, the implementation of efficient numerical techniques is fundamental in the analysis and design of advanced devices. We can save time and obtain insights on physical mechanisms.

Our work is aimed to assess the limit of simple models, such as CMT in nonlinear optics and 2D (effective index method (EIM)) for microresonator analysis. Many alternative approaches are being studied: this contribution is devoted to realize which ones conjugate implementation simplicity, reliability, and a moderate demand of computational resources.

# Chapter 2

# Nonlinear Beam Propagation Method

As we mentioned in section 1.5.3, BPM is widely used to analyse integrated optical devices, is usually included in commercial software packages, can be easily implemented, and many alternative versions have been proposed.

The main limitation of paraxial approximation can be overcome by improving the accuracy of diffraction terms, e.g. by means of Padé approximants, see [17, 37–50]. Bidirectional (2D) algorithms are obtained constructing operators that account for propagation and transmission-reflection at interfaces and combining them in a suitable way to obtain the global effect of propagation in a multilayer structure, see [51–53], that discuss transmission matrix formulations and [54–56] that employ scattering operators. To model 3D problems semivectorial approaches, see [57, 58] can provide a good approximation, but full-vectorial, [16, 59, 60], and [14, 15] are possible too, and physical description is greatly improved.

In this thesis, we will focus on 2D nonlinear versions we implemented, that are able to model SHG and OKE in monodirectional regime. Nevertheless, an implementation of linear and nonlinear biderectional algorithms have been developed as well.

## 2.1 Wide-Angle Linear BPM

We will restrict to TE modes ($\vec{E} = E_y \hat{y}_0$), the TM being only slightly more complicated. Let us start from the scalar Helmholtz equation,

$$\frac{\partial^2 E}{\partial z^2} + \left( \frac{\partial^2}{\partial x^2} + k_0^2 n^2(x,z) \right) E = 0 \tag{2.1}$$

where $k_0 = \frac{2\pi}{\lambda}$ denotes free-space wavenumber, $\lambda$ the free-space wavelength, and $n(x,z)$ is the refractive index. We kept the dependence on $z$, to account for inhomogeneous media along longitudinal direction. [1]

1. Generally bidirectional algorithms assume the generic structure to be composed by a sequence of homogeneous layers separated by abrupt discontinuities, i.e.

$$n(x,z) = n_j(x) \text{ per } z_{j-1} < z < z_j,\ j = 0, 1, \ldots, m+1$$

In order to study a rigorously monodirectional approach, we assume refractive index does not depend on $z$, $n(x,z) = n(x)$, and describe in detail the classical monodirectional BPM. Sometimes, for low index contrasts, also this simple algorithm gives good results, e.g. glass-integrated segmented waveguides. Indeed if index variations are weak enough to neglect reflections, we can update the index profile at each propagation step keeping a single field term.

Let us recall the standard form of wide-angle BPM formulation, based on two operators: square-root operator, $L$, and the propagator, $P$.

$$L = \sqrt{\frac{\partial^2}{\partial x^2} + k_0^2 n^2(x)} = k_0 n_0 \sqrt{I + \frac{\frac{\partial^2}{\partial x^2} + k_0^2\left(n^2(x) - n_0^2\right)}{k_0^2 n_0^2}} = k_0 n_0 \sqrt{I + X} \tag{2.2}$$

where $L$ represents the diffraction and phase delay terms, $I$ the identity matrix and $n_0$ is the reference refractive index, in analogy with the paraxial wave-equation formulation. The propagator is expressed as

$$P = \exp\left(-j\Delta z L\right) \tag{2.3}$$

It is now easy to recast (2.1) as

$$\frac{\partial^2 E}{\partial z^2} + L^2 E = 0 \tag{2.4}$$

and realize that the $P$ operator represents the propagation between two adjacent grid steps along $z$. In fact we can make some manipulations and obtain a monodirectional equation, that constitutes a generalization of the paraxial one,

$$\begin{aligned} \frac{\partial E^+}{\partial z} &= -jLE^+ \\ \frac{\partial E^-}{\partial z} &= jLE^- \end{aligned} \tag{2.5}$$

where $E^+$ and $E^-$ represent the froward and backward propagating solutions, respectively. The formal solution (2.5) is

$$E(x,z) = E(x,0)\exp(\pm jLz) \tag{2.6}$$

then e.g. a forward propagation step can be casted as

$$E(x, z+\Delta z) = PE(x,z) \tag{2.7}$$

alternatively, we can employ slowly-varying envelopes $u$ and write

$$u(x,z) = u(x,0)\exp(\pm j(L - k_0 n_0 I)z) \tag{2.8}$$

it is easy to see that using a first order approximation of the square-root, we can derive the usual paraxial approximation of eq. (1.75): by this argument it should be clear that depending on the method used to compute $L$ and $P$, given a discretization scheme, a better accuracy in the treatment of wide-angle propagation can be obtained.

We will describe in detail in section 2.4 how to calculate a reliable approximation for the BPM operators.

We now focus on the solution of nonlinear problems.

where $z_{-1} = -\infty$ e $z_{m+1} = +\infty$.

## 2.2 Analysis of Second Harmonic Generation

As we reported in section 1.3.2, the effect of a second order nonlinearity is to couple field components at different frequencies. Their propagation is jointly described by a nonlinear system of coupled equations. Our goal is to describe interactions in 2D geometries, taking into account both diffraction and $\chi^{(2)}$ effects. A BPM approach can be derived in many ways, see e.g. [61, 62] and [63].

Basically, we could discretize directly the nonlinear system, use a *split-step* (split-operator) solution, and/or apply an iterative scheme, in which the nonlinear terms are calculated exploiting field estimates provided by a previous propagative run until no remarkable changes are achieved. Required are as usual the stability, convergence, and robustness to large propagation steps.

As stated before, the envelope is calculated on the basis of a reference index and a poor choice leads to cumulation of phase errors, see [49] for a general investigation. For this reason, since dispersion suggests to set different reference indexes for the two harmonics, the sensitivity to phase-mismatch may result critical.

We report here three approaches, that encompass the principles we have recalled above.

We start by recalling the coupled system obtained from SVEA, see 1.3.2,

$$\begin{aligned}\frac{\partial^2 u_\omega(x,z)}{\partial z^2} - 2jk_0 n_{0_\omega}\frac{\partial u_\omega(x,z)}{\partial z} + \frac{\partial^2 u_\omega(x,z)}{\partial x^2} + k_0^2\left[n_\omega^2(x) - n_{0_\omega}^2\right]u_\omega(x,z) = \\ = -k_0^2\chi_j^{(2)}(x)\left[u_\omega(x,z)\right]^* u_{2\omega}(x,z)e^{-j\Delta kz}\end{aligned} \tag{2.9}$$

$$\begin{aligned}\frac{\partial^2 u_{2\omega}(x,z)}{\partial z^2} - 4jk_0 n_{0_{2\omega}}\frac{\partial u_{2\omega}(x,z)}{\partial z} + \frac{\partial^2 u_{2\omega}(x,z)}{\partial x^2} + 4k_0^2\left[n_{2\omega}^2(x) - n_{0_{2\omega}}^2\right]u_{2\omega}(x,z) = \\ = -2k_0^2\chi_j^{(2)}(x)\left[u_\omega(x,z)\right]^2 e^{j\Delta kz}\end{aligned} \tag{2.10}$$

where $k_0 = \frac{\omega}{c}$ is the free space wavenumber of the fundamental frequency, $u_{k\omega}$, with $k = 1, 2$ represent the two envelopes at fundamental and second harmonic (fundamental frequency (FF) and second harmonic (SH)), $n_{0_{k\omega}}$ represent the reference index of BPM propagation, and $\Delta k = 2k_0(n_{0_\omega} - n_{0_{2\omega}})$.

The main problem is that an implicit approach does not lead to a linear system, easy to invert, thus not to lose the stability of linear propagator, we can write a rectangular approximation for NL terms, applying the SVEA

$$\begin{aligned}\frac{2jk_0 n_{0_\omega}}{\Delta z}\left(u_\omega^{m,s+1} - u_\omega^{m,s}\right) = \frac{1}{2}\left(L_\omega^{m,s+\frac{1}{2}} - k_0 n_{0_\omega}\right)\left(u_\omega^{m,s} + u_\omega^{m,s}\right) + \\ k_0^2\chi^{(2)^{m,s}}u_\omega^{m,s*}u_{2\omega}^{m,s}e^{-j\Delta kz_s} \\ \frac{4jk_0 n_{0_{2\omega}}}{\Delta z}\left(u_{2\omega}^{m,s+1} - u_{2\omega}^{m,s}\right) = \frac{1}{2}\left(L_{2\omega}^{m,s+\frac{1}{2}} - k_0 n_{0_{2\omega}}\right)\left(u_{2\omega}^{m,s} + u_{2\omega}^{m,s}\right) + \\ 4k_0^2\chi^{(2)^{m,s}}\left[u_\omega^{m,s}\right]^2 e^{j\Delta kz_s}\end{aligned} \tag{2.11}$$

where $(m, s) \to (m\Delta x, \left(s + \frac{1}{2}\right)\Delta z)$ identifies a grid point, and only the previous propagation step is considered in nonlinear contribution.

Such an approximation can be used as an initial guess for iterative procedures of higher accuracy.

If we would like to preserve the wide-angle features of BPM, it is convenient to apply a split-step algorithm, that at each step computes a linear solution and then uses this one to obtain nonlinear contributions. Iterating the procedure to improve the accuracy of nonlinear contributions leads to better solutions.

Let us outline these methods.

**Compute the linear solution** The propagator can be applied directly to the array of field values in transverse direction

$$\begin{aligned} u_{\omega}^{:,s+1(I)} &= \exp\left(-j\left(L_{\omega} - k_0 n_{0_{\omega}} I\right)\Delta z\right) u_{\omega}^{:,s} \\ u_{2\omega}^{:,s+1(I)} &= \exp\left(-j\left(L_{2\omega} - k_0 n_{0_{2\omega}} I\right)\Delta z\right) u_{2\omega}^{:,s} \end{aligned} \tag{2.12}$$

where the superscript $I$ denotes the intermediate calculation of the split-step approach. The propagation step has been written in compact form, employing propagators and the whole arrays of field values.

**Compute NL contributions**

$$\begin{aligned} \frac{2jk_0 n_{0_{\omega}}}{\Delta z}\left(u_{\omega}^{m,s+1(t)} - u_{\omega}^{m,s+1(I)}\right) = \\ = \frac{1}{2}k_0^2\left(\chi^{(2)^{m,s}} u_{2\omega}^{m,s+1(I)}\left[u_{\omega}^{m,s+1(I)}\right]^* + \chi^{(2)^{m,s+1}} u_{2\omega}^{m,s+1(t-1)}\left[u_{\omega}^{m,s+1(t-1)}\right]^*\right) \\ \frac{4jk_0 n_{0_{2\omega}}}{\Delta z}\left(u_{2\omega}^{m,s+1(t)} - u_{2\omega}^{m,s+1(I)}\right) = \\ = \frac{1}{2}4k_0^2\left(\chi^{(2)^{m,s}} u_{\omega}^{m,s+1(I)} u_{\omega}^{m,s+1(I)} + \chi^{(2)^{m,s+1}} u_{\omega}^{m,s+1(t-1)} u_{\omega}^{m,s+1(t-1)}\right) \end{aligned} \tag{2.13}$$

where the superscript $t$ identify the current iteration which is calculated from the solution of previous one, denoted by $t-1$. The nonlinear components are calculated from the result of the linear propagation (that acts as starting point, $(m,s)$) and the fields computed in the previous iteration (corresponding to the next propagation step) allowing us to write an implicit formalism.

Another strategy could consist on neglecting the phase-mismatch or including the corresponding phase-rotation in a rescaled envelope, see [63]. Starting from eqs. (2.9) and (2.10), we split the linear and nonlinear terms we can write the latter, assuming the same choice of reference indices ($n_{0_{\omega}} = n_{0_{2\omega}}$) as,

$$2jk_0 n_0 \frac{\partial u_{\omega}(x,z)}{\partial z} = k_0^2 \chi_j^{(2)}(x)\left[u_{\omega}(x,z)\right]^* u_{2\omega}(x,z) \tag{2.14}$$

for FF and

$$4jk_0 n_0 \frac{\partial u_{2\omega}(x,z)}{\partial z} = 2k_0^2 \chi_j^{(2)}(x)\left[u_{\omega}(x,z)\right]^2 \tag{2.15}$$

for SH. Now to compute the NL contribution, we pose

$$u_{\omega} = a + jb \quad u_{2\omega} = c + jd$$

NL step of fundamental frequency corresponds to:

$$\frac{\partial a}{\partial z} = \alpha(ad - bc) \quad \frac{\partial b}{\partial z} = -\alpha(ac + bd)$$

where $\alpha$ can be easily obtained. Let us outline the Crank-Nicolson formulation of the latter equation:

$$\frac{a(z+\Delta z)-a(z)}{\Delta z} = \frac{\alpha}{2}\left[a(z)d(z)+a(z+\Delta z)d(z+\Delta z)-b(z)c(z)-b(z+\Delta z)c(z+\Delta z)\right]$$
$$\frac{b(z+\Delta z)-b(z)}{\Delta z} = -\frac{\alpha}{2}\left[a(z)c(z)+a(z+\Delta z)c(z+\Delta z)+b(z)d(z)+b(z+\Delta z)d(z+\Delta z)\right]$$

substituting $y(z+\Delta z) = y(z)+\Delta y$, where $y$ is a generic term, neglecting second order terms (e.g. $\Delta a \Delta d$) and recombining the two envelopes, we obtain for FF:

$$\begin{aligned} u_\omega(x,z+\Delta z) = u_{lin,\omega}(x,z+\Delta z)+ \\ - j\Delta z\frac{k_0^2\chi_j^{(2)}(x)}{4k_0n_0}\left\{\left[u_\omega(x,z+\Delta z)\right]^* u_{2\omega}(x,z)+\left[u_\omega(x,z)\right]^* u_{2\omega}(x,z+\Delta z)\right\} \end{aligned} \tag{2.16}$$

and for SH,

$$u_{2\omega}(x,z+\Delta z) = u_{lin,2\omega}(x,z+\Delta z) - j\Delta z\frac{k_0^2\chi_j^{(2)}(x)}{2k_0n_0}u_\omega(x,z)u_\omega(x,z+\Delta z) \tag{2.17}$$

These equations can be used in an iterative split-step approach or alternatively, we can construct an analytically-invertible matrix, to obtain an implicit approach. This matrix is function of field components at the starting propagation step and acting on each field value,

$$v^{s+1}\mathbf{A} = v^s \tag{2.18}$$

where $v = [a,b,c,d]$ is the row vector of real variables we defined above, considered at a single grid point, and

$$A = \begin{bmatrix} 1+\frac{1}{2}d^s\Delta z & -\frac{1}{2}c^s\Delta z & \frac{1}{2}b^s\Delta z & -\frac{1}{2}a^s\Delta z \\ -\frac{1}{2}c^s\Delta z & 1-\frac{1}{2}d^s\Delta z & \frac{1}{2}a^s\Delta z & \frac{1}{2}b^s\Delta z \\ -\frac{1}{2}b^s\Delta z & -\frac{1}{2}a^s\Delta z & 1 & 0 \\ \frac{1}{2}^s\Delta z & -\frac{1}{2}b^s\Delta z & 0 & 1 \end{bmatrix} \tag{2.19}$$

## 2.3 Analysis of Propagation in Kerr Media

As we noted in section 1.3.3, the optical Kerr effect can be treated as an intensity-dependent perturbation of refractive index,

$$n(x,z) = n_{lin}(x,z) + n_2^I(x,z)I(x,z) \tag{2.20}$$

thus we need only to adapt the refractive index to the local intensity. It is usually obtained in an iterative fashion, computing an initial guess, that could be the linear solution or preferably a rectangular integration (as for SHG), then refractive indices are adapted to the computed field intensity, until no remarkable change can be obtained in field values or refractive indices.

In formulae, we start from the nonlinear wave-equation,

$$\begin{aligned} 2jk_0n_0\frac{\partial u(x,z)}{\partial z}+\frac{\partial^2 u(x,z)}{\partial z^2}+\frac{\partial^2 u(x,z)}{\partial x^2}+k_0^2\left[n^2(x)-n_0^2\right]u(x,z)+ \\ +\frac{3}{4}\frac{\omega^2}{c_0^2}\chi^{(3)}(x)\left|u(x,z)\right|^2 u(x,z) = 0 \end{aligned} \tag{2.21}$$

where $u$ is as usual the field envelope. Then we split linear and nonlinear equations, that is equivalent to construct a new propagation operator. This depends on field contribution at the intermidiate step.

The nonlinear step reads as

$$\frac{\partial u(x,z)}{\partial z} = -j\gamma(x)\left|u(x,z)\right|^2 u(x,z) \tag{2.22}$$

where

$$\begin{aligned}\gamma(x) &= 2\pi n_2(x) n(x) / \left(\lambda_0 n_0\right) \\ n_2(x) &= 3\chi^{(3)}(x) / \left[8n(x)\right]\end{aligned}$$

where the same notation of section 1.3.3 have been used. The nonlinear propagation step then becomes

$$u(x, z+\Delta z) = \exp\left\{-j\gamma(x)\left|u(x,z)\right|^2 \Delta z\right\} u(x,z) \tag{2.23}$$

multiplication of a phase factor $\exp\left\{-j\gamma(x)\left|u(x,z)\right|^2 + \Delta z\right\}$ at each step permits to update the linear propagator.

## 2.4 Numerical Implementation: Padé Approximants

A main point to obtain an efficient and reliable implementation of wide-angle BPM is to treat appropriately the operators of eqs. (2.2) and (2.3).

In a finite difference scheme, we first deal with discretization of field, refractive index, and second order derivative: they are is represented by a column vector, a diagonal matrix, and a tridiagonal matrix, respectively. Denoting $N$ as the number of transverse grid points, the resulting operators are $N \times N$ matrices.

The computation of a $L$ and $P$ could be performed, as usual matrix functions, by means of eigenvalue-eigenvector decomposition of $I + X$. Such an approach is generally too time-consuming, so an approximation is commonly used.

Rational expansions, also referred to as Padé approximants, are usually employed to this extent: indeed Taylor polynomials are not as accurate and the computational effort of matrix inversions is not such a serious penalty, $O\left(N^2\right)$ implementations are available.

Let us recall the basics of this technique, very important also in bidirecitonal algorithms, to deal with excitation of radiative modes at interfaces. Nevertheless it is thoroughly treated in literature, see [17, 38–41, 47, 48, 50–56, 59, 64–66]. We will follow [67].

Let $F(x)$ be an analytic function:

$$F(x) = \sum_{k=0}^{\infty} a_k x^k \tag{2.24}$$

Padé approximant of order $[m/n]$ of $F(x)$ is defined as the rational function $R_{[m/n]}(x)$:

$$R_{[m/n]}(x) = \frac{P_m(x)}{Q_n(x)} \tag{2.25}$$

where $P_m(x)$ e $Q_n(x)$ are polynomials (notice that no constraint is specified on their orders $m$ and $n$):

$$P_m(x) = p_0 + p_1 x + \ldots + p_m x^m \tag{2.26}$$

$$Q_n(x) = q_0 + q_1 x + \ldots + q_n x^n \tag{2.27}$$

Coefficients $p_0, \ldots, p_m$ and $q_0, \ldots, q_n$ can be obtained by truncating the McLaurin expansion at the $(m+n+1)$-th term, setting $q_0 = 1$ (any other value can obtained by a proper rescaling) and imposing:

$$F(x) - \frac{P_m(x)}{Q_n(x)} = 0 \qquad \text{or} \qquad F(x)Q_n(x) - P_m(x) = 0 \tag{2.28}$$

Equating the coefficients of corresponding powers of $x$, we obtain a linear system of $m+n+1$ equations, in $m+n+1$ variables. For example:

$$\begin{gathered} a_0 = p_0 \\ a_1 + a_0 q_1 = p_1 \\ a_2 + a_1 q_1 + a_0 q_2 = p_2 \\ \vdots \end{gathered}$$

The system can be written in matrix form as

$$\begin{bmatrix} 1 & 0 & \ldots & 0 & 0 & 0 & \ldots & 0 \\ 0 & 1 & \ldots & 0 & -a_0 & 0 & \ldots & 0 \\ & & \vdots & & & & \vdots & \\ 0 & 0 & \ldots & 1 & -a_m & -a_{m-1} & \ldots & -a_{m-n+1} \\ 0 & 0 & \ldots & 0 & -a_{m+1} & -a_m & \ldots & -a_{m-n+2} \\ 0 & 0 & \ldots & 1 & -a_{m+2} & -a_{m+1} & \ldots & -a_{m-n+3} \\ & & \vdots & & & & \vdots & \\ 0 & 0 & \ldots & 0 & -a_{m+n-1} & -a_{m+n-2} & \ldots & -a_m \end{bmatrix} \begin{bmatrix} p_0 \\ p_1 \\ \vdots \\ p_m \\ q_1 \\ q_2 \\ \vdots \\ q_n \end{bmatrix} = \begin{bmatrix} a_0 \\ a_1 \\ \vdots \\ a_m \\ a_{m+1} \\ a_{m+2} \\ \vdots \\ a_{m+n} \end{bmatrix} \tag{2.29}$$

Let us apply this principle to exponential function

$$e^x = \sum_{k=0}^{\infty} \frac{x^k}{k!} = 1 + x + \frac{x^2}{2!} + \frac{x^3}{3!} + \ldots$$

$P_m(x)$ and $Q_n(x)$ can be proved to read as

$$P_m(x) = \sum_{k=0}^{m} \frac{(m+n-k)!m!}{(m+n)!k!(m-k)!} x^k \tag{2.30}$$

$$Q_n(x) = \sum_{k=0}^{n} \frac{(m+n-k)!n!}{(m+n)!k!(n-k)!} (-x)^k \tag{2.31}$$

In table 2.1 we reporeted the Padé expansions of $e^x$ up to order [3/3].

In the following section standard techniques to compute $L$ and $P$ will be reported, since they are crucial to properly model propagation problems.

| Order | Approximant |
|---|---|
| [0/0] | $1$ |
| [0/1] | $\frac{1}{1-x}$ |
| [0/2] | $\frac{2}{2-2x+x^2}$ |
| [0/3] | $\frac{6}{6-6x+3x^2-x^3}$ |
| [1/0] | $1+x$ |
| [1/1] | $\frac{2+x}{2-x}$ |
| [1/2] | $\frac{6+2x}{6-4x+x^2}$ |
| [1/3] | $\frac{24+6x}{24-18x+6x^2-x^3}$ |
| [2/0] | $\frac{2+2x+x^2}{2}$ |
| [2/1] | $\frac{6+4x+x^2}{6-2x}$ |
| [2/2] | $\frac{12+6x+x^2}{12-6x+x^2}$ |
| [2/3] | $\frac{60+24x+3x^2}{60-36x+9x^2-x^3}$ |
| [3/0] | $\frac{6+6x+3x^2+x^3}{6}$ |
| [3/1] | $\frac{24+18x+16x^2+x^3}{24-6x}$ |
| [3/2] | $\frac{60+36x+9x^2+x^3}{60-24x+3x^2}$ |
| [3/3] | $\frac{120+60x+12x^2+x^3}{120-60x+12x^2-x^3}$ |

Table 2.1: Padé Approximants of $e^x$

### 2.4.1 Real Padé expansions of square-root

Let us consider $f(x) = \sqrt{1+x}$. Padé expansion of $f$ of order $[p/p]$ can expressed as

$$f(x) \simeq 1 + \sum_{n=1}^{p} \frac{a_n^{(p)} x}{1 + b_n^{(p)} x} = \prod_{n=1}^{p} \frac{1 + c_n^{(p)} x}{1 + b_n^{(p)} x} \tag{2.32}$$

where

$$b_n^{(p)} = \cos^2\left(\frac{n\pi}{2p+1}\right), \quad c_n^{(p)} = \sin^2\left(\frac{n\pi}{2p+1}\right), \quad a_n^{(p)} = \frac{2c_n^{(p)}}{2n+1} \tag{2.33}$$

Notice that those coefficients (Padé primes) are reals, thus for $x \in \mathbb{R}$, Padé expansion assumes only real values. eq. (2.32) is known as *standard Padé*. This approximation could be used to compute $L$.

The propagator $P$ is derived from one-way Helmholtz equation (2.5). Obviously, given an approximation of $L$, we can apply the Crank-Nicolson scheme, that can be proved to be equivalent to $[1,1]$ expansion of the exponential function.

$P$ is then substituted by its Padé approximant in terms of $L$; unfortunately the direct expansion as a function of $X$ may lead to instabilities. Thus we use the $[q/q]$ rational approximation, as illustrated in the previous section, of

$$P \approx e^{-jk_0 n_0 \Delta z S_p(X)} \tag{2.34}$$

where $S_p(X)$ is a Padé expansion of $\sqrt{I+X}$, to which next section is devoted. It is indeed convenient to use a non-standard expansion of the square root operator.

### 2.4.2 Complex Padé approximants

The sequence of eq. (2.32) converges, as $p \to \infty$, to $\sqrt{1+x}$ in the whole complex plane except for the branch cut along the negative real axis $[-\infty, -1]$. Indeed coefficients of eq. (2.32) are real-valued, then a negative real number results in a real-valued approximation. It is crucial to avoid this issue, since negative eigenvalue of transverse operator correspond to evanescent modes, that could be incorrectly modelled as propagating, see [44].

Consider a field propagating in $z > 0$ direction,

$$\frac{\partial E}{\partial z} = -jk_0 n_0 \sqrt{I + X} E \tag{2.35}$$

Let $\{\phi_j(x), \lambda_j\}_{j=1}^{\infty}$ be eigenvalue-eigenvector pair of $k_0^2 n_0^2 (I + X)$. We express a general solution of eq. (2.35) as

$$u(x, z) = \sum_{j=1}^{\infty} \hat{u}_j \phi_j(x) e^{-j\sqrt{\lambda_j} z}$$

If $\lambda_j > 0$, $\phi_j(z) e^{-j\sqrt{\lambda_j} z}$ is a propagating mode, whereas if $\lambda_j < 0$ is evanescent.

Let us insert the Padé approximation of $L$ in eq. (2.35):

$$\frac{\partial E}{\partial z} = -jk_0 n_0 \left( I + \sum_{n=1}^{p} \frac{a_n^{(p)} X}{1 + b_n^{(p)} X} \right) E \tag{2.36}$$

Let us pick an eigenvalue $\lambda_j < 0$ of $k_0^2 n_0^2 (I + X)$, corresponding to the eigenvalue $x_j = \left(\lambda_j - k_0^2 n_0^2\right) / \left(k_0^2 n_0^2\right) < -1$ of $X$: the mode propagates according to

$$u_j(x, z) = \phi_j(x) \exp\left\{ -jk_0 n_0 \left( I + \sum_{n=1}^{p} \frac{a_n^{(p)} x_j}{1 + b_n^{(p)} x_j} \right) z \right\} \tag{2.37}$$

Since coefficients in eq. (2.33) are real-valued, eq. (2.37) represents a propagating mode, not a vanishing one.

Let us report the typical approach to overcome this issue.

#### Rotated branch-cut appraoch

We outline the solution proposed in [50], widely employed in literature, that consists in rewriting $\sqrt{1+x}$ as

$$\sqrt{1+x} = e^{-j\alpha/2} \sqrt{1 + [(1+x)e^{j\alpha} - 1]} \simeq e^{-j\alpha/2} \left[ 1 + \sum_{n=1}^{p} \frac{a_n^{(p)} \tilde{x}}{1 + b_n^{(p)} \tilde{x}} \right] \tag{2.38}$$

where $\tilde{x} = (1+x)e^{j\alpha} - 1$, and $a_n^{(p)}$, $b_n^{(p)}$ are the real coefficients of section 2.4.1, eq. (2.33).

In figure 2.1 we depict the idea behind this calculation: a clockwise rotation of angle $\alpha$ is applied to the real axis around $(-1, 0)$, such that Padé series converges for real arguments, $x \in \mathbb{R}$. In this way the branch cut is moved away from our negative eigenvalues. From [66], we can realize that our eigenvalues have negative imaginary part for $x \in [-\infty, -1]$ [2],

2. In the reference imaginary parts are positive and an opposite rotation is applied, since $-j \leftrightarrow i$.

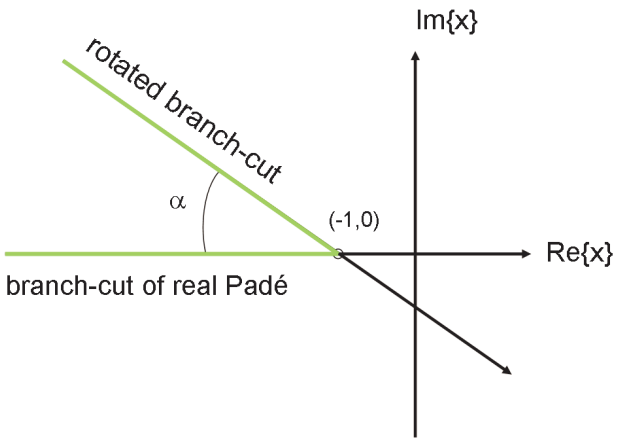


Figure 2.1: Representation of rotated branch cut principle.

then evanescent modes cannot diverge and for adequately large $p$ and $\alpha$, we have a fair representation of those wavenumbers.

Two problems arise, see [47]. First, rotating the real axis, accuracy for $x > -1$ is worse (for the same order) than the classic real case. Second, while standard Padé maps real axis on itself, the complex expansion of eq. (2.38), does not preserve the real approximation for $x > -1$; then it is possible a propagating mode undergoes a spurious attenuation. Increasing $p$ accuracy is improved and sensitivity to the values of $\alpha$ (in $[0^o, 90^o]$) is reduced.

## 2.5 Boundary Conditions

As stated in section 1.5.3, the most efficient technique to avoid spurious reflection inside the computational domain is represented by PMLs. It is not too hard to implement and guarantees a good efficiency (few additional grid point). It consists in placing absorbing layers at the edges of the computational window (corresponding to physical domain), designed to minimize backreflections from boundaries, see figure 2.2.

They can be proposed in two equivalent formulations, as anisotropic absorbing media or as complex coordinate stretching. An anisotropic conducting layer allows to avoid reflection passing form physical domain to absorbing layer, while attenuating the field amplitude.

We call physical domain the region that excludes PMLs and corresponds to the valid simulation domain, and extended or computational domain the one that includes PML, since the calculation is made in it.

Nevertheless we have to terminate the extended domain, and in this case the use of perfect conductors (Dirichelet conditions) is no more an issue, since the field impinges on them after a strong attenuation.

PML parameters have anyway to be chosen carefully, because too strong absorption in too tight layers leads generally to artifacts (propagation inside PMLs, spurious reflections...).

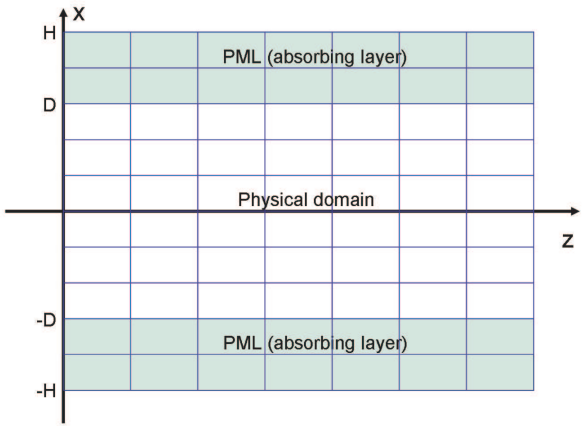


Figure 2.2: Representation of PML in a planar structure.

### 2.5.1 Implementation of Perfectly-Matched Layers in the BPM

The simplest implementation of PMLs is complex coordinate-stretching, i.e. we apply the following transformation

$$\hat{x} = x - j \int_0^x \sigma(\xi) d\xi \tag{2.39}$$

where $\sigma$ is a function representing the profile of absorption coefficient.

This can be thought as integration of Maxwell equations along a path in the complex plane, then defining a map that relates the complex path to infinite real axis (in this way we transform propagation in complex coordinates to absorbing media), and finally truncating the real domain. This results in attenuation of propagation waves.

In the BPM implementation, we use the profile of [68]:

$$\sigma(x) = \begin{cases} 3\sigma_{max} l^2, & l > 0 \\ 0, & l \leq 0 \end{cases} \tag{2.40}$$

with

$$l = (|x| - D)/(H - D)$$

where $D$ and $H$ are the half-size of physical and extended domain respectively, see figure 2.2.

In other words, in internal layers, Maxwell equations (thus the electromagnetic field) are the same as in the absence of PMLs but now with zero boundary conditions moved artificially far away by an artificial absorber. From [25] it is possible to calculate the theoretical reference reflection coefficient for the plane wave,

$$E(x) = \exp(jk_x x)$$

Imposing Dirichelet boundaries at $x = -D$, considering two trips forth and back after perfect reflection,

$$\begin{aligned} \rho_{th} &= -\exp\left\{-2jk_x \int_{-D}^{-H} 1 - j\sigma(x)\, dx\right\} = \\ &= -\exp\left\{-2jk_x \sigma_{max} L_{PML}^3 - j2k_x L_{PML}\right\} \end{aligned} \tag{2.41}$$

Then the maximum absolute value of theoretical reflection is

$$|\rho_{th}| = \exp\left\{-2jk_x\sigma_{max}L_{PML}^3\right\} \tag{2.42}$$

that can be used as a reference to determine the thickness $L$ and the amplitude $\sigma_{max}$ of the PML.

In finite difference schemes, we have obviously a finite number of points for PML layers, $N_{PML}$, then the total grid dimension is $N + 2N_{PML}$. Since they absorb, we can move boundaries near the region of interest, that will not be affected. Anyway the discrete character of PMLs in this case suggests to be careful about their design: a too steep absorption profile could lead to reflection, originated by its staircase approximation. Thus at least 10 discretization steps are necessary.

In order to adapt PML to our finite difference scheme, let us consider $X$, that allows to construct the other operators,

$$X = \frac{\frac{\partial^2}{\partial x^2} + k_0^2(n^2 - n_0^2)}{k_0^2 n_0^2} \tag{2.43}$$

in the new coordinates it becomes

$$X = \frac{\frac{\partial^2}{\partial \tilde{x}^2} + k_0^2(n^2 - n_0^2)}{k_0^2 n_0^2} \tag{2.44}$$

and substituting the definition in eq. (2.39) we can write:

$$X = \frac{\frac{1}{1-j\sigma(x)}\frac{\partial}{\partial x}\left(\frac{1}{1-j\sigma(x)}\frac{\partial}{\partial x}\right) + k_0^2(n^2 - n_0^2)}{k_0^2 n_0^2} \tag{2.45}$$

We have to write the finite difference version of (2.45). we follow [25], where second order derivative is approximated in the general case of non-uniform steps (in our case they extend in the complex plane):

$$\frac{1}{1-j\sigma(x)}\frac{\partial}{\partial x}\left(\frac{1}{1-j\sigma(x)}\frac{\partial E}{\partial x}\right) \longleftrightarrow \frac{2}{S(h,h+1)\Delta x^2}\left[\frac{E(h+1)-E(h)}{\Sigma(h+1)} - \frac{E(h)-E(h-1)}{\Sigma(h)}\right] \tag{2.46}$$

where

$$S(h,h+1) = 2 - j\sigma(h) - j\sigma(h+1)$$

$$\Sigma(h) = 1 - j\sigma(h)$$

It is apparent that inside the physical domain, these expressions are back to the usual central difference, second-order formulas.

We usually apply Dirichelet boundary conditions, that correspond to no other position on field values at domain edges. Anyway also association of TBC and PML is possible.

## 2.6 Sample results

In this latter section, we report some results to prove the validity of the BPM in nonlinear optics.

Two classical examples are shown, soliton propagation and second harmonic generation in quasi phase-matching (QPM) nonlinear gratings, see [18].

It is well known that a positive Kerr effective index corresponds to self-focusing behaviour, that can exactly balance beam diffraction, giving rise to spatial soliton propagation.

We consider a spatial profile obtained as a propagative solution of nonlinear paraxial wave equation in a bulk medium and simulate its propagation by means of BPM (including wide-angle features in linear propagator). In figure 2.3 we show that the beam propagates diffraction-less.

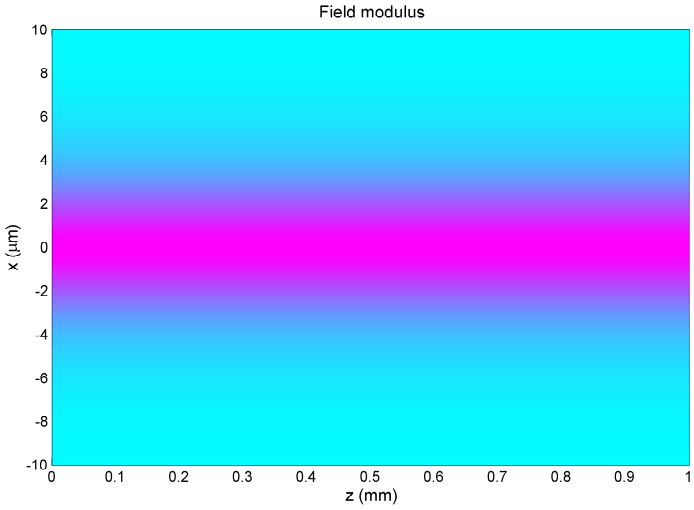


Figure 2.3: BPM simulation of a Kerr spatial soliton. $\lambda = 1.3\mu m$, $n_{lin} = 1.55$, $n_2 = 2.57 \times 10^{-21} \left(m^2/V^2\right)$, see eq. (1.50).

The second example consist in SHG in a QPM periodic structure. Phase-mismatch leads to low conversion efficiency. Obviously we could use birefringent crystal and choose the orientation that guarantees FF and SH indices to match at a given polarization. An alternative approach is to insert a periodicity of nonlinear coefficient. This can be achieved in periodically poled material. A proper design and fabrication of such structure can effectively compensate mismatch.

We report an example in which two guided modes at FF and SH couples via quadratic nonlinear effect, and a periodic inversion of nonlinearity sign permits to achieve total conversion. Not any sort of reflection is considered, but merely the nonlinear step is computed according to the sign of $\chi^{(2)}$, see fig. 2.4.

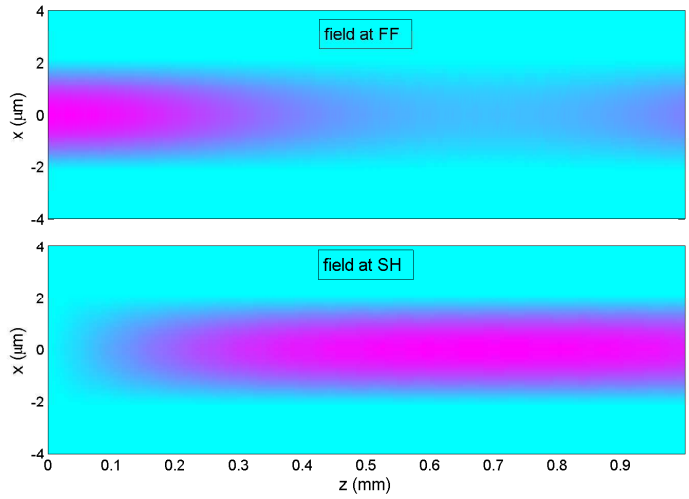


Figure 2.4: Second harmonic generation in a quasi phase-matching grating. Coupling between two guided modes. Original mismatch $\Delta k = -1.25 \times 10^6 m^{-1}$, NL periodicity $\Lambda \approx 5\mu m$. Top: FF, bottom: SH.

# Chapter 3

# Nonlinear Trapping in Waveguide Arrays

## 3.1 Some Remarks on 1D Periodic Structures

Periodic structures have been proved to be among the most interesting systems to achieve light generation and processing in integrated systems. Both linear and nonlinear regimes are affected and it is possible to demonstrate some peculiar phenomena, generally unachievable in bulk, see [13].

In this chapter we are studying a specific propagation regime in arrays of evanescently-coupled waveguides, that are indeed the simplest, 1D, of this class.

The analysed periodic structures have been built in AlGaAs, see figure 3.1 and 3.2(a), as well as in photorefractive materials (where they can be induced optically [70]), or in liquid crystal thin films [71]. Similar dynamics can be observed in Bose-Einstein condensates in optical lattices.

It is well known that there are input angles corresponding to different Bragg orders for which the dominant mechanism is reflection. These angles correspond to opening of forbidden gaps in the value of the longitudinal wave-number (propagation constant), in turn associated with linear solutions which are evanescent in the transverse direction. This represents in two spatial dimensions (in harmonic regime) the analogous of the well-known dispersion relation ($\omega$ vs. $k$, the transverse light momentum) of photonic crystals that exhibit propagation band and band gaps.

In our case diffraction depends on the curvature of our (longitudinal vs. transverse wavenumber) band structure, see fig. 3.2(b).

First of all light injected along the axis of one (or few) of the array guides disperses because of evanescent coupling to the adjacent waveguides. That can be described by a discrete system, see [69, 73, 74], (in this chapter we prefer to use the notation $\exp(-i\omega t)$ for time dependence)

$$i\frac{\mathrm{d}E_n}{\mathrm{d}z} + \Lambda E_n + \Gamma\left(E_{n-1} + E_{n+1}\right) = 0 \tag{3.1}$$

where $E_n$ denotes the field amplitude in the $n$-th waveguide, $\Lambda$ and $\Gamma$ represent the self

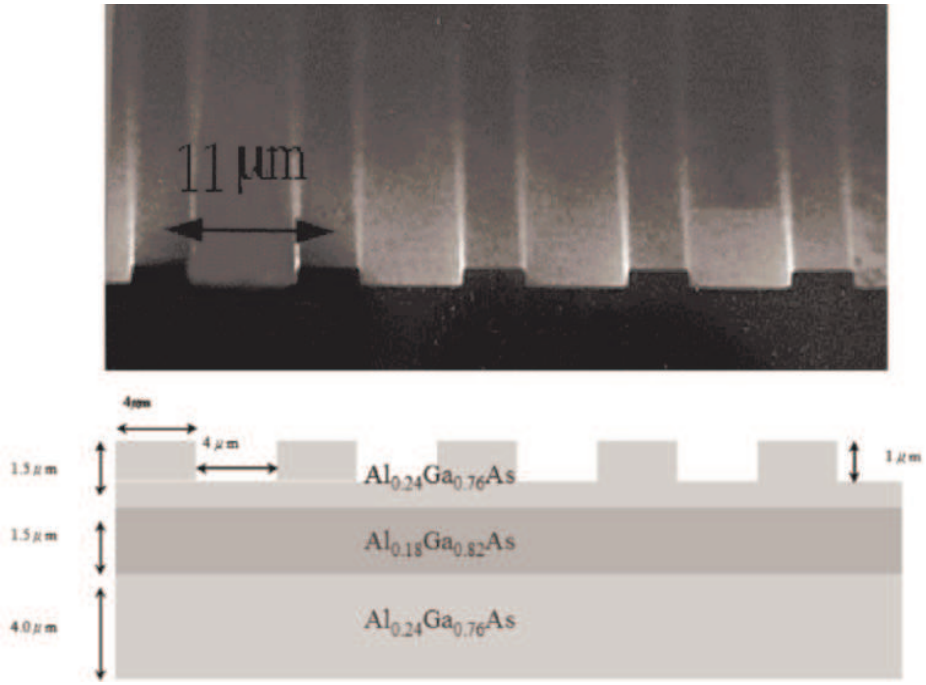


Figure 3.1: Periodic array of single-mode waveguides: SEM image (top) and an axample of realization (bottom), courtesy of Sukhorukov et al., [69].

and mutual coupling respectively. To solve eq. (3.1), in a N waveguide domain we impose boundary values $E_{-N/2} = E_{N/2} = 0$. This model is based on a weak-coupling between non-adjacent waveguides and is analogous to the tight-binding approach of solid-state Physics.

Then the output of linear propagation is completely different from diffraction in homogeneous materials; if excitation of a single waveguide $E_0 \neq 0$

$$E_n(z) = E_0\,(i)^n \exp(i\Lambda z) J_n(2\Gamma z) \tag{3.2}$$

where $J_n$ is the Bessel function of the first kind of order $n$. Two main lobes appear instead of the single-lobed pattern of bulk diffraction.

Then we observe that in our band diagram, there exists a set of angles of diffraction-less propagation (and an exactly determined transverse group velocity).

In the nonlinear regime, e.g. Kerr media, at high intensity self-focusing can exactly compensate diffraction and soliton propagation, field profiles unaffected by longitudinal propagation, can be achieved. The simplest example is represented by discrete solitons (DS) that are obtained in the previously-mentioned front excitation of one or few waveguides.

More generally, we should discuss Floquet-Bloch solitons, that arise when compensation of diffraction is achieved at a specific angle, described by its own propagation characteristics (we obtain a superposition of Bloch waves that do not diffract). These effects are simply the extension of spatial solitons in bulk media.

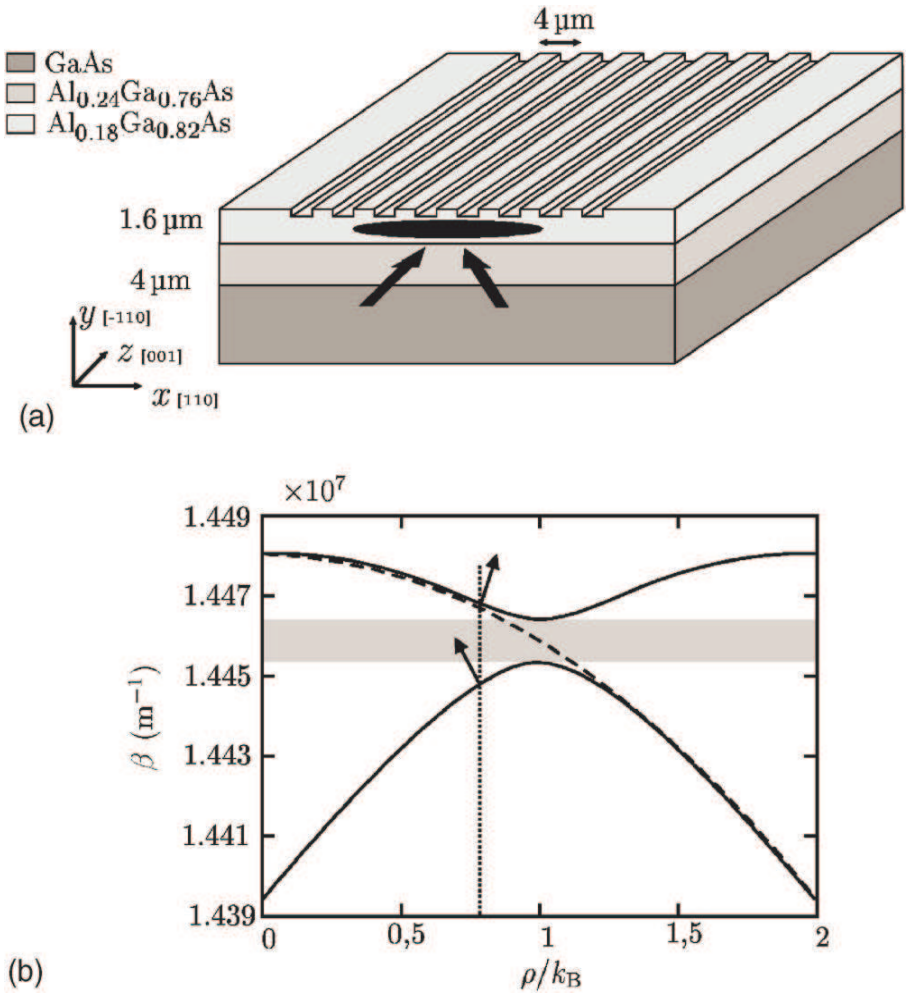


Figure 3.2: (a) Planar periodic structure, its typical front excitation and (b) the associated band, courtesy of Gorza et al., see [72].

Our work has instead been focused on the propagation at wavenumbers inside the photonic band-gap, induced by nonlinearity (in fact they are inaccessible in the linear regime), the *spatial gap-solitons*, [75, 76].

Their analogous in 1D (pulsed) regime is the propagation at frequencies lying inside a forbidden photonic band-gap in the form of so-called gap soliton (GS) [77], (see also [78] and references therein). This concept is well established in fibre Bragg gratings where forward- and backward-propagating components at Bragg frequency (or around it, i.e., within the frequency gap given by the reflection bandwidth) are intrinsically coupled. In this case GS allows, at sufficiently high intensity, for locking the two components in such a way that a pulse can travel slowly (with any velocity between zero and the velocity of light of the host medium) along the structure without being reflected [13, 79]. This kind of propagation exhibits particle-like properties: unstable solutions as well as stable solutions that persist even in interactions are admitted.

Whereas GSs in fibre gratings are hard to obtain due to high reflectivity at each fibre end, and particularly zero-transverse velocity ones, that require a very accurate balance of the pulses interacting inside the grating and are an ideal limit, in the spatial case, we are describing, front excitation is used to demonstrate this sort of regime, see 3.2(a). Two beam envelopes impinging on the structure at opposite Bragg angles can interfere to form a self-trapped GS that tunnels (having longitudinal wave-number in the gap) through the array, as observed recently in different materials and structures [72, 80–82]. It is possible to choose two gaussian profiles, since their superposition generates a modulation of the overall beam that resembles Bloch waves. Moreover transverse velocity can be set by unbalancing the two beams. We refer to this regime as spatial gap soliton (SGS).

In the example of Kerr media this can be explained by the nonlinear index shift that moves upward the propagation band, allowing stable propagation. Recall that zero group velocity is achieved by impressing no transverse momentum to Bloch wave (central point of first band).

The description of such trapping phenomenon has been initially developed on the basis of a simplified version (that neglects diffraction) of CMT [75]. It was then argued that CMT was accurate only for small index changes (narrow bandgap), and the reference model has become a paraxial wave equation with periodic coefficients [74, 76, 83]. Here we compare quantitatively and contrast the two approaches showing that the CMT, in spite of its intrinsic approximations, provides a *good analytical description* of SGS in a wide range of parameters in cases of experimental interest. Our analysis supports the use of CMT as the ground for experimental characterization of SGS [72], and, on the other hand, indicates where CMT should be used with care. The results of the CMT are verified by means of our BPM code.

Finally we report the analysis of trapped solutions in quadratic media, due to mutual interactions of two-colour beams.

## 3.2 Spatial Gap Solitons in Kerr Media

### 3.2.1 Derivation of Coupled Mode equations

We consider a periodic layered medium made of lossless dielectrics with refractive index $n_{1,2} = n_0 \pm \Delta n/2$ [$\Delta n = n_2 - n_1 > 0$] and thickness $\Lambda_{1,2}$, characterized by the pitch $\Lambda = \Lambda_1 + \Lambda_2 \equiv 2\pi/k_g$ along the transverse coordinate $X$.

In the 1+1D approximation ($\partial_Y = 0$), and in the limit of weak inhomogeneity and paraxial conditions, the complex envelope of the electric field $E = E(X, Z)$ propagating along the $Z$-axis (the total electric field is $\mathcal{E}(X, Z, T) = \mathrm{Re}\{E(X, Z)\exp(ikZ - i\omega T)]\}$ and is assumed to be normalized in such a way that $|E(X, Z)|^2$ gives directly the intensity) obeys the wave equation

$$i2k\frac{\partial E}{\partial Z} + \frac{\partial^2 E}{\partial X^2} + 2k_0^2 n_0 \Delta n_p E = 0, \tag{3.3}$$

where

$$\Delta n_p = \Delta n_p(X, E) \tag{3.4}$$

stands for a generic perturbation of the linear background refractive index $n_0$: we have assumed the weak perturbation so that

$$n^2 = (n_0 + \Delta n_p)^2 \simeq n_0^2 + 2n_0 \Delta n_p \tag{3.5}$$

and $k = k_0 n_0 = (\omega/c) = 2\pi/\lambda n_0$ is the average wave-number. The explicit model for SGS that we are interested in can be obtained from eq. (3.3) assuming a perturbation

$$\Delta n_p \equiv \Delta n_{lin} + \Delta n_{nl} \tag{3.6}$$

made by the superposition of a linear periodic contribution whose Fourier expansion is

$$\Delta n_{lin}(X) = \sum_{m=-\infty}^{+\infty} \Delta n_m \exp(imk_g X) \tag{3.7}$$

and a nonlinear Kerr contribution

$$\Delta n_{nl} = n_{2I} |E(X,Z)|^2 \tag{3.8}$$

which yield

$$i\frac{\partial E}{\partial Z} + \frac{1}{2k}\frac{\partial^2 E}{\partial X^2} + k_0 \Delta n_p(X) E + \chi |E|^2 E = 0 \tag{3.9}$$

where $\chi = k_0 n_{2I}$ is the overall nonlinear coefficient.

In the linear case ($\chi = 0$) Bragg reflection occurs at propagation angles $\phi_{Bm}$ with the $Z$-axis [84]

$$\phi_{Bm} = \sin^{-1}\left(\frac{mk_g}{2k}\right) = \sin^{-1}\left(\frac{m\lambda}{2n_0\Lambda}\right). \tag{3.10}$$

Considering only positive values of $m$, the Bragg condition corresponds to waves travelling with transverse wave-number $k_x = k\sin\phi$ equal to a multiple of the halved lattice wave-number, i.e.

$$k_x = \pm k_{xB} = \pm\frac{mk_g}{2} = \pm m\frac{\pi}{\Lambda} \tag{3.11}$$

For beam pairs impinging on the structure with opposite angles close to a given Bragg order, the CMT can be developed by writing the field as a superposition of nearly-resonant envelopes $E_\pm(X,Z)$ as

$$E = \left[E_+(X,Z)e^{ik_{xB}X} + E_-(X,Z)e^{-ik_{xB}X}\right] e^{-i\frac{k_{xB}^2}{2k}Z}, \tag{3.12}$$

where a common longitudinal phase shift has been introduced to account for the well known expression of the overall longitudinal wave-number $k\left(1 - k_{xB}^2/2k^2\right)$ in the paraxial approximation. By inserting the ansatz (3.12) in eq. (3.3), applying the rotating wave approximation, and grouping resonant terms, we end up with the following CMT model which is valid around the $m$-th resonance

$$i\left(\frac{\partial E_+}{\partial Z} + \frac{mk_g}{2k}\frac{\partial E_+}{\partial X}\right) + \frac{1}{2k}\frac{\partial^2 E_+}{\partial X^2} + \Gamma_m E_- + \\ + \chi\left(|E_+|^2 + 2|E_-|^2\right)E_+ = 0, \tag{3.13}$$

$$i\left(\frac{\partial E_-}{\partial Z} - \frac{mk_g}{2k}\frac{\partial E_-}{\partial X}\right) + \frac{1}{2k}\frac{\partial^2 E_-}{\partial X^2} + \Gamma_m E_+ + \\ + \chi\left(|E_-|^2 + 2|E_+|^2\right)E_- = 0, \tag{3.14}$$

where $\Gamma_m = k_0 \Delta n_m$ is the effective Bragg coupling constant.

### 3.2.2 Linear diffraction properties: band diagram

The low-intensity diffraction relation $\beta = \beta(k_x)$ associated with the linear part (i.e., $\chi = 0$) of Eqs. (3.13-3.14) can be easily derived from the solvability condition of the algebraic system obtained by seeking for plane-wave solutions $E_\pm(X,Z) = A_\pm \exp(\pm i k_x X + i\beta Z)$ (note that henceforth $k_x$ represents the deviation of the transverse wave-number from resonant value $k_{xB}$). Substituting the plane wave ansatz, we can obtain

$$\begin{pmatrix} -\left(\beta + \frac{k_x m k_g}{2k} + \frac{k_x^2}{2k}\right) & \Gamma \\ \Gamma & -\left(\beta - \frac{k_x m k_g}{2k} + \frac{k_x^2}{2k}\right) \end{pmatrix} \begin{pmatrix} A_+ \\ A_- \end{pmatrix} = 0 \tag{3.15}$$

that has non trivial solutions that leads to the dispersion (or more precisely saying diffraction) relation of the periodic structure,

$$k_x = \pm\sqrt{\frac{-4k\beta + m^2 k_g^2 \pm \sqrt{\left(m^4 k_g^4 - 8k\beta m^2 k_g^2 + 16k^2\Gamma^2\right)}}{2}} \tag{3.16}$$

that accounts for diffraction terms $\frac{k_x^2}{2k}$ or, neglecting them

$$k_x = \pm\sqrt{\beta^2 - \Gamma^2}\,\frac{2k}{m k_g} \tag{3.17}$$

Beware that $\beta$ is not the physical propagation constant, but a relative one. Indeed the real phase constant can be expressed as follows:

$$\beta_{ph} = \beta - m^2 k_g^2/(8k) + k$$

First of all it is worth comparing those band diagrams (CMT applied with different $m$'s) with the rigorous ones, derived by a transfer matrix approach, see [84]. The CMT model describes the diffraction in the vicinity of a single band-gap of order $m$, whereas the latter provides the full description of the whole set of bands. Using the same convention as above, in the generic period $n$ we express the field as a superposition of couterpropagating transverse waves of fixed longitudinal wavenumber,

$$E(x,z) = \left[a_n^\alpha e^{ik_{\alpha x}(X-n\Lambda)} + b_n^\alpha e^{-ik_{\alpha x}(X-n\Lambda)}\right] e^{i\beta Z} \tag{3.18}$$

$\alpha = 1,2$ indicates which of the two layers we are considering, $k_{\alpha x} = \sqrt{n_\alpha^2 k_0^2 - \beta^2}$ is the corresponding transverse wavenumber.

Imposing continuity conditions of electric field and its derivatives, for TE modes we can derive a link between field values in adjacent periods,

$$\begin{bmatrix} a_{n-1} \\ b_{n-1} \end{bmatrix} = \begin{bmatrix} A & B \\ C & D \end{bmatrix} \begin{bmatrix} a_n \\ b_n \end{bmatrix} \tag{3.19}$$

where field weights are those in layer 1 and

$$\begin{aligned} A &= e^{-ik_{1x}\Lambda_1}\left[\cos\left(k_{2x}\Lambda_2\right) - \frac{1}{2}i\left(\frac{k_{2x}}{k_{1x}} + \frac{k_{1x}}{k_{2x}}\right)\sin\left(k_{2x}\Lambda_2\right)\right] \\ B &= e^{ik_{1x}\Lambda_1}\left[-\frac{1}{2}i\left(\frac{k_{2x}}{k_{1x}} - \frac{k_{1x}}{k_{2x}}\right)\sin\left(k_{2x}\Lambda_2\right)\right] \\ C &= e^{-ik_{1x}\Lambda_1}\left[\frac{1}{2}i\left(\frac{k_{2x}}{k_{1x}} - \frac{k_{1x}}{k_{2x}}\right)\sin\left(k_{2x}\Lambda_2\right)\right] \\ D &= e^{ik_{1x}\Lambda_1}\left[\cos\left(k_{2x}\Lambda_2\right) + \frac{1}{2}i\left(\frac{k_{2x}}{k_{1x}} + \frac{k_{1x}}{k_{2x}}\right)\sin\left(k_{2x}\Lambda_2\right)\right] \end{aligned} \tag{3.20}$$

To obtain an eigenvalue problem, we consider that, by Bloch theorem, field envelop is required to be periodic, i.e.

$$\mathcal{E}(X,Z,T) = \mathrm{Re}\{E_K(X)\exp\left(iKX\right)\exp\left(-i\omega T + i\beta Z\right\} \tag{3.21}$$

with $K$ the Bloch wavenumber and

$$E_K(z+\Lambda) = E_K(z)$$

Applying the latter condition to eq. (3.19), we can write

$$e^{-iK\Lambda}\begin{bmatrix} a_n \\ b_n \end{bmatrix} = \begin{bmatrix} A & B \\ C & D \end{bmatrix}\begin{bmatrix} a_n \\ b_n \end{bmatrix}$$

then diffraction diagram results

$$K(\beta,\omega) = \frac{1}{\Lambda}\cos^{-1}\left[\frac{1}{2}\left(A+D\right)\right] \tag{3.22}$$

and consequently Bloch wave in the layer 1 of the $n$-th period is

$$E_K(x)e^{iKX} = \left[\left(a_0 e^{ik_{1x}(X-n\Lambda)} + b_0 e^{-ik_{1x}(X-n\Lambda)}e^{-iKx+in\Lambda X}\right)\right]e^{iKX} \tag{3.23}$$

where eigenvectors are expressed as

$$\begin{bmatrix} a_0 \\ b_0 \end{bmatrix} = \begin{bmatrix} B \\ \exp\left(-iKx\right) - A \end{bmatrix} \tag{3.24}$$

times any arbitrary constant.

Propagation bands correspond to $\left|\frac{1}{2}\left(A+D\right)\right| < 1$, while forbidden bands to $\left|\frac{1}{2}\left(A+D\right)\right| > 1$. Band edges are individuated by transition points.

In fig. 3.3 we compare results obtained from (3.16) (dashed line) and (3.22) (solid line) calculated for $m = 1$ and typical parameters ($\lambda_0 = 1.55\mu$m, $\Lambda = 4\mu$m, 50% duty cycle, $\Delta n = 0.008$ yielding $\Gamma_1 \cong 10^4\mathrm{m}^{-1}$, as in [72]; other experiments use similar parameters)

As shown, the two results are in remarkable good agreement (dashed and solid lines are practically coincident) around the upper grey region which represents the first ($m = 1$) gap corresponding to forbidden values of $\beta$ and imaginary values of the transverse wave-number deviation $k_x$. The figure shows also the narrow $m = 2$ gap (which, in the framework of the

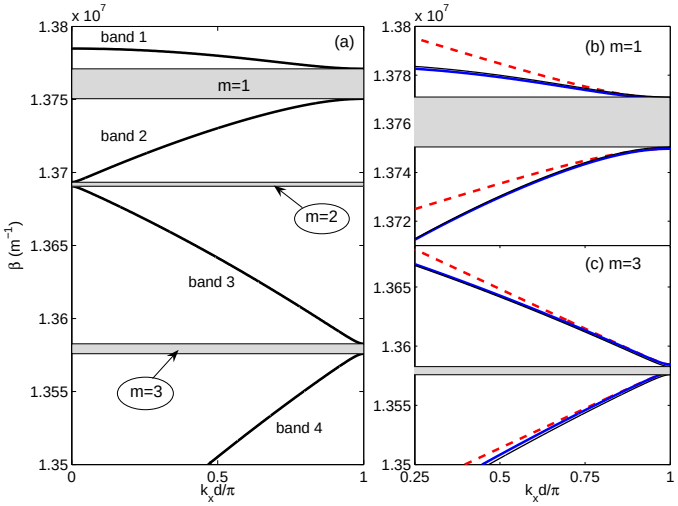


Figure 3.3: Band structure in the first Brillouin zone $k_x = [-\pi/\Lambda, \pi/\Lambda]$ for an array with $\Lambda = 4\mu$m, $\Delta n = 0.008$ (a). The grey areas correspond to $m = 1, 2, 3$ gaps (from top to bottom) where no linear freely propagating modes exist. The CMT diffraction relationships for gaps $m = 1$ (b) and $m = 3$ (c) (dashed line) are compared with the exact result obtained by means of the transfer matrix method (solid line)

CMT, vanishes for a square wave grating with 50% duty cycle) and the $m = 3$ gap (which is again well described by the CMT dispersion relationship with $m = 3$) obtained from the exact results. The two approaches start to show significant discrepancies for refractive index changes usually larger than those involved in experiments, with such discrepancies becoming more severe for higher order gaps.

### 3.2.3 Gap soliton solution

The CMT model (3.13-3.14) entails that freely propagating modes with wavenumber in the gap, which are forbidden in the linear regime, can exist in the nonlinear regime. In order to assess the impact of standard diffraction of the envelopes, taken into account by the second derivatives in Eqs. (3.13-3.14), we introduce the dimensionless variables $x = (2k\Gamma_m/mk_g)X$, $z = \Gamma_m Z$, $U_\pm = \sqrt{\chi/\Gamma_m}E_\pm$, and the right/left propagators $L^\pm \equiv i\partial_z \pm i\partial_x$, which allow us to cast Eqs. (3.13-3.14) in the following form

$$L^\pm U_\pm + U_\mp + \left(|U_\pm|^2 + 2|U_\mp|^2\right) U_\pm = -\varepsilon \frac{\partial^2 U_\pm}{\partial x^2}, \tag{3.25}$$

where $\varepsilon = \frac{2k\Gamma_m}{(mk_g)^2}$ weights the diffraction terms. Since $\varepsilon$ is usually a small quantity (e.g., from [72] we obtain $\varepsilon \cong 0.1$), the right-hand side in fig. (3.25) can be neglected. In this case, the CMT model (identical to that governing counterpropagating pulses in a Bragg grating with $x$ replacing time $t$) possesses a family of GS solutions which has been thoroughly investigated in [78]. These nonlinear localized modes depend on two free parameters that fix the position in the gap and the transverse velocity of the field, respectively. Following the approach of [78], we introduce the normalized parameters $\beta_\Gamma \equiv \beta/\Gamma_m$ and $v = dx/dz$ $(-1 \leq v, \beta_\Gamma \leq 1)$,

and write the GS solutions in the form

$$U_{\pm}(z,x) = A_{\pm}\sqrt{\eta(\zeta)}\ \exp\left[i\beta_{\Gamma}z + i\psi_{\pm}(\zeta)\right] \tag{3.26}$$

where $\zeta \equiv \gamma(x - vz)$ is the transverse coordinate in the GS frame, $\gamma = (1-v^2)^{-1/2}$, and $\eta(\zeta)$ and $\psi_{\pm}(\zeta)$ are the GS intensity and phase profiles, respectively, see [78]. We report their explicit expressions. First let

$$\begin{aligned} A_{+} &= \frac{1}{\gamma\sqrt{|\rho|}}\sqrt[4]{\frac{1+v}{1-v}} \qquad & A_{-} &= -s\frac{1}{\gamma\sqrt{|\rho|}}\sqrt[4]{\frac{1-v}{1+v}} \\ \rho &= 2\left(1-v^2\right) + \left(1+v^2\right) & s &\equiv \mathrm{sign}\left(\rho\right) \end{aligned} \tag{3.27}$$

The intensity and phase profiles depend on the single parameter ($|\delta| < 1$ to have bright solitons)

$$\delta = \gamma\beta_{\Gamma}\ ;\ \delta^2 \leq 1 \Rightarrow \beta_{\Gamma}^2 + v^2 \leq 1 \tag{3.28}$$

The intensity can be explicitly found to be

$$\eta(\zeta) = \frac{2\left(1-\delta^2\right)}{\cosh\left(2\sqrt{1-\delta^2}\zeta\right) + s\delta}, \tag{3.29}$$

while the phases are

$$\phi_{\pm}(\zeta) = \gamma v\beta_{\Gamma}\zeta \mp s\ 4F_{\pm}\tan^{-1}\left[\frac{1-s\delta}{1-\delta^2}\tanh\left(\sqrt{1-\delta^2}\zeta\right)\right]; \tag{3.30}$$

with

$$F_{+} = \frac{1}{4} - \frac{R}{1+R}\ ;\ F_{-} = \frac{1}{4} - \frac{1}{1+R}\ ;\ R \equiv \frac{2(1-v^2)+(1+v)^2}{2(1-v^2)+(1-v)^2} \tag{3.31}$$

Overall form for the soliton is (pose $\delta\omega = v\gamma\beta_{\Gamma}$)

$$\begin{aligned} U_{+}(z,t) =& \frac{1}{\gamma\sqrt{|\rho|}}\sqrt[4]{\frac{1+v}{1-v}}\sqrt{\frac{2\left(1-\delta^2\right)}{\cosh\left(2\sqrt{1-\delta^2}\zeta\right)+s\delta}} \\ &\times\exp\left\{i(\beta_{\Gamma}z - \delta\omega\zeta) - is\ 4F_{+}\tan^{-1}\left[\frac{1-s\delta}{1-\delta^2}\tanh\left(\sqrt{1-\delta^2}\zeta\right)\right]\right\} \\ U_{-}(z,t) =& \frac{-s}{\gamma\sqrt{|\rho|}}\sqrt[4]{\frac{1-v}{1+v}}\sqrt{\frac{2\left(1-\delta^2\right)}{\cosh\left(2\sqrt{1-\delta^2}\zeta\right)+s\delta}} \\ &\times\exp\left\{i(\beta_{\Gamma}z - \delta\omega\zeta) + is\ 4F_{-}\tan^{-1}\left[\frac{1-s\delta}{1-\delta^2}\tanh\left(\sqrt{1-\delta^2}\zeta\right)\right]\right\} \end{aligned} \tag{3.32}$$

Peak power is

$$|U_{\pm}|^2_{max} = \sqrt{\frac{1\pm v}{1\mp v}}\ \frac{1-v^2}{2(1-v^2)+(1+v^2)}\ \frac{2\left(1-\delta^2\right)}{1+s\delta} \tag{3.33}$$

and FWHM is

$$\zeta_{FWHM} = \frac{1}{\sqrt{1-\delta^2}}\cosh^{-1}(2+\delta) \tag{3.34}$$

To summarize the main features, we remark that SGS localized modes have been proved to exist in the unit circle of the parameter plane, i.e. $\beta_{\Gamma}^2 + v^2 \leq 1$, and to possess the following features:

1. the amplitude and inverse width of SGS envelopes is fixed by the input (around Bragg) angle of the two beams, or equivalently by the position in the gap, decreasing (increasing) as the lower (upper) edge of the gap is approached;

2. the interference pattern formed by the two envelopes has a progressive phase shift with respect to the grating due to the nonlinear phase terms $\psi_{\pm}(\zeta)$;

3. the transverse velocity of the soliton (that does not depend on the input angle) can be tuned by playing on input beam imbalance (amplitudes $A_{\pm}$), since the beam acquires a transverse velocity in the direction of the stronger beam.

In the following we restrict to the case of zero transverse velocity $v = 0$, which requires perfectly balanced input intensities. In order to verify that diffraction does not hamper the localization phenomenon we could integrate numerically Eqs. (3.25) and verify that they possess localized solutions that can be obtained numerically by continuation of the analytical ones when with $\varepsilon \neq 0$. However, the validity of all the approximations implicit in the CMT can be assessed even better by seeking for localized nonlinear modes $E(X, Z) = U(X)\exp(i\beta_s Z)$ of eq. (3.9), which yields

$$-\beta_s U + \frac{1}{2k}\frac{\partial^2 U}{\partial X^2} + k_0 \Delta n_p(X) U + \chi U^3 = 0. \tag{3.35}$$

We integrate eq. (3.35) numerically by means of a relaxation approach, i.e. we discretise it in order to obtain a system of nonlinear equations. Then for each $\beta_s$ (propagation constant of the soliton, that reads as $\beta_s = \beta_\Gamma \Gamma_m - m^2 k_g^2/(8k)$), we solve it using the Newton iteration for systems, a simple extension of the usual tangent formula,

$$\begin{gathered} F(\xi) = 0,\ \xi = \xi_0 \\ \Downarrow \text{ iteration of} \\ J_F(\xi_n)(\xi_{n+1} - \xi_n) = -F(\xi_n) \Rightarrow \xi_{n+1} \\ \text{until } F(\xi_n) < \text{tol}_f \vee |\xi_n - \xi_{n+1}| < \text{tol}_\xi \end{gathered}$$

where $J_F$ denotes the Jacobian matrix of function $F : \mathbb{R}^k \to \mathbb{R}^k$ and $\xi_n$ and $\xi_{n+1}$ are two subsequent steps of iteration. Since it requires an initial guess, that has to be close enough to final solution, we assume eqs. (3.12) and (3.26) to provide a good approximation and refine it.

Results are reported in figs. 3.4-3.6 for the $m = 1$ gap of an AlGaAs grating ($n_2 = 3.4$, $n_{2I} = 1.5 \times 10^{-17} m^2/W$) with period $\Lambda = 4\mu$m and $\Delta n = 0.008$ (Bragg angle $3.27^o$) [72].

To provide a reliable solution a large number of points is used in relaxation: this is a limit if we study solitons of finite transverse velocity, that would require the full 2D integration, since the soliton profile is not aligned to waveguide axes.

In fig. 3.4 we show the basic structure of a stationary SGS, which has the main dip corresponding to the high index central layer, caused by $E_{\pm}$ being out of phase. Other minima exhibit a progressive displacement with respect to the grating layers due to the nonlinear phase term [feature (2)]. As shown, such features are perfectly replicated by the

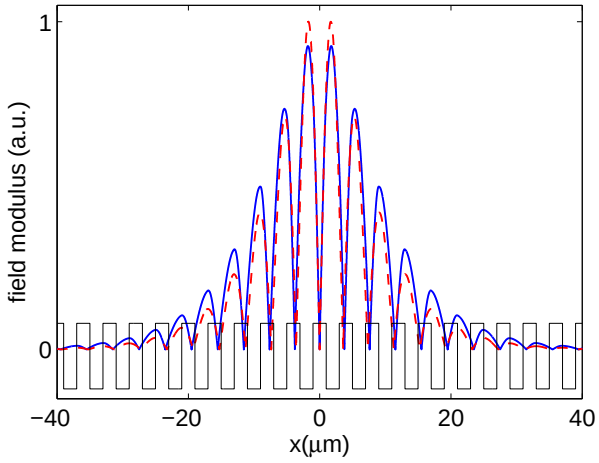


Figure 3.4: Zero-velocity SGS profile belonging to lower half of the first Bragg gap $m = 1$, $\beta_\Gamma = -0.5$), for an array with square-wave distribution $\Delta n_{lin}(X)$ of the linear index with period $\Lambda = 4\mu$m and $\Delta n = 0.008$ (a vertically magnified replica of $\Delta n_{lin}(X)$ is shown on the bottom of the figure). We compare the profile obtained analytically [Eqs. (3.12,3.26)] from the CMT (dashed line) with that obtained numerically from the wave equation (3.35).

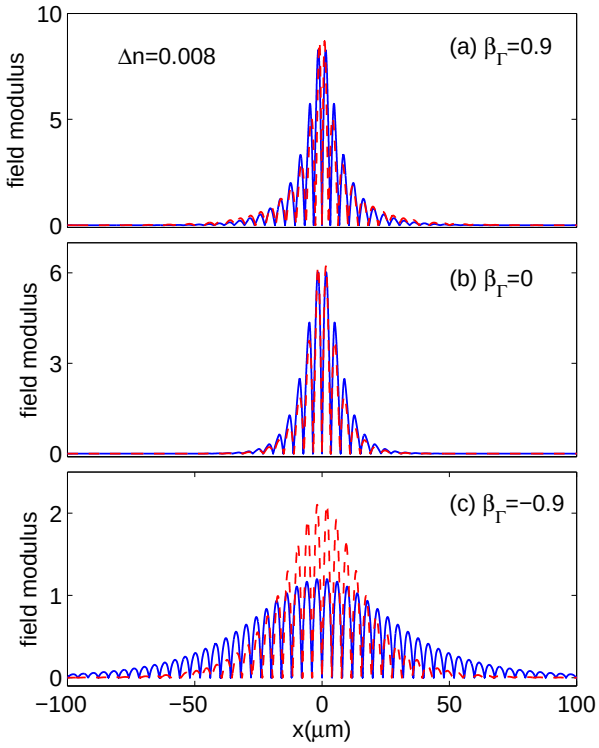


Figure 3.5: SGS profiles obtained for different locations in the $m = 1$ gap fixed by the reported value of the parameter $\beta_\Gamma$ (same array as in fig. 3.4). The profiles obtained analytically [Eqs. (3.12,3.26)] from the CMT (red dashed line) are compared with the solutions obtained numerically from eq. (3.35) (blue solid line). The field is in $\mathrm{GW}^{1/2}/\mathrm{cm}$.

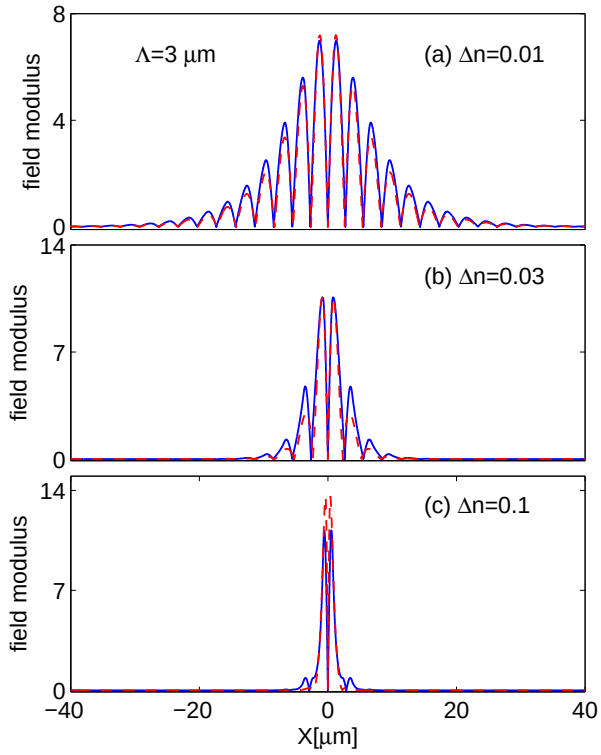


Figure 3.6: As in fig. 3.5 for an array with $\Lambda = 3\mu$m and increasing values of the periodic perturbation $\Delta n$.

outcome of the relaxation method [eq. (3.35)] which exhibits a remarkable agreement with the analytical expression [eqs. (3.12) and (3.26)]. In fig. 3.5 we compare the SGS profiles for different locations in the gap fixed by the value of the normalized parameters $\beta_\Gamma$. As shown, the solutions decreases their amplitude and increase their width [feature (1)] by moving from the upper to the lower band edge. We find that the agreement is quite good across the whole gap except for locations close to the bottom edge of the gap [see case (c) corresponding to $\beta_\Gamma = -0.9$], where solitons tend to zero by becoming progressively broader and less intense. In fig. 3.6 we show how the SGS modes are modified when the index change increases (here we consider a fixed grating pitch $\Lambda = 3\mu$m). Importantly, as the index perturbation grows, the gap widens, and the CMT is expected to be less accurate. However, as fig. 3.6 shows, CMT gives an accurate description of localized modes even when the index change is as high as $\Delta n = 0.1$ and the localized mode is almost entirely confined in two guides only.

We have also explored the possibility of SGS solution lying in higher order gaps. As stated above, second order gap is not modelled by CMT, thus we have looked for third-gap SGS, but relaxation procedure suffers from many convergence issues. We can instead obtain a finite CMT second order gap varying the array duty cycle ($\delta_c = \Lambda_{high}/\Lambda$). Particularly convergence is readily obtained for $\delta_c < 50\%$.

Let us seek for solutions in an array of the same parameters as above, but with $\delta_c = 25\%$. In figure 3.7, we report the comparison between CMT and relaxation results.

Then we study an array of larger index step $\Delta n = 0.02$ and a small duty cycle $\delta_c = 20\%$:

in figure 3.8 we plot a detail of CMT approximation of band diagram around the second-order gap of this array. Particularly the upper edge is poorly approximated. Then in figure 3.9 we compare SGS at different positions of second order gap, obtained in this system.

Again we obtain larger discrepancy at the lower edge of the gap, and notice the fast modulation to conform to the corresponding lower edge Bloch wave.

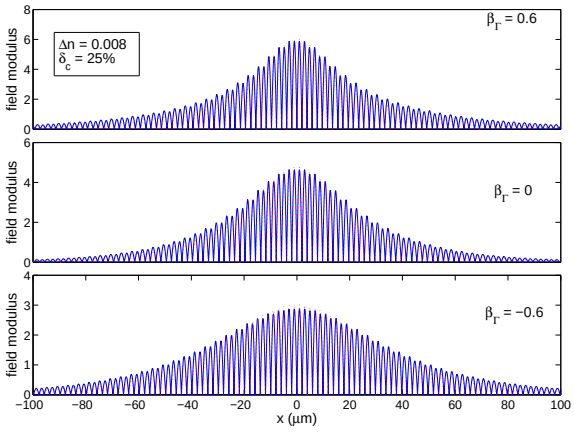


Figure 3.7: SGS profiles obtained for different locations in the $m = 2$ gap fixed by the reported value of the parameter $\beta_\Gamma$. The array is characterized by index step $\Delta n = 0.008$ and duty cycle $\delta_c = 25\%$. The profiles obtained analytically [Eqs. (3.12-3.26)] from the CMT (red dashed line) are compared with the solutions obtained numerically from eq. (3.35) (blue solid line). The field is in $\mathrm{GW}^{1/2}/\mathrm{cm}$.

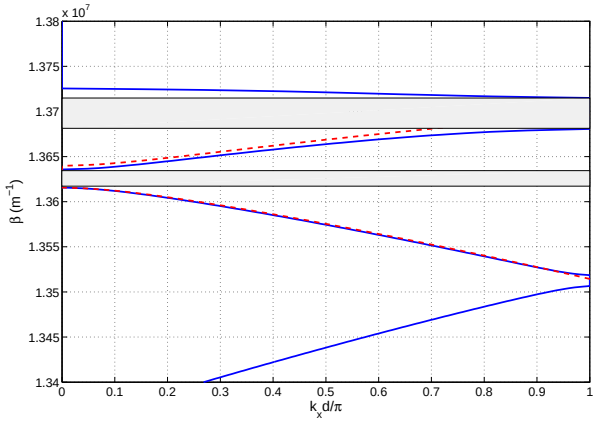


Figure 3.8: Band diagram of a $\Delta n = 0.02$ array of period $4\mu m$, $\delta_c = 20\%$: comparison of rigorous (3.22) and CMT (3.16) ($m = 2$) models, focused on second order gap. As in 3.3, solid and dashed line identify rigorous and CMT solutions, respectively.

The width-peak relationship is the same of the first example, as it can be easily realized.

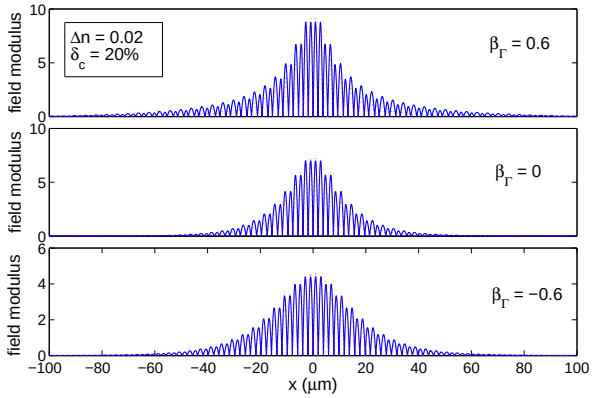


Figure 3.9: Same as fig. 3.7, but different array propertiesare used: index step $\Delta n = 0.02$ and duty cycle $\delta_c = 20\%$.

### 3.2.4 BPM simulation

In order to verify the goodness of CMT and the stability of SGS solutions during propagation, we use our implemented wide-angle nonlinear beam-propagation method. Figure 3.10 displays the result of a BPM simulation with an input beam given by eq. (3.26) [reported in fig. 3.5(b)]. As shown, in the linear case [$\chi = 0$, fig. 3.10(a)] the beam spreads due to Bragg coupling and different opposite transverse velocities of the two components. However, under nonlinear conditions the beam is self-trapped [fig. 3.10(b)]. In spite of the fact that some radiation is shed during propagation, at the output a major fraction of the input SGS power is still confined in few central waveguides, and a comparison between the input and output profiles [Figs. 3.10(c-d)] allows us to conclude that stable trapping is achieved. We can repeat the same simulation for soliton of non zero transverse velocity. Using as excitation the CMT solution, we obtain again a good trapping, proving that CMT solutions are accurate enough, see fig. 3.11.

We have compared two approaches to the description of nonlinear beam trapping in waveguide arrays exhibiting a Bragg forbidden gap in longitudinal wave-number. The CMT is found to give a reasonably accurate description of still SGS solutions across the whole fundamental band-gap, where the approach based on the paraxial equation gives a more reliable estimate of the peak intensity and width that turns out to be appropriate to yield beam trapping. An important exception is that broad solutions that lie close to the lower band edge, that can be explained qualitatively recalling that intensity dependent refractive index causes the Bragg resonance to shift upward in $\beta$ as the intensity grows larger. Therefore, in order to induce transparency, lower intensity is required near the bottom gap edge. However, under these conditions, in Eqs. (3.13, 3.14) the nonlinear terms are so small that diffraction is likely to become comparable and plays a non-negligible role. Conversely, along the rest of the gap, SGSs arise basically from the balance of nonlinear terms and the main diffractive terms, i.e. first-order derivatives and coupling, while diffraction remains negligible.

Several features could moreover be validated by means of a non-paraxial beam propagation method.

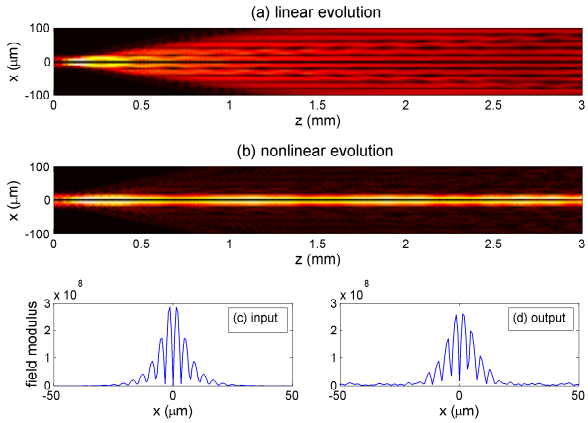


Figure 3.10: BPM simulation of the propagation of an input resonant still GS $\beta_\Gamma = v = 0$) in the $m = 1$ gap. Level plots of the intensity comparing (a) the low intensity (linear, $\chi = 0$) evolution with (b) the nonlinear evolution; (c-d) comparison of the input and output ($Z = 3$ mm). Grating parameters are as in fig. 3.5.

Although the analysis of moving solutions ($v \neq 0$) to compare CMT and its numerical refinement is an interesting topic, we are now passing to quadratic gap solitons. The last remark about moving solutions is that gap solitons are achieved also for detuning that are outside the gap itself in the laboratory framework, see [78]. That can be explained if we consider the soliton frame in which, as normalized transverse velocity approaches unity, i.e. beam approaches Bragg angle, the array undergoes length contraction and then effective gap widens.

## 3.3 Gap Solitons in Quadratic Nonlinear Media

We can generalize the previous discussion, if we look for trapped solutions originating from other nonlinear interactions.

Particularly, let us consider a $\chi^{(2)}$ interaction, that couples two different harmonic fields. It is well known that via a cascading process, we can obtain an effective cubic self-action, in case of large phase-mismatch. Nevertheless, the form of the nonlinear coupled mode system could lead to trapped solutions, also in case of perfect matching.

Since microfabrication techniques permit to achieve quasi-phase-matching, e.g. via periodic poling of magnetic domains in lithium niobate (PPLN), we could obtain two-colour strong simultaneous soliton propagation at the improved efficiency of second order nonlinearity.

We are reporting some results that describe the situation in which both FF and SH lie in a forbidden gap. In case of simultaneous excitation at the same angle, this corresponds to first order and second order gap respectively. In fact since Bragg angle of order $m$ is

$$\phi_{Bm} = \sin^{-1}\left(\frac{mk_g}{2k}\right) = \sin^{-1}\left(\frac{m\lambda}{2n_m\Lambda}\right). \tag{3.36}$$

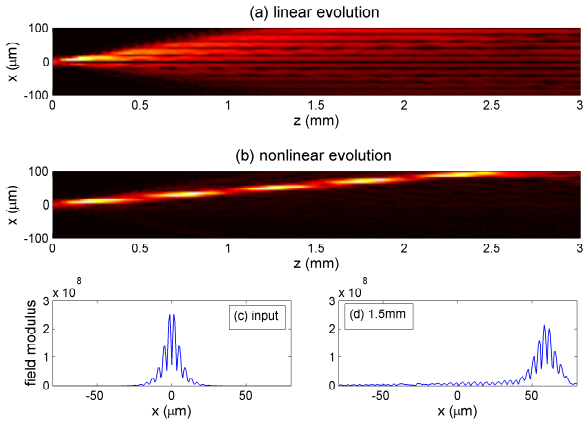


Figure 3.11: Same as figure 3.10, with $\beta_\Gamma = -0.1$, $v = 0.5$. The output profile is computed at $z = 1.5\mu m$.

one can have a spatial Bragg resonance $m = 1$ at $\omega$, $m = 2$ at $2\omega$. The two beams are incident exactly with the same angles provided that $n_1 = n_2$, i.e. SHG is phase-matched, and can be trapped as doubly-resonant spatial gap soliton (SGS).

The nearly superimposition of the two beams permits to envisage the existence of bound states of this sort, composed by two optical harmonics that turn out to be Bragg-resonant at successive orders.

It is worth noting that phase-mismatch acts as an additional degree of freedom, that we do not neglect.

Moreover we recall that CMT approach we have described above does not account for a second order gap (if duty cycle is 50%), while the rigorous approach does. In case of finite mismatch we have to carefully choose the position of soliton wavenumber inside the gap: to obtain solutions decaying away from central zone of excitation spot, SH is not allowed to leave its associated gap: high intensity hence provides an abrupt change in system behavior.

We start from a coupled system of nonlinear equations (for FF and SH) and substitute for each harmonic a superposition of envelopes oscillating in the proximity of their required gap.

### 3.3.1 CMT Model

If we assume a two-colour propagation in a weakly inhomogeneous and nonlinear (quadratic) case, i.e.

$$\begin{aligned}\mathcal{E}(X,Z,T) = \frac{1}{2}E_1(X,Z)\exp(ik_1Z - i\omega T) + \\ + \frac{1}{2}E_2(X,Z)\exp(ik_2Z - i2\omega T) + c.c.\end{aligned} \tag{3.37}$$

where $k_m = (m\omega/c)n_m$ are average wave-numbers, it is easy to obtain, in the paraxial approximation, the coupled system

$$\begin{aligned} i\frac{\partial E_1}{\partial Z} + \frac{1}{2k_1}\frac{\partial^2 E_1}{\partial X^2} + \frac{\omega}{c}\Delta n_p(X)E_1 + \chi E_2 E_1^* e^{i\Delta kZ} = 0, \\ i\frac{\partial E_2}{\partial Z} + \frac{1}{2k_2}\frac{\partial^2 E_2}{\partial X^2} + \frac{2\omega}{c}\Delta n_p(X)E_2 + \chi E_1^2 e^{-i\Delta kZ} = 0. \end{aligned} \tag{3.38}$$

where $\chi = k_0\left(2/\left(\varepsilon_0 c n_2 n_1^2\right)\right)^{1/2}\chi^{(2)}$ and $\Delta k = k_2 - 2k_1$.

We will study as above zero transverse velocity solutions, that can be found in the form

$$\begin{aligned} E_1(X,Z) = e_1(X)\exp(i\beta_s Z) \\ E_2(X,Z) = e_2(X)\exp[i(2\beta_s - \Delta k)Z] \end{aligned}$$

by integrating numerically the following 1D equations with periodic coefficients

$$\begin{aligned} -\beta_s e_1 + \frac{1}{2k_1}\frac{\partial^2 e_1}{\partial X^2} + k_0\Delta n_p(X)e_1 + \chi e_2 e_1^* = 0 \\ -(2\beta_s - \Delta k)e_2 + \frac{1}{2k_2}\frac{\partial^2 e_2}{\partial X^2} + 2k_0\Delta n_p(X)e_2 + \chi e_1^2 = 0 \end{aligned} \tag{3.39}$$

The overall wavenumbers of the two beams, ($k_1 + \beta_s$ at FF and $2(k_1 + \beta_s)$ at SH) must be inside the first two gaps, which are calculated by exact transfer matrix method.

In order to show that the bound states of Eqs. (3.39) can be generated by interference patterns made by pairs of beams at Bragg angle, one can develop a description based on coupled-mode theory. Recalling that Bragg condition corresponds to waves travelling with transverse wave-number $k_x = \pm k_{Bm}$ where $k_{Bm} \equiv m\frac{\pi}{\Lambda}$, we set

$$\begin{aligned} E_1 = \left[E_1^+ e^{ik_{B1}X} + E_1^- e^{-ik_{B1}X}\right] e^{-i\frac{k_{B1}^2}{2k_1}Z} \\ E_2 = \left[E_2^+ e^{ik_{B2}X} + E_2^- e^{-ik_{B2}X}\right] e^{-i\frac{k_{B2}^2}{2k_2}Z} \end{aligned} \tag{3.40}$$

where the longitudinal phase shifts account for the proper expressions of the overall longitudinal wave-numbers $k_m\left(1 - k_{Bm}^2/2k_m^2\right)$ in the paraxial approximation. By inserting the ansatz (3.40) in eq. (3.38), applying the rotating wave approximation after having Fourier expanded the index perturbation as $\Delta n_p(X) = \sum_{m=-\infty}^{+\infty}\Delta n_m \exp(imk_g X)$, and grouping resonant terms, we end up with the following CMT model, 3.13

$$i\left(\frac{\partial E_1^\pm}{\partial Z} \pm \frac{k_g}{2k_1}\frac{\partial E_1^\pm}{\partial X}\right) + \frac{1}{2k_1}\frac{\partial^2 E_1^\pm}{\partial X^2} + \Gamma_1 E_1^\mp + \chi E_2^\pm (E_1^\pm)^* e^{i\Delta k_z Z} = 0, \tag{3.41}$$

$$i\left(\frac{\partial E_2^\pm}{\partial Z} \pm \frac{k_g}{k_2}\frac{\partial E_2^\pm}{\partial X}\right) + \frac{1}{2k_2}\frac{\partial^2 E_2^\pm}{\partial X^2} + \Gamma_2 E_2^\mp + \chi (E_1^\pm)^2 e^{-i\Delta k_z Z} = 0, \tag{3.42}$$

where $\Gamma_m = (m\omega/c)\Delta n_m$ are the effective Bragg coupling coefficients, and

$$\Delta k_z = \left(k_2 - \frac{k_{B2}^2}{2k_2}\right) - 2\left(k_1 - \frac{k_{B1}^2}{2k_1}\right) \simeq \Delta k$$

is the longitudinal wave-number mismatch in the paraxial approximation.

The linear limit corresponds as above to linear diffraction of decoupled harmonics, while in nonlinear regime, we seek SGS solutions in the form

$$E_1^{\pm} = U_1^{\pm}(X)\exp(i\beta Z)$$
$$E_2^{\pm} = U_2^{\pm}(X)\exp[i(2\beta - \Delta k_z)Z]$$

with the profiles $U_{1,2}^{\pm}$ obeying

$$-\beta U_1^{\pm} \pm \frac{k_g}{2k_1}\frac{\partial U_1^{\pm}}{\partial X} + \frac{1}{2k_1}\frac{\partial^2 U_1^{\pm}}{\partial X^2} + \Gamma_1 U_1^{\mp} + \chi U_2^{\pm}(U_1^{\pm})^* = 0, \tag{3.43}$$

$$-(2\beta - \Delta k_z)U_2^{\pm} \pm \frac{k_g}{k_2}\frac{\partial U_2^{\pm}}{\partial X} + \frac{1}{2k_2}\frac{\partial^2 U_2^{\pm}}{\partial X^2} + \Gamma_2 U_2^{\mp} + \chi(U_1^{\pm})^2 = 0, \tag{3.44}$$

Again the nonlinear phase shift $\beta$ is not equivalent to the nonlinear phase shift $\beta_s$ of rapidly varying envelopes $E_{1,2}$.

$$\beta_s = \beta - \frac{k_{B1}^2}{2k_1} = \beta - \frac{(\pi/\Lambda)^2}{2k_1} \tag{3.45}$$

Solitons can be found from the normalized (dimensionless) equations

$$\begin{aligned} \pm i\frac{\partial u_1^{\pm}}{\partial x} - \delta_1 u_1^{\pm} + u_1^{\mp} + u_2^{\pm}(u_1^{\pm})^* &= -\varepsilon\frac{\partial^2 u_1^{\pm}}{\partial x^2} \\ \pm i\frac{2k_1}{k_2}\frac{\partial u_2^{\pm}}{\partial x} - \delta_2 u_2^{\pm} + \Gamma u_2^{\mp} + \frac{(u_1^{\pm})^2}{2} &= -\varepsilon\frac{k_1}{k_2}\frac{\partial^2 u_2^{\pm}}{\partial x^2} \end{aligned} \tag{3.46}$$

where

$$\delta_1 = \beta/\Gamma_1 \qquad \delta_2 = (2\beta - \Delta k_z)/\Gamma_1$$
$$\Gamma = \Gamma_2/\Gamma_1 \qquad x = (2k_1\Gamma_1/k_g)X$$
$$u_1^{\pm} = \sqrt{2}(\chi/\Gamma_1)U_1^{\pm} \qquad u_2^{\pm} = (\chi/\Gamma_1)U_2^{\pm}$$

Usually

$$\varepsilon = \frac{2k_1\Gamma_1}{k_g^2}$$

is a small coefficient and in the limit $\varepsilon \ll 1$ this model is perfectly equivalent to the one governing quadratic temporal GS, see [85].

### 3.3.2 Gap soliton solution

To compare this solution to a relaxation refinement, as we described above, we could integrate eq. 3.46, setting the CMT solution of the cubic case as initial guess. In fact starting from large mismatch (effective cubic action, see below), we can by continuity obtain solutions corresponding to smaller and smaller mismatch. Then we could refine the CMT solutions in the square periodic lattice.

We have preferred to apply directly this procedure to obtain a set of quadratic solitons starting from the cubic solution and a large mismatch, then exploiting the continuous dependence on our new parameter. Let us consider eq. (3.38), posing $\hat{E}_2 = E_2\exp(i\Delta kz)$, we can

write

$$\begin{aligned} i\frac{\partial E_1}{\partial Z} + \frac{1}{2k_1}\frac{\partial^2 E_1}{\partial X^2} + \frac{\omega}{c}\Delta n_p(X)E_1 + \chi \hat{E}_2 E_1^* = 0, \\ i\frac{\partial \hat{E}_2}{\partial Z} + \frac{1}{2k_2}\frac{\partial^2 \hat{E}_2}{\partial X^2} + \frac{2\omega}{c}\Delta n_p(X)\hat{E}_2 + \Delta k \hat{E}_2 + \chi E_1^2 = 0. \end{aligned} \tag{3.47}$$

In case of large mismatch $\Delta k$, assuming SH adiabatically adapting to FF, i.e.

$$\Delta k >> \Delta n_p, |\partial_Z E_2|$$

, we can obtain from the second equation of (3.47),

$$\hat{E}_2 = -\frac{\chi}{\Delta k} E_1^2 \tag{3.48}$$

and the FF field can be obtained approximately by en effective cubic equation,

$$i\frac{\partial E_1}{\partial Z} + \frac{1}{2k_1}\frac{\partial^2 E_1}{\partial X^2} + k_0 \Delta n_p(X)E_1 + \chi_3 |E_1|^2 E_1 = 0 \tag{3.49}$$

where $\chi_3 = -\frac{\chi}{\Delta k}$.

Then our procedure consists in discretizing the system (3.39) and applying Newton iteration to it using as initial FF guess the cubic soliton and SH is calculated according to (3.48).

Since this assumption is valid under large mismatch, once we have obtained a doubly resonant solution, we span the $\Delta k$ range up to phase-matching and study how peak power and beam width are affected. Moreover we need to set carefully the position inside the first gap of FF, hence the whole cannot be spanned to look for solutions. We neglect instead the dispersion of linear index step: once a mismatch is fixed, we set accordingly both high and low indices of diffraction.

We are reporting several preliminary results, to outline the properties of this sort of solutions. The array is characterized by $\Delta_n^{FF,SH} = 0.008$, $\Lambda = 4\mu m$, $n_2 = 3.4$ (high index), and $\chi = 5\,10^{-4}$, to obtain at high mismatch, $\Delta k = -4 \times 10^3$, a value of $k_0 n_{2I} = \frac{\chi}{|\Delta k|} = 6.25 \times 10^{-11}$, similar to that used for Kerr effect in the previous case.

In figure 3.12, we compare for large phase-mismatch, quadratic solution and the starting guess (cubic solution obtained obtained by relaxation). Remind that the Kerr effective index is a function of mismatch itself. Results confirm our first approximation attempt, i.e. the cubic limit can be used at large mismatch, although as guess. In this case we kept a 50% duty cycle to prove that despite CMT does not predict them, inside the narrow second order gap, SH can tunnel in the nonlinear regime.

Then we show how a stronger conversion efficiency affect solutions: in figure 3.13 keeping the same parameters of the previous one, we set $\Delta k = -10$.

Since we realized that SH lying inside its second order gap permit to achieve solutions following this procedure, we have to study wider gaps, i.e. structures of duty cycle $\delta_c \neq 50\%$. A third example is then obtained by modifying gap widths, see figure 3.14, where duty cycle is increased to 70%.

Finally an important characterization is provided by the effect of phase-mismatch of beam peak and width values, see fig. 3.15. A predictable result is that as long as we approach phase

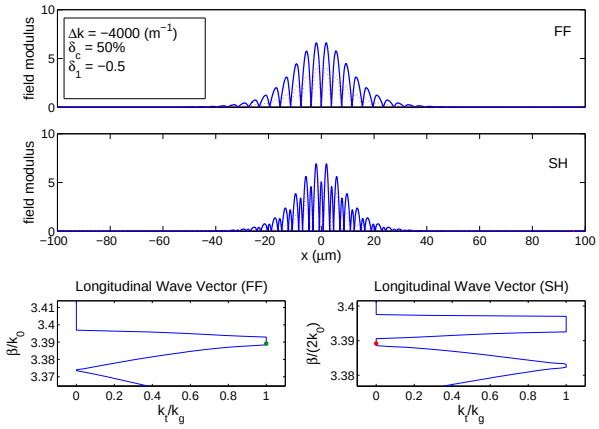


Figure 3.12: $\chi^{(2)}$ SGS. Top: fundamental, center: second harmonic, bottom: location of longitudinal wavevectors. Initial (cubic solution) guess (red dashed) compared with relaxed solution (blue solid). Once $\delta_1 = -0.5$ is set, the SH detuning inside its gap is fixed accordingly. The array parameters are, as above, $\Delta n = 0.008$, $\Lambda = 4\mu m$. In this case, duty cycle is $\delta_c = 50\%$ and phase-mismatch $\Delta k = -4000 m^{-1}$.

matching between FF and SH, a beam of lower total intensity is sufficient to sustain a trapped solution. The fact that peak SH intensity in physical units overcomes FF could be explained by the specific input parameters, indeed we have found that changing position inside gaps or duty cycle lead to a different behaviour: to realize that we report another case, see figure 3.16, that, despite only detuning in gap is modified, exhibits a crossing of FF with SH peak intensity and a nearly flat trend near zero mismatch. The energy intensity is in the latter case remarkably more concentrated. This allows us to conceive the opportunity to generate a trapped SGS injecting FF only, certainly more practical to apply in experiments.

## 3.4 A Remark on Applications

We mentioned in the beginning of this chapter that many technologies permit to fabricate worth-mentioning periodic systems. Moreover, many settings are possible: 2D waveguide arrays can be easily obtained in photorefractive materials, space-time trapping is possible in arrays of coupled resonators optical waveguides, see [9].

Beyond the interesting physics involved in these phenomena, several applications can be imagined, see [73]. Among them we mention low loss bends, AND gate, and all-optical routing. They exploit basically a matrix of waveguiding rods, on $xy$ plane aligned along the $z$ axis (propagation direction). Impressing a transverse motion it is possible to route soliton beam on a specific path and soliton-soliton interaction could permit to control the flow of light.

The application of our numerical tools to those phenomena would be quite interesting, but we focused more on classifying the possible regimes and their properties. The dynamical behaviour of a single soliton solution is quite rich, thus interactions also exhibit sophisticated

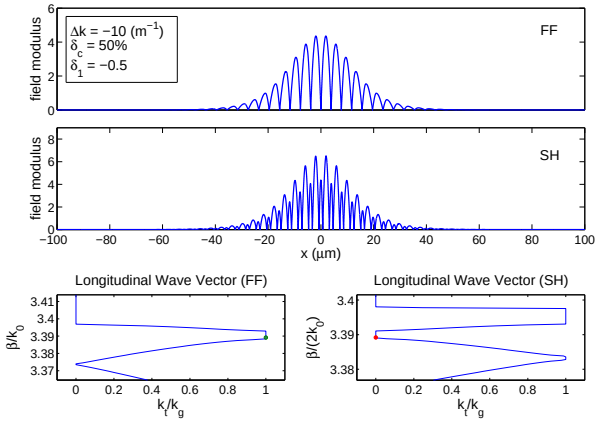


Figure 3.13: Same as fig. 3.12, but a smaller mismatch, $\Delta k = -10m^{-1}$. It can be obtained by continuous assumption, starting from an higher mismatch solution, hence only final solution is shown.

properties, but we find they are beyond the scope of this work.

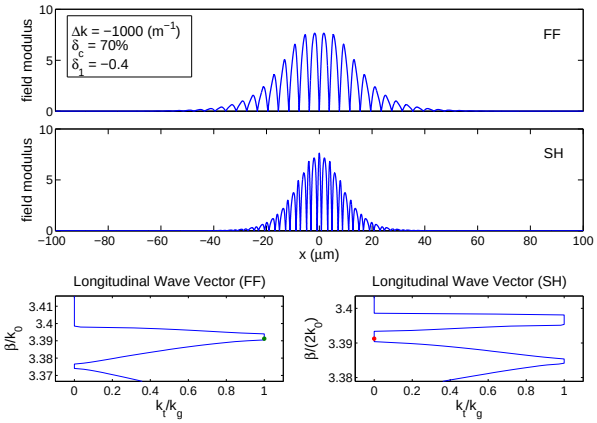


Figure 3.14: Same as fig. 3.12, but $\Delta k = -1000m^{-1}$, $\delta_c = 70\%$, detuning $\delta_1 = -0.4$. Indeed in order that SH wavenumber lies inside its associated gap, we have to set the FF detuning carefully.

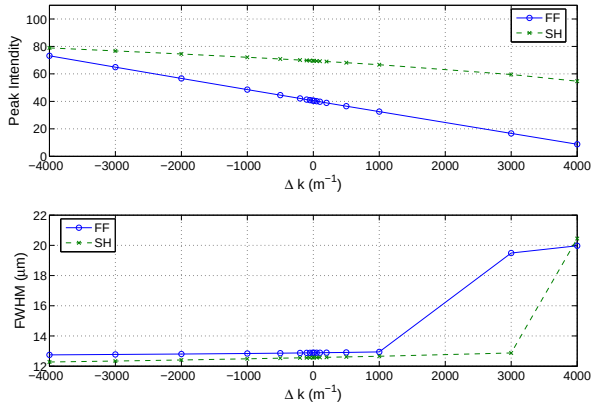


Figure 3.15: Peak intensity and FWHM of quadratic SGSs as a function of phase-mismatch $\Delta k$. The array parameters are the same of figures 3.12 and 3.13, except a different position inside FF gap, $\delta_1 = -0.4$.

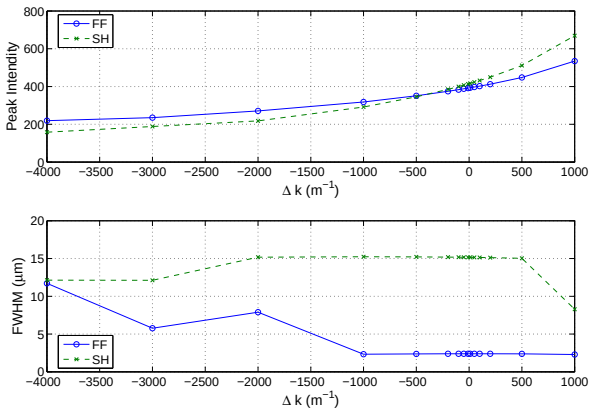


Figure 3.16: Same as figure 3.15, but $\delta_1 = -0.1$. Notice the crossing of FF and SH peak values and the almost flat trend around $\Delta k = 0$.

# Chapter 4

# Analysis of Cylindrical Micro-resonators based on the Aperiodic Fourier Modal Method

## 4.1 Introduction: Micro-resonators and Modelling

Micro-resonators are emerging as a class of very promising and versatile devices for next-generation integrated photonic circuits. Breakthroughs in different fabrication technologies have permitted noteworthy implementations such as microspheres, microdisks, microrings, microgears, microtori, micropillars, and photonic crystal defects, which have proved to be effective in several applications encompassing passive (filters, add&drops, static-delay lines), as well as active (modulators, lasers, switches, programmable delay lines) devices (see [6, 7, 86] for a survey on these technologies). They can play also a key role in cavity-quantum-electrodynamics [6], and nonlinear optics applications such as Raman lasers [87] and coupled resonator structures (e.g. CROWs [9]).

Specifically, cylindrical micro-resonators, such as microdisks, microrings, microgears, and microtori, permit to achieve very large quality factors $Q$ (as high as $Q \approx 10^6$ for silica microtori, [88]). Their modal structure is composed by the so-called whispering-gallery modes (WGMs), named after acoustics. They where discovered by Lord Rayleigh in the St. Paul cathedral in London. Inside its dome focal points can be found: words whispered in one of them can be heard in the others, despite the large distance. They arise from waves circulating in the proximity of a curved surface, bouncing, in a ray-propagation model, on round walls; this explains the losses and determines the intrinsic quality factor of the cavity: modes in resonant structures are intrinsically leaky. WGMs are usually denoted by two integer indices, $m$ and $l$. For example, in figure 4.1 we plot the TM solution of azimuthal order $m = 10$ and radial order $l = 1$ of a microdisk resonator, obtained by a 2D solver.

In our work, we devoted much effort to study this sort of devices, implementing a numerical method and characterizing several integrated optical circuits incorporating them. This chapter is consecrated to reporting an implementation of the aperiodic Fourier-modal method

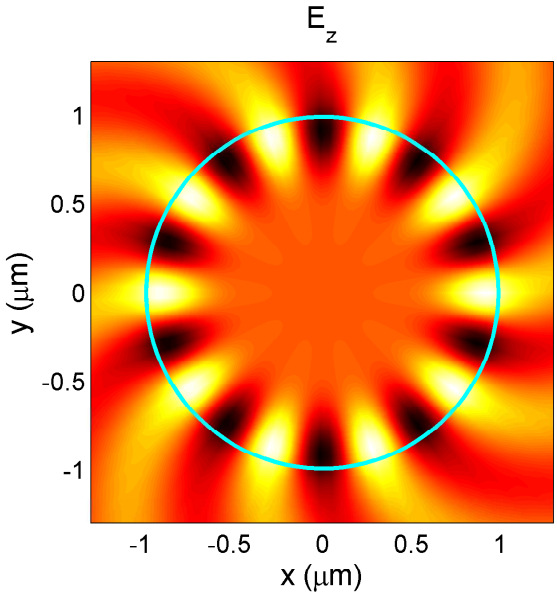


Figure 4.1: Example of WGM of a microdisk resonator: radius $r = 1\mu m$, composed longitudinally by a slab $0.240\mu m$ thick of $n_1 = 3.2$ surrounded by $n_2 = 1.5$. TM mode of azimuthal order $m = 10$, radial order $l = 1$.

in cylindrical coordinates. Our aim has been to develop a 3D description of microdisks and microrings, structures with axial symmetry which are more appealing for planar integration technologies used in integrated optics, e.g. silicon-on-insulator [89]. We are able to calculate resonant wavelengths and quality factors, and in principle we could apply it to every cavity of this symmetry.

Since they are usually multi-mode structures with several resonances, a proper analysis of their optical mode structure is fundamental. Usually, the hybrid character of modal fields results in a poor reliability of 2D-algorithms based upon effective index approximation [1], see [90] where a general discussion on modelling is provided. Though many 3D numerical approaches have been proposed such as finite elements (FEM), integral equations, finite differences (FDTD), and modal-decomposition-based algorithms (see [91] and references therein), the latter ones, despite being somehow dependent on geometry or symmetry properties, are generally faster and provide a clear insight on electromagnetic field distribution in the cavity.

A 3D modal method based on film-mode matching is already available, [92], as well as its application in the design of waveguide-resonator systems, [93], but those works are focused on structures of large radii and small index-step, and are prone to some limitations due to their specific modal approach. Indeed, the main issue with modal methods is the estimation

1. The well known approximation that assumes, in our case, the axial and radial dependence to be separable variables and uses a slab guided modes as longitudinal profile.

of mode-overlap integrals and a proper computation of the eigenvalues of leaky modes, whose a careful description should be accomplished in bounded structures (as those commonly examined by computational methods).

Here, our approach relies on an application of rigorous coupled-wave analysis (RCWA) to waveguiding structures, also known as A-FMM: it approximates modes by Fourier-series, which enables one to reduce the computation of overlap integrals to matrix manipulations.

In principle, such method could be applied also to different structures such as micropillar resonators. Indeed an implementation of a 3D-A-FFM to model micropillars has already been presented [94], based on 2D Fourier discretization on the transverse plane and propagation along the axis. In that case the mode confinement properties resemble those of the fundamental mode of an optical fibre and are less affected by artificial roughness than WGMs. Our algorithm is thus particularly suitable to analyse thin structures in which cylindrical symmetry has to be preserved, while pillars with many distributed Bragg reflector (DBR) layers would require a very large computational window, reducing the efficiency of the method.

The outline of the chapter is as follows. In section 4.2 we introduce our RCWA approach. In section 4.3 we recall the admittance matrix formalism to describe a multilayer device, while in section 4.4 we obtain the eigenvalue problem and solve it in order to obtain resonance wavelengths, $Q$ factors, and modal profiles. Finally we will report specific results in section 4.5, and draw conclusions.

## 4.2 RCWA and its Application in Cylindrical Coordinates

### 4.2.1 RCWA: a general overview

The RCWA approach is a time-harmonic method that originated in the framework of diffraction grating analysis [95], and was later extended to study also guided-wave problems [30]. In the spirit of this approach, a basis of Bloch modes of a virtually infinite periodic structure is used to compute the real modes propagating in an aperiodic one. This is equivalent to analyse an artificially periodic structure, but if this period is sufficiently large or suitable boundaries are applied, it provides a good approximation and has the main advantage of being conceptually and formally simple.

To outline its principles, we consider the solution of a 2D problem under TM polarization, which lead to many problems in the past. This was solved by Lalanne and Morris, see [96], and the mathematical justification was provided by Li, see [97].

The Cartesian equations for TM polarization $(H_y, E_x, E_z)$ in a $Oxz$ system, with $z$ the propagation direction are

$$\begin{aligned} -\frac{\partial E_z}{\partial x} + \frac{\partial E_z}{\partial x} &= -j\omega\mu H_y \\ \frac{\partial H_y}{\partial z} &= -j\omega\epsilon E_x \\ \frac{1}{\epsilon}\frac{\partial H_y}{\partial x} &= j\omega E_z \end{aligned} \tag{4.1}$$

We assume the electric permittivity to be a periodic function of period $\Lambda$ and we suppose to operate in a nonmagnetic medium. By Bloch theorem, the fields themselves are periodic of

the same period. Let us write them in Fourier series and retain a finite number of coefficients, i.e.

$$\epsilon_r = \sum_{m=-M}^{M} \epsilon_m \exp(jmKx)$$
$$H_y = -j\sqrt{\frac{\epsilon_0}{\mu_0}} \sum_{m=-M}^{M} U_m \exp(jmKx)$$
$$E_x = \sum_{m=-M}^{M} S_m \exp(jmKx)$$
$$E_z = \sum_{m=-M}^{M} f_m \exp(jmKx)$$

where $K = \frac{2\pi}{\Lambda}$.

After few algebra, we can obtain a wave equation ruling the generic Fourier coefficient of the magnetic field,

$$\frac{1}{k_0^2}\frac{\mathrm{d}^2 U_n}{\mathrm{d}z^2} = \sum_{m=-M}^{M} \epsilon_{n-m} \sum_{p=-M}^{M} \left[\frac{mK}{k_0}\left(\frac{1}{\epsilon}\right)_{m-p}\frac{pK}{k_0} - \delta_{mp}\right] U_p \tag{4.2}$$

that can be expressed in matrix form as

$$\frac{1}{k_0^2}\frac{\mathrm{d}^2 U}{\mathrm{d}z^2} = \left(EK_x\overline{E}K_x - I\right)U \tag{4.3}$$

where $E$ and $\overline{E}$ are the Toeplitz matrices composed by the Fourier coefficients of $\epsilon$ and its inverse, $K_x$ is the diagonal matrix of terms $nK/k_0$, and $I$ is the identity matrix; $U$ is the array of Fourier coefficients $U_n$, $n = -M, \ldots, M$.

While this approach suits fine to the dual, TE, problem (resulting even simpler), for TM it leads to a incomparable slower convergence. We recall that in TM modes, to ensure continuity of electric induction across interfaces, $E_x$ and $\epsilon$ have concurrent jumps, i.e. although they both are discontinuous, their product is continuous. The construction of the product coefficients as convolution of those of each factor implies the resulting Fourier series not to converge uniformly, then requiring a large number of coefficients. We have rather to introduce an *inverse rule*, that consists in using the inverse of the permittivity Toeplitz matrix whenever it is multiplied by an electric field concurrently jumping, e.g. instead of

$$\frac{\mathrm{d}U_n}{\mathrm{d}z} = k_0 \sum_{m=-M}^{M} (\epsilon)_{n-m} S_m \tag{4.4}$$

where the direct convolution (Laurent rule) is employed, we have to calculate

$$\frac{\mathrm{d}U_n}{\mathrm{d}z} = k_0 \sum_{m=-M}^{M} \left[\frac{1}{\epsilon}\right]^{-1}_{n,m} S_m \tag{4.5}$$

where $\left[\frac{1}{\epsilon}\right]^{-1}_{n,m}$ denotes the $(n,m)$ element of the inverse of the Toeplitz matrix of Fourier coefficients of $1/\epsilon$ [2]. Then equation (4.2) becomes

$$\frac{1}{k_0}\frac{\mathrm{d}^2 U_n}{\mathrm{d}z^2} = \sum_{m=-M}^{M}\left[\frac{1}{\epsilon}\right]^{-1}_{n,m}\sum_{p=-M}^{M}\left[\frac{mK}{k_0}\left[\epsilon\right]^{-1}_{m,p}\frac{pK}{k_0} - \delta_{mp}\right]U_p \tag{4.6}$$

or in matrix form

$$\frac{1}{k_0^2}\frac{\mathrm{d}^2 U}{\mathrm{d}z^2} = \left(\overline{E}^{-1}K_x E^{-1}K_x - I\right)U \tag{4.7}$$

and convergence is improved, despite still worse than in the TE case.

Finally we can write

$$\frac{1}{k_0^2}\frac{\mathrm{d}^2 U}{\mathrm{d}z^2} = AU$$

that implies

$$U_n = \sum_i v_{ni}\left[a_i \exp\left(-jk_0\beta_i z\right) + b_i \exp\left(jk_0\beta_i z\right)\right] \tag{4.8}$$

where $\beta_i$'s are the square root of eigenvalues of matrix $A$ and $v_{ni}$ the elements of its eigenvector matrix. To decide the eigenvalue sign, we have to guarantee a proper evaluation of evanescent waves, then $\mathrm{Im}\,\beta_i < 0$. We notice also that provided that media permittivity is real, eigenvalues of $A$ are real, hence only propagating (real $\beta$) or evanescent (imaginary $\beta$) modes are permitted. This outcome is modified by the use of artificial absorbing boundaries: they will be discussed in a successive section.

### 4.2.2 RCWA in cylindrical coordinates

Our work has been devoted to applying this approach in a cylindrical coordinate system $(r,\theta,z)$ and use RCWA to obtain optical modes along the $z$-axis [see fig. 4.2(a)]. By means of separation of variables, assuming periodic azimuthal dependence of the type $\exp(jm\theta)$, we investigate how modes (describing fields along $z$) depend on the radial coordinate $r$. Though we reduce to two variables, the vectorial nature of the problem requires to deal with the full six components of the field. Similarly to the full vectorial approach employed for optical fibres, we can deal with $E_z$ and $H_z$, while the other components can be reconstructed from them. Finally, as usual in any modal method, the structure under analysis is decomposed into a sequence of radially-uniform layers, see fig. 4.2(b). All sections are characterized by their own $z$-dependence of material parameters. This is equivalent to analysing radially homogeneous media with arbitrary distribution of materials along the $z$-axis in cylindrical symmetry. The modal behaviour is obtained by matching the fields across interfaces that are normal to $r$-axis.

We assume a harmonic time dependence of the fields, $\exp(j\omega t)$, where the frequency $\omega$ can be in general a complex quantity to account for damping (further discussion will be provided

2. The inverse a Toeplitz matrix does not enjoy this property, then $(n,m)$ position does not correspond to $(n-m)$ Fourier coefficient as before.

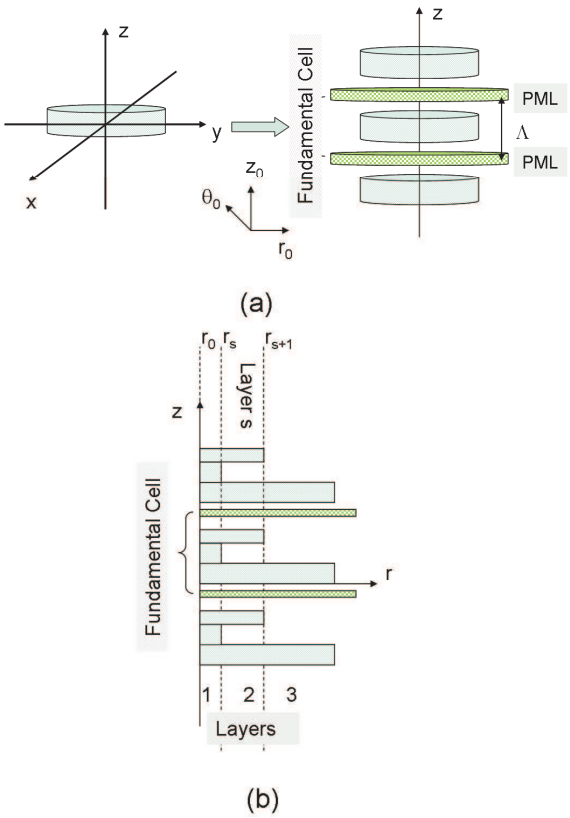


Figure 4.2: (a) Generic micro-resonator with $z-$axis cylindrical symmetry and its periodization on which the Fourier modal method relies; note that PMLs are also included in the periodic window $\Lambda$; (b) Sketch of the radial layer decomposition; $r_s$ denotes the radial position of the generic interface between homogeneous layers.

in a successive section) and decompose the relative dielectric permittivity $\epsilon_r$ and magnetic permeability $\mu_r$ according to (harmonic) Fourier series

$$\epsilon_r = \sum_n \epsilon_n e^{jnKz} \ , \ \mu_r = \sum_n \mu_n e^{jnKz}, \tag{4.9}$$

where $K = 2\pi/\Lambda$, $\Lambda$ being the period of the structure, equivalent to the computation window. In the following, we apply the method to the far most common case of non-magnetic media, (constant permeability $\mu_r \simeq 1$), though its extension to magnetic media can be easily implemented, and the method can be further generalized to deal with anisotropic materials. By truncating the summation of the Fourier expansion to order $M$ ($n = -M, \ldots, M$), and exploiting the Floquet-Bloch theorem, the fields can be expanded according to truncated

series of functions with the same period, namely

$$\begin{aligned}\vec{E} &= \sum_{n=-M}^{M} \left(S_r^n \mathbf{r}_0 + S_\theta^n \theta_0 + S_z^n \mathbf{z}_0\right) e^{jnKz} e^{jm\theta}, \\ \vec{H} &= -j\sqrt{\frac{\epsilon_0}{\mu_0}} \sum_{n=-M}^{M} \left(U_r^n \mathbf{r}_0 + U_\theta^n \theta_0 + U_z^n \mathbf{z}_0\right) e^{jnKz} e^{jm\theta},\end{aligned} \tag{4.10}$$

While $S_{r,\theta}$ and $U_{r,\theta}$ can be related through Maxwell equations to $U_z$ and $S_z$, the latter obey expressions that can be obtained from Helmholtz equations for full vector fields $\vec{E}$ and $\vec{H}$ [3]

$$\nabla^2 \vec{E} + k_0^2 \epsilon_r \vec{E} = -\nabla \left( \frac{\nabla \epsilon_r \cdot \vec{E}}{\epsilon_r} \right), \tag{4.11}$$

and

$$\nabla^2 \vec{H} + k_0^2 \epsilon_r \vec{H} = -j\omega\epsilon_0 \nabla \epsilon_r \times \vec{E}. \tag{4.12}$$

By projecting eq. (4.11) along the $z$-axis, we obtain

$$\nabla^2 E_z + k_0^2 \epsilon_r E_z = -\frac{\mathrm{d}}{\mathrm{d}z}\left(\frac{1}{\epsilon_r}\frac{\mathrm{d}\epsilon_r}{\mathrm{d}z} E_z\right) = -\frac{\mathrm{d}}{\mathrm{d}z}\left(\frac{1}{\epsilon_r}\frac{\mathrm{d}}{\mathrm{d}z}\left(\epsilon_r E_z\right)\right) + \frac{\mathrm{d}^2 E_z}{\mathrm{d}z^2}, \tag{4.13}$$

while from eq. (4.12), considering that, in each radial layer, $\epsilon_r$ is a function of $z$ only, we obtain

$$\nabla^2 H_z + k_0^2 \epsilon_r H_z = 0. \tag{4.14}$$

By inserting the expressions (4.10) in eqs. (4.13) and (4.14), we end up with equations obeyed by the generic Fourier coefficients $S_z^n$ and $U_z^n$ of $E_z$ and $H_z$, respectively [4]

$$\begin{aligned}&\frac{\mathrm{d}^2 S_z^n}{\mathrm{d}r^2} + \frac{1}{r}\frac{\mathrm{d}S_z^n}{\mathrm{d}r} - \frac{m^2}{r^2} S_z^n - nK \sum_p \left[\epsilon\right]_{n,p}^{-1} pK \sum_l \left[\frac{1}{\epsilon}\right]_{p,l}^{-1} S_z^l + k_0^2 \sum_p \left[\frac{1}{\epsilon}\right]_{n,p}^{-1} S_z^p = 0 \\ &\frac{\mathrm{d}^2 U_z^n}{\mathrm{d}r^2} + \frac{1}{r}\frac{\mathrm{d}U_z^n}{\mathrm{d}r} - \frac{m^2}{r^2} U_z^n - \left(nK\right)^2 U_z^n + k_0^2 \sum_p \epsilon_{n-p} U_z^p = 0\end{aligned} \tag{4.15}$$

where $\epsilon_{n-p}$ denotes the $n-p$ Fourier coefficient of $\epsilon_r$, or equivalently the $(n,p)$ element of a Toeplitz matrix, composed by those coefficients, from $-2M$ to $2M$, while $\left[\frac{1}{\epsilon}\right]_{n,p}^{-1}$ is used to identify the $(n,p)$ element of the inverse of the Toeplitz matrix formed by Fourier coefficients of $\frac{1}{\epsilon}$, according to inverse rule.

Thus, we have obtained two systems of Bessel equations that can be casted in the following compact vector form by introducing the vectors

$$S_z = \left[S_z^{-M} \dots S_z^{M}\right]^T$$

and

$$U_z = \left[U_z^{-M} \dots U_z^{M}\right]^T$$

3. We could obtain the same formulas, starting directly from Maxwell equation, but it is slightly cumbersome, specifically to decouple magnetic and electric field components.

4. Recall that $\nabla^2 = \frac{\partial^2}{\partial r^2} + \frac{1}{r^2}\frac{\partial^2}{\partial \theta^2} + \frac{\partial^2}{\partial z^2} + \frac{1}{r}\frac{\partial}{\partial r}$

$$\begin{aligned}
&\frac{\mathrm{d}^2 S_z}{\mathrm{d}r^2} + \frac{1}{r}\frac{\mathrm{d}S_z}{\mathrm{d}r} - \frac{m^2}{r^2} S_z + k_0^2 \overbrace{\left(\overline{E}^{-1} - K_z E^{-1} K_z \overline{E}^{-1}\right)}^{A} S_z = 0 \\
&\frac{\mathrm{d}^2 U_z}{\mathrm{d}r^2} + \frac{1}{r}\frac{\mathrm{d}U_z}{\mathrm{d}r} - \frac{m^2}{r^2} U_z + k_0^2 \underbrace{\left(E - K_z^2\right)}_{B} U_z = 0
\end{aligned} \tag{4.16}$$

where $K_z$ is a diagonal matrix with elements $(k_z)_{nn} = (n - M - 1)K/k_0$, while $E$ and $\overline{E}$ are the Toeplitz matrices obtained from the Fourier coefficients of $\epsilon_r$ and $1/\epsilon_r$.

The general solution of Eqs. (4.16) can be expressed as a superposition of Bessel functions $J_m$, and Hankel functions of the second kind $H_m^{(2)}$ as

$$S_z^n = \sum_i w_{ni} \left[ a_i J_m\left(k_0 \lambda_i^A r\right) + d_i H_m^{(2)}\left(k_0 \lambda_i^A r\right) \right] \tag{4.17}$$

$$U_z^n = \sum_i v_{ni} \left[ \alpha_i J_m\left(k_0 \lambda_i^B r\right) + \delta_i H_m^{(2)}\left(k_0 \lambda_i^B r\right) \right] \tag{4.18}$$

where $\lambda_i^{A,B}$ denote the square root of the $i$-th eigenvalue of matrix $A$ and $B$ respectively, and $w_{ni}, v_{ni}$ denote the elements of the corresponding eigenvector matrices $W$ and $V$, i.e. we can write

$$\begin{aligned}
A &= W^{-1} \operatorname{diag}\left[\left(\lambda_i^A\right)^2, i = -M, \ldots, M\right] W \\
B &= V^{-1} \operatorname{diag}\left[\left(\lambda_i^B\right)^2, i = -M, \ldots, M\right] V
\end{aligned}$$

**A remark** We remark that $H^{(2)}$ function is actually an outgoing wave in radial direction. In fact an asymptotic expression for large argument is, see [98],

$$H_m^{(2)}(z) \approx \sqrt{2/(\pi z)} \exp\left[-j\left(z - \frac{m}{2}\pi - \frac{1}{4}\pi\right)\right],$$

then in analogy with plane waves, we have forward/outgoing waves provided that ($\lambda_i$ is a radial propagation constant of $i$-th axial mode, taking into account that $k_0$ is complex),

$$\begin{aligned}
\operatorname{Re}\{\lambda_i\} &> 0 \\
\operatorname{Re}\{k_0 n_i\} &> 0 \\
\omega^R n_i^R - \omega^I n_i^I &> 0 \\
n_i^R &> \frac{n_i^I}{Q}
\end{aligned} \tag{4.19}$$

i.e. a mode cannot grow at a faster rate than that imposed by the quality factor. This condition is intended to guarantee that $H^{(2)}$ function is actually an outgoing wave in radial direction. We recall that Hankel functions do not enjoy the same nice properties as exponential function.

Importantly, in order to ensure that the supermodes of the periodic structure give a good description of the modes of the physical aperiodic structure, we need to introduce proper boundary conditions that allow to substantially decouple successive periodic repetitions (along $z$). Perfectly matched layers (PMLs) are best suited to this purpose.

### 4.2.3 Perfectly matched layers

We introduce PML in our scheme [see fig. 4.2] following the approach of [99], where a complex coordinate stretching of $z$-axis is implemented. We remark that PMLs applies in general as boundary conditions in the solution of elliptic partial differential equations, see [100]. In section 2.5 we described their implementation in finite difference BPM. Here, we are recalling how they are used in modal methods. Specifically RCWA, where a finite number of harmonic functions is used, no discontinuity is met passing from physical domain to PML. Nevertheless we have to carefully design PML, since other issues could appear.

Let us summarize the main features of PML and their implementation in cylindrical coordinates and modal methods:

1. PMLs can be implemented as anisotropic magnetic media or complex coordinate stretching;
2. it is proved in [101] that both implementations can be used in cylindrical coordinate systems, with some care in the anisotropic media design;
3. the opportunity to obtain an improved accuracy implementing a nonlinear complex coordinate stretching is shown in [99], with examples of applications in RCWA context.
4. using a coordinate stretching approach is equivalent to a slight change in the derivative operator, specifically a multiplication by a known function.
5. dealing with anisotropic layers needs to write more complicated equations, thus we exploit the results of [99].

We remark that, by applying separation of variables, the dependences on $r$ and $z$ are decoupled; hence the application of inverse rule and PMLs is not affected by the use of cylindrical coodinates, since they operate on the longitudinal axis only.

The complex coordinate stretching implementation consists in defining an analytic continuation of the field in the complex plane (to have only outgoing or evanescent waves at the boundary of the physical domain), then mapping the infinite complex plane into the real finite segment of computation. More specifically we integrate the wave equation on an infinite path in the complex plane mapped through a suitable transform into the real segment: no incoming interfering wave is thus allowed.

We solve the electromagnetic problem in the complex space $Z$, mapped on the real axis $z$ as follows

$$Z = F(z) \text{ such that } \begin{cases} z \to \Lambda/2 \Rightarrow Z \to \infty + j\infty \\ |z| \leq \Pi/2 \Rightarrow Z = z \\ z \to -\Lambda/2 \Rightarrow Z \to -\infty - j\infty \end{cases} \tag{4.20}$$

where $\Lambda$ is the width of the computational domain (i.e. the period of RCWA) and $\Pi$ is the width of the physical domain (i.e. $\Lambda$ without PML layers). It is worth noting that following [99] we do not use nor look for an optimal $F$ and that in practice we need only $\left(\frac{\mathrm{d}F}{\mathrm{d}z}\right)^{-1}$, since

$$\frac{\mathrm{d}}{\mathrm{d}Z} = \frac{\mathrm{d}z}{\mathrm{d}Z}\frac{\mathrm{d}}{\mathrm{d}z} = \left(\frac{\mathrm{d}F}{\mathrm{d}z}\right)^{-1}\frac{\mathrm{d}}{\mathrm{d}z} = f(z)f_{PML}(z)\frac{\mathrm{d}}{\mathrm{d}z} \tag{4.21}$$

where $f(z)$ is a continuous function (the mapping itself) and $f_{PML}(z)$ is a piecewise constant complex-valued function, that is equivalent to an anisotropic material contribution. In the RCWA framework the transform of eq. 4.20 requires to substitute $K_z$ with $F_z K_z$, being $F_z$ the Toeplitz matrix of the Fourier coefficients of $f(z)$ and following [99] we can drop the other function, since a nonlinear complex coordinate stretching is shown to be working well enough.

$F$ is chosen to have easy computable Fourier coefficients, particularly

$$f(z) \leftrightarrow f_n \text{ with}$$

$$\begin{aligned} f_n = \delta_n - \frac{q}{2\Lambda}(-1)^n \Big[ \Big(1+\frac{\gamma}{4}\Big) \operatorname{sinc}\Big(\frac{nq}{\Lambda}\Big) + \\ + \frac{1}{2}\operatorname{sinc}\Big(\frac{nq}{\Lambda}-1\Big) + \frac{1}{2}\operatorname{sinc}\Big(\frac{nq}{\Lambda}+1\Big) + \\ - \frac{\gamma}{8}\operatorname{sinc}\Big(\frac{nq}{\Lambda}-2\Big) - \frac{\gamma}{8}\operatorname{sinc}\Big(\frac{nq}{\Lambda}+2\Big)\Big] \end{aligned} \tag{4.22}$$

where $q = \Lambda - \Pi$ and $\gamma$ is a complex parameter characterizing the PML, that is almost equivalent to the imaginary part of the absorbing anisotropic media parameters.

That means a profile $f(z)$ like that of fig. 4.3.

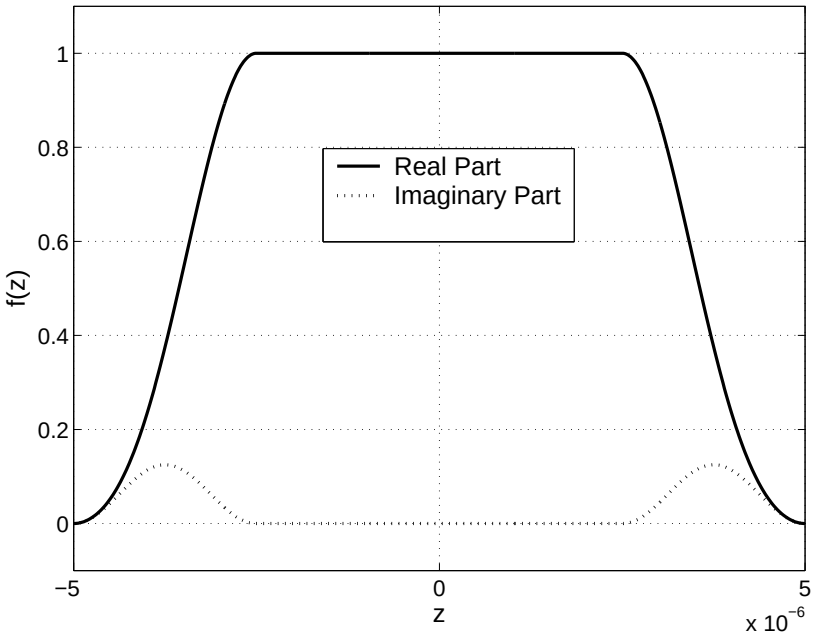


Figure 4.3: Function $f(z)$, that constitutes the PML as nonlinear complex coordinate stretching, $\Pi = \frac{2}{3}\Lambda$, $\gamma = \frac{1}{1+j}$.

We should notice that with respect to [99], we chose a $\gamma$ value with opposite imaginary part. This is due to the opposite sign rule for harmonic dependence. Since in our work we suppose that forward propagating waves are represented by $e^{-jkz}$, an outgoing wave toward $z \to \infty$ must decay as $e^{-j\beta z - \alpha z}$ and for $z \to -\infty$ as $e^{j\beta z + \alpha z}$. In transformed coordinates we deal with $e^{-j\beta Z}$ outgoing waves, thus in order to obtain an evanescent field in the physical

domain,

$$-j\beta = \frac{\mathrm{d}}{\mathrm{d}Z} = f(z)\frac{\mathrm{d}}{\mathrm{d}z} = f(z)(-j\beta - \alpha)$$

from which

$$\beta = f(z)(\beta - j\alpha)$$

and finally we can state that both real and imaginary part of the transformation must be positive, in order to obtain the correct sign of eigenvalues. Figure 4.3 shows this fact [compare with [99]].

This approach is analogous to digital filters design techniques that, via a bilinear transform, map the infinite frequency domain to the primary frequency period of the discrete-time response, avoiding aliasing and uncontrollable results of trivial substitution.

Compared to other modal methods that, if PML or complex frequency are used, face difficulties due to the computation of complex propagation constants, see [29], Fourier modal method is completely free from those issues, reducing them to a matrix eigenvalue problem.

## 4.3 Admittance Matrix Approach

The resonators that we are analysing here are composed by a sequence of radially-uniform layers, each completely described by its index profile and modal structure along $z$. The overall effect of such a combination could be accounted for by means of a single matrix, and different choices are possible [34]. The scattering matrix formulation provides better physical insights, but faces severe numerical problems due to the divergence of Hankel functions at the origin, which can cause imperfect summation of counter-propagating radial waves. Vice-versa the immittance (or admittance, and the equivalent impedance) matrix formalism has been proved to be a powerful numerical tool [92], and here we follow this approach, adapting it to the modal basis discussed in the previous section. The key point, in this case, is to characterize the radial dependence of the field going through the succession of radially uniform layers, imposing continuity at the interfaces, similarly to propagation problems in layered media (e.g., transfer matrix approach).

First, we define implicitly the immittance matrix $\mathbf{U}$ from the relation, see [92],

$$\frac{1}{k_0}\frac{\mathrm{d}\mathbf{p}}{\mathrm{d}r} = \mathbf{U}(r)\mathbf{p} \tag{4.23}$$

where $\mathbf{p}$ is the vector of modal weights as a function of radial direction, i.e. we can rewrite eq. (4.17) and eq. (4.18) in matrix form as

$$\begin{bmatrix} S_z \\ U_z \end{bmatrix} = \begin{bmatrix} W & 0 \\ 0 & V \end{bmatrix} \mathbf{p}(r) \tag{4.24}$$

Then denoting by the integer $s = 0, 1, \cdots, f$ the interfaces between radially homogeneous layers, moving in the radial outward direction ($r_0 = 0$ and $[r_s, r_{s+1}]$ stands for the generic

layer), we can express the general solution of the field expansions, in the form

$$\mathbf{p}(r)=\begin{bmatrix}\mathbf{p}_e(r)\\ \mathbf{p}_h(r)\end{bmatrix}=\begin{cases}\begin{bmatrix}J_0^e(r)a_0\\ J_0^h(r)\alpha_0\end{bmatrix}=J_0(r)A_0,\ r\in[0,r_1]\\ \begin{bmatrix}J_s^e(r)a_s+H_s^e(r)d_s\\ J_s^h(r)\alpha_s+H_s^h(r)\delta_s\end{bmatrix}=J_s(r)A_s+H_s(r)D_s,\ r\in[r_s,r_{s+1}]\\ \begin{bmatrix}H_f^e(r)d_f\\ H_f^h(r)\delta_f\end{bmatrix}=H_f(r)D_f,\ r\in[r_f,\infty\,[\end{cases}\tag{4.25}$$

where superscript $e$ and $h$ refer to the electric and magnetic part, respectively.

To explain the specific form of solutions in the innermost and outermost regions, we consider that, owing to physical consistency, along the symmetry axis of the cylindrical resonator, the field must be finite requiring the absence of Hankel function (only $J_m$ is permitted). Similarly, only outgoing waves are allowed in the outermost layers (no energy comes from infinity), and hence only Hankel ($H_m^{(2)}$) function is permitted.

Moreover, in order to contract the notation as much as possible, we have defined

$$\begin{aligned}&\mathcal{C}_s^e(r)=\mathcal{C}_m\left(k_0N_s^e r\right)\quad &&\overline{\mathcal{C}}_s^e(r)=\left.\frac{\mathrm{d}\mathcal{C}_m}{\mathrm{d}\xi}\right|_{\xi=k_0N_s^e r}\\ &\mathcal{C}_s^h(r)=\mathcal{C}_m\left(k_0N_s^h r\right)\quad &&\overline{\mathcal{C}}_s^h(r)=\left.\frac{\mathrm{d}\mathcal{C}_m}{\mathrm{d}\xi}\right|_{\xi=k_0N_s^h r}\\ &\mathcal{C}_s(r)=\mathcal{C}_m\left(k_0N_s r\right)\quad &&\overline{\mathcal{C}}_s(r)=\left.\frac{\mathrm{d}\mathcal{C}_m}{\mathrm{d}\xi}\right|_{\xi=k_0N_s r}\end{aligned}\tag{4.26}$$

where $\mathcal{C}$ and $\overline{\mathcal{C}}$ indicate a generic Bessel function (either $J_m$ or $H_m^{(2)}$) and its derivative, respectively, of argument $k_0r$ multiplied by a diagonal matrix $N_s^e$, $N_s^h$, or $N_s$ constructed with the set of modal eigenvalues of the electric part (superscript $e$), the magnetic part (superscript $h$), or both (i.e. $N_s=\mathrm{diag}\left\{\lambda_{-M}^A,\ldots,\lambda_M^A,\lambda_{-M}^B,\ldots,\lambda_M^B\right\}$).

We point out that eq. (4.25) together with eq. (4.24), constitute an alternative form of eqs. (4.17) and (4.18).

We are now reporting how immittance matrix transforms while propagating along $r$ and going through interfaces.

### 4.3.1 The propagation step

We start by dealing with the propagation step, i.e. how to compute immittance matrix at the right edge (superscript $R$) of a generic layer, given the one at the left edge (superscript $L$) of the same layer (or vice-versa, right to left). Let us express the derivatives of $\mathbf{p}$ as functions of modal weights at both edges, i.e.

$$\begin{aligned}\frac{1}{k_0}\frac{\mathrm{d}\mathbf{p}\left(r_{s+1}\right)}{\mathrm{d}r}&=\overline{J}_s\left(r_{s+1}\right)A_s+\overline{H}_s\left(r_{s+1}\right)D_s=\\ &=N_s\frac{\overline{J}_s\left(r_{s+1}\right)A_s+\overline{H}_s\left(r_{s+1}\right)D_s}{H_s\left(r_s\right)J_s\left(r_{s+1}\right)-J_s\left(r_s\right)H_s\left(r_{s+1}\right)}\left[H_s\left(r_s\right)J_s\left(r_{s+1}\right)-J_s\left(r_s\right)H_s\left(r_{s+1}\right)\right]=\\ &=\mathbf{G}_s\mathbf{p}\left(r_{s+1}\right)-\mathbf{H}_s\mathbf{p}\left(r_s\right)\end{aligned}\tag{4.27}$$

where we skipped some algebra (basically we sum and subtract a product of Bessel functions that permit to separate the contributions at the two layer ends.) The reciprocal relationship reads as

$$\frac{1}{k_0}\frac{\mathrm{d}\mathbf{p}\left(r_s\right)}{\mathrm{d}r} = \mathbf{E}_s\mathbf{p}\left(r_{s+1}\right) + \mathbf{F}_s\mathbf{p}\left(r_s\right). \tag{4.28}$$

We substitute definition of immittance matrices (4.23) in equations (4.27) and (4.28) and arrive at the following relations (see also [92])

$$\mathbf{U}_s^R = \mathbf{G}_s - \mathbf{H}_s \cdot \left[\mathbf{U}_s^L - \mathbf{F}_s\right]^{-1} \cdot \mathbf{E}_s, \tag{4.29}$$

and

$$\mathbf{U}_s^L = \mathbf{H}_s \cdot \left[\mathbf{G}_s - \mathbf{U}_s^R\right]^{-1} \cdot \mathbf{E}_s + \mathbf{F}_s, \tag{4.30}$$

where, once again, $R$ and $L$ denote the radial positions $r_{s+1}^-$ and $r_s^+$ of successive interfaces, respectively. Furthermore we have posed

$$\begin{aligned}
\mathbf{E}_s &= N_s\left[H\left(r_s\right)\overline{J}\left(r_s\right) - \overline{H}\left(r_s\right)J\left(r_s\right)\right]\cdot\mathbf{X}_s^{-1},\\
\mathbf{F}_s &= N_s\left[\overline{H}\left(r_s\right)J\left(r_{s+1}\right) - H\left(r_{s+1}\right)\overline{J}\left(r_s\right)\right]\cdot\mathbf{X}_s^{-1},\\
\mathbf{G}_s &= N_s\left[H\left(r_s\right)\overline{J}\left(r_{s+1}\right) - \overline{H}\left(r_{s+1}\right)J\left(r_s\right)\right]\cdot\mathbf{X}_s^{-1},\\
\mathbf{H}_s &= N_s\left[H\left(r_{s+1}\right)\overline{J}\left(r_{s+1}\right) - \overline{H}\left(r_{s+1}\right)J\left(r_{s+1}\right)\right]\cdot\mathbf{X}_s^{-1},
\end{aligned} \tag{4.31}$$

where

$$\mathbf{X}_s = H\left(r_s\right)J\left(r_{s+1}\right) - H\left(r_{s+1}\right)J\left(r_s\right). \tag{4.32}$$

### 4.3.2 Continuity at interfaces

Next step is to write how the immitance matrix transforms when it goes through an interface. In this case, continuity of tangential fields requires the field components $E_z$, $H_z$, $E_\theta$, and $H_\theta$ to be continuous across dielectric discontinuities (interfaces).

From Maxwell equations, we can derive the unknown components and obtain for $E_\theta$ and $H_\theta$,

$$\epsilon_r\frac{\partial}{\partial z}\left(\frac{1}{\epsilon_r}\frac{\partial H_\theta}{\partial z}\right) + k_0^2\epsilon_r H_\theta = \frac{1}{r}\left(\epsilon_r\frac{\partial}{\partial z}\left(\frac{1}{\epsilon_r}\frac{\partial H_z}{\partial\theta}\right)\right) - j\omega\epsilon_0\epsilon_r\frac{\partial E_z}{\partial r} \tag{4.33}$$

By duality and considering that the medium is nonmagnetic, we have

$$\frac{\partial^2 E_\theta}{\partial^2 z} + k_0^2\epsilon_r E_\theta = \frac{1}{r}\frac{\partial^2 E_z}{\partial z\partial\theta} + j\omega\mu_0\frac{\partial H_z}{\partial r} \tag{4.34}$$

In an analogous way we can derive $E_r$ and $H_r$,

$$\epsilon_r\frac{\partial}{\partial z}\left(\frac{1}{\epsilon_r}\frac{\partial H_r}{\partial z}\right) + k_0^2\epsilon_r H_r = \epsilon_r\frac{\partial}{\partial z}\left(\frac{1}{\epsilon_r}\frac{\partial H_z}{\partial r}\right) + \frac{j\omega\epsilon_0\epsilon_r}{r}\frac{\partial E_z}{\partial\theta} \tag{4.35}$$

$$\frac{\partial^2 E_r}{\partial^2 z} + k_0^2\epsilon_r E_r = \frac{\partial^2 E_z}{\partial r\partial z} - \frac{j\omega\mu_0}{r}\frac{\partial H_z}{\partial\theta} \tag{4.36}$$

We write vectors of Fourier coefficients of azimuthal components ($E_\theta$, $H_\theta$) according to the same rules we stated above as

$$CU_\theta = -\frac{m}{rk_0}EK_z\overline{E}U_z + \frac{1}{k_0}\overline{E}^{-1}\frac{\mathrm{d}S_z}{\mathrm{d}r} = EK_r\overline{E}U_z + \frac{1}{k_0}\overline{E}^{-1}\frac{\mathrm{d}S_z}{\mathrm{d}r} \tag{4.37}$$

$$BS_\theta = -\frac{m}{rk_0}K_zS_z + \frac{1}{k_0}\frac{\mathrm{d}U_z}{\mathrm{d}r} = K_rS_z + \frac{1}{k_0}\frac{\mathrm{d}U_z}{\mathrm{d}r} \tag{4.38}$$

where $C = \left(-EK_z\overline{E}K_z + E\right)$ and $B = \left(-K_z^2 + E\right)$ (as before), and $K_r = -\frac{m}{rk_0}K_z$.

Continuity relations for Fourier coefficients read as

$$W_s\mathbf{p}_\mathbf{e}^-\left(r_{s+1}\right) = W_{s+1}\mathbf{p}_\mathbf{e}^+\left(r_{s+1}\right), \tag{4.39}$$

$$V_s\mathbf{p}_\mathbf{h}^-\left(r_{s+1}\right) = V_{s+1}\mathbf{p}_\mathbf{h}^+\left(r_{s+1}\right), \tag{4.40}$$

$$\begin{aligned} B_s^{-1}\left[K_r^{s+1}W_s\mathbf{p}_e^-\left(r_{s+1}\right) + V_s\overline{\mathbf{p}_h^-}\left(r_{s+1}\right)\right] = \\ B_{s+1}^{-1}\left[K_r^{s+1}W_{s+1}\mathbf{p}_e^+\left(r_{s+1}\right) + V_{s+1}\overline{\mathbf{p}_h^+}\left(r_{s+1}\right)\right], \end{aligned} \tag{4.41}$$

$$\begin{aligned} C_s^{-1}\left[E_sK_r^{s+1}\overline{E}_sV_s\mathbf{p}_h^-\left(r_{s+1}\right) + \overline{E_s}^{-1}W_s\overline{\mathbf{p}_e^-}\left(r_{s+1}\right)\right] = \\ = C_{s+1}^{-1}\left[E_{s+1}K_r^{s+1}\overline{E}_{s+1}V_{s+1}\mathbf{p}_h^+\left(r_{s+1}\right) + \overline{E}_{s+1}^{-1}W_{s+1}\overline{\mathbf{p}_e^+}\left(r_{s+1}\right)\right], \end{aligned} \tag{4.42}$$

where for the sake of brevity we have indicated $\frac{1}{k_0}\frac{\mathrm{d}\mathbf{p}}{\mathrm{d}r} = \overline{\mathbf{p}}$. After inverting (4.39)–(4.42), and substituting the definition (4.23),

$$\begin{aligned} \begin{bmatrix}\overline{\mathbf{p}_\mathbf{e}^+}\\ \overline{\mathbf{p}_\mathbf{h}^+}\end{bmatrix} &= \begin{bmatrix}W_{s+1}^{-1}\overline{E}_{s+1}C_{s+1}C_s^{-1}E_sK_r^{s+1}\overline{E}_sV_s\mathbf{p}_h^-\\ V_{s+1}^{-1}B_{s+1}B_s^{-1}K_r^{s+1}W_s\mathbf{p}_e^-\end{bmatrix} + \\ &+ \begin{bmatrix}W_{s+1}^{-1}\overline{E}_{s+1}C_{s+1}C_s^{-1}\overline{E}_s^{-1}W_s\left[U_{ee}^-\mathbf{p}_\mathbf{e}^- + U_{eh}^-\mathbf{p}_\mathbf{h}^-\right]\\ V_{s+1}^{-1}B_{s+1}B_s^{-1}V_s\left[U_{he}^-\mathbf{p}_\mathbf{e}^- + U_{hh}^-\mathbf{p}_\mathbf{h}^-\right]\end{bmatrix} - \begin{bmatrix}W_{s+1}^{-1}K_r^{s+1}\overline{E}_{s+1}V_{s+1}\mathbf{p}_\mathbf{h}^+\\ V_{s+1}^{-1}K_r^{s+1}W_{s+1}\mathbf{p}_\mathbf{e}^+\end{bmatrix} = \\ &= \begin{bmatrix}W_{s+1}^{-1}\overline{E}_{s+1}C_{s+1}C_s^{-1}\overline{E}_s^{-1}W_sU_{ee}^- & W_{s+1}^{-1}\overline{E}_{s+1}C_{s+1}C_s^{-1}\overline{E}_s^{-1}W_sU_{eh}^-\\ V_{s+1}^{-1}B_{s+1}B_s^{-1}V_sU_{he}^- & V_{s+1}^{-1}B_{s+1}B_s^{-1}V_sU_{hh}^-\end{bmatrix}\times \\ &\times \begin{bmatrix}W_s^{-1}W_{s+1} & 0\\ 0 & V_s^{-1}V_{s+1}\end{bmatrix}\begin{bmatrix}\mathbf{p}_e^+\\ \mathbf{p}_h^+\end{bmatrix} + \\ &+ \begin{bmatrix}\left[W_{s+1}^{-1}\overline{E}_{s+1}C_{s+1}C_s^{-1}E_sK_r^{s+1}\overline{E}_sV_{s+1} - W_{s+1}^{-1}K_r^{s+1}\overline{E}_{s+1}V_{s+1}\right]\mathbf{p}_h^+\\ \left[V_{s+1}^{-1}B_{s+1}B_s^{-1}K_r^{s+1}W_{s+1} - V_{s+1}^{-1}K_r^{s+1}W_{s+1}\right]\mathbf{p}_e^+\end{bmatrix} \end{aligned} \tag{4.43}$$

Now, exploiting definition again, we can write the final expression as

$$\begin{aligned} \mathbf{U}_{s+1}^+ = \begin{bmatrix}\mathbf{U}_{ee}^+ & \mathbf{U}_{eh}^+\\ \mathbf{U}_{he}^+ & \mathbf{U}_{hh}^+\end{bmatrix} = \\ = \begin{bmatrix}W_{s+1}^{-1}\overline{E}_{s+1}C_{s+1}C_s^{-1}\overline{E}_s^{-1}W_s & 0\\ 0 & V_{s+1}^{-1}B_{s+1}B_s^{-1}V_s\end{bmatrix}\overbrace{\begin{bmatrix}\mathbf{U}_{ee}^- & \mathbf{U}_{eh}^-\\ \mathbf{U}_{he}^- & \mathbf{U}_{hh}^-\end{bmatrix}}^{\mathbf{U}_{s+1}^-}\begin{bmatrix}W_s^{-1}W_{s+1} & 0\\ 0 & V_s^{-1}V_{s+1}\end{bmatrix} \\ + \begin{bmatrix}0 & W_{s+1}^{-1}\overline{E}_{s+1}C_{s+1}C_s^{-1}E_sK_r^{s+1}\overline{E}_sV_{s+1}\\ V_{s+1}^{-1}B_{s+1}B_s^{-1}K_r^{s+1}W_{s+1} & 0\end{bmatrix} + \\ - \begin{bmatrix}0 & W_{s+1}^{-1}K_r^{s+1}\overline{E}_{s+1}V_{s+1}\\ V_{s+1}^{-1}K_r^{s+1}W_{s+1} & 0\end{bmatrix}, \end{aligned} \tag{4.44}$$

where $+ \mapsto r_{s+1}^+$ and $- \mapsto r_{s+1}^-$ denote the right and left edge of an interface, respectively.

Interchanging subscripts $s$ and $s+1$ as well as superscripts $+$ and $-$ allows us to express the reverse transformations going inwardly (from $+$ to $-$ edge of a generic interface). We have expressed immittance matrices as two-by-two block-matrices, that relate electric, magnetic and electro-magnetic weights at each interface, because the use of inverse rule of the FMM results in different expressions of coupling coefficients.

A chain rule that allows us to transform the immitance matrix going through the succession of radially homogeneous layers and discontinuities is provided by Equation (4.44) and eq. (4.29) [or equivalent eq. (4.30)]. This constitutes the basis of the method that allows us to compute resonances and relative field profiles, as explained in the next section.

## 4.4 The Homogeneous Problem and its Solution

As usual in guided wave theory, the resonance frequencies (free oscillations) of a resonator can be obtained from the solution of a proper eigenvalue problem, usually expressed as a homogeneous system of linear equations, that depends on eigenvalue in a nonlinear fashion. Knowing the location of resonances could simplify their identification during experimental characterization. Here we discuss how to obtain the homogeneous problem for micro-resonators. In principle, being WGMs intrinsically lossy, two different choices can be made: (i) to compute the complex resonant frequency of modes for a fixed azimuthal order $m$; (ii) to compute a complex azimuthal propagation constant at any fixed physical (real) wavelength.

The first gives rise to issues on normalization (in fact a complex oscillation implies unbounded fields at $r \to \infty$), that one has to face if the model is applied to the analysis of interaction between different systems using, for example, coupled-mode theory: a possible solution is discussed in [102]. Vice-versa, when employing a complex azimuthal wave-number [case (ii)], a special attention should be paid when dealing with Bessel functions of complex order, since they can face several numerical issues, as discussed in detail in [92].

Nevertheless we opt for the approach (i) which lends itself to a more physically transparent picture, since resonant wavelengths are readily obtained. In this spirit, for damped oscillations, we can calculate the quality factor (see e.g. [103, p. 311]) from the complex resonant frequencies $\omega_c \in \mathbb{C}$, as follows

$$Q = \frac{\mathrm{Re}\{\omega_c\}}{2\,\mathrm{Im}\{\omega_c\}}, \tag{4.45}$$

or equivalently from the complex resonant wavelengths, as

$$Q = -\frac{\mathrm{Re}\{\lambda_c\}}{2\,\mathrm{Im}\{\lambda_c\}}. \tag{4.46}$$

The starting point to obtain the homogeneous problem is to consider that physical consistence, introduced by eq. (4.25), implies a simple form for immittance matrices at both radial extrema, that read as

$$\mathbf{U}_1 = \mathbf{U}(r_1) = \frac{N_0 \overline{J}_m(k_0 N_0 r_1)}{J_m(k_0 N_0 r_1)}, \tag{4.47}$$

at the innermost interface and

$$\mathbf{U}_f = \mathbf{U}(r_f) = \frac{N_f \overline{H}_m^{(2)}(k_0 N_f r_f)}{H_m^{(2)}(k_0 N_f r_f)}, \tag{4.48}$$

at the outermost one.

Then we choose an interface where the eigenmode field is expected to be strong, say $s'$, and starting from $\mathbf{U}_1$ we iterate through the sequence of interfaces, by applying iteratively eq. (4.44) (interfaces), and eq. (4.29) (homogeneous layer propagation), in order to obtain $\mathbf{U}_{s'}^{L-}$. In the same way (using (4.30) for propagation), we compute $\mathbf{U}_{s'}^{L+}$, propagating inward from $\mathbf{U}_f$.

Finally, by imposing that these two matrices match, we end up with the homogeneous problem, whose solutions correspond to WGMs

$$\left(\mathbf{U}_{s'}^{L-} - \mathbf{U}_{s'}^{L+}\right) \mathbf{p}\left(r_{s+1}^{-}\right) = 0. \tag{4.49}$$

Non-trivial solutions of eq. (4.49) give resonant wavelengths (as complex zeros of matrix determinant), as well as modal weights $\mathbf{p}$. However, solving this sort of problem is not straightforward, since we deal with full matrices and complex zeros of a nonlinear function. In spite of the fact that the matrix dimension is not very large, the computation of the determinant can lead to numerical divergence and/or loss of accuracy. Many alternative methods were proposed and discussed, see [32, 104–107], that exploit basically matrix manipulations or some complex calculus. Among linear algebra tools, singular value decomposition (SVD) is known to be generally implemented as a very robust routine. Therefore, we have chosen to implement singular value (SV) minimization (as described in detail in [104] and outlined below), which, though being a bit computational demanding, turns out to be the most reliable method among those described in the literature.

By denoting the $n$-by-$n$ matrix of the homogeneous system (4.49) as $A \equiv \left(\mathbf{U}_{s'}^{L-} - \mathbf{U}_{s'}^{L+}\right)$, we can find non-trivial solutions by searching for values of $\lambda$ that makes the minimum singular value of $A$ to be zero. Let us denote the map

$$\lambda \to f(\lambda) = \min_k \sigma_k(A); \quad k = 1, ..., n \tag{4.50}$$

where $\{\sigma_k\}_k$ is the set of singular values of $A = A(\lambda)$ (which can be proven to be non-negative real numbers), and $f$ is a function that maps the complex plane $\mathbb{C}$ into its semi-axis $\mathbb{R}^+$. Then the solution $\lambda = \lambda_c$ of the homogeneous problem can be written as

$$\lambda_c = \arg \min_{\lambda \in \mathbb{C}, \mathrm{Re}\{\lambda\} > 0, \mathrm{Im}\{\lambda\} < 0} f. \tag{4.51}$$

Thus, we have reduced the calculations of resonances and modes to solve a minimization problem. Compared with [104], we do not look for a minimum point in a line segment, but in a plane, using a Nelder-Mead minimization routine [108].

Modal weights result as the right singular vector corresponding to the last computed $f$.

Then from eqs. (4.27) and (4.28), and continuity conditions of field $z$ components, we can calculate modal weight in every point, e.g.

$$\mathbf{p}\left(r_s\right) = \left[\mathbf{U}_s^L - \mathbf{F}_s\right]^{-1} \mathbf{E}_s \mathbf{p}\left(r_{s+1}\right) \tag{4.52}$$

and

$$\mathbf{p}\left(r_s^-\right) = \begin{bmatrix} W_{s+1}^{-1} W_s & 0 \\ 0 & V_{s+1}^{-1} V_s \end{bmatrix} \mathbf{p}\left(r_s^+\right) \tag{4.53}$$

Finally, after having computed $\mathbf{p}$ vectors in two separate points, specifically at two layer edges the coefficients of Bessel-Hankel functions can be readily computed, using the same notation of eq. (4.25) we write

$$\begin{aligned} A_s &= \left[H_s\left(r_s\right)\mathbf{p}\left(r_{s+1}\right) - H_s\left(r_{s+1}\right)\mathbf{p}\left(r_s\right)\right] \cdot \mathbf{X_s}^{-1} \\ D_s &= \left[J_s\left(r_s\right)\mathbf{p}\left(r_{s+1}\right) - J_s\left(r_{s+1}\right)\mathbf{p}\left(r_s\right)\right] \cdot \mathbf{X_s}^{-1} \end{aligned} \tag{4.54}$$

## 4.5 Results and Discussion

### 4.5.1 Two basic examples: microring and microdisk

We can now discuss reliability and performance of our method, by focusing specifically on rings or disks with small radii which guarantee high planar integrability in photonic chips. We test our results by comparing them with those obtained by means of *ab-initio* time domain simulations of discretized Maxwell equations, using our own implemented 3D-FDTD [20]. To clarify the crucial role of the vectorial nature of modes, we compare the results also with those obtained by means of a 2D algorithm based on the effective index approximation of axial modes [102]. In particular we consider two typical examples. The first one is a microring, with internal and external radii $1\mu m$ and $1.2\mu m$ respectively, $0.300\mu m$ thick, composed by Silicon ($n_r = 3.48$) immersed in Silica ($n_s = 1.44$). The second one consists of a microdisk, $0.77\mu m$ in radius, composed by a material of refractive index $n_d = 3.2$, completely surrounded by a material of index $n_s = 1.5$, corresponding to insulator-passivated semiconductor. The disk thickness is $t = 0.240\mu m$. In figure 4.4 we show these structures.

For both devices, we compute complex resonant wavelengths of a set of overall modes with increasing azimuthal index $m$, for both quasi-TE and -TM polarisations. The results are summarized in tables (4.1) and (4.2) for the microring, and tables (4.3) and (4.4) for the microdisk, respectively. The implemented modal method is used with a period (or equivalently a computational window) of $6\mu m$ and truncation order $M \simeq 100$ at which we reach convergence (see fig. 4.6). Conversely FDTD is employed in the case of the ring with a discretized cell $\Delta x = \Delta y = \Delta z = 25nm$, a box of $60 \times 60 \times 28$-cells with a boundary of 8 cells, and $\Delta t = 2.4073 \times 10^{-17} s$ with 90000 steps, whereas in the case of the disk $\Delta x = \Delta y = \Delta z = 20.6nm$, a box of $97 \times 97 \times 97$-cells with a boundary of 8 cells for the disk, and $\Delta t = 1.985 \times 10^{-17} s$ with 90000 steps. The quality factor from the FDTD time-series is computed by means of the Harminv code [109, 110].

By looking at the tables, and comparing values obtained by means of the three approaches, we notice that the results of our 3D vectorial method show a satisfactory agreement with the 3D-FDTD, whereas the results obtained by means of the 2D approach exhibit larger discrepancies, thus allowing us to conclude that a 2D approach is not reliable in terms of predicting correct values of the resonances. It is worth pointing out that the computation of quality factors starting from FDTD time-series is sometimes sensitive to simulation parameters, and a

| **m** | 11 | 12 | 13 | 14 | 15 |
|---|---|---|---|---|---|
| **3D-FDTD** | | | | | |
| $\lambda$ | 1.2277 | 1.1767 | 1.1312 | 1.0900 | 1.0537 |
| Q | 142 | 371 | 1081 | 2224 | 6224 |
| **C-RCWA** | | | | | |
| $\lambda$ | 1.2193 | 1.1820 | 1.1037 | 1.0948 | 1.0606 |
| Q | 170 | 400 | 1518 | 2694 | 5297 |
| **2D** | | | | | |
| $\lambda$ | 1.2749 | 1.2124 | 1.1587 | 1.1115 | 1.0692 |
| Q | 87 | 216 | 586 | 1717 | 5355 |

**Table 4.1: Resonant wavelength and quality factor of quasi-TE modes with azimuthal order $m$ of a microring resonator. The results from the 3D full vectorial algorithm (C-RCWA) are compared with a 3D-FDTD model and a simple EIM-based 2D approach.**

| **m** | 11 | 12 | 13 | 14 | 15 |
|---|---|---|---|---|---|
| **3D-FDTD** | | | | | |
| $\lambda$ | 1.3344 | 1.2769 | 1.2248 | 1.1770 | 1.1313 |
| Q | 657 | 1916 | 4303 | 11369 | 12109 |
| **C-RCWA** | | | | | |
| $\lambda$ | 1.3899 | 1.2700 | 1.2512 | 1.1697 | 1.1372 |
| Q | 721 | 1814 | 5226 | 7632 | 9042 |
| **2D** | | | | | |
| $\lambda$ | 1.3928 | 1.3242 | 1.2628 | 1.2073 | 1.1566 |
| Q | 317 | 859 | 2470 | 7429 | 23064 |

**Table 4.2: As in Table 4.1 for quasi-TM modes of a microring resonator.**

| **m** | 5 | 6 | 7 | 8 | 9 | 10 |
|---|---|---|---|---|---|---|
| **3D-FDTD** | | | | | | |
| $\lambda$ | 1.5760 | 1.4036 | 1.2685 | 1.1592 | 1.0690 | 0.9924 |
| Q | 19 | 40 | 86 | 194 | 438 | 1036 |
| **C-RCWA** | | | | | | |
| $\lambda$ | 1.5735 | 1.4019 | 1.2655 | 1.1583 | 1.0694 | 0.9938 |
| Q | 16 | 34 | 82 | 175 | 350 | 828 |
| **2D** | | | | | | |
| $\lambda$ | 1.6290 | 1.4425 | 1.2961 | 1.1788 | 1.0830 | 1.0031 |
| Q | 8 | 16 | 33 | 69 | 150 | 336 |

**Table 4.3: As in Table 4.1 for quasi-TE modes of a microdisk resonator.**

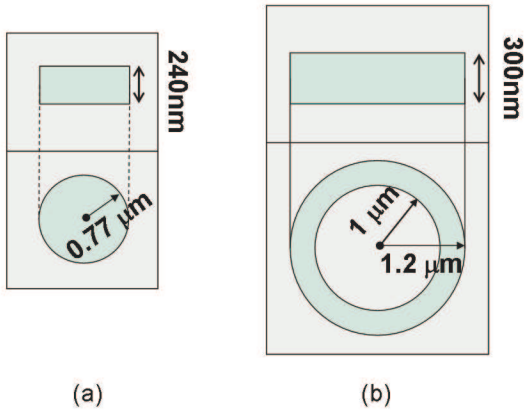


Figure 4.4: Schematic representation of the simulated structures, (a) microdisk and (b) microring.

fine tuning of the proposed algorithm is needed, particularly concerning PML settings. While in the FDTD method, the PML can show unattended reflection due to the spatial discretization, in modal methods, the PMLs affect the electromagnetic eigenvalue map and the modal profiles. Thus a special care must be taken to avoid artefacts. In particular, as discussed in [111], infinite PML absorption corresponds to replacing radiative modes with leaky modes, that diverge at an open infinite boundary. Moreover they do not describe rigorously every kind of guided propagation phenomenon. Similarly, in our case, strong PMLs give rise to high peaks inside the PML layer, and a noticeable bending of modal eigenvalues away from the imaginary axis. Following the approach of [99], and using the same notation as above, i.e. denoting as $\Pi$ the portion of fundamental cell $\Lambda$ that corresponds to the physical domain, and $\gamma$ the absorption figure, we find that it is convenient not to exceed $\gamma = \frac{2}{1+j}$, and to set $0.3 < \frac{\Pi}{\Lambda} < 0.7$, in order not to have an extremely strong absorbing effect, [111]. Furthermore, in our implementation, we have not usually performed any piecewise mapping [$f_{PML} = 1$ in the notation of [99] and of eq. (4.21)].

To this end, we report several eigenvalue maps, that show the effect of using a complex frequency or including PMLs; they refer to a slab with longitudinal profile equal to that of microdisk.

We notice that the use of a complex $k_0$ [figures 4.5(b) and 4.5(d)] implies that eigenvalues are not any more concentrated along real or imaginary axis. The effect of PMLs, in both cases [figs. 4.5(c) and 4.5(d)] leads to a stretching, depending on the Fourier series truncation, of the "eigenvalue line" away from its "normal" position. Whereas, passing from real to complex wavelength, without PML [figures 4.5(a) and 4.5(b)] we can observe that eigenvalues keep staying on the same line, while with PMLs, as $M$ grows larger, the distribution of eigenvalues plunges into the complex plane. If PMLs are used, it is harder to distinguish eigenvalues

| **m** | 6 | 7 | 8 | 9 | 10 | 11 |
|---|---|---|---|---|---|---|
| **3D-FDTD** | | | | | | |
| $\lambda$ | 1.3113 | 1.2081 | 1.1179 | 1.0471 | 0.9759 | 0.9183 |
| Q | 24 | 52 | 111 | 251 | 568 | 1524 |
| **C-RCWA** | | | | | | |
| $\lambda$ | 1.3079 | 1.2045 | 1.1122 | 1.0358 | 0.9706 | 0.9132 |
| Q | 25 | 52 | 105 | 215 | 536 | 1254 |
| **2D** | | | | | | |
| $\lambda$ | 1.3398 | 1.2280 | 1.1340 | 1.0539 | 0.9848 | 0.9246 |
| Q | 11 | 20 | 40 | 83 | 178 | 401 |

**Table 4.4: As in Table 4.1 for quasi-TM modes of a microdisk resonator.**

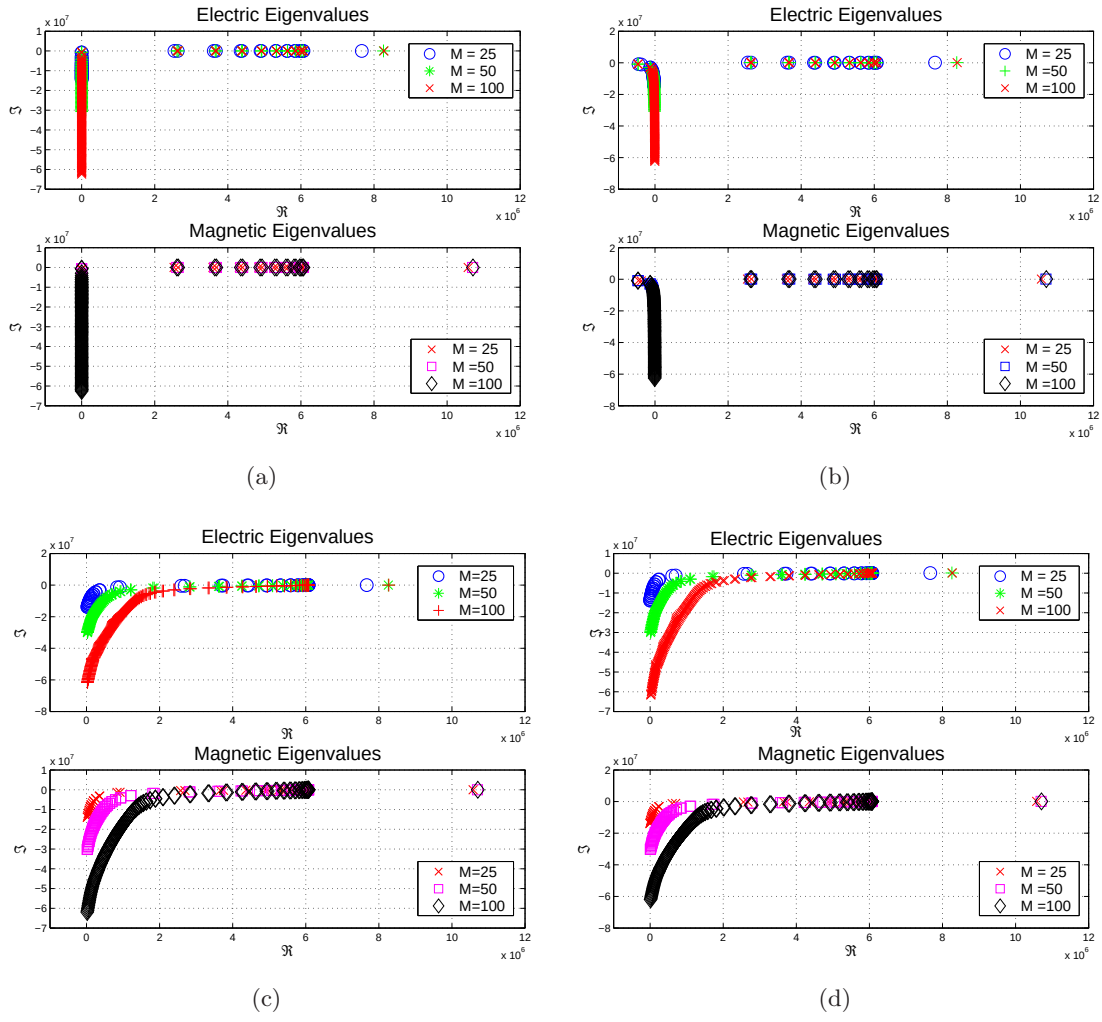


Figure 4.5: Eigenvalue maps in the complex plane ($k_0 n_i^{TE,TM}$), $\Lambda = 8\mu m$. The images in the first row are obtained without, in the second with PMLs. Similarly, the first column refers to real frequencies and the second to complex ones. $M$ varies according to legends. Where PML applies, $\Pi = 0.7\Lambda$, $\gamma = 1/(1+j)$.

corresponding to real and complex frequency, see figs. 4.5(c) and 4.5(d), particularly those pertaining evanescent modes.

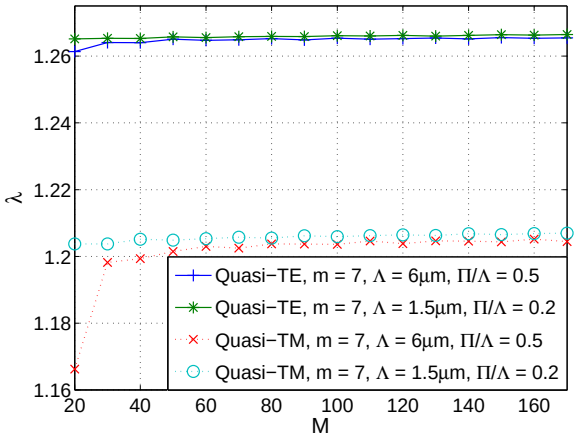


Figure 4.6: Convergence plots for microdisk quasi-TE and -TM modes of order $m = 7$: resonant wavelengths vs. truncation order $M$ for two different values of the window (period) $\Lambda$, and ratio $\Pi/\Lambda$ of physical to total window. Here the absorption figure of the PML is set to be $\gamma = 0.5 - j0.5$.

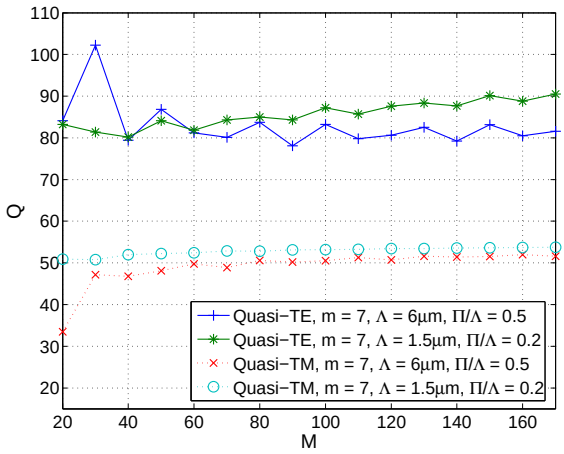


Figure 4.7: Same as fig. 4.6, but quality factors $Q$ vs. truncation order $M$.

The typical dependence of the results on the truncation order $M$ is shown in fig. 4.6 and 4.7 for quasi-TE and -TM modes of azimuthal number $m = 7$, and two different values of computational window $\Lambda$ and ratio $\Pi/\Lambda$. As shown, the value of the resonant wavelength converges rapidly as $M$ increases, while the final value is affected slightly (the relative change $\Delta\lambda/\lambda$ is of the order of $10^{-3}$) by the choice of the parameters of the computational window. The $Q$ values convergence seems worse, but the dependence on a small imaginary part of complex wavelength should be considered: it is thus prone to accuracy issues and the choice of parameters, indeed the computation of SV of least magnitude

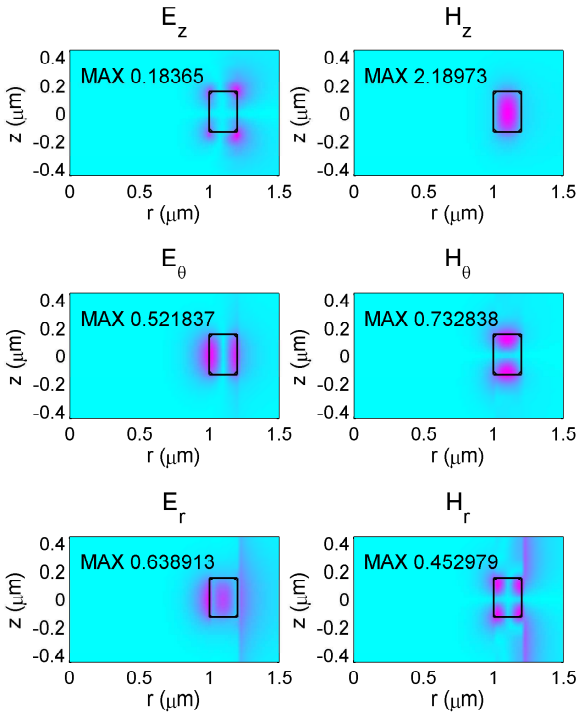


Figure 4.8: Microring resonator: cross sectional view of the absolute value of electric and magnetic (normalized by $-j\sqrt{\epsilon_0/\mu_0}$) field components of quasi-TE mode of azimuthal order $m = 12$, with resonant wavelength $\lambda = 1.1820\mu m$ and $Q = 400$. The box represents the section of the ring, while the reported numbers are the maximum value of the relative quantities. Top: distribution of axial vertical components $E_z$ and $H_z$; centre: azimuthal components $E_\theta$ and $H_\theta$; bottom: radial components $E_r$ and $H_r$.

Moreover, in order to show the importance of using a 3D method to compute the true vectorial nature of the modes, we report few example of modal profiles in figs. 4.8 and 4.9. Both figures show the hybrid character of the WGM eigensolutions. In order to highlight the order of magnitude of the field components we have reported in both figures the maximal absolute value of the relative component (notice that we kept the normalization of magnetic field as in eq. (4.10), i.e. magnetic fields are normalized by $-j\sqrt{\epsilon_0/\mu_0}$ to obtain the same units). In particular the small disk TM mode is characterized by field components virtually of the same order, as shown in fig. 4.9. The peak of $E_z$ is twice as much of the peak value of $H_z$, while it is the opposite for $\theta$ components. $H_r$ is instead far larger than $E_r$: those properties seem related to the small disk diameter only, while varying $m$ does not affect much this trend. The hybrid character of the microring quasi-TE mode in fig. 4.8 is weaker, as expected by its larger size. The magnetic field is mainly directed along $z$, while the electric field is on the ring plane.

Finally, we point out that, compared to usual FDTD full vectorial simulations, our approach turns out to be much faster. To obtain a resonant mode of fixed azimuthal order, it takes no longer than a quarter-hour on a modern personal computer, in spite of the fact

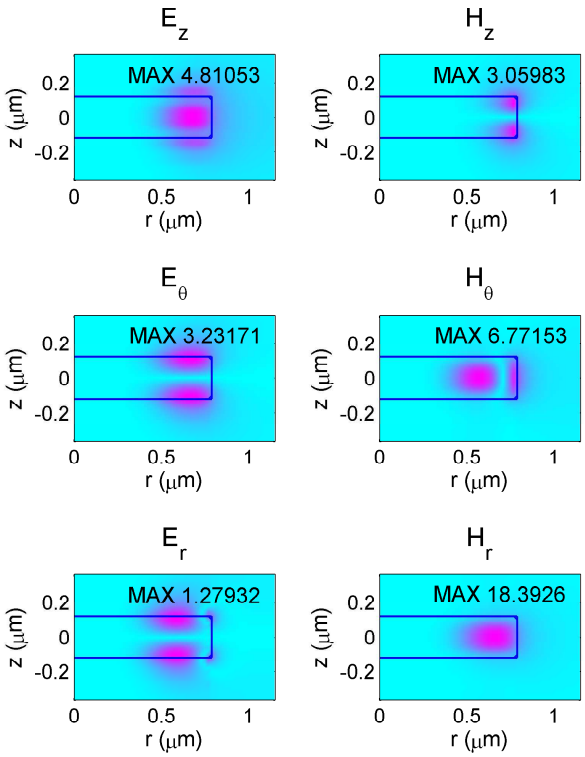


Figure 4.9: As in fig. 4.8 for the microdisk, quasi-TM mode of order $M = 9$, with resonant wavelength $\lambda = 1.0358\mu m$ and $Q = 215$. Top: distribution of axial vertical components $E_z$ and $H_z$; centre: azimuthal components $E_\theta$ and $H_\theta$; bottom: radial components $E_r$ and $H_r$.

that it is implemented in Matlab®, while our parallel FDTD code (in Fortran) takes about an hour on a 4-machine cluster. This is due also to the fact that a Cartesian FDTD, when applied to describe cylindrical devices, suffers from a staircase approximation whose impact could be reduced only at expenses of making the discretization mesh sufficiently fine.

### 4.5.2 Sandwich microdisk

The slot waveguide proposed by Barrios, see [112], based on anti-guiding confinement, have attracted a lot of attention in recent years, because it permits to overcome the diffractive limit of classic TIR waveguides. It consists in light confinement in a thin silica film (called slot) surrounded by two wider silicon layers (called slices): this is possible in TM polarization ($E$ normal to interfaces) if low index region extremely thin, $20 - 70nm$, due to the proximity of two field jumps induced by high index step. We noticed in section 1.3 that nonlinear effects can be enhanced by confining light in small volumes. This concept applies also to emitting devices and the response of modulators: along with the requirement of high quality factor of a cavity, that microtori and microspheres guarantee at the highest degree, see [113], a small modal volume is a crucial factor, see [114]. For example, Purcell factor that represent the enhancement of spontaneous emission rate in a cavity compared to that of bulk material, depend inversely on modal volume, see [115] and [116]. Fabrication of this sort of devices is

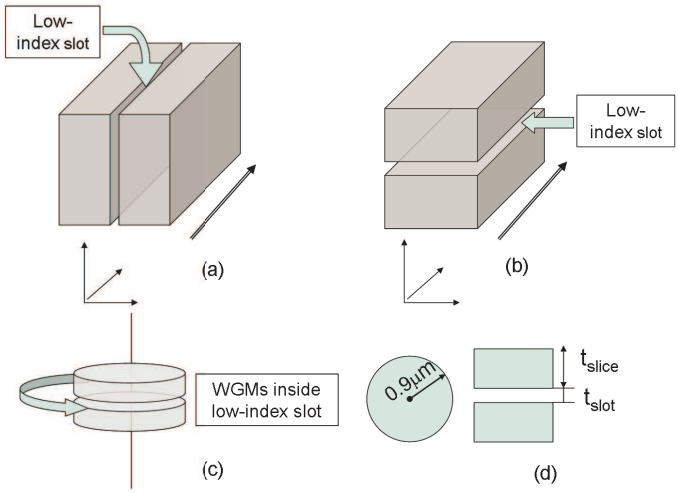


Figure 4.10: Antiguiding slot waveguide and its application to resonators. In (a) the original principle, in (b) the stacked version (sandwich). In (c) the use of sandwich confinement in a microdisk is reported and in (d) we sketch the physical dimensions of simulated structure.

possible also in a stack configuration, we refer to as *sandwich waveguide*, see [117]. This new configuration can be even preferable because it guarantees slot uniformity, harder to obtain by silicon vertical etching and silica filling. The upper silicon film have instead to be of very pure and manageable properties. Since the guiding region is made of silica, we can dope it with erbium ions or silicon nanoclusters, see [5], and possibly obtain silicon-based active devices.

Here we are interested in a microresonator that confines longitudinally on the basis of this principle, that we will refer to as *sandwich microdisk*. We then report few considerations about such structures, starting from the 2D model. Let us assume a modal profile expressed, as follows, by the transverse electric field component, the discontinuous one; let us denote $t_{slot} = 2a$ the thickness of silica slot and $t_{slice} = b - a$ the thickness of silicon slice, i.e. $\pm a$ and $\pm b$ are used as coordinate of interfaces. We have, compare to [112],

$$E_x(x) = A \begin{cases} \dfrac{1}{n_S^2} \cosh(\gamma_S x), & |x| < a \\ \dfrac{1}{n_H^2} \cosh(\gamma_S a) \cos[\kappa_H (|x| - a)] + \dfrac{\gamma_S}{n_S^2 \kappa_H} \sinh(\gamma_S a) \sin[\kappa_H (|x| - a)], & a < |x| < b \\ \dfrac{1}{n_C^2} \left\{ \cosh(\gamma_S a) \cos[\kappa_H (b - a)] + \dfrac{\gamma_S}{n_S^2 \kappa_H} \sinh(\gamma_S a) \sin[\kappa_H (b - a)] \right\} \times \\ \times \exp[-\gamma_C (|x| - b)], & |x| > b. \end{cases} \tag{4.55}$$

where $\kappa_H$ is the transverse wavenumber in the high index region, $\gamma_C$ is the field decay coef-

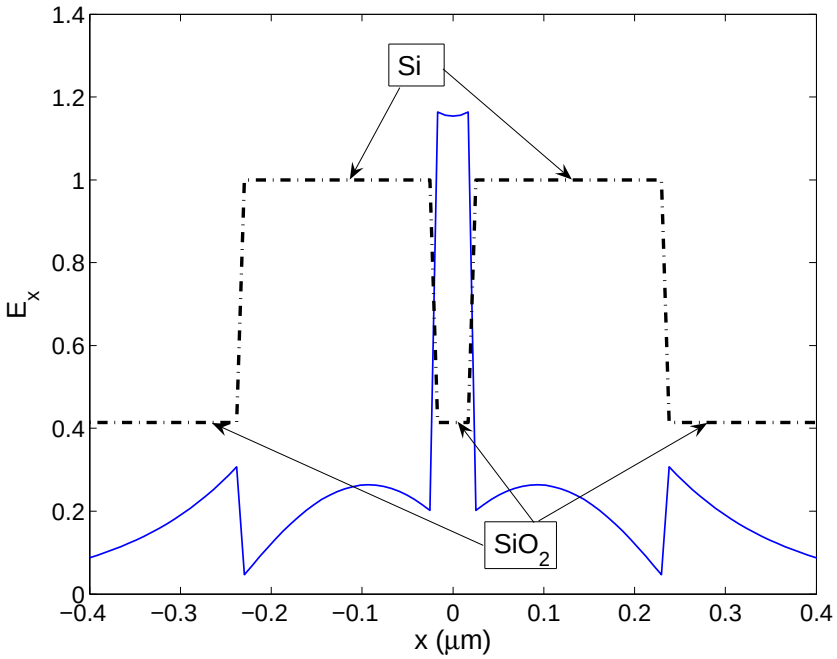


Figure 4.11: Field profile of a guided mode inside a slot waveguide, that confines light in low-index nanoscaled layer. $t_{slice} = 200nm$, $t_{slot} = 50nm$, $n_{Si} = 3.48$ and $n_{SiO_2} = 1.44$.

ficient in the cladding, $\gamma_S$ is the field decay coefficient in the slot, and

$$A = A_0 \frac{\sqrt{k_0^2 n_H^2 - \kappa_H^2}}{k_0},$$

with $A_0$ an arbitrary constant. The transverse parameters $\kappa_H$, $\gamma_S$, and $\gamma_C$ simultaneously obey the relations

$$k_0^2 n_H^2 - \kappa_H^2 = k_0^2 n_C^2 + \gamma_C^2 = k_0^2 n_S^2 + \gamma_S^2 = \beta^2$$

where $\beta$ is the eigenmode propagation constant, which can be calculated by solving the transcendental characteristic equation

$$\begin{aligned} \tan\left[\kappa_H (b-a) - \Phi\right] &= \frac{\gamma_S n_H^2}{\kappa_H n_S^2} \tanh\left(\gamma_S a\right) \\ \text{with } \Phi &= \arctan\left(\frac{\gamma_C n_H^2}{\kappa_H n_C^2}\right). \end{aligned} \tag{4.56}$$

From eq. (4.55), it is apparent that at slot-slice interface, the field immediately inside the slot is $n_H^2/n_S^2$ times higher than the field on the other interface side.

In figure 4.11, we report the field profile of the guided mode confined inside the low-index slot. It shows that the interaction of two classic guided modes of slices produce a strong peak inside the slot.

Then we discuss how the confinement can be modified by changing input parameters. Let us define, as in [116] the confinement factor of a TM mode in layer $i$ of multislab configuration

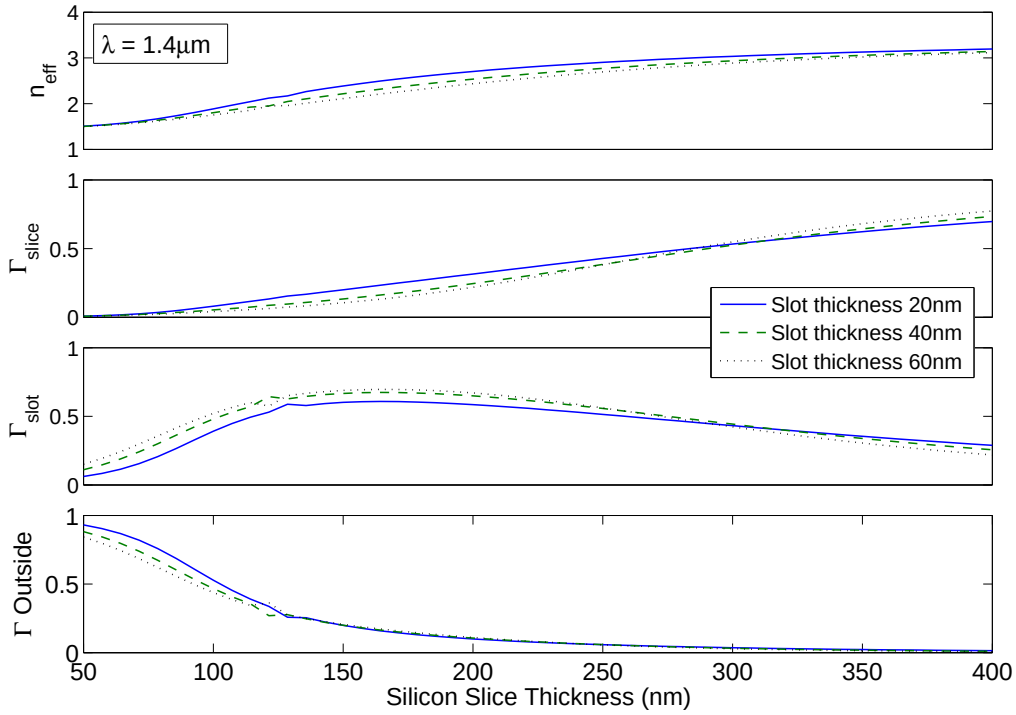


Figure 4.12: Representation of effective index, confinement factor in each layer as function of slice thickness. The computation accounts for 3 different slot thickness values. Weak dependence on $t_{slot}$ is apparent.

as

$$\Gamma_i^{TM} = \frac{\int_{layer\,i} |E_x|^2 \, \mathrm{d}x}{\int_{-\infty}^{\infty} |E_x|^2 \, \mathrm{d}x} \tag{4.57}$$

We then plot effective index and confinement in each region of our structure to realize how radiation is vertically restrained and how much energy can be stored in the low-index region; $n_{Si} = 3.48$ and $n_{SiO_2}$ are assumed. We have three parameter: the free-space wavelength, slice and slot thicknesses. In figure 4.12 we report the results of $n_{eff}$ and $\Gamma$ as functions of $t_{slice}$, setting $\lambda = 1.4\mu m$ and including several $t_{slot}$. It is apparent that the impact of slot thickness is small, whereas varying the Si dimension a maximum confinement in the slot can be achieved.

Moreover it is important to understand how effective index and confinement factors depend on wavelength, see figure 4.13 and 4.14.

In a 2D model, based on EIM, the effective refractive index represents a figure of the axial confinement and is therefore connected to the quality factor of the resonator. It is thus important to compare the sandwich $n_{eff}$ with that of classical confinement. It is apparent from figure 4.12 that they can be almost equal, because effective index increases as the slice width is increased; moreover flatness over $\lambda$ is guaranteed, see fig. 4.13 and 4.14.

The longitudinal confinement permits to better estimate the behaviour of energy distribution inside the structure: a maximum in slot confinement can be achieved.

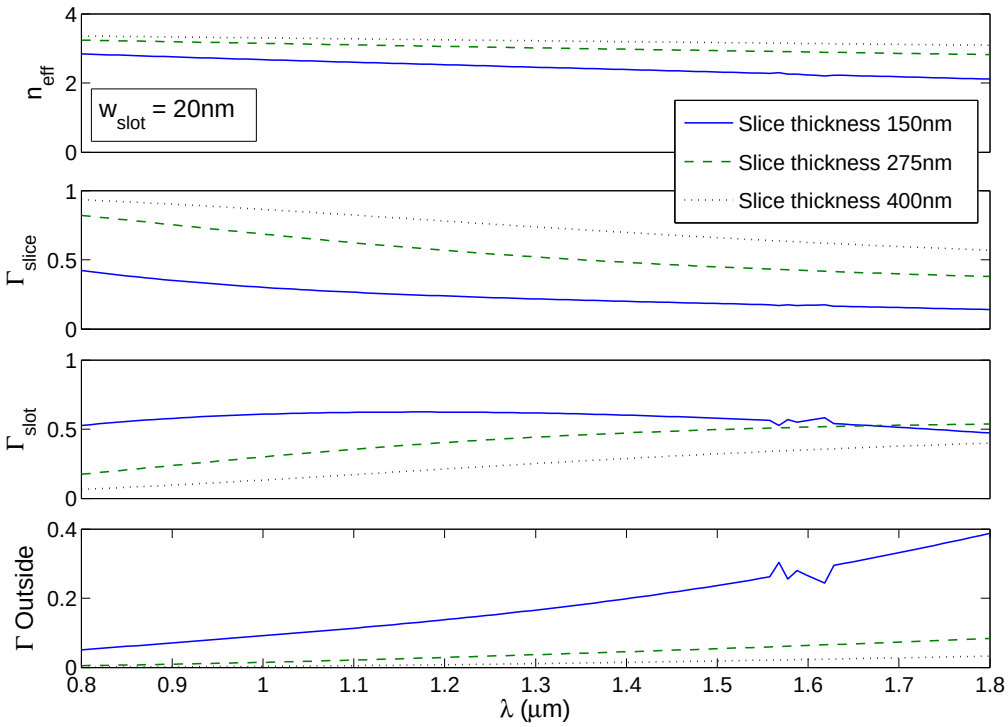


Figure 4.13: 1D confinement properties of antiguiding structure as a function of wavelength. 3 values of slice thickness are included. The slot width is in turn very small $t_{slot} = 20nm$. Changing slice width impacts tremendously on confinement.

Finally, to understand the reduction of modal volume, we discuss the guiding properties of the overall structure. Indeed, except for the tunnelling through the slot, the whole structure can support classical guided waves. If slices are too thin the guided mode is too wide, the field does not undergo a significant jump, and evanescent tails in the cladding are remarkably large; if they are too wide, we obtain a mode in each slice, with insufficient coupling to undergo an enhancement inside the slot.

We applied to the 3D structure of sandwich microdisk our A-FMM; in table 4.5, we report some comparison between different methods, as we did before. The device parameters are: $t_{slot} = 50nm$, $t_{slice} = 200nm$, diameter $d = 1.8\mu m$. In this case EIM seems quite unreliable, particularly as far as quality factors are concerned.

We then report a 3D plot of WGM in a microdisk exploiting this principle, figure 4.15. The confinement is apparently enhanced with respect to the previously studied structures, the main electric field $E_z$ component is concentrated by antiguiding mechanism.

To express more precisely those properties, let us recall the definition of effective mode volume, see [114].

From Fermi golden rule, we can compute the spontaneous emission rate of an emitting dipole inside a cavity as

$$\Gamma_{rad} = \frac{2\pi}{\hbar} \int_{-\infty}^{\infty} \left\langle \left| \vec{p}_a \cdot \alpha \vec{E}\left(\vec{r}_e\right) \right|^2 \right\rangle \rho_c(\omega)\rho_e(\omega)\,\mathrm{d}\omega \tag{4.58}$$

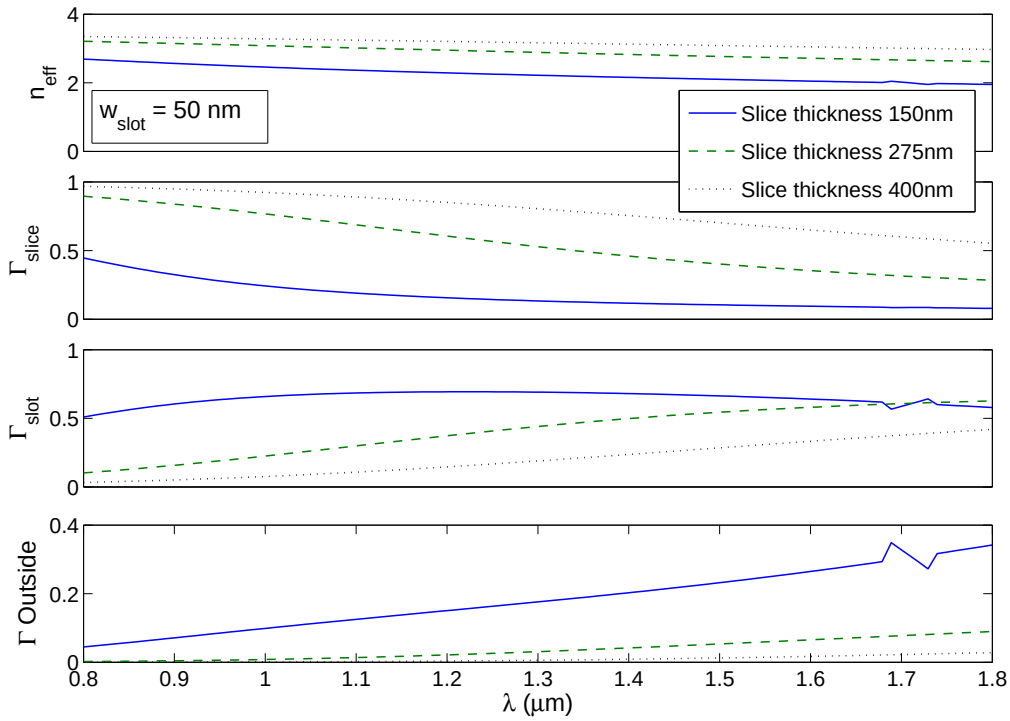


Figure 4.14: As in fig. 4.13, but slot dimension are relaxed to $t_{slot} = 50nm$. In this case we have not any significant change of performance, except there is more room to confinement at the higher edge of the considered band, i.e. for thin slices, the confinement degradation occurs at higher wavelength.

where $\rho_c(\omega)$ is the density of photon modes inside the cavity, $\rho_e(\omega)$ is the mode density for the dipole transition (material emission spectrum), $\vec{p}_a$ is the atomic dipole moment, and $\vec{E}(\vec{r}_e)$ is the electric field at the location of the emitter normalized by a factor

$$\alpha^2 \equiv \frac{\hbar\omega}{2} \frac{4\pi}{\int_{-\infty}^{\infty} \epsilon(\vec{r}) \vec{E}^2(\vec{r}) \, \mathrm{d}\vec{r}}$$

to fix the correct zero energy.

Thus, for a given emitter $\rho_e(\omega)$, we have two ways to enhance the spontaneous emission rate: to increase the photon mode density, then $Q$, or to increase the normalized electric field at the emitter, $\alpha\vec{E}(\vec{r}_e)$. This is inversely proportional to effective volume $V_{eff}$ of the electromagnetic energy inside the cavity. Thus a common figure of merit of an emitting cavity is $Q/V_{eff}$. This is characteristic of the so-called Purcell factor ($F_p$). Let us then make some simplifications on eq. (4.58): we assume that the emitter is placed at the peak of the electric field and the cavity resonant frequency equals the peak emission frequency ($\omega_e$), the ratio of spontaneous emission rate in the cavity compared to bulk can be written as

$$F_p = \frac{\Gamma}{\Gamma_0} = \frac{6Q\left(\frac{\lambda}{2n}\right)^3}{\pi^2} \frac{\epsilon(\vec{r}_{max}) \max\left|\vec{E}(\vec{r})\right|^2}{\int_{-\infty}^{\infty} \epsilon(\vec{r}) \left|\vec{E}(\vec{r})\right|^2 \mathrm{d}\vec{r}} = \frac{6Q\left(\frac{\lambda}{2n}\right)^3}{\pi^2 V_{eff}} = \frac{6Q}{\pi^2 \tilde{V}_{eff}} \tag{4.59}$$

| m | 8 | 10 | 12 |
|---|---|---|---|
| C-RCWA | | | |
| lambda | 1.3490 | 1.1596 | 1.0061 |
| Q | 460 | 651 | 12564 |
| 3D-FDTD | | | |
| $\lambda$ | 1.3376 | 1.1497 | 1.0069 |
| Q | 186 | 855 | 13251 |
| 2D | | | |
| $\lambda$ | 1.3397 | 1.1555 | 1.0241 |
| Q | 66 | 324 | 2092 |

**Table 4.5: As in Table 4.1 for quasi-TM modes of a sandwich-microdisk resonator.**

where $n$ is the index of refraction at the field peak (i.e., $\vec{r}_{max}$).

We define the normalized unitless effective mode volume as

$$\tilde{V}_{eff} = V_{eff}\left(\frac{2n\left(\vec{r}_{max}\right)}{\lambda}\right)^3 = \frac{\int \epsilon\left(\vec{r}\right)\left|\vec{E}\left(\vec{r}\right)\right|^2 \mathrm{d}\vec{r}}{\epsilon\left(\vec{r}_{max}\right)\max\left[\left|\vec{E}\left(\vec{r}\right)\right|^2\right]}\left(\frac{2n\left(\vec{r}_{max}\right)}{\lambda}\right)^3, \tag{4.60}$$

where maximal values are computed in the region where interactions take place, $\vec{r}_{max}$ representing the coordinates of the maximal squared field.

The main advantage of the anti-guiding structure is shown in [115] to be an enhancement of Purcell factor of the order of $\left(\epsilon_H/\epsilon_L\right)^{5/2}$ when compared to the classical confinement case, i.e. without the tunnel slot. A simple result that can be obtained if we realize that comparing modes with or without slot the integral of equation (4.60) are almost equal, but the maximum occurs in a layer of index $n(\vec{r}_{max}) = n_S$, and the peak value is $n_H^2/n_S^2$ higher.

To verify this possibility, we have performed many calculations of $F_p$ by means of our cylindrical A-FMM. We compute modal volumes as,

$$\begin{aligned}\int \epsilon\left(\vec{r}\right)\left|\vec{E}\left(\vec{r}\right)\right|^2 \mathrm{d}\vec{r} = \\ = \int_{r=0}^{r_i}\int_{\theta=0}^{2\pi}\int_{z=-\infty}^{\infty} r\epsilon(r,\theta,z)\left(|E_z|^2+|E_\theta|^2+|E_r|^2\right)\mathrm{d}r\,\mathrm{d}\theta\,\mathrm{d}z \approx \\ \approx 2\pi\Delta r\sum_k r_k\int_{-\Lambda/2}^{\Lambda/2}\epsilon(z)\left(|E_z|^2+|E_\theta|^2+|E_r|^2\right)\mathrm{d}z.\end{aligned} \tag{4.61}$$

where we wrote a simple rectangular rule to integrate on $r$. Since Fourier coefficients are known, we can apply directly Parseval theorem and calculate

$$\int \epsilon\left(\vec{r}\right)|E\left(\vec{r}\right)|^2\,\mathrm{d}\vec{r} \approx 2\pi\Delta r\Lambda\sum_k r_k\sum_{m=-M}^{M}\overline{E}^{-1}\left(|S_z|^2+|S_\theta|^2+|S_r|^2\right) \tag{4.62}$$

where first we multiply matrix $\overline{E}^{-1}$ (inverse rule) and the arrays of electric field Fourier coefficient, then we sum the elements of the resulting vector, according to Parseval's theorem.

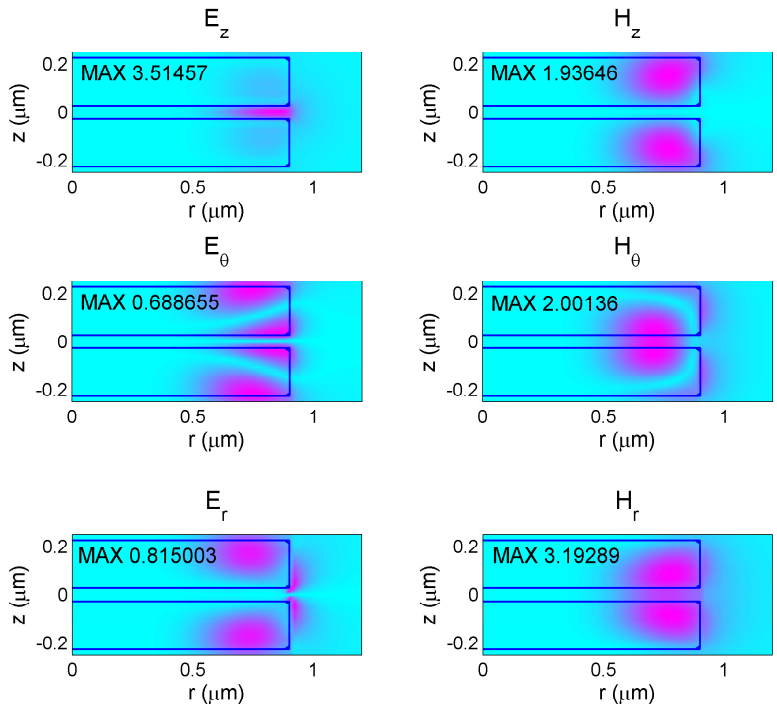


Figure 4.15: As in fig. 4.8 for the microdisk, quasi-TM mode of order $M = 10$, with resonant wavelength $\lambda = 1.1596\mu m$ and $Q = 651$. Top: distribution of axial vertical components $E_z$ and $H_z$; centre: azimuthal components $E_\theta$ and $H_\theta$; bottom: radial components $E_r$ and $H_r$.

In figure 4.16, we show that varying the geometry of this sandwich structure, a strong enhancement of $F_p$ can be obtained, corresponding to reduction of modal volume and increased vertical confinement, as it could be inferred by the slot confinement plot of figure 4.12.

## 4.6 Conclusion

In summary, we have applied the Aperiodic Fourier-modal method to cylindrical coordinate system to study rotationally invariant structures. We have proved how it simplifies the computation of a modal basis (along the vertical direction) and overlap integrals. We remark that we do not have to put any boundary in radial direction, since we know exactly how each mode depends on $r$ up to infinity. Moreover the method allows to include PML boundaries to improve the accuracy of modal analysis along $z$. An admittance matrix formulation permits to obtain good quantitative results and to study a variety of structures with cylindrical symmetry. Though we obtained in general a reliable and fast 3D mode solver to analyse micro-integrated devices, we point out that the computation can be improved in specific situations by working on the choice of simulation parameters. A thorough investigation of solving methods for the electromagnetic eigenvalue problem is crucial to improve the convergence.

The application of our method to innovative devices, such as sandwich microdisk, permits

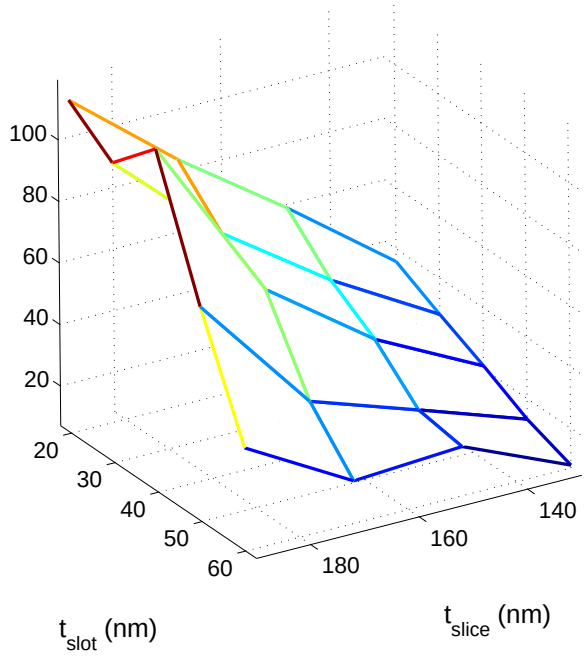


Figure 4.16: Purcell factor, $F_p$, of silicon sandwich disk resonator, with silica slot. Material refractive indices and disk diameter $d = 1.8\mu m$ are kept constant.

to better assess their benefits.

# Chapter 5

# Design, Fabrication and Characterization of Microdisk-based Devices

While the previous chapter was devoted to a 3D numerical method that models isolated cylindrical cavities, in this chapter we are reporting some details about a few simple systems based on planar integrated waveguides and cavities. Based on a circuit model, we describe which operation regimes are available and which design trade-offs have to be considered. Then several details on fabrication and characterization are provided and sample experimental results shown.

## 5.1 Microdisk-Based Devices: Design Principles

Our characterization work has been focused on systems composed by two building blocks: microresonators and waveguides.

We sketch a simple approach that assumes both cavity parameters and the impact of coupling with waveguides are known, see [118–121]. This resembles a circuit theory model, where every element is characterized by an input-output function. The dependence of two-port model on the geometry and composition of each element is determined by e.g. FDTD or other methods, such as the modal method we introduced in the previous chapter, combined with a CMT approach: for example [122] provides a 2D CMT model intended to answer these questions, a 3D application can be found in [93].

### 5.1.1 Laser source

The first example of cavity-guide interaction is represented by a microdisk laser, see figure 5.1. A microdisk of sufficiently high quality factor (to allow light circulation) fabricated in an active material (InP for example) is necessary. Then disk lasing can be achieved by a suitable population inversion and radiation is made available via waveguide coupling. Obviously the waveguide perturbs the cavity modal structure, then a trade-off between collectable

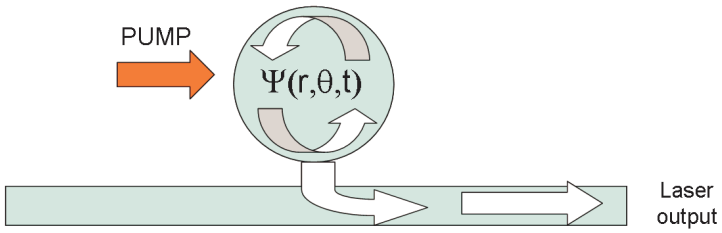


Figure 5.1: Schematic representation of a microdisk laser. Population inversion is provided by a pump mechanism, light is generated and amplified inside the cavity and collected via a waveguide.

energy and perturbation has to be considered. This demonstrates that disk-guide spacing is a crucial parameter, if it is too large leads to insufficient coupling, if too small a stronger perturbation and a higher threshold may result (the perturbation generally implies quality factor to degrade). We will further discuss this problem.

In this case we consider to operate in the same regime as in the previous chapter, where a complex resonant frequency is used. As we outlined there, this regime, usually denoted as *free oscillation* is an infinite energy regime. Indeed damping is supposed to start at $t \to -\infty$, then finite energy at any time implies it is infinite at the beginning and then radiated energy toward the space boundaries cannot be bounded. Nevertheless, this regime is practical to represent the output light-flow, but we have to fix a finite initial time at which energy is stored inside the cavity. Lasing requires that the stored energy is kept up by pumping at a level that overcomes the cavity leakage. More precisely, we can imagine that threshold condition corresponds to the compensation of cavity losses so that stable (instead of damped) oscillation is achieved.

To outline a simple model we can consider, as above, damped oscillations (in [121] this concept is directly applied to stored energy) or leaky propagation in a circular waveguide, see e.g. [118]. We follow the first one.

We denote as $\Psi$ the mode amplitude inside the cavity, then

$$\Psi \propto \exp\left[(j\omega_{res} - \alpha - \alpha_c)\, t\right] \tag{5.1}$$

where $\omega_{res}$ is the resonant (angular) frequency, $\alpha$ the intrinsic loss of resonator, and $\alpha_c$ the coupling losses: being $Q_{tot} = \omega_{res}/(2\alpha_{tot})$, the quality factor is limited by the stronger source of leakage, i.e. the well-known formula

$$\frac{1}{Q_{tot}} = \frac{1}{Q_{int}} + \frac{1}{Q_{coupling}} \tag{5.2}$$

where $Q_{int}$ is the intrinsic quality factor (i.e. due to resonator geometry and consequently exhibited by isolated cavity), $Q_{coupling}$ represents the degradation of energy leakage due to

external perturbation and $Q_{tot}$ the overall effect, as it can be measured.

The radiated and guided power can be distinguished accordingly,

$$\frac{\mathrm{d}\,|\Psi|^2}{\mathrm{d}t} \propto P_r + P_g \tag{5.3}$$

where $r$ and $g$ subscripts denote the radiated and guided losses (we assume no other coupling mechanism occurs, e.g. material losses, scattering, etc...) and simply

$$P_g = 2\alpha_c\,|\Psi|^2\,. \tag{5.4}$$

### 5.1.2 Band-suppressing filter

While the first example was intended to illustrate the principle of this simple analysis, the second is directly related to our activity. A filter, specifically a band-rejecting one, can be obtained simply in the previous configuration: if a broad spectral width source is injected into the waveguide, we collect at its output a transmission spectrum that does not include a set of frequencies corresponding to cavity resonances, see fig. 5.2.

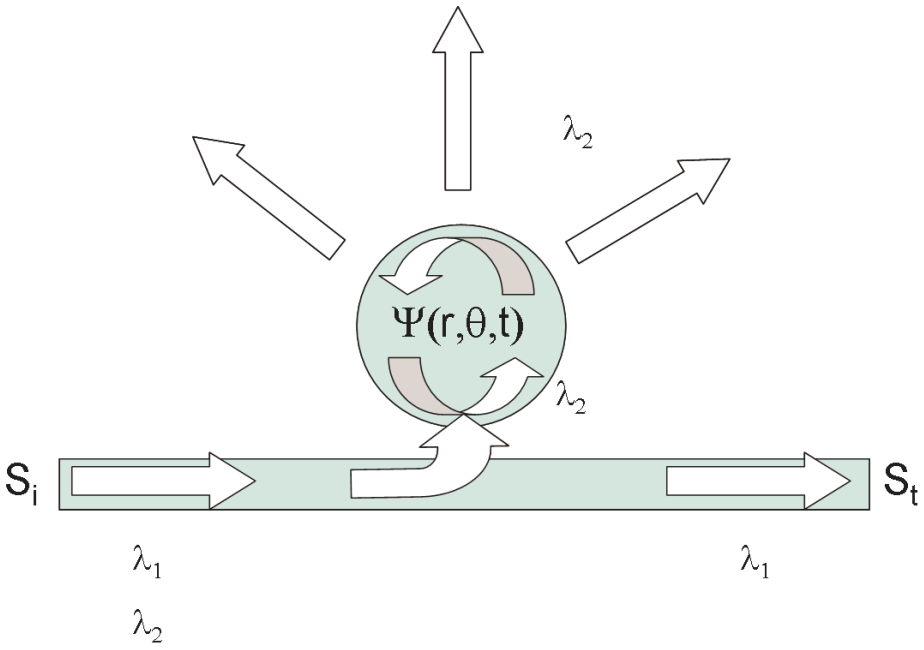


Figure 5.2: Schematic representation of a microdisk-based band rejecting filter. Frequency bands corresponding to cavity resonances are extracted from waveguide. Performance in terms of flatness and bandwidth can be tailored by putting several resonators side by side.

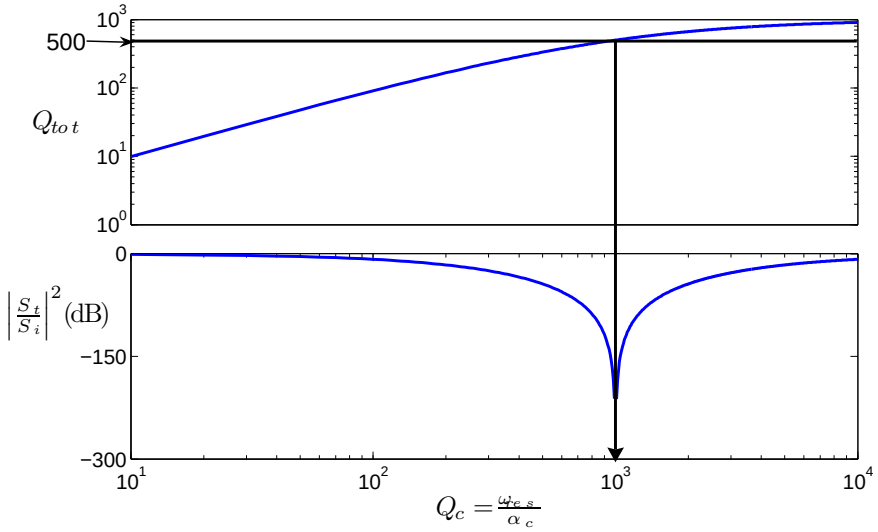


Figure 5.3: Plot of overall quality factor (logarithmic scale) and energy extiction ratio (dB) of a waveguide-coupled resonator as a function of disk-guide coupling. This is expressed in terms of a quality factor $Q_c$. We assume to work on-resonance and $Q_{int} = 1000$.

Assuming the same time-dependence of (5.1), we write

$$\begin{aligned} \frac{\mathrm{d}\Psi}{\mathrm{d}t} &= (j\omega_{res} - \alpha - \alpha_c)\,\Psi - j\mu S_i \\ S_t &= S_i - j\mu\Psi \end{aligned} \tag{5.5}$$

where $S_i$ and $S_t$ are the field amplitude at waveguide input and output (such that their squared modulus gives power), and $\mu$ is the disk-waveguide coupling, in general a complex number. If we exclude any gain mechanism inside the cavity, $(\alpha, \alpha_c) > 0$, the previous expression accounts for the injection of light from waveguide to cavity (effectiveness depends on detuning from resonances), that can be radiated or even partly recoupled into the waveguide and reach the output port.

Notice that if $S_i = 0$, we return to the previous case. Consider

$$P_g = 2\alpha_c\,|\Psi|^2 = |S_t|^2 = |-j\mu\Psi|^2 \tag{5.6}$$

then this equivalence holds: $\mu^2 = 2\alpha_c$.

Assuming a forcing excitation $S_i = e^{j\omega t}$ we could easily obtain, in the steady state,

$$S_t = \frac{j\,(\omega - \omega_{res}) + \alpha - \alpha_c}{j\,(\omega - \omega_{res}) + \alpha + \alpha_c} S_i \tag{5.7}$$

that is equivalent to other models such as in [118], but distinguishes explicitly the detuning with respect to resonance and the coupling contribution.

We obtain perfect filtering if $\omega = \omega_{res}$ and $\alpha = \alpha_c$. In this case $Q_{tot} = Q_{int}/2$; nevertheless the closer is the waveguide, the lower is the overall quality factor, but extinction ratio assumes a minimum, ideally zero, that corresponds to halved $Q$, see figure 5.3.

### 5.1.3 Multiplexer-Demultiplexer

We now deal with the so-called add&drop (A&D), that is able to select a wavelength channel from a set of packed signal and direct it separately to another output (drop) or to include a channel in an incoming broadband modulated signal (add).

A figure can better describe its behaviour and its microdisk-based implementation, 5.4. Two waveguides and a cavity that acts as coupler between them are necesssary.

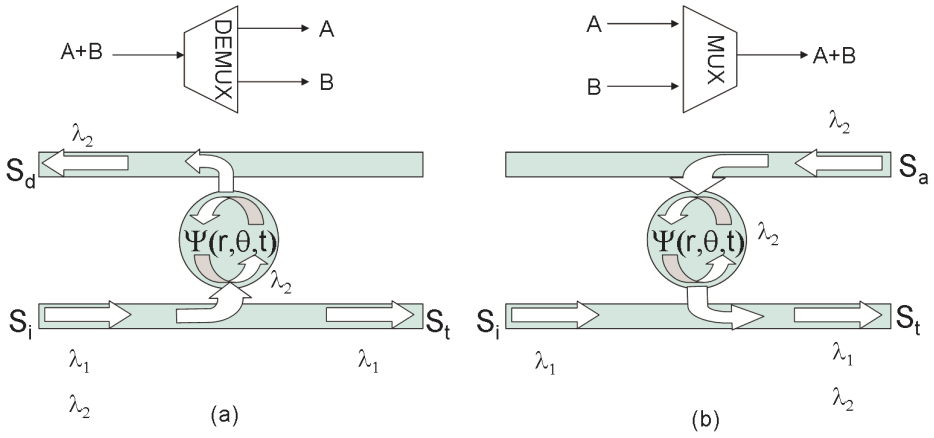


Figure 5.4: Schemtatic representation of demultiplexing (a) and multiplexing (b) functionalities and their implementation by means of planar microdisks and waveguides. Exploiting the selectivity properties of resonators and evanescent coupling, a channel can be moved from a waveguide to another.

We concentrate on the drop function that consists in extracting a wavelength from a first waveguide and putting it into the other, relying upon the cavity selective coupling.

Basically, as in the filter case, we have different coupling conditions, depending on guide-disk distances. If waveguides are too distant from resonator, no radiation is effectively extracted by that. If they are too close, light circulates in the cavity and is recoupled inside the input waveguide. This is twice as severe: direct channel is still noisy in the selected band, drop/output channel brings a low intensity signal. We have a simple coupler between two waveguides and no more a resonant extraction of a selected band, see fig. 5.5.

Let us employ the very same procedure to determine the optimal coupling; we distinguish two coupling terms, $\alpha_{c1}$ and $\alpha_{c2}$,

$$\begin{aligned} \frac{\mathrm{d}\Psi}{\mathrm{d}t} &= \left(j\omega_{res} - \alpha - \alpha_{c1} - \alpha_{c2}\right)\Psi - j\mu_1 S_i \\ S_t &= S_i - j\mu_1\Psi \\ S_d &= -j\mu_2\Psi \end{aligned} \tag{5.8}$$

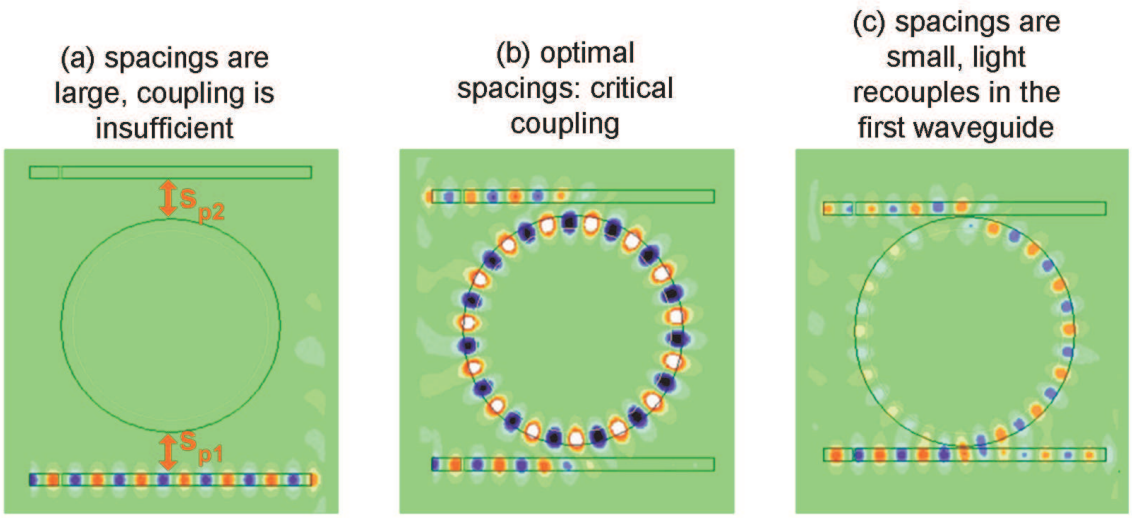


Figure 5.5: 2D-FDTD simulations of a lateral coupling add&drop. Different coupling regimes are shown. In (a) and (c) the opposite conditions of too large and too small disk-guide spacing, while (b) represents the optimal extraction from through and injection in drop channel.

the coupling to drop channel $S_d$ is expressed in terms of $\mu_2$, that can be related to $\alpha_{c2}$ by $\mu_2^2 = 2\alpha_{c2}^2$, as before.

$$S_t = \frac{j\left(\omega - \omega_{res}\right) + \alpha + \alpha_{c2} - \alpha_{c1}}{j\left(\omega - \omega_{res}\right) + \alpha + \alpha_{c2} + \alpha_{c1}} S_i \tag{5.9}$$

Thus to attain optimal coupling, at resonance, $\alpha_{c1} = \alpha + \alpha_{c2}$ is required. This means that:

- it does not correspond to equal spacings: $\alpha_{c1} \neq \alpha_{c2}$;
- it depends on a single parameter, one of the two disk-waveguide separations, that is equivalent to setting the quality factor for the whole system,

$$Q = \frac{\omega_{res}}{2\left(\alpha + \alpha_{c1} + \alpha_{c2}\right)} = \frac{\omega_{res}}{4\alpha_{c1}}. \tag{5.10}$$

It is easy to realize that optimal demultiplexer, like that we have sketched, does not behave symmetrically as multiplexer, because we inject the second input in the farthest waveguide, then coupling is insufficient, we should use more intensity in the second channel to obtain balanced levels on the multiplexed output. Thus a trade-off should be made: if balanced spacings are used, $\alpha_{c1} = \alpha_{c2} = \alpha_c$, we can obtain the maximal extinction ratio

$$\left|\frac{S_i}{S_t}\right|^2_{max} = \left|1 + 2\frac{\alpha_c}{\alpha}\right|^2 \tag{5.11}$$

and we can indefinitely increase it to the detriment of the loaded-cavity quality factor.

### 5.1.4 Splitting of degeneracies

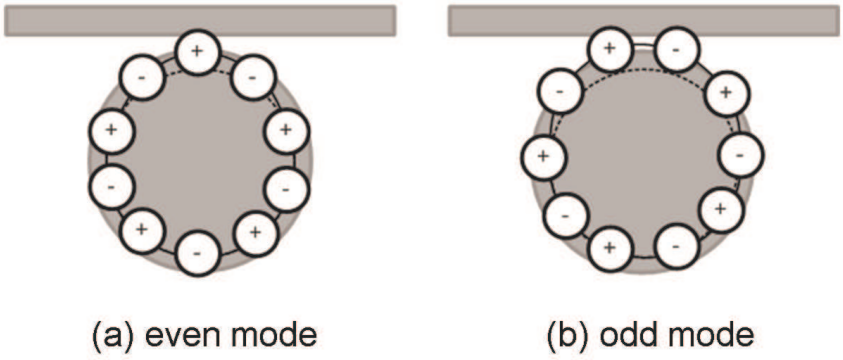


Figure 5.6: Schematic representation of even and odd WGM. Dashed lines represent unperturbed modes, solid lines the effect of waveguide perturbation.

The whispering-gallery modes are intrinsically degenerate, due to the cylindrical symmetry. Hence, once we fix a coordinate system, we can distinguish odd and even modes, according to the positions of maximum field values: even modes are symmetrical with respect to an axis, odd anti-symmetrical. Nevertheless, whatever the system we define, isolated cavity modes are always degenerate.

Obviously a guide at its side defines an axes system, then odd and even modes are properly distinguished. If an FDTD simulation is performed, we notice that waveguide and cavity influence each other and this leads to the even mode to be attracted by waveguide less than odd: this is the usual explanation of the splitting of degeneracy that causes a doublet to appear instead of the single resonance. In fact the optical path results different from one to another modal profile, requiring a slightly larger (odd) or smaller (even) wavelength to achieve resonance. If the overall quality factor is large enough, the splitting can be detected.

Another explanation is provided in [120]. A two-by-two matrix that accounts for propagation in a straight and curved (i.e. a WGM resonator) waveguide and the coupling between them cannot explain this phenomenon, but if we include the back-reflection of light from the coupling area, we obtain a reliable explanation. The two approaches are equivalent if we recall that the mode perturbation leads to reflections, such as every discontinuity of modal bases. Figure 5.6 shows the physical principle of the splitting.

Finally each peak composing the doublet is characterized by its own quality factor, and extinction ratio. The previously cited circuit model does not account for that. WGM symmetry breaking corresponds to attracted or repulsed field configurations, then also distance and coupling are modified.

In a successive section we discuss our attempt to mitigate this issue, that can hamper the application of these microcavities to light processing.

After depicting the design concepts, we are now passing to technology and experiments.

**A remark** In the following, we will report our experimental results. They have been focused on devices based on large diameter microdisks. Despite in literature we find 3D numerical studies of devices which employ very large diameter microdisks, see [93], they deal with small refractive index step. Moreover the modal approach is different from what we presented in chapter 4. We have not studied a CMT approach relying on our implementation, nor we master it to the extent we predict the resonant properties of isolated large diameter disks. In fact, even if the calculation of resonances is possible, the presence of many transverse modes with large imaginary part (to properly represent the continuum modes) causes numerical issues. Finally such large resonators are affected by an extreme sensitivity to fabrication imperfections, that limits the quality factors to values well below the theoretical predictions.

## 5.2 Passive Components in SOI

Here, we are studying optical chips fabricated in SOI: the samples we have characterised were fabricated at the CEA-LETI laboratories in Grenoble according to our specifications.

This is a natural choice, since SOI allows to effectively guide light due to its high refractive index contrast and is compatible to CMOS processes of microelectronics. As it is shown in figure 5.7, SOI is fabricated starting from pure crystal Si wafers on which a thermal oxidation is performed. We then make two of such wafers adhere by molecular bonding, and finally the resulting wafer is thinned down to about $400nm$ by means of, e.g., Smart-cut$^{TM}$ process. We obtain a guiding layer of Si, that plays as core and a buffer layer of silica, that functions as cladding. Its thickness is usually about $1\mu m$.

Obviously, the SOI wafer is then processed to build integrated devices.

### 5.2.1 Technological process

To fabricate integrated optical chips, we have to face several issues. Each function is achieved by using different structures. Hence we consider optical waveguides to carry light, adiabatic (direct) taper to inject a sufficient amount of radiation inside guides, and in our case microdisks or microgears to filter and process signals.

Each element needs a special care to optimize its fabrication. First of all single mode, low loss waveguides are needed and many techniques are available, from among we have to choose the most suitable to our purposes.

The first step consists in thinning the silicon layer down to $300-380nm$. A metal mask is then deposited: the required patterns are etched on it. On this mask, a photoresist is spread out and then exposed through a "mother" mask by deep UV lithography at $\lambda = 193nm$. The resist is then developed and the metal mask is etched. Reactive ion etching (RIE) is used to transfer those patterns on silicon, to obtain $300nm$ wide waveguides separated from microdisk

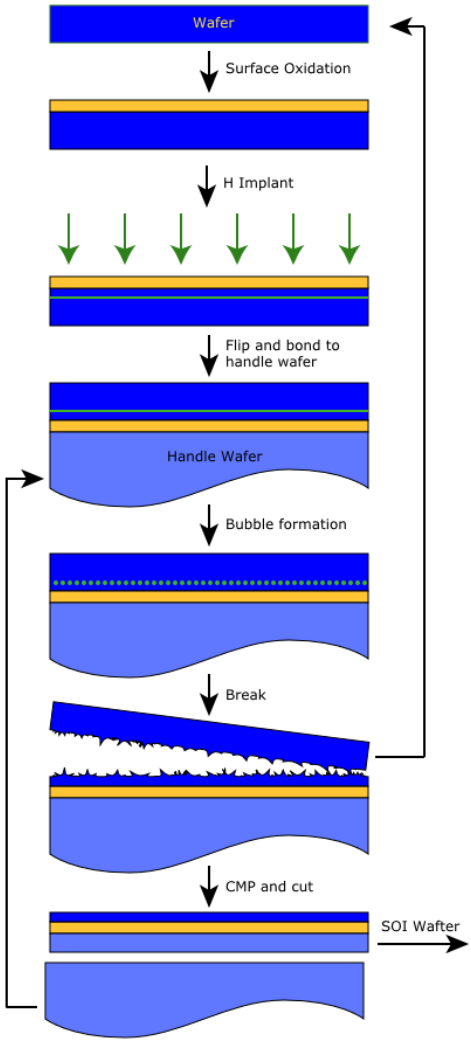


Figure 5.7: SOI wafer fabrication: Smart-cut$^{TM}$ technique, see [123].

by down to $100nm$. Metal is then eliminated and devices are finally embedded in a silica layer $500nm$ high, deposited by means of plasma-enhanced chemical vapour deposition (PECVD).

This latest step is necessary to mitigate the mechanical fragility of the resulting samples.

We recall that also electron beam lithography can be employed, but since it works on small windows, it faces intolerable alignment issues.

We now briefly describe the properties of the fabricated waveguides.

### 5.2.2 Waveguide properties and injection

The single mode character of the resulting waveguides can be verified, by injecting light at one end and detecting output. According to polarization, the shape of output spot impressed on an infrared camera allows us to understand if any high order mode is possible.

Working in the $\lambda = 1.55\mu m$ range the sample we have studied carries single mode propagation for TM polarization only, since TE waves leaks in the substrate.

As it is well known, while optical fibre section is quite large ($8\mu m$ core and $125\mu m$ with

cladding and other sheaths), due to small index contrast, micro integrated waveguides on silicon are rather small. Thus to inject light into such a waveguide an integrated taper, that brings the original section ($300nm$) to a width of $2\mu m$, is designed to adapt adiabatically the modal width of the injection fibre to that of the integrated waveguide; the taper length is about $100\mu m$ and is a low loss element (virtually no losses). Moreover, monomode lensed fibres are used both to inject and to collect light from the circuit. They permit to focus a spot of about $2.5\mu m$ at $6\mu m$ of focal distance. Usually input fibres are polarization-maintaining in order to guarantee proper TM excitation.

We are now reporting some data about the experiments we performed. We devoted to an extremely selective resonator: a microdisk of $8\mu m$ diameter. Two configurations have been studied: filters and add&drop. They differ only in the fact the latter recollects the coupled signal in another guide. Particularly, we focused on the trade-off between extinction ratio and selectivity of the overall device. Moreover we tried to verify if the emerging of doublets instead of singlets, due to guide-disk coupling, can be mitigated by architectural solutions. Indeed, at high quality factors, we can often distinguish two paired peaks for each resonance, due to the splitting of degenerate modes of the combined disk-guide system.

## 5.3 Experimental Results

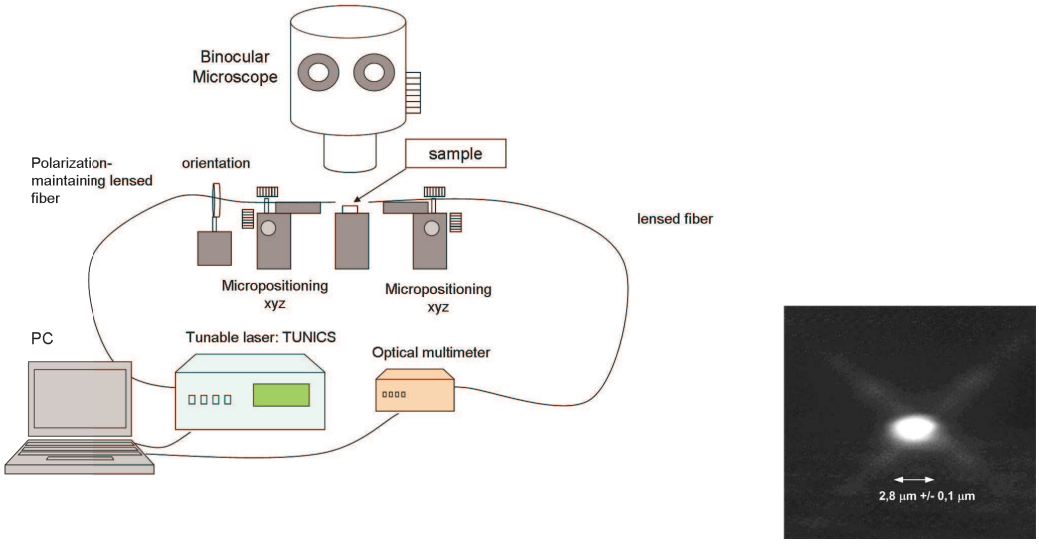


(a) (b)

Figure 5.8: (a)Schematic representation of our experimental set-up. Acquisition is driven by a PC, that controls a tunable laser and reads power from an optical multimeter. A couple of micro-positioning mechanisms is used to align input/output fibres to the sample. (b) Near infra-red (NIR) photograph of a waveguide output spot.

First of all we show a schematic picture of our experimental setup, see fig. 5.8. We have two possible ways to perform a spectral analysis of our structures:

- use of a broad band source [e.g., amplified spontaneous emission (ASE)] and an optical spectrometer to study where the input has been modified by cavity selectivity;
- use a tunable laser [Tunics PRI, by Photonetics, is available at IMEP laboratory] as a source and an optical multimeter to measure the collected power at each wavelength: a computer drives the source and synchronizes the acquisition of output power.

It is convenient to collect the output radiation in air by means of a tapered-lensed fibre.

We choose the second approach since we need very fine tuning to measure $Q \approx 10^5$ and the available spectrum analyser has a resolution of $0.07nm$. Tunics can instead scan with $1pm$ resolution and no additional limit is imposed by output detection.

After having orientated the input fibre (polarization-maintaining) to the desired polarization, and adjusting the position of fibres to align them to the selected structure, we could start the characterization itself.

### 5.3.1 Band-rejecting filter

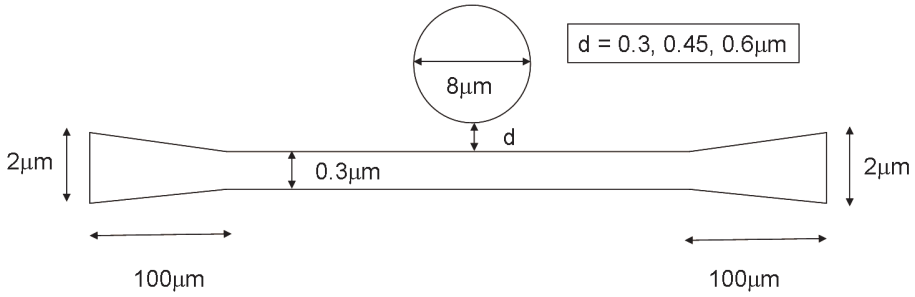


Figure 5.9: Schematic representation of the integrated band-rejecting filter, implemented using a microdisk resonator.

We start by studying a filter configuration, that is schematically represented in figure 5.9. As reported in figure, different spacings are available, $0.3, 0.45, 0.6\mu m$, then we show the dependence of resonance wavelength and quality factor upon the disk-guide separation.

From figure 5.10, it is apparent that increasing the spacing, i.e. decreasing the perturbation, the resonant wavelength moves downwards and the quality factor increases. Recall that coupling to a waveguide stretches the mode optical path, then the less the perturbation, the smaller the resonant wavelength; the $Q$ factor behaviour has been explained above, in terms of energy leakage due to coupling.

Moving the waveguide away from the disk, the extinction ratio is expected to increase up to a maximal value and then decrease. In our case passing from $0.3\mu m$ to $0.45\mu m$ spacings, we have a decreasing extinction ratio and we extrapolate that the maximum coupling occurs probably for distances around the first one, but it is hard to determine if above or below it.

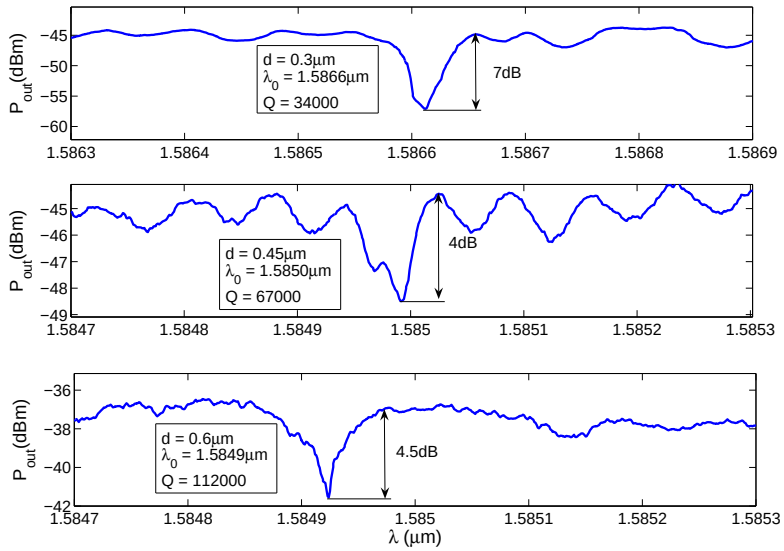


Figure 5.10: Comparison between three different filters based on $8\mu m$ diameter microdisk, and different guide-disk spacings. A single resonance around $\lambda = 1585nm$ is tracked to investigate the effect of coupling.

The quality factor of the first structure, fig. 5.10 (top), is not sufficiently high to permit the identification of a double peak. Moreover, the second device seems to exhibit a better extinction than the third and splitting appears (quality factor is estimated for the right-hand peak). It should be observed also in the third filter, but it is not the case. Thus we should explain it by other factors affecting the shape of resonances. Fabrication issues, such as shape defects and unwanted roughness that induce light scattering, absorption by impurities, or other coupling phenomena, perturb modal symmetry, see [124]. Nevertheless we have not performed a scanning electron microscopy measure yet, thus it is difficult to precisely characterise this problem. Apart from imperfections of the second structure, we could suppose that what we observe for the second (centre) is composed by interference effects along the waveguide or insufficient coupling occurs in the third (bottom diagram in figure), thus perturbation is not effective.

Indeed we observe relatively fast oscillations around each resonance. They are usually ascribed to high reflectivity at chip facets passing from silicon guide to air. This permits the built-in of standing waves and we observe a frequency response, composed by a sequence of resonances, of a multiple cavity formed by waveguide segments. It can be verified that this is the effect of three combined cavities: the whole long guide and their first and last parts, involving guide segments from facet to resonator. They are usually named Fabry-Pérot oscillations.

This is an annoying issue, particularly when extreme situation are tackled, e.g. a very large quality factor cavity which is difficult to couple light in and whose resonances are masked by spurious oscillations. We can obviously try to reduce reflections at facets, e.g. using a refractive-index-matching liquid. Nevertheless the best strategy seems to be an estimation

of the parameters of each cavity type (waveguide sections and resonator), see [125]. In that way we could characterize at once the whole device behaviour, provided the fitting model is accurate enough.

### 5.3.2 Demultiplexer based on large diameter disk

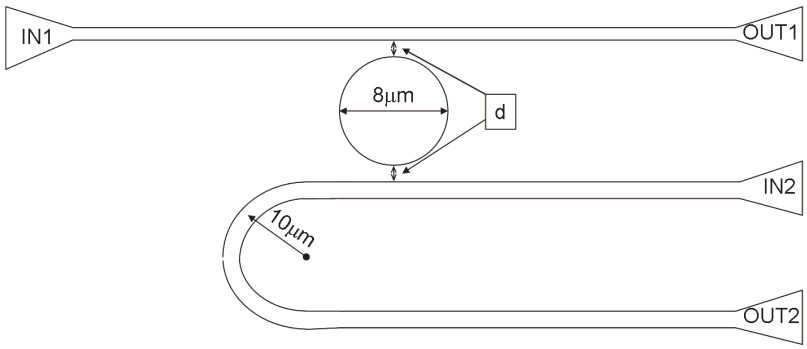


Figure 5.11: Schematic representation of an integrated add&drop device. Equal spacing is used. Through port corresponds to OUT1, drop port to OUT2. The large bent is necessary to collect output on the same side.

Drop function requires a single input, then is simply manageable with the IMEP facilities and we focus on it.

To access transmitted (through) and dropped channel, they have to lay on the same chip side, then one waveguide is straight, while the other is bent half-turn to reach the same side. To adopt a trade-off, we choose equal spacings at each cavity side, since it is hard to predict the quality factor of the resonator and design accurately the optimal features, according to eq. (5.9) and (5.11); these features are summarized in figure 5.11.

Obviously, we can use the device as a filter, without investigating the drop port. Selectivity properties are in general deteriorated due to the additional load of the second waveguide: quality factors are lower with respect to a single waveguide at the same distance. As indicated by equation (5.11), extinction ratio can ever be improved drawing waveguides closer and closer to microresonator.

We should also characterize the second output (dropped), at resonances. Anyway we have not performed such measures, but only tried to detect doublets in through port and understand how a design 'trick' can help mitigate this issue.

As for the filter, several structures with different guide-disk spacing were fabricated.

First of all we report the through port response corresponding to the resonance reported in figure 5.10. In figure 5.12, we focus our comparison on the most selective among those we showed above, $0.6\mu m$ spacing, and verify that increasing the load on the cavity implies a decrease of $Q$. Resonant wavelength has further decremented. We could conjecture that this

fact is ascribed to technological tolerances: no information on resonant frequency perturbation is provided by the method of section 5.1.3.

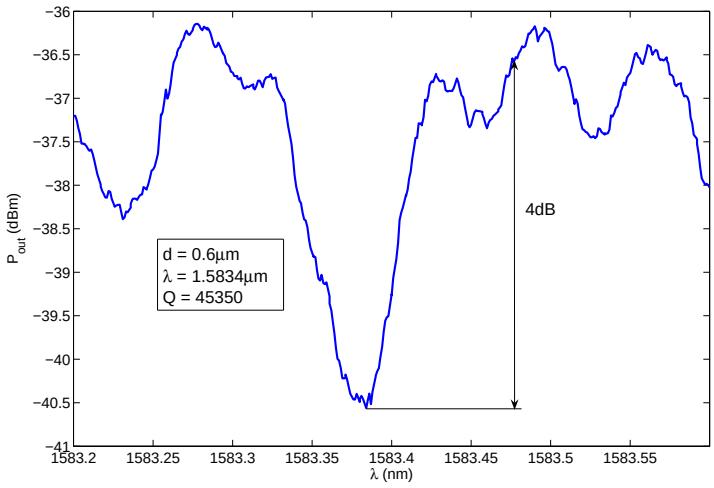


Figure 5.12: Through port response of an add&drop based on a $8\mu m$ diameter microdisk. Extraction peak correspond to those of figure 5.10

### Improving demultiplexer design

As we mentioned above, splitting of degeneracy is an important limiting issue of waveguide-coupled cavities. It leads to a wider resonant response (if $Q$ is not excessively high) or to the appearance of two distinct peaks. This limits the applicability of those structures.

Despite there exist several concurrent causes of splitting and despite we were not able to detect a doublet in our multiplexing device, we are discussing briefly a slight modification of A&D structure that may help mitigate the splitting phenomenon.

We modify the drop guide by a slight bend (about a degree), in such a way that the guide path in the proximity of the resonator is protracted, see fig. 5.13.

The idea is based on further perturbing the cavity modal structure and partially recover path balance between even and odd WGMs. Moreover, we could suppose that the additional bends lead to propagation losses that reduce the impact of reflection along the waveguide.

The design of such a device concentrated on bend angle and the disk-guide distance was set *a-priori* to $0.6\mu m$.

We did not detect splitting in our classical add&drop, even for a medium spacing that may allow to discern resonances while observing doublets. Anyway we compare two corresponding resonances of classical and new structure (of smallest bend angle).

From figure 5.14, we observe that the two peaks differ in quality factor (in (b) is larger) and extinction ratio (in (b) is smaller). This two data may be interpreted as a decreased coupling, then probably a technological misfit lead to a spacing larger in the second case than in the first. Not any other significant change is observed, nor in the other structures of this set.

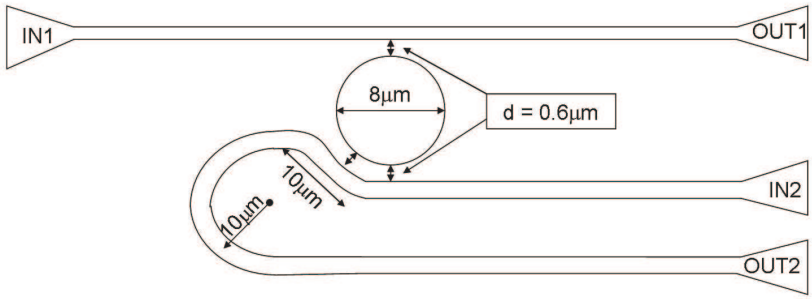


Figure 5.13: Same as 5.11, to show the design correction we applied, the drop guide is slightly bent in the proximity of microdisk. The oblique part is $10\mu m$ long. Several bend angles are used, $0.8°, 1.0°, 1.2°, 1.4°, 1.6°$.

## 5.4 Microgear-based Devices

As discussed in the introduction of chapter 4, cylindrical microresonators based on WGMs are multimode structures: both in azimuthal and radial directions. While radial modes of order larger than one enjoy in general a smaller quality factor, since their optical path has a small radius of curvature, varying azimuthal order does not lead to abrupt change in quality factor: azimuthal order and quality factor are almost directly dependent, increasing azimuthal order leads to higher $Q$s (and lower resonant wavelength). Then the typical spectral response of such a resonator presents a large number of resonances with a variety of $Q$s, then a reliable application to, e.g., selecting a specific band can be hampered by that property.

Specifically in laser applications, the competition between different high-$Q$ modes can be detrimental. Then Fujita and Baba proposed, see [126], to associate the selectivity properties of a cavity and a Bragg grating, in the so-called, *microgear*. It is composed by a disk surrounded by a periodic *multiteeth* structure. If one has to select the azimuthal mode of order $m$, a periodicity of $2m$ permits to achieve this result, see figure 5.15.

Teeth act as scatterers that induce two counterpropagating waves to establish, that in turn, as in Bragg gratings, permit to select specific modal structure, by forming specific interference patterns along the edge. This is the operating principle.

The new structure supports mainly two modes: the one whose maxima lie in the teeth and the one whose zeroes lie in the teeth. The first undergoes a selectivity improvement, its WGM is further compressed and confined in teeth; the second moves away from periphery, then its quality factor decreases, see [102].

The light coupling inside such devices is difficult, since if energy is coupled from a waveguide to a, e.g., clockwise mode, counterclockwise is excited and a reflected pulse can recouple into the waveguide itself. Hence isolated cavity performance are improved, but the simple coupling with a straight waveguide is not effective.

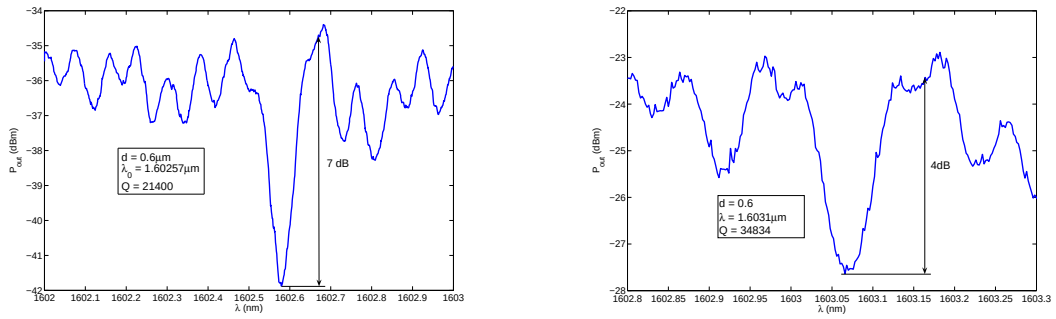


(a) (b)

Figure 5.14: Comparison between two add&drop structures, through channel response. In (a) the standard case that use two straight waveguides, in (b) the corresponding rejection peak of the modified one: drop waveguide bends to obtain a longer path near disk. $0.6\mu m$ spacings in both cases; oblique part is $10\mu m$ long, $0.8^\circ$ bend.

Supporting standing-waves crucially affects microgear performance, its behavior is different from simple microdisk resonators, based on travelling wave propagation, see [127].

Several microgear-based structures have been available, planar structures in both filter and add&drop configuration were fabricated.

Nevertheless we have not obtained any noticeable results, Fabry-Pérot oscillations mask resonances in almost every case.

For the sake of completeness we mention that, while a 2D modelling approach is available, see [128], a 3D version of that formalism has not been considered; many numerical issues will perhaps occur.

## 5.5 Conclusion and Perspectives

In this chapter we have described a few applications of microresonators and reported the results of several measures we performed. Many other applications could be achieved, particularly nonlinear effects can lead to bistability, also at relatively low injected power.

Silicon has a large thermo-optic coefficient, $\partial n/\partial T = 2 \times 10^{-4} K^{-1}$, thus if we excite a cavity resonance much energy is stored in it and via linear absorption is converted into heat; the temperature increases and in turn refractive index is increased, thus resonant wavelength is shifted upwards: an equivalent (focusing) Kerr effect is exhibited. Hence the static spectral response can be remarkably modified, see [129]. Dynamic measures can even detect multistability phenomena, in which many effects plays different roles, see [130]. Thermo-optic effect dominates in strength but is very slow with respect to nonlinear absorption and Kerr effect. An attempt to investigate at least the heat-induced bistability has been performed, by using fibres of smaller spot size, but no result has been obtained, also due to the accuracy of micropositioners.

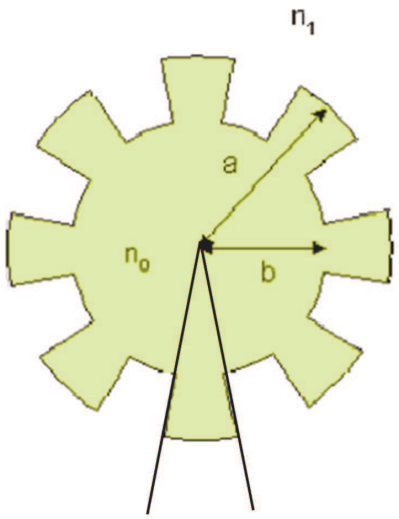


Figure 5.15: Schematic representation of a micro gear resonator, $a$ is the maximum radius, $b$ the minimum. $a - b$ is the teeth depth.

# Chapter 6

# Conclusions and Perspectives

In this work we presented several results of simulation and characterization of integrated optical devices.

We have focused on numerical methods that operate in the harmonic time-regime. They present analogies and differences: finite-difference schemes are generally more versatile, but demand more resources than modal methods. Indeed modal decomposition applies only to linear propagation and to specific geometries.

Our BPM implementation, in chapter 2 and appendix A, includes many advanced features, despite propagation methods based on finite difference schemes are being still improved, see [131] and [132]. We implemented this method to perform nonlinear optics analysis, like those presented in chapter 3, where we describe an interesting nonlinear trapping phenomenon, that could also serve in dynamic optical routing and processing.

One of the most important modal methods has been applied to cylindrical symmetric microresonators: the A-FMM described in chapter 4 permits to overcome the issues that typically affect other modal methods, i.e. the estimation of propagation constants (if complex), mode profiles and their overlap integrals. Our version is focused on describing the free-oscillation regime of microcavities, and a special attention has been used in solving the global eigenvalue problem to provide complex wavelengths. The application to simple cylindrical cavities (disk and ring) provides an accurate description; its critical comparison with simpler analyses (e.g., 2D EIM-based) and *ab-initio* approaches (e.g. FDTD) points out its benefits. The study of a new concept device (sandwich microdisk) has been sketched. It is well-known how the research in the field of microcavities has been flourishing all over the world for many years, and many applications have to be improved. Specifically the influence of technological tolerances and misfits have to be investigated. In this spirit, we characterized several structures, filters and add&drop's were analysed.

Our future projects encompass the improvement of NLBPM performance and accuracy, in order to obtain reliable results in briefer time, further investigation of the nonlinear optical regimes studied in chapter 3, to describe WGMs of micropillars and in general speed-up the cylindrical A-FMM code, to apply post-processing methods to properly detect resonant peaks masked by Fabry-Pérot oscillations in integrated optical circuits, and improve design criteria to obtain reliable and compact optical integrated devices.

# Appendix A

# Bidirectional BPM

In this appendix, we report an approach to adapt the BPM, as described in chapter 2, to bidirectional propagation, namely bidirectional BPM (BiBPM).

We employ the so-called *scattering-matrix* (S matrix) formalism, that consists in constructing reflection-transmission matrices at every interface and combine them to account for the overall transmission and reflection characteristic of a device.

It is the alternative approach to the admittance-impedance calculations of transmission lines, that we applied to the A-FMM, see chapter 4.

It can be argued that scattering matrices in microwave circuit engineering suppose to treat a single mode and how it combines at waveguide discontinuities or at the insertion of another electronic component. In optics we use this to denote simply a generalization of Fresnel formulas for plane-wave reflection-refraction applied to a superposition of many terms.

In, e.g., [34] this is applied to RCWA, while in, e.g., [26, 54, 55] the application in the BPM framework is faced.

It overcomes the stability issues of transmission matrix approach, that multiplies propagation and interface terms, without having care of the diverging behaviour of inverse propagators. Propagator indeed can be composed by evanescent terms, that after inversion can lead to large magnitude values and thus to accuracy or stability issues.

Consider that, while modal method use eigenmodes or their approximation, BPM can be considered to use a sum of field values in different points, a sort of Dirac comb as a basis.

The purpose of having a bidirectional BPM is to exploit the extensive versatility of the beam propagation method (that is able to describe nonlinear propagation, anisotropic media...), adding a crucial feature that permit to simulate 1D periodic structures, such as gratings, DBR, where interesting effects can be achieved (e.g., Kerr-effect induced bistability in Bragg grating), see [65].

The main limit of this approach is that wide-angle features are only approximated, 3D implementation would be too demanding in terms of resources (as much or even more than the other 3D finite difference methods) and nonlinearities are included as perturbative terms, then can sometimes fail in providing reliable results (both for accuracy and convergence issues).

## A.1 Definition of Scattering Matrix

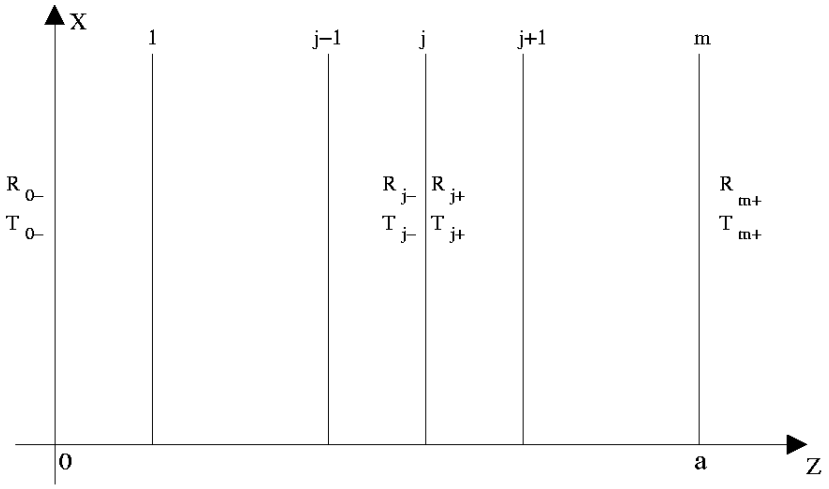


Figure A.1: Representation of a piecewise homogeneous planar structure. Abrupt discontinuities generate partial reflection-refraction of field components.

We follow the derivation of [55]. Let us consider a planar waveguide with propagation axis along $z$ (figure A.1), and let us assume that for $z < 0$ and $z > a$ no longitudinal discontinuities occur. In $[0, a]$ $m$ differenent sections compose our guiding structure: they are $z$-invariant for $z_{j-1} < z < z_j$ with $j = 1, 2, \ldots, m$, where $z_0 = 0$ and $z_m = a$. TE polarized field is ruled in each section by Helmholtz equation, that we express as, compare with (2.1)

$$\frac{\partial^2 E}{\partial z^2} + \left( \frac{\partial^2}{\partial x^2} + k_0^2 n^2(x, z) \right) E = 0, \tag{A.1}$$

where as usual $k_0 = \frac{2\pi}{\lambda}$ is the free-space wavenumber, the refractive index profile $n(x, z)$ is piecewise constant in $z$, i.e.

$$n(x, z) = n_j(x) \text{ for } z_{j-1} < z < z_j, \ j = 0, 1, \ldots, m + 1$$

where $z_{-1} = -\infty$ and $z_{m+1} = +\infty$ are assumed.

We recall the definition of square root, $L_j$, and linear propagation, $P_j$, operators for $j$-th layer are defined as

$$L_j = \sqrt{\frac{\partial^2}{\partial x^2} + k_0^2 n_j^2(x)} = k_0 n_0 \sqrt{I + \frac{\frac{\partial^2}{\partial x^2} + k_0^2 \left( n_j^2(x) - n_0^2 \right)}{k_0^2 n_0^2}}, \tag{A.2}$$

$$P_j = \exp\{-j(z_j - z_{j-1}) L_j\}. \tag{A.3}$$

The implementation is made in the same way used in sections 2.4 and 2.5. Helmholtz equation can be expressed in the following form,

$$\frac{\partial^2 E}{\partial z^2} + L_j^2 E = 0. \tag{A.4}$$

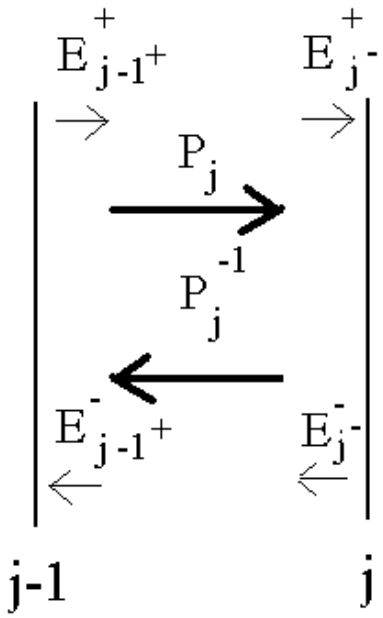


Figure A.2: Schematic representation of fields terms and propagators.

In each layer we express the electric field as a superposition of two counterpropagating waves, ($E^+$ towards $z = +\infty$ and $E^-$ towards $z = -\infty$): obviously they separately satisfy

$$\frac{\partial E^+}{\partial z} = -jL_j E^+ \tag{A.5}$$

$$\frac{\partial E^-}{\partial z} = jL_j E^- \tag{A.6}$$

for $z_{j-1} < z < z_j$, $E = E^+ + E^-$.

The formal solution of (A.4) in $z_{j-1} < z < z_j$ reads as

$$E(x,z) = E^+_{j-1^+} e^{-jL_j(z-z_{j-1})} + E^-_{j-1^+} e^{jL_j(z-z_{j-1})} \tag{A.7}$$

Then, compare with fig. A.2, we can write

$$E^+_{j^-} = P_j E^+_{j-1^+} \tag{A.8}$$

$$E^-_{j^-} = P_j^{-1} E^-_{j-1^+} \tag{A.9}$$

where

$$E^+_{j^-} = \lim_{z \to z_j^-} E^+(x,z)$$

$$E^+_{j-1^+} = \lim_{z \to z_{j-1}^+} E^+(x,z)$$

$$E^-_{j^-} = \lim_{z \to z_j^-} E^-(x,z)$$

$$E^-_{j-1^+} = \lim_{z \to z_{j-1}^+} E^-(x,z)$$

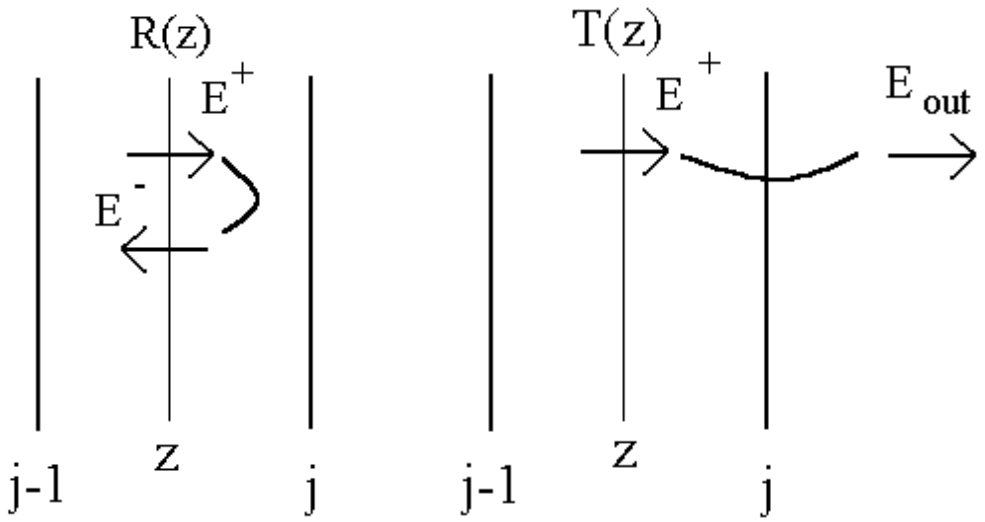


(a) (b)

Figure A.3: Schematic view of reflection (a) and transmission (b) operators as they operate on field components.

In general the overall *reflection matrix* $R(z)$ is defined by $R(z)E^+(x,z) = E^-(x,z)$, see fig. A.3(a) and the *transmission matrix* is in turn defined by $T(z)E^+(x,z) = E(x,z_m^+)$, see fig. A.3(b): they permit to calculate the global effect of the contribution of direct field (toward $z > 0$) to the reflected component in the same point and in the rightmost edge of the structure. The linear response of a multilayer structure is then readily obtained. Their value at each interface edge reads as

$$R_{j^+}E^+_{j^+} = E^-_{j^+} \tag{A.10}$$

$$R_{j^-}E^+_{j^-} = E^-_{j^-} \tag{A.11}$$

$$T_{j^+}E^+_{j^+} = E^+_{m^+} \tag{A.12}$$

$$T_{j^-}E^+_{j^-} = E^+_{m^+} \tag{A.13}$$

Input is supposed to come only from the left side of the structure, i.e. from $z < 0$, see fig. A.4, then scattering matrices at the rightmost side are known: the solution is provided starting from

$$R_{m^+} = 0, \quad T_{m^+} = I \tag{A.14}$$

A chain rule has to be derived to compute $T_{0^-}$ and $R_{0^-}$, finally we solve the problem and $E^-_{0^-}$ and $E^+_{m^+}$ can be obtained from $E^+_{0^-}$.

That consists in relating S matrices at the left and right edges of a longitunal homogeneous layer, and determining how they transform in crossing an interface.

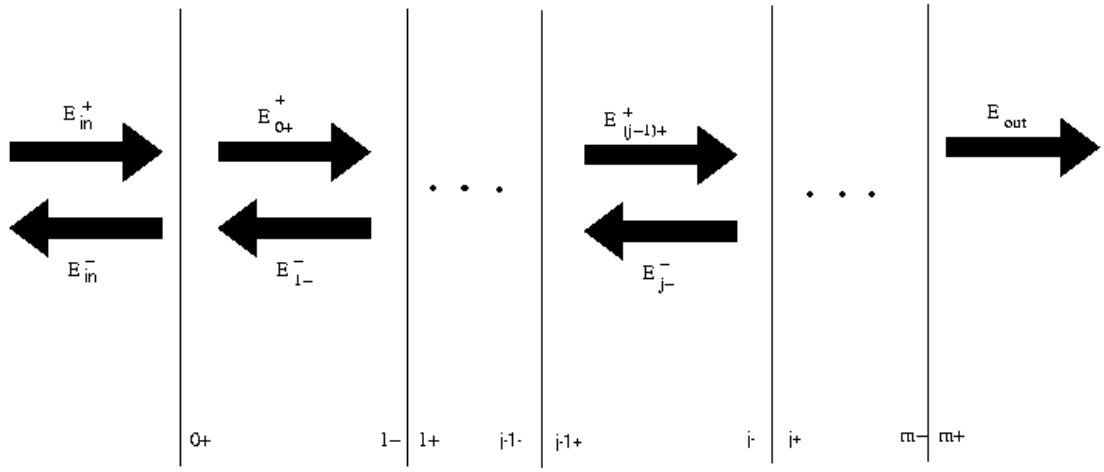


Figure A.4: Field components inside a multilayer structure.

### A.1.1 Propagation step

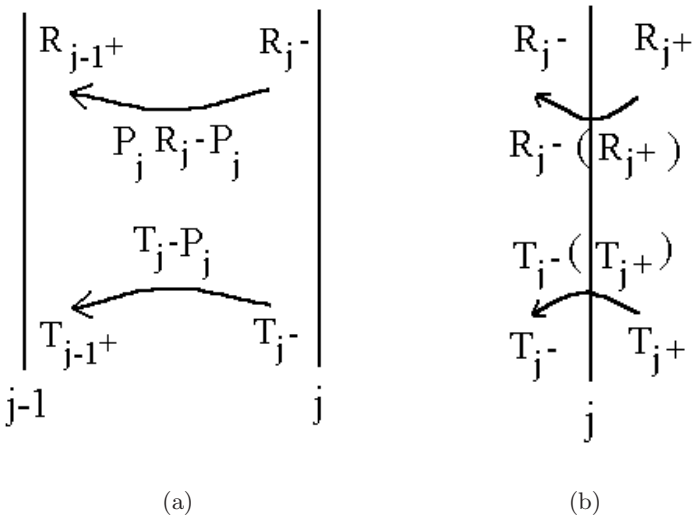


(a) (b)

Figure A.5: Propagation step for $R$ and $T$ (a) and interface continuity (b).

The relation between $R_{j-1^+}$ and $R_{j^-}$ allows to propagate backward the $R$ matrix along

a $z$-invariant layer.

$$\begin{aligned} R_{j-1^+}E^+_{j-1^+} &= E^-_{j-1^+} = \\ &= P_j E^-_{j^-} = \\ &= P_j R_{j^-} E^+_{j^-} = \\ &= \left(P_j R_{j^-} P_j\right) E^+_{j-1^+} \\ &\Downarrow \\ R_{j-1^+} &= P_j R_{j^-} P_j, \end{aligned} \tag{A.15}$$

where (inverted) A.9, A.11, and A.8 were substituted.

The same procedure permits to obtain $T_{j-1^+}$ as a function of $T_{j^-}$.

$$\begin{aligned} T_{j-1^+}E^+_{j-1^+} &= E^+_{m^+} = \\ &= T_{j^-} E^+_{j^-} = \\ &= T_{j^-} P_j E^+_{j-1^+} \\ &\Downarrow \\ T_{j-1^+} &= T_{j^-} P_j, \end{aligned} \tag{A.16}$$

where A.13 and A.8 are applied.

Figure A.5(a) summarizes these equations.

### A.1.2 Interface crossing

Scattering operators have also to be transformed passing from $z_j^+$ to $z_j^-$, two opposed sides of a longitudinal discontinuity, figure A.5(b).

TE polarization requires that the field and its derivative are continuous at interfaces.

Field at $z_j^-$ is expressed as

$$\begin{aligned} E_{j^-} &= E^+_{j^-} + E^-_{j^-} = \\ &= E^+_{j^-} + R_{j^-} E^+_{j^-} = \\ &= \left[I + R_{j^-}\right] E^+_{j^-} \end{aligned} \tag{A.17}$$

and at $z_j^+$

$$\begin{aligned} E_{j^+} &= E^+_{j^+} + E^-_{j^+} = \\ &= E^+_{j^+} + R_{j^+} E^+_{j^+} = \\ &= \left[I + R_{j^+}\right] E^+_{j^+} \end{aligned} \tag{A.18}$$

Derivatives can be formally expressed as

$$\frac{\mathrm{d}}{\mathrm{d}z} E_{j^-} = jL_j \left[-I + R_{j^-}\right] E^+_{j^-} \tag{A.19}$$

$$\frac{\mathrm{d}}{\mathrm{d}z} E_{j^+} = jL_{j+1} \left[-I + R_{j^+}\right] E^+_{j^+} \tag{A.20}$$

Continuity conditions are summarized as

$$\begin{cases} \left[I + R_{j^-}\right] E^+_{j^-} = \left[I + R_{j^+}\right] E^+_{j^+} \\ L_j \left[-I + R_{j^-}\right] E^+_{j^-} = L_{j+1} \left[-I + R_{j^+}\right] E^+_{j^+} \end{cases} \tag{A.21}$$

After a few algebra we obtain

$$R_{j^-} = (I + C)^{-1}(I - C) \tag{A.22}$$

where

$$C = L_j^{-1} L_{j+1} \left[I - R_{j^+}\right] \left[I + R_{j^+}\right]^{-1} \tag{A.23}$$

From A.12 and A.13 we can write, for $T$,

$$T_{j^-} E^+_{j^-} = E^+_{m^+} = T_{j^+} E^+_{j^+}$$

We multiply by $\left[I + R_{j^-}\right]$ and using eq. (A.21),

$$T_{j^-} = T_{j^+} \left[I + R_{j^+}\right]^{-1} \left[I + R_{j^-}\right] \tag{A.24}$$

Let us summarize the procedure:

- $R_{m^+} = 0$, $T_{m^+} = I$
- For $j = m, m-1, \ldots, 1, 0$
  - $C = L_j^{-1} L_{j+1} \left[I - R_{j^+}\right] \left[I + R_{j^+}\right]^{-1}$
  - $R_{j^-} = (I + C)^{-1}(I - C)$
  - $T_{j^-} = T_{j^+} \left[I + R_{j^+}\right]^{-1} \left[I + R_{j^-}\right]$
  - If $j > 0$
    - $R_{j-1^+} = P_j R_{j^-} P_j$
    - $T_{j-1^+} = T_{j^-} P_j$
- $E^-_{0^-} = R_{0^-} E_{in}$
- $E_{out} = T_{0^-} E_{in}$

TM polarisation can be modeled as well, see [56].

To compute the field values all along the device, scattering matrices at both sides of each layer are stored. At each interface we can compute reflection and propagate backwards to obtain the total field. Calculating transmission at the same discontinuity, we then propagate forwards until the successive interface is reached.

## A.2 Nonlinear BiBPM

This section will be devoted to a brief discussion about the inclusion of nonlinear effects in the BiBPM. We refer to [65], where a split step solution is combined to scattering matrix formalism.

As stated in section 1.5, to consider third order self-action is quite simple, we have only to adapt refractive index according to local intensity. The analysis of second-order effects, such as SHG, is instead precluded to modal method, except if undepleted-pump approximation is used (the nonlinear effect generates a SH, but does not subtract energy from FF), see [35].

### A.2.1 Third order nonlinearities

As in section 1.3, we assume two counterpropagating waves, at frequency $\omega$, to interact in a periodic structure and develop a CMT system. Let $E^+(x,z) = u^+(x,z)\exp(-jk_0n_0z)$ the forward field expressed in terms of a slowly varying envelope and a phase rotation of reference index $n_0$, we write

$$\begin{aligned}-2jk_0n_0\frac{\partial u^+(x,z)}{\partial z} + \frac{\partial^2 u^+(x,z)}{\partial z^2} + \frac{\partial^2 u^+(x,z)}{\partial x^2} + k_0^2\left[n_j^2(x) - n_0^2\right]u^+(x,z) + \\ + \frac{3}{4}\frac{\omega^2}{c_0^2}\chi_j^{(3)}(x)\left[\left|u^+(x,z)\right|^2 + 2\left|u^-(x,z)\right|^2\right]u^+(x,z) = 0\end{aligned} \tag{A.25}$$

and posing the backward wave, $E^-(x,z) = u^-(x,z)\exp(-jk_0n_0z)$,

$$\begin{aligned}2jk_0n_0\frac{\partial u^-(x,z)}{\partial z} + \frac{\partial^2 u^-(x,z)}{\partial z^2} + \frac{\partial^2 u^-(x,z)}{\partial x^2} + k_0^2\left[n_j^2(x) - n_0^2\right]u^-(x,z) + \\ + \frac{3}{4}\frac{\omega^2}{c_0^2}\chi_j^{(3)}(x)\left[\left|u^-(x,z)\right|^2 + 2\left|u^+(x,z)\right|^2\right]u^-(x,z) = 0\end{aligned} \tag{A.26}$$

$n_j(x)$ and $\chi_j^{(3)}(x)$ are linear refractive index and nonlinear susceptibility of layer $j$. As in chapter 3, self and cross action appear.

Following the *split-step* method, we solve linear and nonlinear problems separately. Linear problem reads as,

$$\frac{\partial^2 u^\pm(x,z)}{\partial z^2} \mp 2jk_0n_0\frac{\partial u^\pm(x,z)}{\partial z} + \frac{\partial^2 u^\pm(x,z)}{\partial x^2} + k_0^2\left[n_j^2(x) - n_0^2\right]u^\pm(x,z) = 0 \tag{A.27}$$

that we can solve also using wide-angle Padé approximation, while for NL step we limit to paraxial propagation as in CMT, i.e.

$$\frac{\partial u^+(x,z)}{\partial z} = -j\gamma_j(x)\left[\left|u^+(x,z)\right|^2 + 2\left|u^-(x,z)\right|^2\right]u^+(x,z) \tag{A.28}$$

$$\frac{\partial u^-(x,z)}{\partial z} = j\gamma_j(x)\left[\left|u^-(x,z)\right|^2 + 2\left|u^+(x,z)\right|^2\right]u^-(x,z) \tag{A.29}$$

for forward and backward envelopes, where

$$\begin{aligned}\gamma_j(x) &= 2\pi n_{2,j}(x)n_j(x)/(\lambda n_0)\\ n_{2,j}(x) &= 3\chi_j^{(3)}(x)/[8n_j(x)]\end{aligned}$$

$n_{2,j}(x)$ represents nonlinear index profile in section $j$.

As in chapter 2 an iterative split-step method permits to successively refine solutions. From eqs. (A.28) and (A.29), we can derive the nonlinear propagation step,

$$u^+(x,z+\Delta z) = \exp\left\{-j\gamma_j(x)\left[\left|u^+(x,z)\right|^2 + 2\left|u^-(x,z)\right|^2\right]\Delta z\right\} u^+(x,z) \tag{A.30}$$

$$u^+(x,z-\Delta z) = \exp\left\{-j\gamma_j(x)\left[\left|u^-(x,z)\right|^2 + 2\left|u^+(x,z)\right|^2\right]\Delta z\right\} u^-(x,z) \tag{A.31}$$

To obtain a scattering matrix formulation for this problem, it is sufficient to construct propagator and diffraction (square-root) operators including the nonlinear modulation of refractive indices.

Let us start from propagators,

$$p^+_{j,q_{NL}} = \exp\left\{-j\gamma_j(x)\left[\left|u^+(x,z)\right|^2 + 2\left|u^-(x,z)\right|^2\right]\Delta z\right\}\Big|_{z=z_{j-1}+(q-1)\Delta z} I \tag{A.32}$$

$$p^-_{j,q_{NL}} = \exp\left\{-j\gamma_j(x)\left[\left|u^-(x,z)\right|^2 + 2\left|u^+(x,z)\right|^2\right]\Delta z\right\}\Big|_{z=z_j-(q-1)\Delta z} I \tag{A.33}$$

where $I$ is the identity matrix. We propagate for a small step, form $(q-1)$ to $q$, inside the $j$-th layer to improve accuracy. $Q$ substeps are assumed to constitute layer $j$, $z_j - z_{j-1} = Q\Delta z_j$, then the overall propagator in that section becomes

$$P^\pm_j = \prod_{q=1}^{Q} p^\pm_{j,q_{NL}} p_{j_{LIN}} \tag{A.34}$$

where $p_{j_{LIN}}$ denotes simply the propagator inside layer $j$, for the small substeps. We obtain two different propagators, depending on propagation direction: this is indeed the cause of bistability phenomena.

To impose continuity conditions, we consider that index profiles are functions of the field intensity, i.e.,

$$n^\pm_j(x) = n_j(x) + n_{2,j}(x)\left[\left|u^\pm_{j^-}\right|^2 + 2\left|u^\mp_{j^-}\right|^2\right], \tag{A.35}$$

$$n^\pm_{j+1}(x) = n_{j+1}(x) + n_{2,j+1}(x)\left[\left|u^\pm_{j^+}\right|^2 + 2\left|u^\mp_{j^+}\right|^2\right], \tag{A.36}$$

where $+$ and $-$ are index profiles as experienced by forward and backward waves respectively. Four square-root operators are thus involved at each interface, $L^+_j$, $L^-_j$, $L^+_{j+1}$, and $L^-_{j+1}$.

Operators are thus to be updated at each refinement step. The same results of section A.1 are obtained, except for the fact operator,

$$R_{j-1^+} = P^-_j R_{j^-} P^+_j \tag{A.37}$$

and

$$T_{j-1^+} = T_{j^-} P^+_j \tag{A.38}$$

apply to propagation along a section, and

$$R_{j^-} = (I + C_2)^{-1}(I - C_1) \tag{A.39}$$

$$T_{j^-} = T_{j^+} \left[I + R_{j^+}\right]^{-1} \left[I + R_{j^-}\right] \tag{A.40}$$

with

$$C_1 = \left(L_j^+\right)^{-1} \left[L_{j+1}^+ - L_{j+1}^- R_{j^+}\right] \left[I + R_{j^+}\right]^{-1} \tag{A.41}$$

$$C_2 = \left(L_j^-\right)^{-1} \left[L_{j+1}^+ - L_{j+1}^- R_{j^+}\right] \left[I + R_{j^+}\right]^{-1} \tag{A.42}$$

apply to interface crossing.

At each iteration we must calculate field amplitude at each grid step, and update every operator.

### A.2.2 SHG simulation

Let us assume quadratic interactions take place mainly between co-propagating beams. An ansatz composed by two couterpropagating FF and SH fields is used to obtain a CMT system, slightly more complicated with respect to section 1.3; $n_{0,2\omega} = 2n_{0,\omega}$ is supposed, that is a phase-matching condition. This is not rigorously achieved, and sometimes causes accuracy issues, since envelopes include excess phase rotation that amplify numerical errors.

FF envelopes obey (superscripts + and − denote propagation direction):

$$\begin{aligned} \frac{\partial^2 u_\omega^\pm(x,z)}{\partial z^2} \mp 2jk_0 n_0 \frac{\partial u_\omega^\pm(x,z)}{\partial z} + \frac{\partial^2 u_\omega^\pm(x,z)}{\partial x^2} + k_0^2 \left[n_j^2(x) - n_0^2\right] u_\omega^\pm(x,z) = \\ = -k_0^2 \chi_j^{(2)}(x) \left[u_\omega^\pm(x,z)\right]^* u_{2\omega}^\pm(x,z) \end{aligned} \tag{A.43}$$

where $\chi_j^{(2)}(x)$ is the profile of nonlinear susceptibility in section $j$.

SH envelopes obey

$$\begin{aligned} \frac{\partial^2 u_{2\omega}^\pm(x,z)}{\partial z^2} \mp 4jk_0 n_0 \frac{\partial u_{2\omega}^\pm(x,z)}{\partial z} + \frac{\partial^2 u_{2\omega}^\pm(x,z)}{\partial x^2} + 4k_0^2 \left[n_j^2(x) - n_0^2\right] u_{2\omega}^\pm(x,z) = \\ = -2k_0^2 \chi_j^{(2)}(x) \left[u_\omega^\pm(x,z)\right]^2 \end{aligned} \tag{A.44}$$

The solution of eqs. (A.43) and (A.44) is accomplished by split-step approach, as in section 2.2. Linear propagators in $j$ layer substeps, $p_{j,\omega}$ and $p_{j,2\omega}$, are in the same form of those reported in section A.2.1.

In each generic layer $j$ we write nonlinear contributions as additive contributions, i.e.

$$E_{t,j^-}^+ = P_{t,j} E_{t,j-1^+}^+ + X_{t,j}^+ \tag{A.45}$$

$$E_{t,j-1^+}^- = P_{t,j} E_{t,j^-}^- + X_{t,j}^- \tag{A.46}$$

where $t = \omega, 2\omega$.

Kerr effect leads to additional phase rotation, then we have described a construction of new operators multiplying intensity-dependent contributions; in this case we consider instead a combination of additive terms,

$$X_{t,j}^\pm = \sum_{q=1}^{Q} p_{t,j}^{(Q-q)} \left(x_{t,j}^\pm\right)_q \tag{A.47}$$

where

$$x_{t,j}^{\pm} = \begin{cases} -j\Delta z \dfrac{k_0^2 \chi_j^{(2)}(x)}{4k_0 n_0} \left\{ \left[ u_\omega^{\pm}(x, z \pm \Delta z) \right]^* u_{2\omega}^{\pm}(x,z) + \right. & \text{if } t = \omega \\ \left. + \left[ u_\omega^{\pm}(x,z) \right]^* u_{2\omega}^{\pm}(x, z \pm \Delta z) \right\} e^{\mp j k_0 n_0 z} & \\ -j\Delta z \dfrac{k_0^2 \chi_j^{(2)}(x)}{2k_0 n_0} u_\omega^{\pm}(x,z) u_\omega^{\pm}(x, z \pm \Delta z) e^{\mp j 2k_0 n_0 z} & \text{if } t = 2\omega \end{cases} \tag{A.48}$$

To couple FF and SH, additive terms have to be considered also in scattering matrices,

$$R(z)E^+(x,z) + W_t(x,z) = E^-(x,z) \tag{A.49}$$

$$T(z)E^+(x,z) + K_t(x,z) = E^+(x,a^+) \tag{A.50}$$

where $W_t(x,z)$ and $K_t(x,z)$ account for nonlinear interaction. Iterative split-step allows us to solve independently FF and SH problems, constructing the two additive terms as column vectors depending on previously calculated field values.

Let us derive the $t = \omega$ relations. Initial conditions for matrices $R_\omega$ and $T_\omega$ and vectors $W_\omega$ and $K_\omega$ are set to

$$\begin{aligned} R_{\omega,m^+} &= 0, \quad T_{\omega,m^+} = I \\ W_{\omega,m^+} &= 0, \quad K_{\omega,m^+} = 0 \end{aligned}$$

A new chain rule to compute $R_{\omega,0^-}$, $T_{\omega,0^-}$, $W_{\omega,0^-}$, and $K_{\omega,0^-}$ permits to calculate the global device response.

While (A.15) and (A.16) are still valid, from (A.45)–(A.50) we derive

$$W_{\omega,j-1^+} = P_{\omega,j} R_{\omega,j^-} X_{\omega,j}^+ + P_{\omega,j} W_{\omega,j^-} + X_{\omega,j}^- \tag{A.51}$$

$$K_{\omega,j-1^+} = K_{\omega,j^-} + T_{\omega,j^-} X_{\omega,j}^+. \tag{A.52}$$

In fact, e.g.,

$$\begin{aligned} R_{\omega,j-1^+} E_{\omega,j-1^+}^+ + W_{\omega,j-1^+} &= E_{\omega,j-1^+}^- = \\ &= P_{\omega,j} E_{\omega,j^-}^- + X_{\omega,j}^- = \\ &= P_{\omega,j} \left[ R_{\omega,j^-} E_{\omega,j^-}^+ + W_{\omega,j^-} \right] + X_{\omega,j}^- = \\ &= P_{\omega,j} R_{\omega,j^-} P_{\omega,j} E_{\omega,j-1^+}^+ + \\ &+ P_{\omega,j} R_{\omega,j^-} X_{\omega,j}^+ + P_{\omega,j} W_{\omega,j^-} + X_{\omega,j}^-. \end{aligned} \tag{A.53}$$

It is easy to verify that eqs. (A.15) and (A.51) can be extracted from (A.53).

Continuity conditions should be modified according to rigorous electromagnetic theory, but nonlinear contributions are proven to be negligible, see [68]. To obtain the interface crossing formulas, we thus start from

$$\begin{cases} \left[ I + R_{\omega,j^-} \right] E_{\omega,j^-}^+ + W_{\omega,j^-} = \left[ I + R_{\omega,j^+} \right] E_{\omega,j^+}^+ + W_{\omega,j^+} \\ L_{\omega,j} \left\{ \left[ -I + R_{\omega,j^-} \right] E_{\omega,j^-}^+ + W_{\omega,j^-} \right\} = L_{\omega,j+1} \left\{ \left[ -I + R_{\omega,j^+} \right] E_{\omega,j^+}^+ + W_{\omega,j^+} \right\} \end{cases} \tag{A.54}$$

Eqs. (A.22)–(A.23) are still valid and we add

$$W_{\omega,j^-} = \left\{ \left[I + R_{j^+}\right] \left[-I + R_{j^+}\right]^{-1} L_{j+1}^{-1} L_j - I \right\}^{-1} \left\{ \left[I + R_{j^+}\right] \left[-I + R_{j^+}\right]^{-1} - I \right\} W_{\omega,j^+} \tag{A.55}$$

$$K_{\omega,j^-} = T_{\omega,j^+} \left[I + R_{j^+}\right]^{-1} \left[W_{\omega,j^-} - W_{\omega,j^+}\right] + K_{\omega,j^+} \tag{A.56}$$

As above, the computation of scattering operators and nonlinear perturbations permits to obtain the input-output response of a periodic system. In order to compute field amplitudes at each step, their stored value at each interface are required. The additional nonlinear terms are computed starting from field values obtained in the previous iteration. This iterative procedure is aimed to refine the results, until only negligible changes are achieved.

It is difficult to choose a proper initial guess, specifically to consider bidirectional propagation at both harmonics. The use of FF linear solution as guess is sometimes useful, particularly in a weak conversion regime.

Nevertheless the simulation of strong nonlinear regimes requires many iterations and a fine mesh, otherwise convergence is quite rarely achieved.

# Appendix B

# Solution of electromagnetic eigenvalue problems

In chapter 4 we have discussed the computation of resonant wavelength of cylindrical microresonators.

In a large class of electromagnetic problems, such as solution of mode propagation constants, we have to solve a nonlinear eigenvalue problem, i.e. a problem that can be expressed as

$$A(\lambda)x = 0, \tag{B.1}$$

where $A$ is a matrix function of the eigenvalue $\lambda$ and $x$ is the corresponding eigenvector.

If we deal with real eigenvalues, like wavenumbers of slab guided modes, it is easy to recast (B.1) in a nonlinear equation or system, and solve it by means of standard methods. The problem is harder if leaky modes are required. Similar problems are tackled in the classical modal method, if PMLs are used, see [29].

In the A-FMM, this is no more an issue, but our approach operates in the free oscillation (complex frequency) regime, then a crucial and difficult task is to obtain *complex resonant wavelengths*, for high $Q$ quasi-TE and -TM modes.

In section 4.4 we have discussed how to obtain a *homogeneous linear system* of algebraic equations and how we solve it.

Here we are summarizing the main approaches we analysed before choosing the SVD minimization.

The trivial solutions of (B.1) are provided for $\lambda$ that satisfy

$$\det A = 0. \tag{B.2}$$

Usually, despite not dealing with very large matrices, $(4M+2)\times(4M+2)$ with $M \simeq 100$, computing the determinant of $A$ in equation (B.1) leads to overflow errors. This can be faced by using a logarithmic scale and/or a suitable rescaling of matrix coefficients, to prevent accuracy losses in treating numerical values.

## B.1 Zero Eigenvalue Searching

It is worth noticing that eq. (B.1) can be alternatively tackled as the computation of the complex frequencies corresponding to matrices with at least one *zero eigenvalue*, thus the solving function is computed as the nearest-to-zero eigenvalue. In formulae,

$$Ax = \mu x, \text{ with } \mu = 0.$$

This approach requires that this null eigenvalue is of unitary multiplicity, otherwise two or more near-to-zero eigenvalues can lead to uncertainty on eigenvector choice, because the null space of the matrix has, at least numerically, a dimension larger than one.

In both determinant and zero eigenvalue approaches we must look for a numerical zero of a function such as

$$f : \mathbb{C} \to \mathbb{C} \tag{B.3}$$

with

$$\lambda \to f(\lambda) = \det A \tag{B.4}$$

or

$$\begin{aligned} \lambda \to f(\lambda) &= \min_j \{|\mu_j|\} \text{ with} \\ A(\lambda)\zeta_j &= \mu_j \zeta_j \end{aligned} \tag{B.5}$$

then this approach is still a root-finding in the complex plane. In general is not very reliable, since we deal with a nearly singular matrix, eigenvalues are generally far away from one another. This can cause numerical issues, but the idea of matrix decomposition can be better exploited, thus we consider the *singular value decomposition* (SVD).

## B.2 SVD and Minimization

The solution used in our work is, as already recalled, based upon minimization of least-magnitude singular value (SV), see [104].

We recall that in general SVD applies to complex rectangular matrices, $A \in \mathbb{C}^{m \times n}$, and can be expressed as

$$A = U\Sigma V^+ = U \begin{pmatrix} \sigma_1 & & & & \\ & \sigma_2 & & & \\ & & \ddots & & \\ & & & 0 & \\ & & & & 0 \end{pmatrix} V^+ \tag{B.6}$$

where $\Sigma$ is a diagonal $p \times p$ matrix, where $p = \min\{n, m\}$ and

$$\sigma_1 \geq \sigma_2 \geq \cdots \sigma_k > 0 \text{ are all non-negative real numbers, } k \leq p, \tag{B.7}$$

and

$$A^+A = V \begin{pmatrix} \sigma_1^2 & & & & \\ & \sigma_2^2 & & & \\ & & \ddots & & \\ & & & 0 & \\ & & & & 0 \end{pmatrix} V^+ \tag{B.8}$$

$$AA^+ = U \begin{pmatrix} \sigma_1^2 & & & & \\ & \sigma_2^2 & & & \\ & & \ddots & & \\ & & & 0 & \\ & & & & 0 \end{pmatrix} U^+ \tag{B.9}$$

(B.10)

with $^+$ we denote the conjugate transpose and from the latter equation U and V turn out to have as columns, respectively, left and right singular vectors of $A$, or the right eigenvectors of $AA^+$ and $A^+A$, respectively. The SVD existence is based on the fact that this latter two matrices are positive semidefinite ($n \times n$ and $m \times m$ respectively.)

Solving our problem in this form is no more a root-finding formulation, but nonlinear function minimization. Let $A$ is $n \times n$ and $\text{rank}(A) = n$,

$$A = U\Sigma V^+ = U \begin{pmatrix} \sigma_1 & & & & \\ & \sigma_2 & & & \\ & & \ddots & & \\ & & & \sigma_{n-1} & \\ & & & & \sigma_n \end{pmatrix} V^+ \tag{B.11}$$

to satisfy eq. (B.2) one among the SVs $\sigma_k$ has to be zero. From eq. (B.7), since SVs are all *real* and *non-negative* and zero-crossing is never attained, we must calculate $\lambda$ for which $\sigma_n \to 0$: a minimization of $\sigma_n$ to meet this condition correspond to solving (B.1). The modal weights are thus expressed by the last column of $V$.

Although root-finding is generally easier than minimization, numerical properties of matrices involved in many electromagnetic problems suggest using this strategy, see [104]. In formulae,

$$f : \mathbb{C} \to \mathbb{R}^+ \tag{B.12}$$

with

$$\lambda \to f(\lambda) = \min_{1\ldots 4M} \sigma\left(A\right) \tag{B.13}$$

The solution can be written as

$$\lambda : \min_{\lambda \in \mathbb{C}, \text{Re}\{\lambda\}>0, \text{Im}\{\lambda\}<0} f = 0 \tag{B.14}$$

and the algorithm is expressed by eq. (4.51).

We must then be able to solve two numerical problems, compute the smallest singular value and minimize the resulting function.

SVD is generally computationally demanding; in addition to direct methods, which calculate all singular value and singular vectors and are among the most robust linear algebra applications, there exist iterative methods particularly suitable for large sparse matrices (to exploit compact storage features), that compute a few SVs among the largest and smallest ones quite quickly; we mention Arnoldi and Lanczos methods, see [133]. It is also possible to consider preconditioned [1] methods, that avoid singular value clustering (too many small SVs in the same range) and large matrix norm, that generally could mean slow convergence in iterative linear algebra algorithms.

Nevertheless, we verified that our matrix dimensions are compatible to the use of classical direct computation of the full SVD.

As far as minimization is concerned, we have used *Nelder-Mead* algorithm for non-linear unconstrained minimization, see [108] for some notes and an example of *Mathematica*® implementation. This approach, also known as *simplex method* does not require to compute derivatives (in optimization problems such a method is referred as *direct*) and is based on geometrical considerations. It constructs a simplex (the generalization of a 2D triangle in $\mathbb{R}^n$) and shrinks, moves or rebuild it comparing the function values at vertices. This method is proved to converge slowly but quite safely in a wide range of applications (also for "ill-behaved" functions). In order not to fall outside a proper range, a coordinate transform is applied to Nelder-Mead method to adapt it to bounded region, see [134].

Other direct methods include the minimization of a model (usually an interpolation) describing (hopefully accurately) the objective function.

The combination of iterative SVD (when applies, to compute the smallest SV only) and minimization (intrinsically iterative) has to be treated with care. SVs have to be computed to meet a sufficiently small tolerance with respect to minimization tolerance. [2]

Finally we observe that even with direct SVD and simplex minimization, that are generally very robust, convergence is sometimes not reliable, minimization stops in implausible points. This depend on the shape of the function to minimize: this issue affecting SVD and the fact that determinant computation diverges are strictly related: if determinant has poles, the minima of SVs are very sharp, so it is not easy to "dive" exactly into them.

However this method seems the most promising among those we studied.

## B.3 Fictitious System Inversion

An alternative approach based upon linear algebra consideration was proposed by Sudbø, see [32].

1. Preconditioning is aimed to reduce the *condition number* of a matrix involved in a linear algebra problem. This parameter measures how a perturbation in data or operation affects final results.

2. Generally speaking, a method of linear algebra, such as iterative SVD usually stops iterating when $||E|| < tol\,||A||$, where E is the perturbation, A is the problem matrix, *tol* a specified tolerance, and $||\cdot||$ denotes a matrix norm.

Let us construct a fictitious linear system starting from eq. (B.1); take any vector $y$ with a non-negligible component along $x$, i.e. $y \cdot x \neq 0$ and solve the linear system

$$A(\lambda)x' = y \tag{B.15}$$

for $x'$, by means of a standard solver of linear equations. Obviously as $\lambda$ approaches an eigenvalue, $\lambda \to \lambda_0$, the norm of $x'$ diverges, $\|x'\| \to \infty$. So does the solution provided by the linear solver, but if normalized it can be proven to approximate the corresponding eigenvector. Thus a procedure for solving our problem can start constructing a map of the norm of $x'$ as a function of $\lambda \in \Omega \subset \mathbb{C}$ where a solution is believed to exist. Then we focus on a subregion $\bar{\Omega} \subset \Omega$ where $\|x'\| >> \|v\|$. In such a region, consider

$$f(\lambda) = \frac{1}{x'_p}$$

where $x'_p$ denotes the $p$ component of $x'$. We assume $p$ is chosen so that the $p$ component of the true solution $x$ is not negligible. In a region sufficiently close to the eigenvalue $\lambda_0$, $f(\lambda)$ is a continuous complex function of a single complex variable that undergoes zero-crossing at the eigenvalue, provided that this latter is isolated and nondegenerate.

We have thus recasted our nonlinear eigenvalue problem in a root-finding combined to the simplest and less computational demanding linear algebra tools (linear system solution). In the complex plane we cannot bracket solutions[3] as easily as on the real axis, but secant method or higher order ones work properly.

## B.4 Complex Integration

Another idea is to use fundamental results of complex function theory. We recall here some important results, mainly due to A. Cauchy:

**Theorem B.4.1 (Cauchy's Integral Theorem)** *Let $U$ be an open subset of $\mathbb{C}$ which is simply connected (i.e. it has no holes), let $f : U \to \mathbb{C}$ be a holomorphic function, and let $\gamma$ be a rectifiable closed path in $U$. Then,*

$$\oint_\gamma f(z)\, dz = 0 \tag{B.16}$$

**Theorem B.4.2 (Cauchy's Integral Formula)** *Let $U$ be an open subset of the complex plane $\mathbb{C}$, $f : U \to \mathbb{C}$ is a holomorphic function, and the simply connected region $D$ is completely contained in $U$. Let $\gamma$ be the closed path forming the boundary of $D$. Then we have for every $a$ in the interior of $D$:*

$$f(a) = \frac{1}{2\pi i} \oint_\gamma \frac{f(z)}{z - a}\, dz \tag{B.17}$$

3. We mean to use e.g. bisection method for delimiting a real range where Newton or equivalent approaches are expected to converge.

**Theorem B.4.3 (Cauchy's Argument Principle)** *Let us consider a meromorphic function $f(z)$ (i.e. analytic except in a finite number of isolated points, that are required to be* poles*) on $D$ whose contour is the simple closed path $\gamma$. If $f$ has no zeros or poles on $\gamma$, then*

$$\oint_\gamma \frac{f'(z)}{f(z)}\,dz = 2\pi i(N-P) \tag{B.18}$$

*where $N$ and $P$ denote respectively the number of zeros and poles in $D$, counted respectively as many as their multiplicity and order.*

In literature we found several examples of applications of these facts to the computation of complex zeros of electromagnetic problems, [105], [106], [107].

We studied in more details the Abd-ellal, Delves, and Reid (ADR) method as described in [106], since does not require the function to be analytic inside the inspection region, nor its derivative computation. We outline a prove of it, since it is not provided in the mentioned paper.

Consider a function $f(z)$ such as B.3, suppose it can have inside a fixed complex region $N$ zeros, $z_0, z_1, \cdots, z_{N-1}$ and no matter how many poles. Suppose the region has contour $\gamma$, a closed simple regular path, that does not cross any zero of $f$. Thus $1/f(z)$ has exactly $N$ poles, that are the unknown solutions of our problem. If we factor out these poles we obtain an analytic function on the region. Then by Cauchy's Integral Theorem, its contour integral must be zero. Posing

$$h(z) = \frac{(z-z_0)(z-z_1)\cdots(z-z_{N-1})}{f(z)}$$

it results

$$\oint_\gamma h(z)\,dz = \oint_\gamma \frac{p_N(z)}{f(z)}\,dz = 0$$

where $p_N(z) = c_0 + c_1 z + c_2 z^2 + \cdots + c_{N-1}z^{N-1} + z^N$ denotes the polynomial whose zeros are our solutions. Since we have $N$ unknown coefficients, we need at least $N$ equations. Multiplying $h(z)$ by $z^k$, with $k = 0, 1, 2, \cdots, N-1$, does not change the regularity of the resulting function, then we can write

$$\oint_\gamma z^k h(z)\,dz = 0 \tag{B.19}$$

Then posing

$$G_k = \oint_\gamma \frac{z^k}{f(z)}\,dz, \text{ for } k = 0, 1, 2, \cdots, 2N-1 \tag{B.20}$$

we can express B.19 as a linear system

$$\sum_{j=0}^{N-1} c_j G_{r+j} + G_{r+N} = 0, \text{ for } r = 0, 1, 2, \cdots, N-1 \tag{B.21}$$

Solving this system we obtain the coefficients of $p_N(z)$ and compute its zeros.

A suitable choice of integration path and a correct estimate of $N$ allows us to be quite sure of having found accurate solutions, for which a *refinement step*, by Müller method for example (three point method that does not require derivatives), is quickly accomplished.

In fact if we start looking for too many zeros (more than how many they actually are), we obtain very large $G_k$ values for highest $k$s. We should arrange a procedure to check if they are too large and discard them; we then reduce $N$ and compute solutions of a lower order polynomial (it should be equal to the number of zeros in the region). The risk of not doing so is to have large inaccuracy on coefficients $c_i$, to find spurious solutions, and also to affect their accuracy, slowing down or failing in refinement. If a polynomial order less than number of zeros is chosen, we include poles inside the region and this affect the final value of every integral, then we could not obtain any good result.

Notice that we have to compute function values only once, then we could compute a lot of integrals, select the maximum $N$ to avoid round-off errors, i.e. we discard too large $G_k$, and solve the linear system. Then a method to divide the initial region in subregions is to be provided, computation of zeros in each subregion and comparison (in total number and position) between zeros in the old region and in its parts permit to decide whether we have reached a suitable partition, compatible with the threshold above which we discard the $G_k$s. Otherwise we can repeat the partition procedure until we reach a desired accuracy.

Since determinant calculation leads to overflow, this approach is not simple to apply in our case, but can be useful to locate efficiently leaky modes of guiding structures.

In figure B.1 we show how the ADR approach operates in the complex plane.

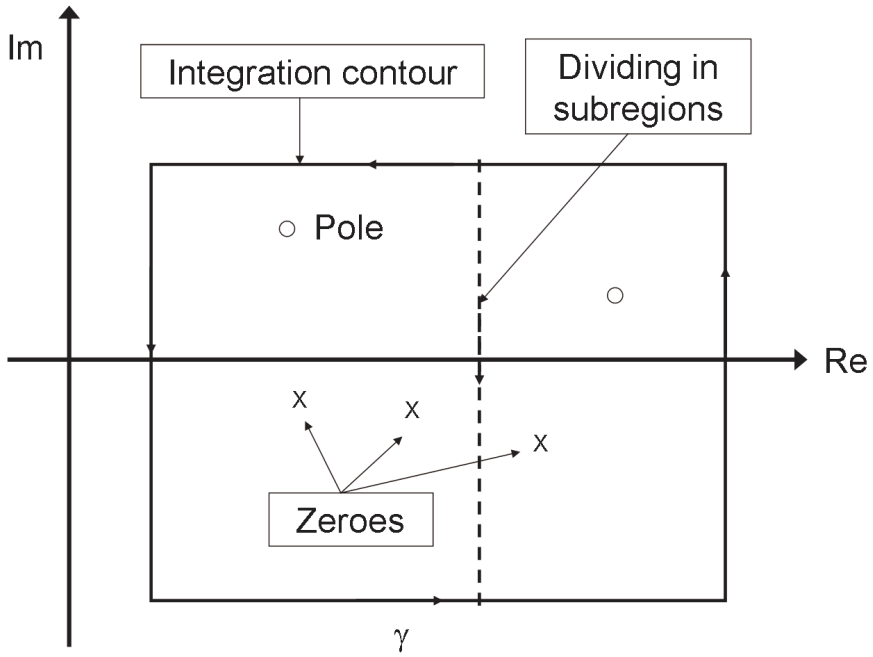


Figure B.1: The ADR method is based on complex integration. Zeroes of a complex function (e.g. dispersion relation) are factored out and the problem is reduced to a polynomial zero finding procedure. Local refinement of solutions and division in subregions is employed to improve accuracy. This is required if a large number of zeroes lies inside the region.

# Appendix C

# Acronyms

**A-FMM** aperiodic Fourier modal method

**ASE** amplified spontaneous emission

**BPM** beam propagation method

**BiBPM** bidirectional BPM

**CMOS** complementary metal oxide semiconductor

**CMT** coupled-mode theory

**C-QED** cavity QED

**C-RCWA** cylindrical RCWA (used to denote our implementation of A-FMM)

**CROW** coupled-resonator optical waveguide

**EIM** effective index method

**FDTD** finite-difference time-domain method

**FF** fundamental frequency

**FMM** Fourier modal method

**FWHM** full width at the half maximum

**GS** gap soliton

**MOSFET** metal-oxide-semiconductor field-effect transistor

**NL** nonlinear

**NLO** nonlinear Optics

**ODE** ordinary differential equation

**OKE** optical Kerr effect

**PDE** partial differential equation

**PECVD** plasma-enhanced chemical vapour deposition

**PML** perfectly-matched layer

**QPM** quasi phase-matching

**RCWA** rigorous coupled-wave analysis (original name of A-FMM for grating theorists)

**RIE** reactive ion etching

**SGS** spatial gap soliton

**SH** second harmonic

**SHG** second harmonic generation

**SOI** silicon on insulator

**SVEA** slowly-varying envelope approximation

**SV** singular value

**SVD** singular value decomposition

**UV** ultraviolet

**WGM** whispering-gallery mode

# Appendix D

# Publications

## D.1 International peer-review journals

1. A. Armaroli, S. Valentini, G. Bellanca, S. Trillo, "Modeling of spatial gap solitons in nonlinear waveguide arrays," *Microwave and Optical Technology Letters*, Vol. 48, No. 12, pp. 2591–2595, 28 Sept. 2006.

2. A. Armaroli, A. Morand, P. Benech, G. Bellanca, and S. Trillo, "Three-dimensional analysis of cylindrical microresonators based on the aperiodic Fourier modal method," *J. Opt. Soc. Am. A*, Vol. 25, no. 3, pp. 667–75, March 2008.

## D.2 International conferences without proceedings

3. A. Armaroli, S.Valentini, G. Bellanca, S. Trillo, "Spatial gap solitons in arrays of evanescently coupled optical waveguides," Third Workshop on Metamaterials and Special Materials for Electromagnetic Applications and TLC, Rome 30-31 March 2006.

4. A. Armaroli, A. Morand, P. Benech, G. Bellanca, S. Trillo, "3D Modelling of Microdisk Resonators Based on Fourier Modal Method," XVI International Workshop on Optical Waveguide Theory and Numerical Modelling, OWTNM 2007, Copenhagen 27-28 April 2007, Poster session, PO-01.15.

## D.3 Italian national conferences with proceedings

5. A. Armaroli, S.Valentini, G. Bellanca, S. Trillo, "Modellizzazione di solitoni di gap spaziali in array di guide non lineari," XVI Riunione Nazionale di Elettromagnetismo, RiNEM 2006, Genova, 18–21 September 2006.

## D.4 Papers in preparation

6. A. Armaroli, A. Morand, P. Benech, G. Bellanca, and S. Trillo, "Sandwich microdisk: improving cavity performance in highly integrated systems", *in preparation.*

7. A. Armaroli, G. Bellanca, C. Conti, and S. Trillo, "Doubly resonant two color spatial gap solitons", *in preparation.*

# List of Figures

# List of Tables

# Bibliography


[1] H. Rong, R. Jones, A. Liu, O. Cohen, D. Hak, A. Fang, and M. Paniccia, "A continuous-wave Raman silicon laser," *Nature*, vol. 433, pp. 725–728, Feb. 2005.

[2] A. Liu, R. Jones, L. Liao, D. Samara-Rubio, D. Rubin, O. Cohen, R. Nicolaescu, and M. Paniccia, "A high-speed silicon optical modulator based on a metal-oxide-semiconductor capacitor," *Nature*, vol. 427, pp. 615–618, Feb. 2004.

[3] A. W. Fang, H. Park, Y.-H. Kuo, R. Jones, O. Cohen, D. Liang, O. Raday, M. N. Sysak, M. J. Paniccia, and J. E. Bowers, "Hybrid silicon evanescent devices," *Materials Today*, vol. 10, no. 7-8, pp. 28–35, 2007.

[4] N. Engheta and R. W. Ziolkowski, *Metamaterials*. New York: Wiley-Interscience, 2006.

[5] L. Pavesi and G. Guillot, *Optical Interconnects: the Silicon Approach*. Berlin: Springer, 2006.

[6] K. J. Vahala, "Optical microcavities," *Nature*, vol. 424, pp. 839–846, Aug. 2003.

[7] A. B. Matsko and V. S. Ilchenko, "Optical resonators with whispering-gallery modes—part I: basics," *IEEE J. Sel. Topics Quantum Electron.*, vol. 12, pp. 3–14, Jan.–Feb. 2006.

[8] V. S. Ilchenko and A. B. Matsko, "Optical resonators with whispering-gallery modes—part ii: applications," *IEEE J. Sel. Topics Quantum Electron.*, vol. 12, pp. 15–32, Jan.–Feb. 2006.

[9] A. Yariv, Y. Xu, R. K. Lee, and A. Scherer, "Coupled-resonator optical waveguide: a proposal and analysis," *Opt. Lett.*, vol. 24, no. 11, pp. 711–713, 1999.

[10] S. Mookherjea, S. Mookherjea, and A. Yariv, "Coupled resonator optical waveguides," *IEEE J. Sel. Topics Quantum Electron.*, vol. 8, no. 3, pp. 448–456, 2002.

[11] M. Bayer, T. Gutbrod, J. P. Reithmaier, A. Forchel, T. L. Reinecke, P. A. Knipp, A. A. Dremin, and V. D. Kulakovskii, "Optical modes in photonic molecules," *Phys. Rev. Lett.*, vol. 81, pp. 2582–2585, Sep 1998.

[12] S. V. Boriskina, T. M. Benson, and P. Sewell, "Photonic molecules made of matched and mismatched microcavities: new functionalities of microlasers and optoelectronic

components," in *Laser Resonators and Beam Control IX. Edited by Kudryashov, Alexis V.; Paxton, Alan H.; Ilchenko, Vladimir S.. Proceedings of the SPIE, Volume 6452, pp. 64520X (2007).*, vol. 6452 of *Presented at the Society of Photo-Optical Instrumentation Engineers (SPIE) Conference*, p. 64520X, Mar. 2007.

[13] R. Slusher and B. J. Eggleton, *Nonlinear Photonic Crystals*. Berlin: Springer-Verlag, 2003.

[14] E. E. Kriezis, P. Pantelakis, C. S. Antonopoulos, and A. G. Papagiannakis, "Full vector beam propagation method for axially dependent 3-D structures," *IEEE Trans. Magn.*, vol. 33, pp. 1540–1543, March 1997.

[15] E. Kriezis and A. Papagiannakis, "A three-dimensional full vectorial beam propagation method for z-dependent structures," *IEEE J. Quantum Electron.*, vol. 33, pp. 883–890, May 1997.

[16] W. Huang and C. Xu, "Simulation of three-dimensional optical waveguides by a full-vector beam propagation method," *IEEE J. Quantum Electron.*, vol. 29, pp. 2639–2649, Oct. 1993.

[17] G. R. Hadley, "Wide-angle beam propagation using Padé approximant operators," *Opt. Lett.*, vol. 17, no. 20, pp. 1426–1428, 1992.

[18] R. Boyd, *Nonlinear Optics*. Boston: Academic Press, 2003.

[19] A. Snyder and J. Love, *Optical Waveguide Theory*. Boston: Kluwer Academic, 1983.

[20] A. Taflove and S. Hagness, *Computational Electrodynamics*. Boston: Artech House, 2000.

[21] M. Lauritano, A. Parini, G. Bellanca, S. Trillo, M. Conforti, A. Locatelli, and C. De Angelis, "Bistability, limiting, and self-pulsing in backward second-harmonic generation: a time-domain approach," *Journal of Optics A: Pure and Applied Optics*, vol. 8, no. 7, pp. S494–S501, 2006.

[22] Q. H. Liu, "The PSTD algorithm: A time-domain method requiring only two cells per wavelength," *Microwave and Optical Technology Letters*, vol. 15, no. 3, pp. 158–165, 1997.

[23] D. Yevick and B. Hermansson, "Efficient beam propagation techniques," *IEEE J. Quantum Electron.*, vol. 26, pp. 109–112, Jan. 1990.

[24] G. R. Hadley, "Transparent boundary condition for beam propagation," *Opt. Lett.*, vol. 16, no. 9, pp. 624–626, 1991.

[25] C. Vassallo and F. Collino, "Highly efficient absorbing boundary conditions for the beam propagation method," *J. Lightw. Technol.*, vol. 14, pp. 1570–1577, June 1996.

[26] P. L. Ho and Y. Y. Lu, "An efficient numerical method for dfb structures based on period doubling and rational approximations," in *Proceedings of the U. S. ARO-FE Conference 2001*, 2001.

[27] P. L. Ho and Y. Y. Lu, "A mode-preserving perfectly matched layer for optical waveguides," *Photonics Technology Letters, IEEE*, vol. 15, no. 9, pp. 1234–1236, Sept. 2003.

[28] R. Scarmozzino, A. Gopinath, R. Pregla, and S. Helfert, "Numerical techniques for modeling guided-wave photonic devices," *IEEE J. Sel. Topics Quantum Electron.*, vol. 6, pp. 150–162, Jan.–Feb. 2000.

[29] P. Bienstman and R. Baets, "Optical modelling of photonic crystals and VCSELs using eigenmode expansion and perfectly matched layers," *Optical and Quantum Electronics*, vol. 33, pp. 327–341, Apr. 2001.

[30] P. Lalanne and E. Silberstein, "Fourier-modal methods applied to waveguide computational problems," *Opt. Lett.*, vol. 25, no. 15, pp. 1092–1094, 2000.

[31] M. Lohmeyer, "Wave-matching method for mode analysis of dielectric waveguides," *Optical and Quantum Electronics*, vol. 29, pp. 907–922, Sept. 1997.

[32] A. S. Sudbø, "Film mode matching: a versatile numerical method for vector mode field calculations in dielectric waveguides ," *Pure Applied Optics*, vol. 2, pp. 211–233, May 1993.

[33] J. Čtyroký, "Improved bidirectional-mode expansion propagation algorithm based on Fourier series," *J. Lightwave Technol.*, vol. 25, no. 9, pp. 2321–2330, 2007.

[34] L. Li, "Formulation and comparison of two recursive matrix algorithms for modeling layered diffraction gratings," *J. Opt. Soc. Am. A*, vol. 13, no. 5, pp. 1024–1035, 1996.

[35] W. Nakagawa, R.-C. Tyan, and Y. Fainman, "Analysis of enhanced second-harmonic generation in periodic nanostructures using modified rigorous coupled-wave analysis in the undepleted-pump approximation," *J. Opt. Soc. Am. A*, vol. 19, no. 9, pp. 1919–1928, 2002.

[36] B. Maes, P. Bienstman, and R. Baets, "Modeling of Kerr nonlinear photonic components with mode expansion," *Optical and Quantum Electronics*, vol. 36, pp. 15–24, Jan. 2004.

[37] Y.-P. Chiou and H.-C. Chang, "Efficient beam-propagation method based on Padé approximants in the propagation direction," *Opt. Lett.*, vol. 22, no. 13, pp. 949–951, 1997.

[38] G. R. Hadley, "Multistep method for wide-angle beam propagation," *Opt. Lett.*, vol. 17, no. 24, pp. 1743–1745, 1992.

[39] Y. Y. Lu and P. L. Ho, "Beam propagation method using a $[(p-1)/p]$ Padé approximant of the propagator," *Opt. Lett.*, vol. 27, no. 9, pp. 683–685, 2002.

[40] Y. Y. Lu and P. L. Ho, "A single scatter improvement for beam propagation methods," *Photonics Technology Letters, IEEE*, vol. 14, no. 8, pp. 1103–1105, Aug 2002.

[41] P. L. Ho and Y. Y. Lu, "Improving the beam propagation method for TM polarization," *Optical and Quantum Electronics*, vol. 35, pp. 507–519, Mar. 2003.

[42] S. L. Chui and Y. Y. Lu, "A propagator-$\theta$ beam propagation method," *Photonics Technology Letters, IEEE*, vol. 16, no. 3, pp. 822–824, March 2004.

[43] L. D. S. Alcantara, F. L. Teixeira, A. C. Cesar, and B.-H. Borges, "An improved wide-angle FD-BPM for nonlinear and nonreciprocal waveguides," *IEEE Trans. Magn.*, vol. 39, pp. 1223–1226, May 2003.

[44] Y. Y. Lu, "A complex coefficient rational approximation of $\sqrt{1+x}$," *Appl. Numer. Math.*, vol. 27, no. 2, pp. 141–154, 1998.

[45] D. Yevick, M. Glasner, and B. Hermansson, "Numerical studies of split-operator finite-difference alternating-direction implicit propagation techniques based on generalized Padé approximants," *Opt. Lett.*, vol. 17, no. 10, pp. 725–727, 1992.

[46] H. El-Refaei, I. Betty, and D. Yevick, "The application of complex Padé approximants to reflection at optical waveguide facets," *IEEE Photon. Technol. Lett.*, vol. 12, pp. 158–160, Feb. 2000.

[47] D. Yevick and D. J. Thomson, "Complex Padé approximants for wide-angle acoustic propagators," *Acoustical Society of America Journal*, vol. 108, pp. 2784–2790, Dec. 2000.

[48] D. Yevick, "The application of complex Padé approximants to vector field propagation," *IEEE Photon. Technol. Lett.*, vol. 12, pp. 1636–1638, Dec. 2000.

[49] I. Ilic, R. Scarmozzino, and R. M. Osgood, Jr., "Investigation of the Padé approximant-based wide-angle beam propagation method for accurate modeling of waveguiding circuits," *J. Lightw. Technol.*, vol. 14, pp. 2813–2822, Dec. 1996.

[50] F. A. Milinazzo, C. A. Zala, and G. H. Brooke, "Rational square-root approximations for parabolic equation algorithms," *Acoustical Society of America Journal*, vol. 101, pp. 760–766, Feb. 1997.

[51] H. Rao, R. Scarmozzino, and R. M. Osgood, Jr., "A bidirectional beam propagation method for multiple dielectric interfaces," *IEEE Photon. Technol. Lett.*, vol. 11, pp. 830–832, July 1999.

[52] H. El-Refaei, D. Yevick, and I. Betty, "Stable and noniterative bidirectional beam propagation method," *IEEE Photon. Technol. Lett.*, vol. 12, pp. 389–391, April 2000.

[53] Y. Y. Lu and S. H. Wei, "A new iterative bidirectional beam propagation method," *Photonics Technology Letters, IEEE*, vol. 14, no. 11, pp. 1533–1535, Nov 2002.

[54] Y. Y. Lu and P. L. Ho, "An improved perfectly matched layer for optical waveguides," in *Proceedings of the U. S. ARO-FE Conference 2001*, 2001.

[55] P. L. Ho and Y. Y. Lu, "A stable bidirectional propagation method based on scattering operators," *Photonics Technology Letters, IEEE*, vol. 13, no. 12, pp. 1316–1318, Dec 2001.

[56] P. L. Ho and Y. Y. Lu, "A bidirectional beam propagation method for periodic waveguides," *Photonics Technology Letters, IEEE*, vol. 14, no. 3, pp. 325–327, Mar 2002.

[57] P.-L. Liu, S. Yang, and D. Yuan, "The semivectorial beam propagation method," *IEEE J. Quantum Electron.*, vol. 29, pp. 1205–1211, April 1993.

[58] P.-C. Lee and E. Voges, "Three-dimensional semi-vectorial wide-angle beam propagation method," *J. Lightw. Technol.*, vol. 12, pp. 215–225, Feb. 1994.

[59] S. L. Chui and Y. Y. Lu, "Wide-angle full-vector beam propagation method based on an alternating direction implicit preconditioner," *J. Opt. Soc. Am. A*, vol. 21, no. 3, pp. 420–425, 2004.

[60] Y.-L. Hsueh, M.-C. Yang, and H.-C. Chang, "Three-dimensional noniterative full-vectorial beam propagation method based on the alternating direction implicit method," *J. Lightw. Technol.*, vol. 17, pp. 2389–2397, Nov. 1999.

[61] H.-F. Chou, C.-F. Lin, and G.-C. Wang, "An iterative finite difference beam propagation method for modeling second-order nonlinear effects in optical waveguides," *J. Lightw. Technol.*, vol. 16, pp. 1686–1693, Sept. 1998.

[62] H.-F. Chou, C.-F. Lin, and S. Mou, "Comparisons of finite difference beam propagation methods for modeling second-order nonlinear effects," *J. Lightw. Technol.*, vol. 17, pp. 1481–1486, Aug. 1999.

[63] A.-D. Capobianco, D. Brillo, C. De Angelis, and G. Nalesso, "Fast beam propagation method for the analysis of second-order nonlinear phenomena," *IEEE Photon. Technol. Lett.*, vol. 10, pp. 543–545, April 1998.

[64] Y. Y. Lu and P. L. Ho, "Beam propagation modeling of arbitrarily bent waveguides," *Photonics Technology Letters, IEEE*, vol. 14, no. 12, pp. 1698–1700, Dec. 2002.

[65] A. Locatelli, D. Modotto, C. D. Angelis, F. M. Pigozzo, and A.-D. Capobianco, "Nonlinear bidirectional beam propagation method based on scattering operators for periodic microstructured waveguides," *J. Opt. Soc. Am. B*, vol. 20, no. 8, pp. 1724–1731, 2003.

[66] H. Rao, M. J. Steel, R. Scarmozzino, and R. M. Osgood, Jr., "Complex propagators for evanescent waves in bidirectional beam propagation method," *J. Lightw. Technol.*, vol. 18, pp. 1155–1160, Aug. 2000.

[67] M. Vajta, "Some remarks on Padé approximations," in $3^{rd}$ *TEMPUS-INTCOM Symposium*, September 9–14 2000.

[68] A. Locatelli, F.-M. Pigozzo, F. Baronio, D. Modotto, A.-D. Capobianco, and C. De Angelis, "Bidirectional beam propagation method for second-harmonic generation in engineered multilayered waveguides," *Optical and Quantum Electronics*, vol. 35, pp. 429–452, Mar. 2003.

[69] A. Sukhorukov, Y. Kivshar, H. Eisenberg, and Y. Silberberg, "Spatial optical solitons in waveguide arrays," *IEEE J. Quantum Electron.*, vol. 39, pp. 31–50, Jan. 2003.

[70] J. W. Fleischer, M. Segev, N. K. Efremidis, and D. N. Christodoulides, "Observation of two-dimensional discrete solitons in optically induced nonlinear photonic lattices," *Nature*, vol. 422, pp. 147–150, Mar. 2003.

[71] A. Fratalocchi, G. Assanto, K. A. Brzdakiewicz, and M. A. Karpierz, "Optical multiband vector breathers in tunable waveguide arrays," *Opt. Lett.*, vol. 30, no. 2, pp. 174–176, 2005.

[72] S.-P. Gorza, D. Taillaert, R. Baets, B. Maes, P. Emplit, and M. Haelterman, "Experimental characterization of optical-gap solitons in a one-dimensional photonic crystal made of a corrugated semiconductor planar waveguide," *Phys. Rev. B*, vol. 74, no. 23, p. 235327, 2006.

[73] D. N. Christodoulides, F. Lederer, and Y. Silberberg, "Discretizing light behaviour in linear and nonlinear waveguide lattices," *Nature*, vol. 424, pp. 817–823, Aug. 2003.

[74] J. Fleischer, G. Bartal, O. Cohen, T. Schwartz, O. Manela, B. Freedman, M. Segev, H. Buljan, and N. Efremidis, "Spatial photonics in nonlinear waveguide arrays," *Opt. Express*, vol. 13, no. 6, pp. 1780–1796, 2005.

[75] J. Feng, "Alternative scheme for studying gap solitons in an infinite periodic Kerr medium," *Opt. Lett.*, vol. 18, no. 16, pp. 1302–1304, 1993.

[76] R. F. Nabiev, P. Yeh, and D. Botez, "Spatial gap solitons in periodic nonlinear structures," *Opt. Lett.*, vol. 18, no. 19, pp. 1612–1614, 1993.

[77] W. Chen and D. L. Mills, "Gap solitons and the nonlinear optical response of superlattices," *Phys. Rev. Lett.*, vol. 58, pp. 160–163, Jan 1987.

[78] C. Conti and S. Trillo, "Bifurcation of gap solitons through catastrophe theory," *Phys. Rev. E*, vol. 64, p. 036617, Aug 2001.

[79] B. J. Eggleton, R. E. Slusher, C. M. de Sterke, P. A. Krug, and J. E. Sipe, "Bragg grating solitons," *Phys. Rev. Lett.*, vol. 76, pp. 1627–1630, Mar 1996.

[80] D. Mandelik, R. Morandotti, J. S. Aitchison, and Y. Silberberg, "Gap solitons in waveguide arrays," *Phys. Rev. Lett.*, vol. 92, no. 9, p. 093904, 2004.

[81] D. Neshev, A. A. Sukhorukov, B. Hanna, W. Krolikowski, and Y. S. Kivshar, "Controlled generation and steering of spatial gap solitons," *Phys. Rev. Lett.*, vol. 93, p. 083905, Aug 2004.

[82] F. Chen, M. Stepić, C. Rüter, D. Runde, D. Kip, V. Shandarov, O. Manela, and M. Segev, "Discrete diffraction and spatial gap solitons in photovoltaic $LiNbO_3$ waveguide arrays," *Opt. Express*, vol. 13, no. 11, pp. 4314–4324, 2005.

[83] A. A. Sukhorukov and Y. S. Kivshar, "Nonlinear guided waves and spatial solitons in a periodic layered medium," *J. Opt. Soc. Am. B*, vol. 19, no. 4, pp. 772–781, 2002.

[84] A. Yariv and P. Yeh, *Optical Waves in Crystals: Propagation and Control of Laser Radiation*. New York: Wiley-Interscience, 2002.

[85] A. V. Buryak, P. D. Trapani, D. V. Skryabin, and S. Trillo, "Optical solitons due to quadratic nonlinearities: from basic physics to futuristic applications," *Physics Reports*, vol. 370, pp. 63–235, Nov. 2002.

[86] T. Benson, S. Boriskina, P. Sewell, A. Vukovic, S. Greedy, and A. Nosich, "Micro-optical resonators for microlasers and integrated optoelectronics," in *Frontiers in Planar Lightwave Circuit Technology* (S. Janz, J. Čtyroký, and S. Tanez, eds.), pp. 39–70, Springer, 2006.

[87] S. M. Spillane, T. J. Kippenberg, and K. J. Vahala, "Ultralow-threshold Raman laser using a spherical dielectric microcavity," *Nature*, vol. 415, pp. 621–623, Feb. 2002.

[88] D. K. Armani, T. J. Kippenberg, S. M. Spillane, and K. J. Vahala, "Ultra-high-$Q$ toroid microcavity on a chip," *Nature*, vol. 421, pp. 925–928, Feb. 2003.

[89] A. Morand, Y. Zhang, B. Martin, K. P. Huy, D. Amans, P. Benech, J. Verbert, E. Hadji, and J.-M. Fédéli, "Ultra-compact microdisk resonator filters on soi substrate," *Opt. Express*, vol. 14, no. 26, pp. 12814–12821, 2006.

[90] P. Bienstman, S. Selleri, L. Rosa, H. Uranus, W. Hopman, R. Costa, A. Melloni, L. Andreani, J. Hugonin, P. Lalanne, D. Pinto, S. Obayya, M. Dems, and K. Panajotov, "Modelling leaky photonic wires: A mode solver comparison," *Optical and Quantum Electronics*, vol. 38, pp. 731–759, July 2006.

[91] T. M. Benson, S. V. Boriskina, P. Sewell, A. Vukovic, S. C. Greedy, and A. I. Nosich, "Microcavities: An inspiration for advanced modelling techniques," in *Proceedings of 7th* International Conference Transparent Optical Networks *(ICTON), Barcelona, Spain, July 3–7*, July 3–7 2005.

[92] L. Prkna, M. Hubàlek, and J. Čtyroký, "Field modeling of circular microresonators by film mode matching," *IEEE J. Sel. Topics Quantum Electron.*, vol. 11, pp. 217–223, Jan–Feb 2005.

[93] R. Stoffer, K. R. Hiremath, M. Hammer, L. Prkna, and J. Čtyroký, "Cylindrical integrated optical microresonators: Modeling by 3-D vectorial coupled mode theory," *Optics Communications*, vol. 256, pp. 46–67, Dec. 2005.

[94] P. Lalanne, J. P. Hugonin, and J. M. Gérard, "Electromagnetic study of the quality factor of pillar microcavities in the small diameter limit," *Applied Physics Letters*, vol. 84, no. 23, pp. 4726–4728, 2004.

[95] M. G. Moharam, E. B. Grann, D. A. Pommet, and T. K. Gaylord, "Formulation for stable and efficient implementation of the rigorous coupled-wave analysis of binary gratings," *J. Opt. Soc. Am. A*, vol. 12, no. 5, pp. 1068–1076, 1995.

[96] P. Lalanne and G. M. Morris, "Highly improved convergence of the coupled-wave method for tm polarization," *J. Opt. Soc. Am. A*, vol. 13, no. 4, pp. 779–784, 1996.

[97] L. Li, "Use of Fourier series in the analysis of discontinuous periodic structures," *J. Opt. Soc. Am. A*, vol. 13, no. 9, pp. 1870–1876, 1996.

[98] M. Abramowitz and I. A. Stegun, *Handbook of Mathematical Functions with Formulas, Graphs, and Mathematical Tables*. New York: Dover, ninth Dover printing, tenth GPO printing ed., 1964.

[99] J. P. Hugonin and P. Lalanne, "Perfectly matched layers as nonlinear coordinate transforms: a generalized formalization," *J. Opt. Soc. Am. A*, vol. 22, no. 9, pp. 1844–1849, 2005.

[100] S. G. Johnson, "Notes on perfectly matched layers (PMLs)." MIT Open courseware, available online at http://dedekind.mit.edu/~stevenj/18.369/pml.pdf, November 11, 2007.

[101] F. L. Teixeira and W. C. Chew, "Systematic derivation of anisotropic PML absorbing media in cylindrical and spherical coordinates," *IEEE Microw. Guided Wave Lett.*, vol. 7, pp. 371–373, Nov. 1997.

[102] K. P. Huy, A. Morand, D. Amans, and P. Benech, "Analytical study of the whispering-gallery mode in two-dimensional microgear cavity using coupled-mode theory," *J. Opt. Soc. Am. B*, vol. 22, no. 8, pp. 1793–1803, 2005.

[103] L. Landau, E. M. Lifshitz, and L. P. Pitaevskii, *Electrodynamics of Continuous Media: Volume 8*. Oxford: Butterworth-Heinemann, 1984.

[104] V. Labay and J. Bornemann, "Matrix singular value decomposition for pole-free solutions of homogeneous matrix equations as applied to numerical modeling methods," *IEEE Microw. Guided Wave Lett.*, vol. 2, pp. 49–51, Feb. 1992.

[105] E. Anemogiannis and E. N. Glytsis, "Multilayer waveguides: efficient numerical analysis of general structures," *J. Lightw. Technol.*, vol. 10, pp. 1344–1351, Oct. 1992.

[106] E. Anemogiannis, E. N. Glytsis, and T. K. Gaylord, "Efficient solution of eigenvalue equations of optical waveguiding structures," *J. Lightw. Technol.*, vol. 12, pp. 2080–2084, Dec. 1994.

[107] O. Conradi, "Determining the resonator wavelength of VCSELs by Cauchy's integral formula," *Optical and Quantum Electronics*, vol. 31, pp. 1047–1058, Oct. 1999.

[108] J. H. Mathews, "Nelder-Mead search for a minimum." Available online at http://math.fullerton.edu/mathews/n2003/NelderMeadMod.html, 2004.

[109] V. A. Mandelshtam and H. S. Taylor, "Harmonic inversion of time signals and its applications," *The Journal of Chemical Physics*, vol. 107, no. 17, pp. 6756–6769, 1997.

[110] S. G. Johnson, "Harminv implementation." Available at http://ab-initio.mit.edu/wiki/index.php/Harminv, July 4, 2006.

[111] P. Bienstman and R. Baets, "Advanced boundary conditions for eigenmode expansion models," *Optical and Quantum Electronics*, vol. 34, pp. 523–540, May 2002.

[112] V. R. Almeida, Q. Xu, C. A. Barrios, and M. Lipson, "Guiding and confining light in void nanostructure," *Opt. Lett.*, vol. 29, no. 11, pp. 1209–1211, 2004.

[113] B. Min, T. J. Kippenberg, L. Yang, K. J. Vahala, J. Kalkman, and A. Polman, "Erbium-implanted high-$Q$ silica toroidal microcavity laser on a silicon chip," *Phys. Rev. A*, vol. 70, p. 033803, Sep 2004.

[114] C. A. Barrios and M. Lipson, "Electrically driven silicon resonant light emitting device based on slot-waveguide," *Opt. Express*, vol. 13, no. 25, pp. 10092–10101, 2005.

[115] J. T. Robinson, C. Manolatou, L. Chen, and M. Lipson, "Ultrasmall mode volumes in dielectric optical microcavities," *Phys. Rev. Lett.*, vol. 95, no. 14, p. 143901, 2005.

[116] T. D. Visser, H. Blok, B. Demeulenaere, and D. Lenstra, "Confinement factors and gain in optical amplifiers," *IEEE J. Quantum Electron.*, vol. 33, pp. 1763–1766, Oct. 1997.

[117] E. Jordana, J.-M. Fedeli, P. Lyan, J. P. Colonna, P. Gautier, N. Daldosso, L. Pavesi, Y. Lebour, P. Pellegrino, B. Garrido, J. Blasco, F. Cuesta-Soto, and P. Sanchis, "Deep-UV lithography fabrication of slot waveguides and sandwiched waveguides for nonlinear applications," in *Proc. 4th IEEE International Conference on Group IV Photonics*, pp. 1–3, 19–21 Sept. 2007.

[118] A. Yariv, "Universal relations for coupling of optical power between microresonators and dielectric waveguides," *Electronics Letters*, vol. 36, pp. 321–322, 17 Feb. 2000.

[119] G. Cusmai, F. Morichetti, P. Rosotti, R. Costa, and A. Melloni, "Circuit-oriented modelling of ring-resonators," *Optical and Quantum Electronics*, vol. 37, pp. 343–358, Jan. 2005.

[120] J. Čtyroký, I. Richter, and M. Šiňor, "Dual resonance in a waveguide-coupled ring microresonator," *Optical and Quantum Electronics*, vol. 38, pp. 781–797, July 2006.

[121] B. E. Little, S. T. Chu, H. A. Haus, J. Foresi, and J.-P. Laine, "Microring resonator channel dropping filters," *J. Lightw. Technol.*, vol. 15, pp. 998–1005, June 1997.

[122] A. Morand, K. Phan-Huy, Y. Desieres, and P. Benech, "Analytical study of the microdisk's resonant modes coupling with a waveguide based on the perturbation theory," *J. Lightw. Technol.*, vol. 22, pp. 827–832, March 2004.

[123] Wikipedia, "Silicon on insulator — Wikipedia, The Free Encyclopedia (Wikimedia Foundation Inc.)." [encyclopedia on-line] http://en.wikipedia.org/wiki/Silicon_on_insulator, updated on 29 January 2008, 15:45 UTC. Retrieved 4 February 2008.

[124] M. Borselli, T. Johnson, and O. Painter, "Beyond the Rayleigh scattering limit in high-$Q$ silicon microdisks: theory and experiment," *Opt. Express*, vol. 13, no. 5, pp. 1515–1530, 2005.

[125] W. Liang, L. Yang, J. K. Poon, Y. Huang, K. J. Vahala, and A. Yariv, "Transmission characteristics of a Fabry-Pérot etalon-microtoroid resonator coupled system," *Opt. Lett.*, vol. 31, no. 4, pp. 510–512, 2006.

[126] M. Fujita and T. Baba, "Proposal and finite-difference time-domain simulation of whispering gallery mode microgear cavity," *IEEE J. Quantum Electron.*, vol. 37, pp. 1253–1258, Oct. 2001.

[127] V. M. N. Passaro, F. D. Leonardis, and G. Z. Mashanovich, "Investigation of coupling conditions in microgear resonators," *Opt. Express*, vol. 15, no. 3, pp. 797–808, 2007.

[128] K. Phan-Huy, A. Morand, and P. Benech, "Modelization of the whispering gallery mode in microgear resonators using the Floquet-Bloch formalism," *IEEE J. Quantum Electron.*, vol. 41, no. 3, pp. 357–365, 2005.

[129] V. R. Almeida and M. Lipson, "Optical bistability on a silicon chip," *Opt. Lett.*, vol. 29, no. 20, pp. 2387–2389, 2004.

[130] T. J. Johnson, M. Borselli, and O. Painter, "Self-induced optical modulation of the transmission through a high-$Q$ silicon microdisk resonator," *Opt. Express*, vol. 14, no. 2, pp. 817–831, 2006.

[131] D. Bhattacharya and A. Sharma, "Split step non-paraxial finite difference method for 3D scalar wave propagation," *Optical and Quantum Electronics*, vol. 39, pp. 865–876, Aug. 2007.

[132] K. Busch and D. N. Chigrin, "Krylov-subspace based solver for the linear and nonlinear Maxwell equations," *Physica Status Solidi B Basic Research*, vol. 244, no. 10, pp. 3479–3496, 2007.

[133] Z. Bai, *Templates for the Solution of Algebraic Eigenvalue Problems*. Philadelphia: Society for Industrial and Applied Mathematics, 2000.

[134] J. D'Errico, "Bound constrained optimization using fminsearch." Matlab® Central, available for download at http://www.mathworks.com/matlabcentral/fileexchange.

## Résumé

### Modélisation et caractérisation de dispositifs guidés micro-structurés en optique intégrée

Dans cette thèse, on présente des outils de modélisation pour étudier des structures à bandes interdites photoniques non-linéaires et des microcavités. Premièrement, une CMT et une BPM non linéaires ont été développées pour prouver la propagation de solitons spatiaux dans une structure périodique composée d'une série de guides droits. Suite à ces résultats théoriques notables, des fonctions actives sont envisagées grâce à ces régimes. Une autre méthode a ensuite été développée pour modéliser en trois dimensions des cavités optiques ayant une symétrie circulaire telles que des microdisques. La méthode est validée en comparant des résultats avec la FDTD. Il est aussi montré la possibilité de confiner le champ dans une couche de faible indice de réfraction insérée au milieu d'un microdisque de Silicium en gardant un fort coefficient de qualité et des petites volumes modales. Enfin, la caractérisation de microdisques en SOI avec des Q supérieures à 50000 est présentée.



**Mots-clés** : Optique intégrée sur Silicium, mode de galerie, microdisque, RCWA, méthode de propagation de faisceaux non-linéaire (BPM), optique non-linéaire dans guides à semiconducteur, effet Kerr, solitons spatials.



### Modelling and characterization of guiding micro-structured devices for integrated optics

In this thesis we show several modelling tools which are used to study nonlinear photonic band-gap structures and microcavities. First of all a nonlinear CMT and BPM were implemented to test the propagation of spatial solitons in a periodic device, composed by an array of parallel straight waveguides. In addition to noteworthy theoretical considerations, active functionalities are possible by exploiting these nonlinear regimes. Another algorithm was developed for the three-dimensional modelling of photonic cavities with cylindrical symmetry, such as microdisks. This method is validated by comparison with FDTD. We also show the opportunity to confine a field in a region of low refractive index lying in the centre of a silicon microdisk. High Q-factor and small mode volumes are achieved. Finally the characterization of microdisks in SOI with Q-factor larger than 50000 is presented.



**Key-words**: Silicon-integrated optics, whispering-gallery modes, microdisk resonator, RCWA, beam propagation method (BPM), nonlinear optics in semiconductor waveguides, Kerr effect, spatial solitons.



IMEP-LAHC—Institut de Microélectronique Electromagnétisme et Photonique—Minatec-INPG
3, Parvis Louis Néel BP 257 F - 38016 Grenoble Cedex 1
ENDIF—Dipartimento di Ingegneria—UNIFE
1, via Saragat, 44100 Ferrara (Italie)
andrea.armaroli@unife.it